Spectroscopic investigations of mycobacterial cytochromes

Rowan Walters

Doctor of Philosophy

University of York

Department of Chemistry

September 2024

Abstract

The study of bioenergetics has been built upon measurements from ex-vivo techniques. These techniques are powerful but necessarily divorced from the cellular reality in which bioenergetic systems operate. This thesis presents a non-invasive spectroscopic technique allowing *in situ* measurement of the electron transport chain (ETC), an essential part of the bioenergetic system.

The approach developed here, remission spectroscopy, measures back-scattered visible-wavelength light from the culture. Cytochromes absorb strongly in the visible region, and the absorbance depends on their redox state. They are mechanistically essential to the function of the ETC and are excellent spectroscopic handles for noninvasively measuring bioenergetics *in vivo*. The system is used to explore *Mycobacterium smegmatis*, a safe model mycobacterium for *M. tuberculosis*, which is currently the worst global infectious killer. Recently, the approval of the ATP-synthase inhibitor bedaquiline (BDQ) has focused attention on mycobacterial bioenergetics as a target space. However, the study of mycobacterial bioenergetics has been hampered by a lack of methods.

Methods for making spectroscopic measurements on mycobacteria in defined growth conditions are developed, as are effectors to perturb the bioenergetic system. Preliminary experiments with *in vivo* spectra demonstrated that data from homologous enzymes is incompatible with mycobacterial ones. The spectral characterisation of the mycobacterial cyt *bcc:aa*$_3$ supercomplex using spectroelectrochemistry addresses this. Complete analysis of this data required an integrated model of spectra and statistical thermodynamics, using computational and mathematical tools. Using the developed model provides an effective tool for measuring $\Delta\Psi$ *in vivo*, using endogenous and direct signals in a manner that allows the measurement before and after perturbations. The foundations for future biochemistry on other cytochrome signals are established. These could be used similarly characterised the other mycobacterial cytochromes leading to a spectral-thermodynamic model of the whole mycobacterial ETC. This would be an unprecedented window into bacterial bioenergetics.

Declaration

I declare that this thesis is a presentation of original work and has been written by me. Appropriate credit has been given to collaborative work that has been performed with others. This work has not previously been presented for a degree or other qualification at this University or elsewhere. All sources are acknowledged as references.

I acknowledge that I received assistance from Jamie Blaza, Ben Hartman, Roger Walters and Grammarly to proofread sections of this thesis. This is in line with the Policy on Transparency in Authorship in PGR Programmes.

Acknowledgements

I am enormously grateful to Jamie Blaza for sharing his enthusiasm on the subject of bioenergetics with me and thankful for his guidance and support over the years. I am also extremely grateful to Roger Springett for the lending of his chamber, his expertise in spectroscopy and the time he has taken to explain aspects of statistical thermodynamics to me.

I am very grateful to the whole of the Blaza group for their support and company in the lab. I am particularly thankful to Suzy for her shared struggle in our initial experiments with the chamber, Morwan for their extensive knowledge of mycobacteria and their genetic expertise that made my life a lot easier, Pooja for her steadfast company and early guidance with purifying difficult proteins. I would also like to thank Ben who has shared my enthusiasm for cytochromes and has been endlessly helpful and kind.

To the whole of YSBL, the technicians who have made working in the lab so much easier I am endlessly grateful. Everyone's company at coffee has generated many ridiculous conversations guaranteed to make me smile, this PhD would not have been the same without it.

To Milton, thank you for bringing so much joy into my life, and tolerating me when I get hungry. To Morven and Sula, I'm so thankful for their sisterhood and support even when things are tough. To Dad, I'm very grateful for the constant debate and sarcasm you have instilled in me. And finally to MM, thank you for your endless childlike wonder about the world that you have shared with me.

Table of Contents

Chapter 1

1.1 The discipline of bioenergetics

Life is the short-term fight against entropy as popularised by Schrödinger in his book ‘What is Life?’ (Schrodinger, 1944). Like many other physicists in the early 20th century, he had become intrigued by how cells maintain this fight against the inevitable entropy of the universe. Max Delbrück, who in part inspired Schrödinger to consider the physics of life, and other early biophysicists, spurned on the age of molecular biology, particularly in their initial work on the molecular basis of genetic inheritance (Delbrück, 1970). Within the development of biophysics, the study of how cells operate within the laws of thermodynamics has come to be known as bioenergetics. This encompasses how external energy sources are transformed into useful forms of energy that the cell can use to function. This useful energy for the cell is typically in the form of ATP, the cell's energy currency. Central to maintaining the cells ‘energy pool’ is the energy-transducing membrane and the ion gradients that define it. These gradients are not only important for the synthesis of ATP but also defines what is and is not the cell in the case of bacteria.

1.2 ATP synthesis by energy transducing membranes

Energy transducing membranes are key to the maintenance of the ATP pool, keeping the pool in a favourable ratio to allow other endothermic processes in the cell to occur. Some soluble processes can catalyse the synthesis of ATP but the vast majority of ATP synthesis is catalysed by energy-transducing membranes. The plasma membranes of respiratory bacteria are one type of energy-transducing membrane and the focus of this thesis. However, other types of energy-transducing membranes also include the plasma membrane of photosynthetic bacteria, the inner membrane of mitochondria and the thylakoid membrane of chloroplasts. They all allow the transduction of one form of energy (chemical or light energy) to useful energy for the cell.

Energy transducing membranes are characterised by complexes that are involved in the generation and consumption of the Δp, a proton electrochemical gradient across the energy transducing membrane. For example, in oxidative phosphorylation, the electrons released from the oxidation of carbon sources are transported down the electron transport chain (ETC) to reduce oxygen to water. The ‘downhill’ movement of electrons through the complexes is coupled to the net movement of protons across the membrane, from the N-side to the P-side of the membrane generating the Δp. Some complexes will directly translocate protons across

the membrane, known as pumped protons. Other complexes can contribute to the proton electrochemical gradient via chemical protons where protons are taken up from one side of the membrane and released on the other via spatially separated processes. This can also be net across several complexes in the form of redox loops, such as the loop between formate dehydrogenase and nitrate reductases in *E. coli* (Jormakka et al., 2002). This is closer to the theory originally envisioned by Peter Mitchell when he proposed the chemiosmotic theory (Mitchell, 1966).

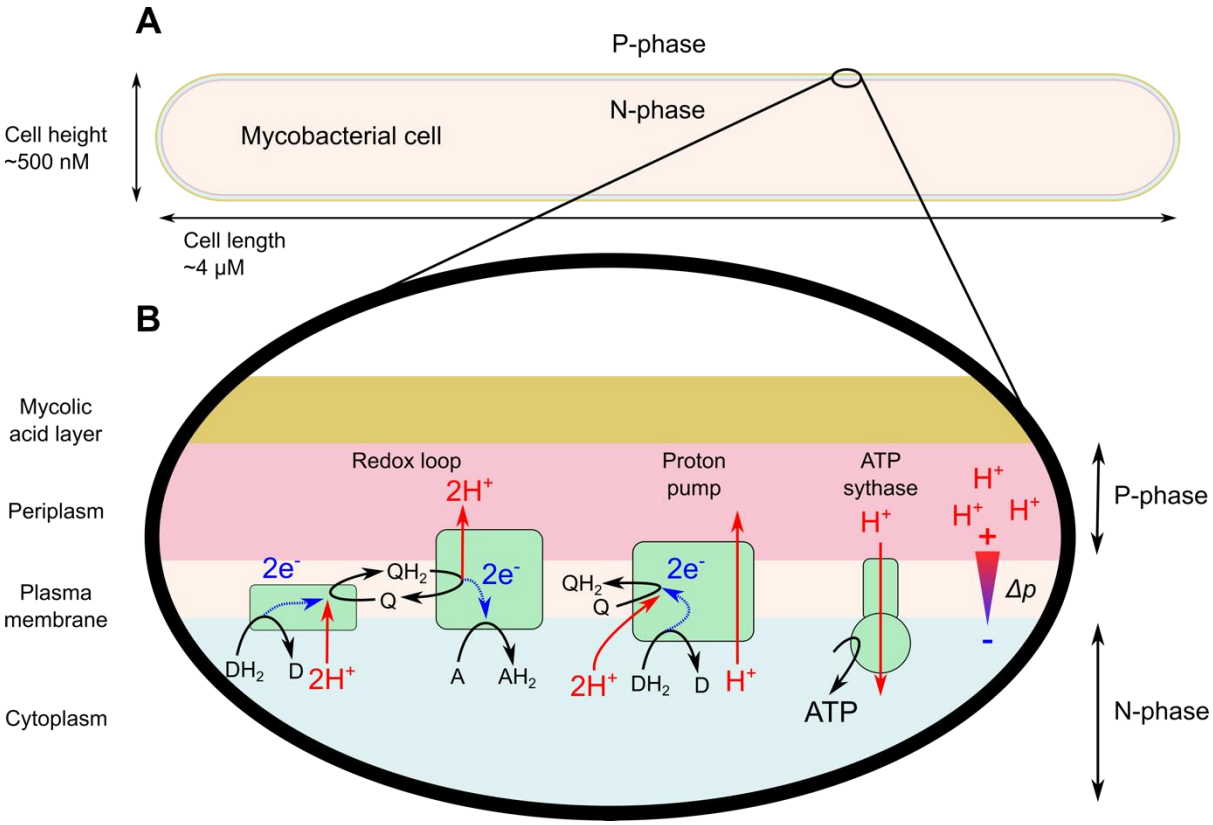

Figure 1.1 - The energy-transducing membrane *(**A**) A cartoon representation of a mycobacterial cell with the approximate dimensions. (**B**) In the cell envelope of mycobacteria, the plasma membrane is the energy-transducing membrane. This is enclosed by the periplasm and the mycolic acid layer, which makes up the P-Phase (positively charged). The cytoplasm of the cell is the N-Phase (negatively charged). The Δp can either be indirectly built through processes like redox loops or protons can be directly pumped by complexes of the energy-transducing membrane. This Δp is then used by ATP synthase to generate ATP.*

To allow the conversion of this generated Δp into useful energy for the cell, all energy-transducing membranes will contain an ATP synthase. ATP synthase couples the translocation of protons to either the synthesis or hydrolysis of ATP depending on circumstances. In the case of ATP synthesis protons move from the P-phase to the N-phase, consuming the Δp. For ATP hydrolysis this proton movement is in reverse, generating Δp.

1.3 The proton electrochemical gradient

The membrane and its associated proton electrochemical gradient are key to the energy transduction process. The membrane allows systems to be held away from the natural equilibrium, storing potential energy. The proton electrochemical gradient is a special form of an ion electrochemical gradient. Any ion electrochemical gradient will be made up of two components, the difference in charge (bulk charge of the aqueous phase separated by the membrane) and the difference in concentration between the two compartments. Eq. 1.1 describes the Gibbs free energy change for moving 1 mol of ion Xm^+ across a membrane with an electrical potential of ΔΨ (in mV).

$$\Delta G = -mF\Delta\Psi + RTln\frac{[X_{in}^{m+}]}{[X_{out}^{m+}]} \qquad \text{Equation 1.1}$$

The first part describes energy change for moving down the electrical potential and so depends on the size of the membrane potential. The second part describes the energy charge for a concentration gradient. The Gibbs free energy change for the proton electrochemical gradient is referred to as $\Delta\mu_{H+}$ (units $kJmol^{-1}$). It also means the equation can be simplified to Eq. 1.2 by using ΔpH

$$\Delta\mu_{H^+} = -F\Psi + 2.3\,RT\,\Delta pH \qquad \text{Equation 1.2}$$

Peter Mitchell defined the proton motive force (pmf or Δp) as Eq. 1.3 (Mitchell, 1966, 1961). This converts the units to mV which allows an easier comparison to the redox potentials of the electrochemical processes used to generate the Δp.

$$\Delta p = -\frac{\Delta\mu_{H+}}{F} \qquad \text{Equation 1.3}$$

This gives the more commonly used equation to describe the Δp Eq 1.4.

$$\Delta p = 2.3\,\frac{RT}{F}\Delta pH \qquad \text{Equation 1.4}$$

The membrane allows there to be a maintained difference in concentration of proton and other ions in the aqueous phase on the ‘inside’ and ‘outside’ of the membrane. This membrane allows the maintenance of a significant gradient over a short spatial distance. It is the physical properties of the membrane that determine the size of the gradient it can support, typically in bioenergetic systems this is ~200 mV.

1.4 Oxidative phosphorylation

Oxidative phosphorylation describes how the generation of Δp is coupled to the reduction of oxygen to water at the end of the transport chain. This is why oxygen is referred to as the final or terminal acceptor in connection to the ETC. Various reducing equivalent products as part of central metabolism are oxidised by specific dehydrogenase of the electron transport chain, 'feeding' electrons into the chain. Oxidative phosphorylation occurs under aerobic conditions, however, under anaerobic conditions, other compounds can serve as the final electron acceptor, including nitrate (NO_3^-), fumarate, sulphate (SO_4^{2-}), or elemental sulphur. Anaerobic respiration may not yield the same Δ*E* from reducing equivalents as the result of the less favourable redox potentials of non-oxygen electron acceptors or due to a shift of the energy landscape to a more negative redox potential generally. Anaerobic respiration can also require other pathways to facilitate the process, such as the dissimilatory sulfate process (Broco et al., 2005). Table 1.1 presents the redox potentials of several common electron donors and electron acceptors that participate in either OxPhos or anaerobic respiration.

This thesis will be focused on bacterial oxidative phosphorylation and the complexes associated with it. The mammalian ETC is arguably more well-characterised than the bacterial ETC. It is in some ways simpler in the mammalian ETC as there is only one enzyme catalysing each reaction. In the bacterial ETC, there are often multiple enzymes that catalyse the same reaction, likely reflecting use to adapt to different environmental conditions and stress, such as oxygen and nutrient availability.

As energy-transducing processes occur at a membrane, the complexes involved in these processes are predominantly membrane proteins. As such the recent expansion of milder non-ionic detergents, such as DDM, has greatly aided the study of these complexes. They are still challenging complexes to isolate and study, often composed of multiple subunits and several cofactors, some of which involve complex biosynthesis pathways. Similar to the advantages that newer detergents have offered, the advancement of Cryo-EM has increased the number of structures of energy-transducing complexes, which has perhaps left the harder functional studies behind in the search for even greater resolution structures. Before the determination of many of the complexes' protein structures, a great deal was determined about the nature of the associated complexes via the use of specific inhibitors of complexes combined with spectroscopic techniques.

Table 1.1 - Redox potentials of common electron donors and electron acceptors involved in respiration

Redox couples	$E_{m,7}$ (mV)	Reference
SO_4^{2-}/HSO_3^-	-516	(Thauer et al., 1977)
$H^+/^1/_2H_2$ (at 1 atm)	-420	(Nicholls and Ferguson, 2013)
NAD+/NADH	-320	(Nicholls and Ferguson, 2013)
S/HS^-	-270	(Thauer et al., 1977)
$Oxaloacetate^{2-}/malate^{2-}$	-172	(Thauer et al., 1977)
MQ/MQH_2	-74	(Schnort, 1966; Thauer et al., 1977; Wagner et al., 1974)
Fumarate/succinate	+30	(Nicholls and Ferguson, 2013)
UQ/UQH_2	+70	(Sarewicz et al., 2021)
PQ/PQH_2	+110	(Sarewicz et al., 2021)
NO_2^-/NO	+350	(Thauer et al., 1977)
NO_3^-/NO_2^-	+433	(Thauer et al., 1977)
$^1/_2O_2$(at 1 atm)/H_2O	+820	(Nicholls and Ferguson, 2013)

As part of their redox functions bioenergetics complexes contain redox cofactors facilitating them to accept electrons, before transferring them within the complex or to partner redox proteins. The chemical nature of these redox cofactors often provides an experimental handle that can be measured with spectroscopic techniques; the utilisation of the visible wavelength spectral handles of cytochromes is the focus of much of this thesis. The rate of the electron transfer between the cofactors is dictated by this distance between the cofactors, the redox potentials of the cofactors and the nature of the space in between the cofactors as described by the Marcus equation (Marcus and Sutin, 1985). This was greatly simplified by Moser and Dutton, deriving a 'ruler' dictating that centres within 14 Å of each other should facilitate rapid transfer of electrons sufficient to sustain catalytic rates typically observed for bioenergetic reactions, which are 100-1000 s^{-1} (Moser et al., 1992). Effectively, once centres are within 14 Å, there is no evolutionary pressure to bring them closer as the electron transfer rate between them will already not be rate-limiting. This has been borne out by subsequent structures

where cofactors where the rate of electron between them is not the rate-limiting step have been within 14 Å of each other (Page et al., 1999).

Iron sulphur clusters, flavins, and haems are the most common and well-studied of the redox cofactors found in electron transport chains. Flavoproteins and cytochromes describe proteins containing flavin and cytochromes respectively. The spectral handles of these redox cofactors reflect the surrounding protein environment, meaning that a specific spectral signal can be used to probe the function of a specific centre. Despite the growing number of experimental structures of cytochromes, there is no published work towards predicting the spectral properties of haems based on their protein environment, as far as I am aware. Spectroscopic techniques can provide information on the subtle changes that structural techniques cannot provide due to limitations in resolution (protonation; fine structure), or difficulty in accessing low-abundance catalytic intermediates (transition states). There is some work towards predicting how the E_m of a centre will change upon the mutation of surrounding residues (Guberman-Pfeffer, 2023; Hardy et al., 2024) but not directly predicting a centre's E_m based on the structure alone.

Beyond the redox cofactors the complexes contain, they are typically classified based on the specific redox reactions that they perform. Below is a summary of the main complexes that make up the ETC and their function within the chain.

1.4.1 Dehydrogenase and electron donors to the chain

Dehydrogenase enzymes oxidise reducing equivalents and donate electrons to an electron acceptor. This class of enzymes is not exclusive to the ETC. For the dehydrogenases associated with the ETC, the electron acceptors of the dehydrogenases are quinones, the mobile membrane electron carrier. Dehydrogenases are specific to the substrate that they oxidise. The architecture of the substrate-bound complex, active site and cofactor configuration allows for the transfer of electrons. This will often allow for the interaction of one and two-electron processes, facilitated by redox cofactors that have multiple different redox states. Electrons are sequentially passed along the intra-complex electron transfer pathways. The dehydrogenases that are part of the ETC are a mixture of monotopic and transmembrane complexes. Depending on the ΔE across the enzyme (difference in the redox potential of the reducing equivalent and the quinone the electrons are transferred between) and if the complex spans the whole membrane, the intra-complex electrons transfers can be coupled to protons are translocated across the membrane.

1.4.1.1 NADH dehydrogenase

Nicotinamide adenine dinucleotide, NADH, is one of the main reducing equivalents used to drive the reduction of the ETC. NADH is generated in several steps of the Tricarboxylic cycle (TCA cycle, also known as the citric acid cycle) and glycolysis. There are two types of NADH dehydrogenase, proton pumping Type-I and non-proton pumping Type-II. Mammalian complex I is a type I NADH dehydrogenase. The enzyme contains two domains, a hydrophilic domain and a hydrophobic domain. The hydrophilic domain faces into the N-Phase and contains a flavin mononucleotide (FMN) and a chain of iron-sulphur clusters, and these domains are evolutionarily related to hydrogenase. This cofactor arrangement allows for the transfer of electrons from NADH to quinone, at a Q site close to the interface of the hydrophobic and hydrophilic domain.

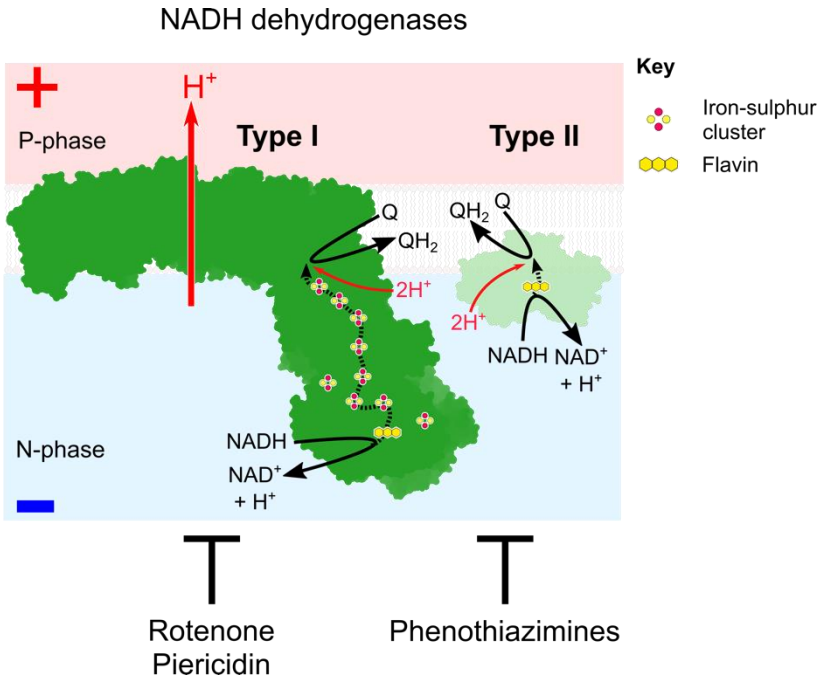

Figure 1.2 – Examples of the two types of NADH dehydrogenases*. An example of a type-I NADH dehydrogenase structure the M. smeg Nuo is shown with its cofactors in dark green (Liang et al., 2023). NADH is oxidised in the hydrophilic domain. The electrons are transferred to a Q-site within the membrane to reduce quinone. The hydrophobic domain will then translocate protons, driven by conformational changes caused by the transfer of electrons in the hydrophilic domain. This is 4 protons per 2 electrons in the mammalian ubiquinone-using enzyme (Ripple et al., 2013a) but this may be less in menaquinone-using enzymes due to the difference in the ΔE across the enzyme. An example of a type-II NADH dehydrogenase the Ndh from Caldalkalibacillus thermarum is shown in light green (Heikal et al., 2014). It only has a flavin cofactor and does not translocate protons.*

The hydrophobic domain contains proton translocating modules that are structurally related to the Na^+/H^+ antiporter. Conformational changes in the hydrophilic domain induced by the redox reactions are transmitted to the hydrophobic domain leading to proton pumping. Type I NADH dehydrogenase can be inhibited by several compounds including rotenone and piericidin (Lümmen, 1998).

Bacterial species generally favour the non-pumping type II NADH dehydrogenase. It is a monotopic membrane protein containing either a flavin mononucleotide (FMN) or a flavin dinucleotide (FAD) cofactor. Because these complexes are only monotopic it means that they cannot directly translocate protons across the membrane. Type II NADH dehydrogenases are widespread in the genomes of bacteria, fungi, plants and unicellular eukaryotes such as yeast and parasites, but they are not found in the mammalian genome. As such it is an attractive drug target for pathogenic species. For type-II dehydrogenases, there are less well-characterised inhibitors. Phenothiazines such as thioridazine have been demonstrated to inhibit type II NADH dehydrogenase (Yano et al., 2006) but these compounds may have other effects other than direct Ndh2 inhibition (Nakatani et al., 2020). Several candidate inhibitors are in development to target the Ndh2 of pathogenic bacteria (Murugesan et al., 2018).

1.4.1.2 Succinate dehydrogenases and fumarate reductase

Succinate dehydrogenases (SDH) oxidise succinate to fumarate. The electrons released from this process are utilised to reduce quinols. Succinate dehydrogenases are one of the few enzymes that are part of the ETC and the TCA cycle, directly connecting these important cellular processes. The different classes of succinate dehydrogenases have been well-reviewed (Iverson et al., 2023). The core of the enzyme is composed of 3 to 4 conserved subunits, typically encoded for in the same operon *sdhABC(D)*. Two of these core conserved subunits are the hydrophilic SdhA, a flavoprotein with a single FAD cofactor, and SdhB a subunit containing three Iron-Sulphur clusters. The remaining subunit/subunits make up the hydrophobic core. This varies between one or two subunits depending on the class of the succinate dehydrogenase, it can also contain additional cofactors, between zero to two *b*-haems, or additional Iron-sulphur clusters or a zinc ion. Figure 1.3A shows the subunits and Sdh2 from *M. smeg* which contains two subunits and two *b*-haems in its hydrophobic core. In Sdh2 there is also an additional accessory single transmembrane helix subunit (SdhF as shown in Figure 1.3B), encoded outside the core subunit's operon. Multimeric states are common in succinate dehydrogenase, Sdh2 forms a trimer (Fig 1.3C)

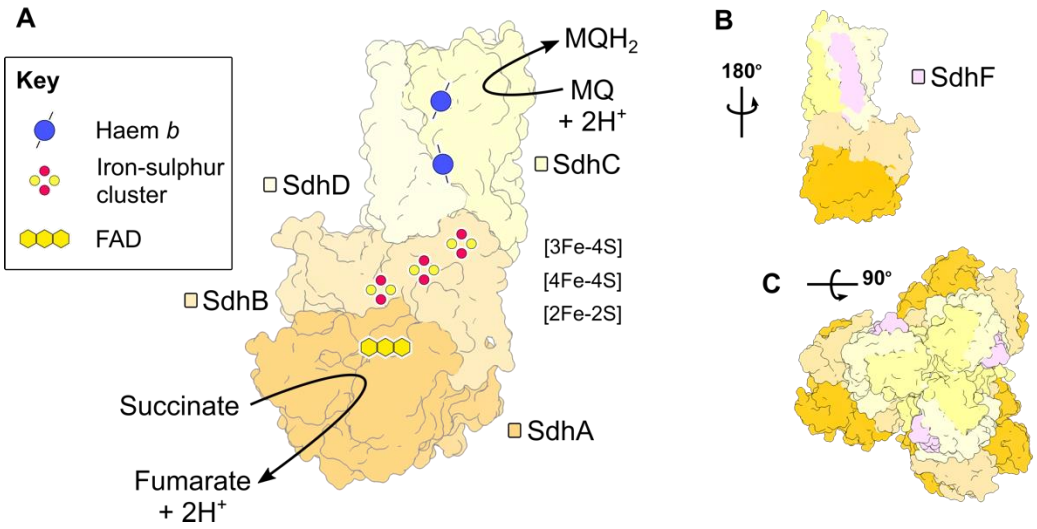

Figure 1.3 - Example of a succinate dehydrogenase subunit organisation, cofactors, and multimeric state. *(**A**) The structure of the class A succinate dehydrogenase from M. smegmatis Sdh2 monomer (PDB:6LUM, Gong et al., 2020). SdhA - a flavo-subunit that contains the site for succinate/fumarate catalysis. SdhB - a subunit containing iron-sulphur clusters. SdhC/SdhD - the transmembrane domain that contains the Q site and can contain b haem cofactors. (**B**) Additional view of Sdh2 monomer rotated by 180^{o} to show the additional SdhF subunit. (**C**) The structure of the trimer of Sdh2.*

Succinate dehydrogenases are structurally related to fumarate reductases which catalyse the reverse reaction typically under anaerobic conditions in bacteria. It is not possible to determine with certainty what reaction an enzyme will catalyse from sequence or structure alone. The membrane-associated succinate dehydrogenases and fumarate reductases have been classified into 6 different classes, A to F as demonstrated in Figure 1.4. This classification is based on the cofactors present in the enzyme and the number of subunits in the hydrophobic core (Karavaeva and Sousa, 2023; Lancaster, 2013). Even though most of the classes are composed of transmembrane complexes, the electron transfer pathway does not always extend into the membrane domain. This means that the q-site, where the quinone is reduced to quinol can be towards the P-Phase or the N-Phase. All of the cofactors do not have to participate in the electron transfer pathway, instead, they can help to poise components of the electron transfer pathway. This is the case in the Class C succinate dehydrogenase, which has a *b* haem not directly involved (Tran et al., 2007).

Classes of succinate dehydrogenases/fumarate reductases

	Class A *M.smeg* Sdh2 PDB 6LUM	Class B *W. succ* QFR PDB 2BS2	Class C *S. scrofa* CII PDB 1ZOY	Class D *E. coli* QFR PDB 1L0V	Class E? *C. jejuni*	ClassF *M. smeg* Sdh1 PDB 7D6V
No. core hydrophic subunits	2	1	2	2	2	1
Multimeric state	Trimer	Dimer	Monomers & trimers	Monomer	?	Monomer

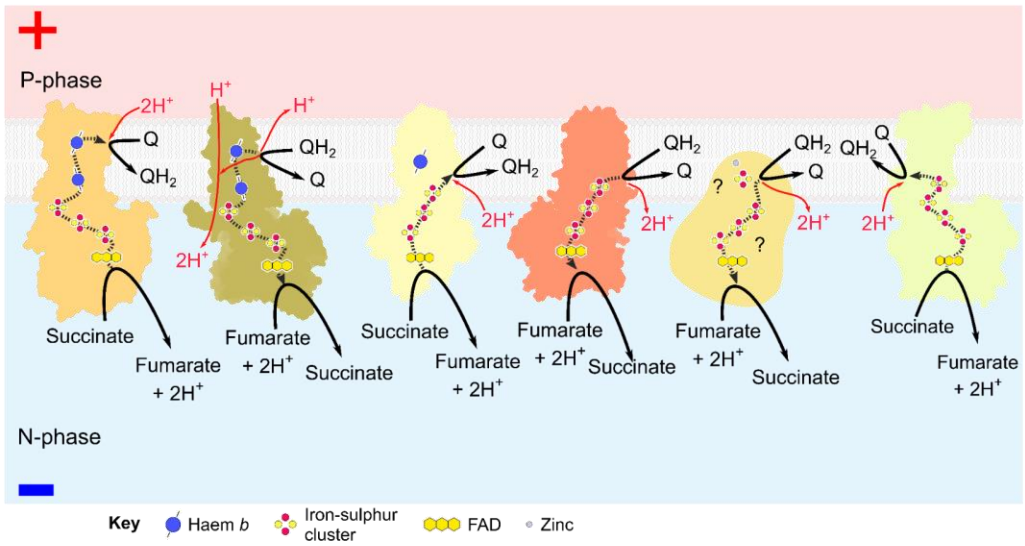

Figure 1.4 - Classification of succinate dehydrogenases and fumarate reductases. *An example of the structure of each of the classes is shown. The classification is based on the number of core subunits in the membrane domain and the haem content of the enzyme. Class A has two subunits in the membrane domain and two b haems (PDB:6LUM, Gong et al., 2020). Class B has one subunit in the membrane domain and two b haems (PDB:2BS2, Madej et al., 2006)*. Class C has 2 subunits in the membrane domain and one *b haem, (PDB:1ZOY, Sun et al., 2005)). It is found in E. coli and mitochondrial chains where it is known as complex II. Class D has 2 subunits in the membrane domain and no haem groups (PDB:1L0V, Iverson et al., 2002). Class E is a putative fumarate reductase identified in the sequences of several species such as Sulfolobus tokodai (Hamann et al., 2009). It has been demonstrated to contain a zinc ion and an extra Iron sulphur cluster in addition to the three conserved clusters. Unlike the other classes, class E is monotopic with two subunits in the membrane domain. Class F has one subunit in the membrane domain and an extra iron sulphur cluster (PDB:7D6V, Zhou et al., 2021). This is a recreation of a figure in Iverson et al., 2023*.

Succinate dehydrogenases and fumarate reductase can work with either ubiquinone or menaquinone, however, the difference in the redox potential between the two quinones means that the reduction of menaquinone by succinate is unfavourable and so an endergonic reaction. In comparison the reduction of ubiquinone is favourable and so an endothermic

reaction. To manage the unfavorability of the menaquinone reduction, some succinate dehydrogenases appear to couple the reaction to the consumption of the Δp (Gong et al., 2020). They are, however, putative menaquinone succinate dehydrogenases that do not appear to consume the Δp (Hards et al., 2019; Zhou et al., 2021). It is unclear how the unfavourable reaction is driven in these enzymes, these prior publications have hypothesised they may work with polyketide quinones which have been hypothesised higher potential quinones{ref}. Alternatively, the complex may be a fumarate reductase instead.

1.4.1.3 Other Q-linked dehydrogenases

Particularly in bacterial ETCs, there are numerous other Q-linked dehydrogenases. This allows for the use of different nutrient sources. This includes dehydrogenases for proline, formate, lactate, glycerol-3-phosphate, carbon monoxide, as well as hydrogenases (Hards and Cook, 2018). It also includes monotopic membrane protein malate:quinone oxidoreductase (Mqo) which couples the oxidation of malate to the reduction of quinone. Mqo is not present in all organisms (Harold et al., 2022) as the soluble malate dehydrogenase (mdh) can serve the same function. Mdh couples the oxidation of malate to the reduction of NAD^+ and is more widespread in bacteria. As this conversion of malate to oxaloacetate is part of the TCA cycle, Mqo provides another link of the ETC to the TCA cycle, in addition to succinate dehydrogenase (Fig 1.5 A).

The β-oxidation of fatty acids also provides another source of electrons for the ETC (Fig 1.5). β-oxidation is the process by which fatty acids are sequentially cleaved into the two-carbon molecule acetyl-CoA through a cycle of oxidation, hydration, oxidation and thiolysis steps. This provides electrons for the ETC at several points. In the first oxidation step of the cycle, fatty acyl CoA is used to reduce acyl-CoA dehydrogenase. These electrons are transferred to the ETC via electron transport flavoproteins (ETF) to ETF:quinone oxidoreductase via a series of redox reactions. Once the electrons have reached ETF:quinone oxidoreductase they will be used to reduce quinone. During the second oxidation step of the cycle, NADH is generated, feeding into the chain via NADH dehydrogenases. The thiolysis step cleaves off the acetyl-CoA that can then join the TCA cycle generating more reducing equivalent to feed into the ETC. Other than acyl-CoA dehydrogenases, the ETF can also facilitate the transfer of electrons from soluble redox reactions to the ETC (Nicholls and Ferguson, 2013).

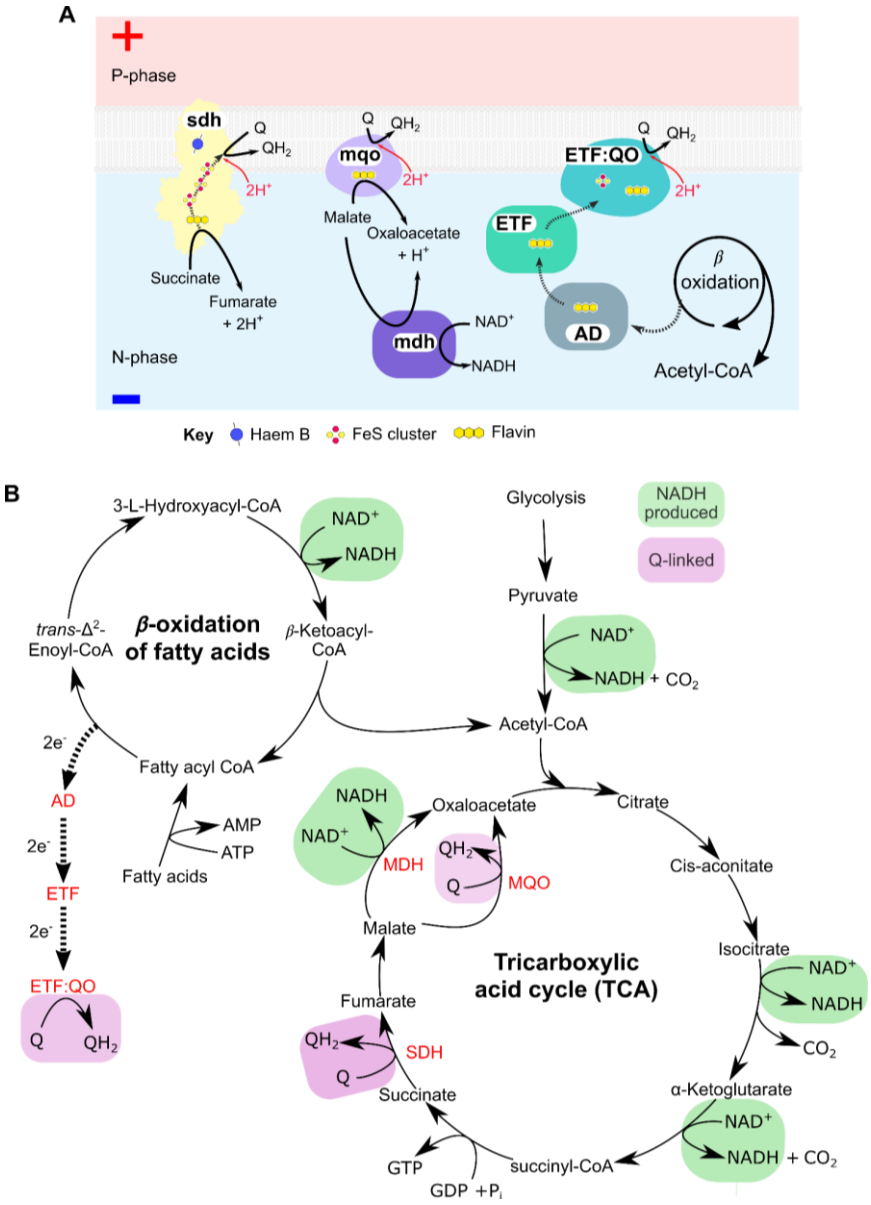

Figure 1.5 - The connection between central metabolism and the ETC. *(**A**) Succinate dehydrogenase (Sdh) is the most well known connection between the ETC and the TCA cycle. The structure complex II from Sus scrofa is shown as an example, PDB:1ZOY (Sun et al., 2005). In some species another step of the TCA cycle, malate to oxaloacetate, can be catalysed by a Q-linked step by the enzyme malate:quinone oxidoreductase (Mqo). In other systems, this is catalysed by Mdh which is instead linked to the reduction of NAD^+. β-oxidation of fatty acids provides is also linked to the reduction of quinone. Electrons are transferred from the oxidation of fatty acyl-CoA by Acyl-CoA dehydrogenase (AD) to an electrotransfer protein (ETF). This then reduces ETF quinone oxidoreductase (ETF: QO). (**B**) The connection between the TCA cycle and β-oxidation of fatty acids. The steps that generate NADH or are directly Q-linked are highlighted in pink and green respectively.*

1.4.2 The mobile electron carriers of the chain

1.4.2.1 Quinones

Key to the movement of electrons between the complexes of the ETC are mobile electron carriers. Quinones are the group of molecules that facilitate electron transfer within the membrane between different complexes, broadly as the interaction between dehydrogenases and oxidases. The quinone pool (Q-pool) present in the chain will exist at a significant molar excess to the quantity of the complexes of the ETC. The most widespread quinones are derivatives of 1,4-benzoquinone (ubiquinone & plastoquinone) or 1,4-naphthoquinone (menaquinone). Plastoquinones (E_m +110 mV) participate in the photosynthetic electron transport chain, whereas ubiquinone (E_m +70 mV) is used in the mitochondrial ETC and the ETC of some bacteria. Menaquinone (E_m -74 mV) is involved in the ETC of bacteria. Common to all the quinones that participate in ETCs is a long hydrocarbon chain with isoprene repeats. The number of repeats can differ between organisms.

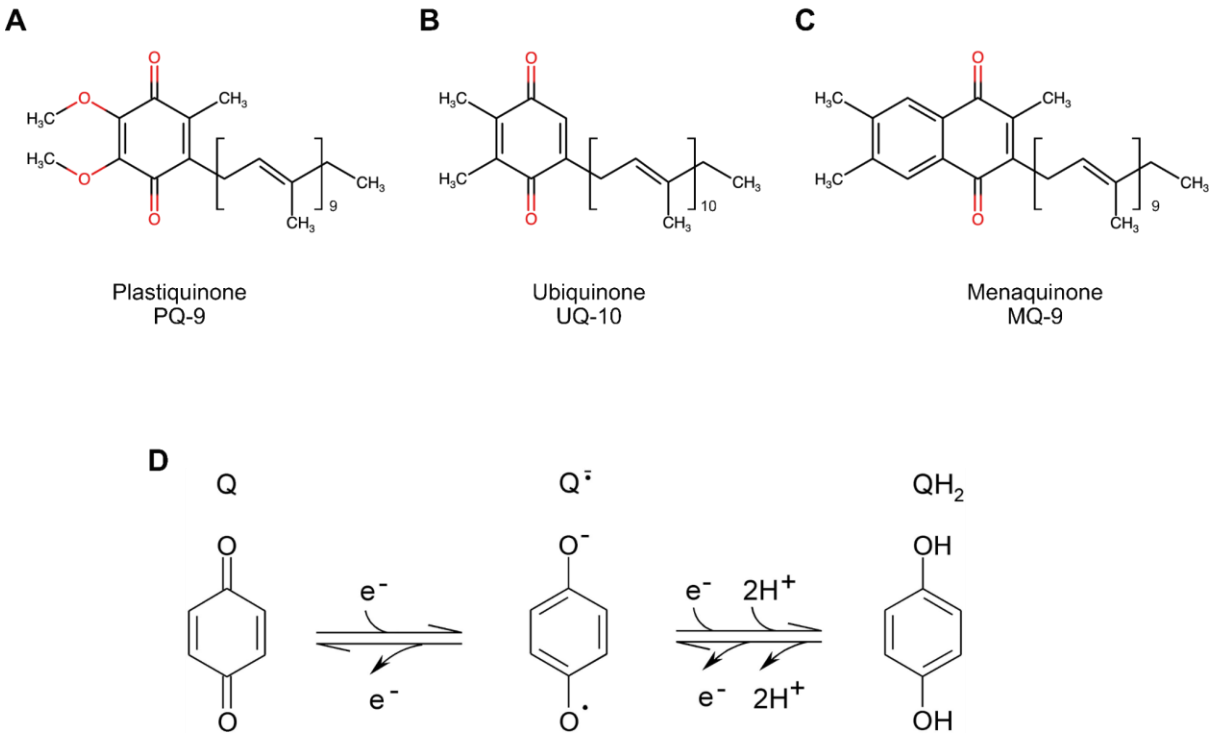

Figure 1.6 - Structures and reactions of quinones *(**A**) Plastoquinone-9 (**B**) Ubiquinone-10, as is found in the mitochondria. (**C**) Menaquinone-9 as is found in Mycobacteria, length of isoprene repeat are found elsewhere in nature. (**D**) Example of the redox reaction of quinone head group. Taken from Nowicka and Kruk, 2010, an extensive review of quinones and their properties.*

The other key aspect of quinone functions within the chain is its ability to perform a reversible two-electron, two-proton redox reaction. This is described in Eq. 1.5, where Q is the oxidised quinone form and QH_2 is the reduced quinol form.

$$Q + 2H^+ + 2e^- \leftrightarrow QH_2 \qquad \text{Equation 1.5}$$

This process can be divided into two, one-electron steps as shown by Eq. 1.6-7 and the reaction scheme in Figure 1.6D.

$$Q + e^- \leftrightarrow SQ^{\cdot -} \qquad \text{Equation 1.6}$$

$$SQ^- + e^- + 2H^+ \leftrightarrow QH_2 \qquad \text{Equation 1.7}$$

This involves an unstable semiquinone (SQ) intermediate, which can be stabilised by the protein environment. The E_m of the quinone couple (Q/QH_2) will reflect the average E_m of the two couples (Q/SQ^- and SQ^-/QH_2).

The range of redox potentials of the quinone will reflect changes to the energy landscape of the chains they participate in, resulting in the shifting of the redox potential of cofactors that interact with the quinones (Bergdoll et al., 2016). Some species can produce more than one type of quinone. A well-described example of this is when *E. coli* transition from aerobic conditions to anaerobic conditions with a switch from ubiquinone to more negative redox potential quinones menaquinone or demethylmenaquinone (Wallace and Young, 1977). This facilitates the more negative redox potential involved under anaerobic conditions. It is unclear how widespread having multiple quinones is in bacterial ETCs.

1.4.2.2 Other mobile electron carriers

Other than quinols, several small redox proteins transfer electrons between the complexes of the latter half of the ETC. The most well-known example, cytochrome *c,* transfers electrons from cyt bc_1 complexes downstream to haem copper oxidases via diffusion in the intermembrane space. Cyt *c* is found on the P-side of the membrane and can be soluble, like in the case of mitochondrial cyt *c*, or membrane-tethered. This membrane tether can either be in the form of a transmembrane helix or a lipid anchor. Mitochondria only have one cyt *c* but other species can have more than one cyt *c*, for example, *Paracoccus denitrificans* (Otten et al., 2001). In the case of *P. denitrificans*, the two cyt *c* fulfil different roles, cyt c_{552} will only reduce aa_3 type cyt c oxidases, whereas cyt c_{550} will reduce both cyt *c* oxidases.

In bacteria, the nature of the cell envelope influences which type of *cyt* c is. Many gram-negative bacteria, which have an outer membrane, have both soluble and membrane-tethered cyt *cs* like in the case of cyt c_2 (soluble) in *Rhodobacter capsulatus* and cyt c_{552} (membrane-tethered) in *P. denitrificans.* Gram-positive bacteria, which do not have an outer membrane, appear to have exclusive membrane-tethered cyt *c*s. For example, *Bacillus subtilis* contains one transmembrane anchored cyt c_{500} encoded for by *CccA* and one diacylglycerol membrane-anchored cyt c_{551} encoded for by *CccB*. This is distinct from the *c* haem in subunit II of the caa_3 oxidase (Lauraeus et al., 1991).

Plastocyanin and ferredoxin are other examples of small redox proteins that transfer electrons between complexes. Plastocyanin is a blue copper-containing redox protein that transfers electrons in photosynthetic ETC, between cyt b_6f and photosystem I. Ferredoxin is an iron-sulphur protein that is also found in the photosynthetic chain as well as in anaerobic bacteria acting as a mobile electron carrier. For example, ferredoxins transfer electrons between photosystem I and ferredoxin-NADP+ reductase in photosynthesis.

1.4.3 Cytochrome *bc* type complexes

Cytochrome *bc* type complexes are quinol:cytochrome *c* oxidoreductases and key components of both respiratory and photosynthetic ETCs. The complex is a homodimer with C2 composed of 3 core subunits, cytochrome *b* subunit, cytochrome *c* subunit, and the iron sulphur protein (ISP) (Fig 1.7 A & C). Typically there are two *b*-haems in the cytochrome *b* subunit. These *b*-haems have different redox potentials so they are assigned b_H (more positive redox potential) and b_L (more negative redox potential). These *b*-haems are also sometimes known as b_N and b_P respectively, reflecting the side of the membrane that each is closer to. There is a 2Fe-2S cluster, also known as the Rieske, in the ISP and a *c* haem in the cytochrome c subunit, often referred to as c_1. Cyt *bc* type complexes also contain two Q-sites, Q_o and Q_i which are within the membrane close to the P-phase and the N-Phase respectively. This, like the *b*-haems, leads to their notation as Q_P and Q_N.

The complex is defined by two-electron pathways that result from a bifurcation reaction of a quinol that occurs at the Q_o site. The 1st electron follows the c path or high potential route and the 2nd electron follows the b path or low potential route to the second Q-site, Q_i. These two electron pathways operate as part of the Q-cycle, see next section, to transfer electrons to cyt *c* and build the *pmf*. The redox potentials will reflect the redox potential of the quinol substrate being used (Bergdoll et al., 2016). The distance between the two haem b_L of the cyt *bc* complex facilitates the transfer of electrons between the monomers (Świerczek et al.,

2010). This molecular 'bus bar' likely helps to manage the ROS produced by the complex (Shinkarev and Wraight, 2007; Świerczek et al., 2010).

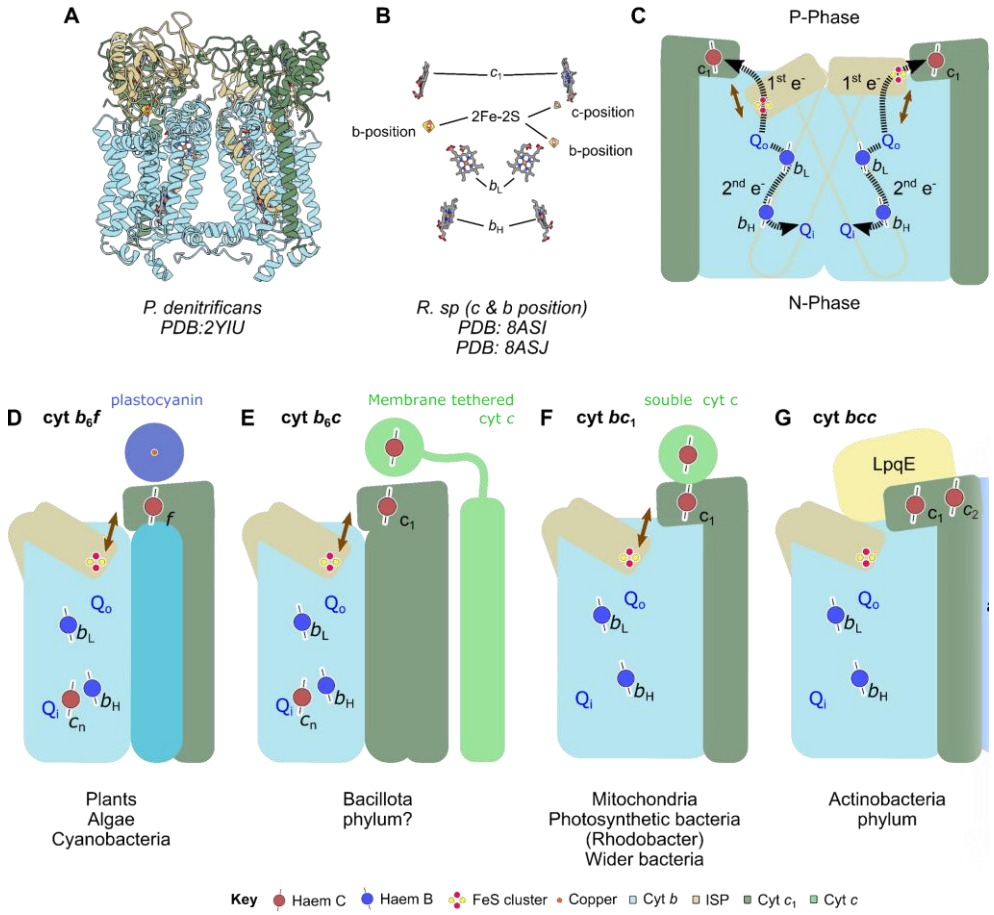

Figure 1.7 - The cyt bc type complexes. *(**A**) Structure of the cyt bc_1 complex from P. denitrificans (PDB: 2YIU,* Kleinschroth et al., 2011)*. (**B**) Location of the cofactors of the complex, including the iron-sulphur cluster in the b-b position (PDB: 8ASI) and the b-c position (PDB: 8ASJ)* (both from Swainsbury et al., 2023)*. (**C**) Cartoon representation of the cyt bc dimer showing the two-electron pathways and the domain movement of the ISP, left b position, right c position (**D-G**) Cartoon representation of the different types of cyt bc type complexes: (**D**) Cyt b_6f complex (**E**) Cyt b_6c complex (**F**) Cyt bc_1 complex and (**G**) Cyt bcc complex.*

1.4.3.1 Variations of a theme of cyt *bc*

There are several variations on the cyt *bc* type complex found across nature. The most well-described is the canonical cyt bc_1 complex found in mitochondria (Iwata et al., 1998) and bacteria (Fig 1.7 F), such as *P. denitrficians* (Kleinschroth et al., 2011) and the phototrophic bacteria *Rhodococcus sphaeroides* (Swainsbury et al., 2023). The mitochondrial cyt bc_1, also known as complex III, uses ubiquinol to reduce soluble cyt *c*. In the Actinobacteria phylum,

there is an extension of the cytochrome c_1 subunits to contain an additional *c* haem (Niebisch and Bott, 2001), Fig 1.7 G). This extension facilitates the transfer to the cyt aa_3 oxidases. As the phylum lacks a soluble cyt *c*, the di-haem cyt *cc* subunit is the only route by which electrons can reach the cyt aa_3 oxidase, meaning that the supercomplex formed between the cyt *bc* and the oxidase is obligate. As Actinobacteria use menaquinol the E_m of the cofactors in the cyt *bcc:aa*$_3$ supercomplex are shifted to more negative redox potentials to operate with this quinol (Kao et al., 2016).

The other two types of cyt *bc* type complex have variations in the cytochrome *b* subunit, indicated by the b_6 notation. In the Bacillota phylum, the cyt *bc* type complex is referred to as either cyt b_6c or cyt b_6 (Fig 1.7 E). In this complex, the cytochrome *b* subunit is shortened to just the four-helix bundle that encloses the two *b*-haems (Sone et al., 1996). This bundle also contains an extra *c* haem placed in between b_H and the Q_i site. The sequences corresponding to other transmembrane helices of canonical cytochrome *b* are fused to the cytochrome c subunit. The cyt b_6c complex donates electrons from menaquinone to membrane-tethered cyt *cs.* Cyt b_6f which is very similar to the Bacillota phylum is found in the photosynthetic ETC of plants, algae and cyanobacteria (Sarewicz et al., 2021, Fig 1.7 D). It has the same shorter cytochrome *b* subunit with the additional *c* haem. The 'missing' transmembrane helices are instead encoded by an additional subunit (subunit IV). The cytochrome *c* subunit is replaced by a cytochrome *f* subunit. This like the cytochrome *c* subunits contains a c-type haem that is referred to as cyt *f.* Cyt b_6f complexes used plastoquinol to reduce plastocyanin.

The phylogeny of cyt *bc* type complexes and the general trend of their energy landscapes matching their quinone partners redox potential has been previously analysed (Baymann et al., 2012; Bergdoll et al., 2016). However, it is not clear if the different type of the cyt *bc* complex exclusive work with one type of quinone, i.e. do cyt bc_1 type complexes exclusive work with ubiquinone. This may be possible to tease apart with phylogenetic analysis of quinone type and cyt *bc* type present in one organism. There may also be further variations of the theme of the cyt *bc* complex as yet unappreciated.

1.4.3.2 The Q-cycle

The pathway of electrons through cyt *bc* complexes is referred to as the Q-cycle, an elegant mechanism of maximising the redox potential of the Q-pool to build Δp. It is a modified cycle to Mitchell's initially proposed Q-cycle, which proposed that one electron was donated from the N-side of the enzyme (Mitchell, 1975). Instead, in the modified Q-cycle, a bifurcation reaction occurs in the Q_o site on the P side (Crofts et al., 1983). This model was built on enzymatic studies using specific inhibitors of the Q-sites and structures of the cyt bc_1 complex that were used to tease apart this mechanism.

A schematic of the Q-cycle is shown in Figure 1.8. The first oxidation of the quinol at the Q_o site results in the reduction of the iron-sulphur cluster whilst it is in the b position (state I). This first oxidation leaves a semiquinone in the Q_o site and releases protons into the P-phase, building the Δp. The ISP moves, taking the iron-sulphur cluster away from the Q_o site to the c position (state II). From here it can reduce the cyt c_1/f which then in turn can reduce its electron carrier partner (cyt c, plastocyanin). The second electron from the oxidation of the semiquinone radical reduces cyt b_L (state III). This electron is passed against the $\Delta\Psi$ to b_H and eventually to a quinone bound at the Q_i site forming semiquinone at this site. A second cycle of this will result in the reduction of this semiquinone bound at the Q_i site to quinol (states IV-VI), taking up two protons from the N-Phase, again building the Δp.

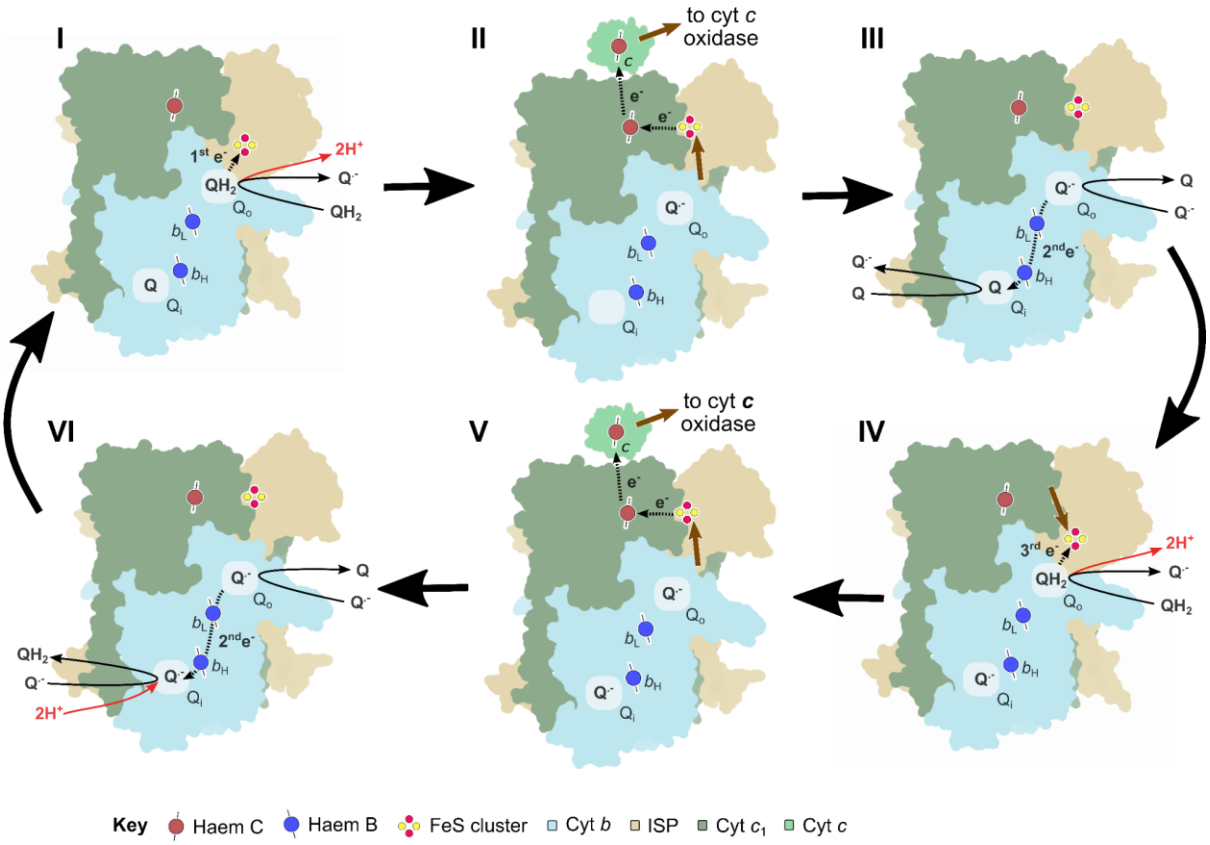

Figure 1.8 - Schematic of the Q cycle. *State I - oxidation of quinol at the Q_o site, with the 1st electron reducing the iron sulphur cluster, State II - the movement of the iron sulphur cluster allows the reduction of cyt c_1 and then cyt c, State III - the 2nd electron is transferred down the low potential path transferring between the b-haems to the Q_i site to reduce quinone to semiquinone. State IV-VI, a second quinol is oxidised at Q_o following the same steps, but resulting in the semiquinone at Q_i being reduced to quinol. The structures from (Swainsbury et al., 2023) are used to represent the two conformations of the ISP.*

As the cyt bc_1 complex has been better studied and the main system used to develop the understanding of the Q-cycle it is often referred to as the canonical cyt *bc*. The Q-cycle of all cyt *bc*'s may not follow the same sequence of events as occurs in the canonical cyt bc_1. The ISP movement that occurs as part of the cycle does not appear to occur in the cyt *bcc* complex. The ISP and the cyt *cc* are more restrained by surrounding additional subunits preventing their movement. In mycobacteria, this predominantly is the result of the LpqE subunit sitting 'on top' of the domains. A similar domain is found in the *C. glut* homolog (Kao et al., 2022). This means that the distance between the iron-sulphur cluster and the *c* haem is further than when the iron-sulphur cluster is in the c-position in the canonical enzyme. The Q-cycle also is less well understood in the cyt b_6 complexes. The role of the additional *c*, haem in between b_H and Q_i is particularly interesting.

1.4.3.3 Inhibitors of the cyt *bc* complexes

Several naturally occurring inhibitors have been characterised to inhibit cyt *bc* complexes. These typically bind to the Q-sites and are divided based on which Q-site they tend to inhibit Q_o or Q_i. Antimycin A is the best-known Q_i inhibitor. Its binding prevents the reduction of quinone at the Q_i site. In the presence of oxygen and reduced quinol it can result in the oxidant-induced reduction of any *b*-haems not previously reduced (Wikström and Berden, 1972). This is the result of electrons from the Q_o site being donated to the *b*-haems and being unable to be transferred onto the Q_i site. Myxothiazol A and stigmatellin A are the most well-described Q_o site inhibitors. The two compounds can be differentiated by their effect on the ISP. Stigmatellin A fixes the position of the ISP in the b-position via the formation of a hydrogen bond with one of the histidines that ligates the iron-sulphur cluster. Myxothiazol A does not stabilise the ISP but does block the entry of quinol to the Q_o site. Several synthetic Q-site inhibitors have been developed, including to treat pathogenic microorganisms by inhibiting the cyt *bc* complex. This includes Atovaquone which is a naphthoquinone derivative that is used to treat malaria (Hudson et al., 1991). It has a similar mode of action to stigmatellin, stabilising the ISP (Kessl et al., 2003).

1.4.4 Oxidases

The final step in aerobic respiratory ETC is the four-electron reduction of oxygen to water, as described in Eq. 1.8.

$$O_2 + 4e^- + 4H^+ \rightarrow 2H_2O \qquad \text{Equation 1.8}$$

For simplicity, the reduction of ½ a molecule of dioxygen to one water molecule is sometimes used. The oxidases that participate in the ETC fall into three different superfamilies of oxidases with different complements of cofactors, haem copper oxidase (HCO), cytochrome

bd quinol oxidase, and alternative oxidases (AOX). Figure 1.9 summarises the structure of each of the superfamilies and their standard complement of cofactors. The superfamilies also translocate protons to variable degrees, with the HCO directing pumping protons whereas cyt *bd* and AOX do not. The cyt *bd* and AOX both use quinols to reduce oxygen, whereas HCOs can use either quinols or cyt *c* to reduce oxygen. Some organisms encode for multiple oxidases which may be used under different environmental conditions. Apart from the HCOs, the other families of oxidases are restricted to certain domains of life: AOX - the mitochondrial of higher plants, fungi, protists and some animal species, cyt *bd* - prokaryotes. Oxidase inhibitors such as azide and cyanide inhibit the superfamilies to varying degrees based on the difference in the oxygen reduction site.

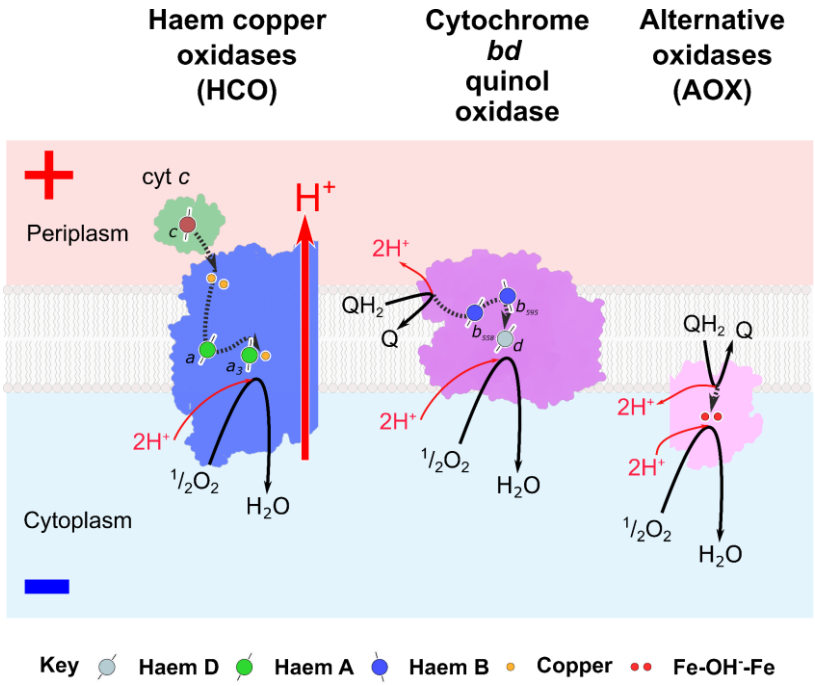

***Figure 1.9 - The different superfamilies of oxidases**. A monomer of a mammalian haem-copper oxidase (HCO) is shown in dark blue (Bos taurus, PDB: 8H8R, (Muramoto and Shinzawa-Itoh, 2023). Unlike the other oxidases, it can directly translocate protons. Haem copper oxidases can be reduced by cyt c (Merlino, 2018) or quinols. HCOs can exist as a dimer. The Cyd cyt bd quinol oxidase is shown in purple (from M. tb, PDB: 7NKZ, (Safarian et al., 2021). A monomer of the monotopic alternative oxidases (AOX) is shown in pink (from Trypanosoma brucei, PDB: 3VV9, (Shiba et al., 2013). AOX can also exist as a dimer. Each of the oxidases is defined by different oxygen binding sites, haem-copper (HCO), haem D (cyt bd), and di-iron carboxylate (AOX).*

1.4.4.1 Haem copper oxidases

The haem copper oxidases are the most well-studied including the mitochondrial cyt aa_3 enzyme. The mitochondrial homologue is referred to as complex IV. The HCOs are defined by the presence of a haem-copper binuclear site where oxygen reduction takes place. This is accompanied by an additional haem cofactor in the same catalytic subunit, often referred to as subunit I. The haems in this can be haem A, haem O (similar chemical structure to haem A), and haem B. The cytochrome composition will be reflected in the cytochrome nomenclature of the oxidase, with the haem in the binuclear site given the subscript three like in the cyt aa_3.

The HCO family has been further divided into 3 families of oxidases (A-C) based on the cofactor composition of subunit II and the nature of the proton channel to the binuclear site (Pereira et al., 2001). Subunit II contains the peripheral domain that receives the electron from the donor (cyt *c* or quinol). This peripheral domain can contain cofactors such as the two copper atoms, as in the cyt aa_3, or haem C(s) or both. The lack of copper or haem binding sites in subunit II is an indicator that the complex works with quinol (Murali et al., 2022). Inhibitors such as cyanide and azide have a high affinity for the binuclear site blocking the access of oxygen (Lim and Holm, 1998).

1.4.4.2 Cytochrome *bd* quinol oxidases

The cytochrome *bd* quinol oxidases are exclusive prokaryotic enzymes that reduce oxygen with quinols. Cyt *bd* contains three haems, a low spin *b* haem, a high spin *b* haem and a *d* haem. The *b*-haems are often notated as b_{558} (low spin) and b_{595} (high spin) to reflect their spectral maxima in *E. coli* cyt *bd*-I (Koland et al., 1984). The oxidase is made up of two core subunits. All three haem groups and the quinol binding loop, where quinol is oxidised, are located in subunit I, often referred to as cydA. The first structure revealed an unexpected triangular arrangement of the haem groups (Safarian et al., 2016). This disproved the prior hypothesis that the b_{595} and *d* formed a binuclear oxygen binding site as in HCOs. Instead, the *d* haem is the oxygen binding site. The second subunit, CydB, is evolutionarily related to the CydA subunit and can contain bound quinones (Theßeling et al., 2019). The *d* haem is located close to the interface of the two subunits.

Some organisms can have more than one cyt *bd* oxidase, for example in *E. coli* which has two cyt *bd*s, *bd*-I and *bd*-II (Brøndsted and Atlung, 1996; Dassa et al., 1991). It appears that these two oxidases are used under different environmental conditions. An ABC transporter (cydCD) is often found alongside the cyt *bd*, in the same operon or neighbouring operons (Georgiou et al., 1987). The role of this ABC transporter role is unclear but structures have

shown it with haem bound, thought to help the complex formation and regulation of the redox state of the cell (Wu et al., 2023).

Cyt *bd* does not pump protons however they do still contribute to the Δp. Upon the oxidation of quinols, they release protons to the P-phase and they uptake protons from the N-phase for the reduction of oxygen, both contributing to the Δp. Some families with the cyt *bd* superfamily may not contain the same complement of haems. For example, the cyt *bd* isolated from *Caldivirga maquilingensis* did not have the spectral features for a d-type haem and was highly insensitive to cyanide (Murali et al., 2021). This lack of haem D may be indicative of the subfamily of cyt *bd* that are cyanide-insensitive. The other subfamily of cyanide-sensitive cyt *bd* are still less susceptible to KCN than the HCOs, KCN can inhibit the function of these cyt *bd* at higher concentrations (Borisov et al., 2011).

1.4.4.3 Alternative oxidases

The alternative oxidases (AOX) are composed of non-haem-containing monotopic oxidases. Instead, they have a di-iron carboxylate active site for the reduction of oxygen by quinols (Shiba et al., 2013). Because of their monotopic nature, they do not contribute to the Δp. Instead, they likely facilitate the turnover of pools of reductants and the TCA (El-Khoury et al., 2022). Presumably, as a result of the difference in their oxygen binding site, they are resistant to cyanide (Huq and Palmer, 1978).

1.4.5. ATP synthase

Whilst ATP synthase is not strictly part of the ETC, it is key to OxPhos allowing the conversion of Δp into ATP. The enzyme is composed of a hydrophobic domain (F_0) and a hydrophilic domain, F_1, which is protected into the N-phase. The two domains, F_0 F_1 are connected by a central stalk and a second periphery stalk. The translocation of protons through the F_o domain from the P-phase to the N-phase generates torsion in the complex. This is translated to the F_1 domain via the stalk. The F1 domain then catalyses the phosphorylation of ADP to ATP. The process as a whole consumes the Δp built up by the complexes of the ETC to generate ATP.

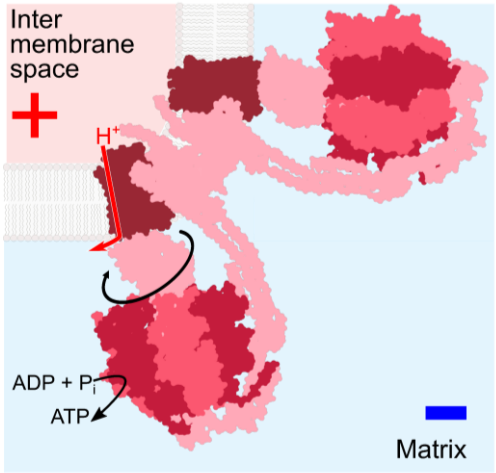

Figure 1.10 - Structure of mitochondrial ATP synthase dimer. *Protons are translocated back from the P-phase to the N-phase through the F_0 domain. This translocation drives the clockwise rotation of the central stalk that causes the phosphorylation of ADP by the F_1 domain to synthesise ATP. The complex can work in the opposite direction to hydrolysis ATP to ADP and drive the generation of the Δp. The complex forms a dimer that helps to form the curvature of the cristae of the mitochondria* ***(****PDB: 7AJB (Spikes et al., 2021)*

Different species have different stoichiometry of subunits in the c-ring (Watt et al., 2010). This alters the ATP synthesis per proton that is translocated back through the complex. The differences in the c-ring stoichiometry may reflect the different energy demands of different organisms or environmental niches (Preiss et al., 2013). ATP synthases can form oligomeric states. Dimeric states have been observed for mammalian and yeast mitochondria, contributing to the curvature of the cristae (Blum et al., 2019). Hexameric assemblies have been observed in the parasite *Toxoplasma gondii* leading to uniquely shaped cristae (Mühleip et al., 2021). Different organisms have strategies to prevent uncontrolled ATP hydrolysis that would consume the ATP pool, in the mitochondria this is prevented by IF_1 (ATPase inhibitory factor 1), which binds to the F_1 domain under low matrix pH conditions (Cabezón et al., 2000). ATP synthase can also be inhibited by small molecules. Several inhibitors bind the c-ring such as oligomycin, venturicidin A, and bedaquiline. The targeting of mycobacterial ATP synthase by bedaquiline as a strategy for treating the human pathogen *Mycobacterium tuberculosis* has invigorated new interest in mycobacterial bioenergetics.

1.5 Mycobacteria

1.5.1 The mycobacteria genus and bacterial physiology

Mycobacteria are a genus of acid-fast medically important bacteria that are members of the actinobacteria phylum that also includes other industrial and medically important species such as *Corynebacterium glutamicum* and *Corynebacterium diphtheriae*. Actinobacteria are characterised by a high G/C content which can make genetic engineering more difficult. Mycobacteria have a complex cell envelope, characterised by an external layer of mycolic acids. This is attached to a complex network of sugars called the arabinogalactan, which itself is attached to the plasma membrane via glycolipids such as lipoarabinomannan. Between the arabinogalactan and the plasma membrane, there are cross-linked layers of peptidoglycan that help to maintain the cell's shape. Like other bacteria, the plasma membrane is the energy-transducing membrane of mycobacteria and the location of the complexes of the ETC. The structure and permeability of the mycobacterial cell envelope is key to how pathogenic mycobacteria survive in the host and the intrinsic drug tolerance of the species.

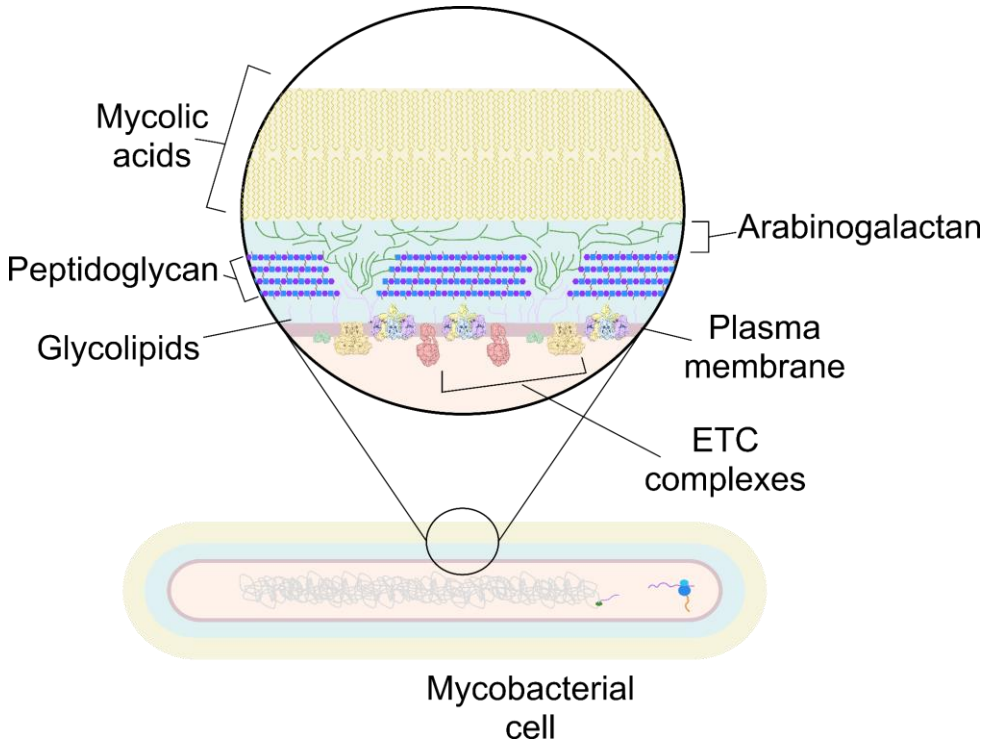

***Figure 1.11 - Structure of the mycobacterial cell envelope**. The plasma membrane containing the ETC complexes also contains glycolipids that allow the attachment of other components of the envelope, the layers of peptidoglycan layers and the sugar network of*

arabinogalactan. Mycolic acids surround the arabinogalactan layer. Beyond the mycolic acid layer, there is a capsule (not shown in this diagram).

A number of the members of the mycobacterial genus cause human disease, most notably *Mycobacterium tuberculosis* which causes the human disease tuberculosis (TB). Other pathogenic species include *M. leprae* which causes Leprosy. Mycobacterial species are also widespread in the environment. Environmental bacteria tend to have shorter duplication times than the slower-growing pathogenic mycobacteria. *M. smegmatis*, a soil mycobacteria, has a doubling time of ~2/3 hrs whereas *M. tb* has a doubling time of ~ 24 hrs. Because *M. smeg* is a faster-growing safe mycobacterial species it is often used as a laboratory model for mycobacteria generally. Other environmental mycobacteria species, sometimes referred to as Nontuberculous mycobacteria (NTM), can cause infections akin to tuberculosis in patients with compromised immune systems or lung damage. The treatments for these NTM species are less successful than those for *M. tb*.

1.5.2 Tuberculosis, treatment, resistance, and the need for new anti-TB agents

Tuberculosis (TB), despite its low prevalence in developed countries, is still a significant global health burden, killing 1.3 million people in 2022 (WHO, 2023). TB is a treatable disease, but the rise of multidrug-resistant TB (MDR-TB) is posing a threat to its treatability. Antibiotics that are used to treat TB include those that target cell wall synthesis, nucleic acid synthesis and protein synthesis (Fig 1.12). The introduction of antibiotics to treat TB dramatically improved clinical outcomes. However, monotherapies quickly resulted in the development of resistance as such subsequent current standard treatment regimens for *M. tb* will contain multiple agents. The length and side effects of the multi-drug regimens can reduce the tolerance of the treatments. Consequently, there have been efforts to develop new mycobacterial agents to tackle MDR-TB and to allow shorter treatment. One of the newer anti-TB target spaces that has developed in recent years is mycobacterial bioenergetics.

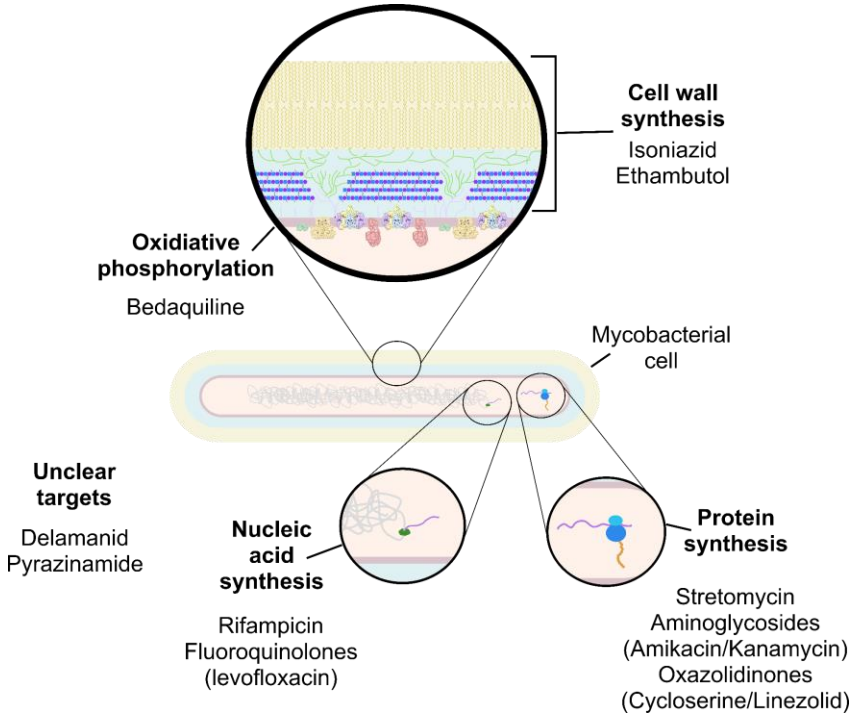

***Figure 1.12 - The mycobacterial targets of anti-TB agents**. Examples of anti-TB agents are given for each target space (nucleic acid synthesis, protein synthesis, cell wall synthesis, and oxidative phosphorylation or bioenergetics). For classes of anti-TB agents, i.e. aminoglycosides, examples of drugs are given. Some standard anti-TB agents have disputed mechanisms of action or potential multiple modes of action. This is based on a figure from Nasiri et al., 2017.*

1.5.3 Mycobacteria bioenergetics

1.5.3.1 An overview of mycobacterial bioenergetics

Mycobacteria are obligately aerobic for growth (Cook et al., 2014). Some species, such as *M. tb*, can utilise fumarate as a final acceptor. This is thought to prevent the build-up of reductants rather than supporting the growth of the bacteria. Mycobacteria are also able to co-catabolise multiple carbon sources at once to generate energy and sustain cellular metabolism. This has resulted in an ETC with a great deal of plasticity, allowing the cell to quickly adapt to changing conditions. The plasticity of the chain is reflected in the numerous dehydrogenases. The mycobacterial mobile membrane electron carrier is menaquinone-9, sometimes referred to as MK-9 reflecting the structural relationship to vitamin K and the 9 isoprene repeats found in the quinone. It has been suggested that an additional polyketide quinone may be utilised by mycobacteria, however, its functional relevance has not been proven {ref}. The route beyond the menaquinone pool is more restricted but still has a greater

number of routes than the mammalian chain, Figure 1.13. There are some differences in the complexes present in the *M. smeg* and *M. tb* as indicated in Figure 1.13 and Table 1.2. Compounds that dissipate the membrane potential are bactericidal to growing and non-growing mycobacterial cells (Rao et al., 2001, 2008) demonstrating the essentiality of maintaining an energised membrane in mycobacteria.

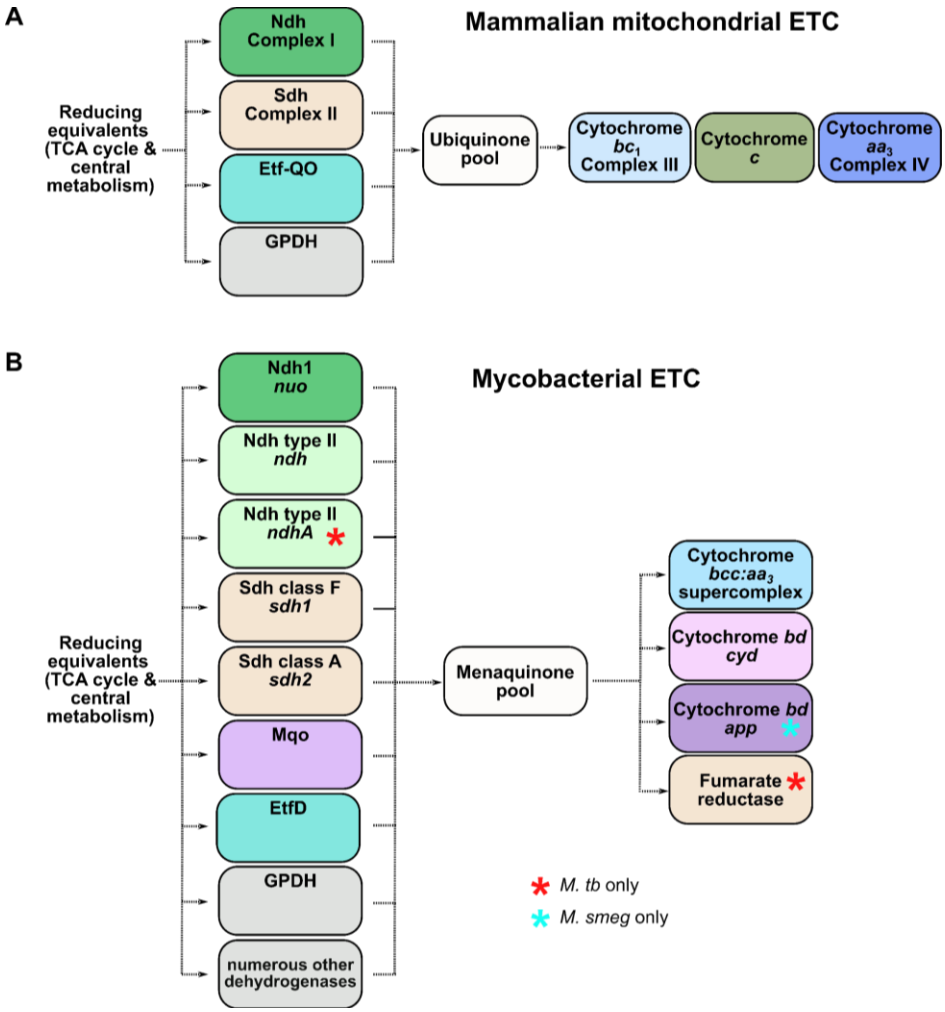

Figure 1.13 - Comparison of the plasticity of the mammalian ETC as compared to the mycobacterial chain *(**A**) The mammalian mitochondrial chain. It has several dehydrogenases. Ubiquinone transfers electrons from these dehydrogenases to the restricted route to oxygen (**B**) The mycobacterial chain. It has numerous dehydrogenases. Menaquinone donates electrons from these dehydrogenases to several terminal reductases. The exact complexes present in the genome will vary between species as indicated. The operon names are given to distinguish similar complexes. Complexes with shared structures are in the same colour. Etf-QO/EtfD - Electrotransfer flavoprotein quinol oxidoreductase. GPDH - Glycerol-3-phosphate dehydrogenase.*

Table 1.2 The operon(s) for the mycobacterial bioenergetic complexes. **Mdh is not directly linked to the ETC, instead it reduces NADH. **There are 4 different GDPH present in the mycobacterial genome, the operon numbers are shown for the D2 type.*

Complex gene or operon name	*M. smeg* operon(s)	PDB	*M. tb* H37Rv operon(s)
Nuo (ndh-I)	2050-2064	8E9G	rv3145-rv3158
Ndh (ndh-II)	3621		rv1854c
NdhA (ndh-II)	-		rv0392c
Sdh1	0417-0419	7D6V	rv0247c-rv0249c
Sdh2	1669-1672, 5791	6LUM	rv3316-rv3319
Mqo	2613		rv2852c
Mdh*	-		rv2852c
EtfD	0690		rv0338c
GDPH (D2)**	6761		Rv3302c
Cyt *bcc:aa*$_3$ supercomplex	0835, 0987, 4260-4263, 4267-4268, 4437,4692-4693, 6087	7RH5	rv0432, rv2193-rv2196, rv2199c-2200c, rv3043c, rv2468A-rv2468c,Rv3584
Cyd (Cyt *bd*)	3232-3233	7D5I	rv1622c-rv1623c
CydDC	3230-3231	8IPQ	rv1620c-rv1621c
App (Cyt *bd*)	5605-5606		-
Frd	-		rv1552-rv1555
ATP synthase	4935-4942	7JG5	Rv1304-Rv1311

1.5.3.2 Dehydrogenase

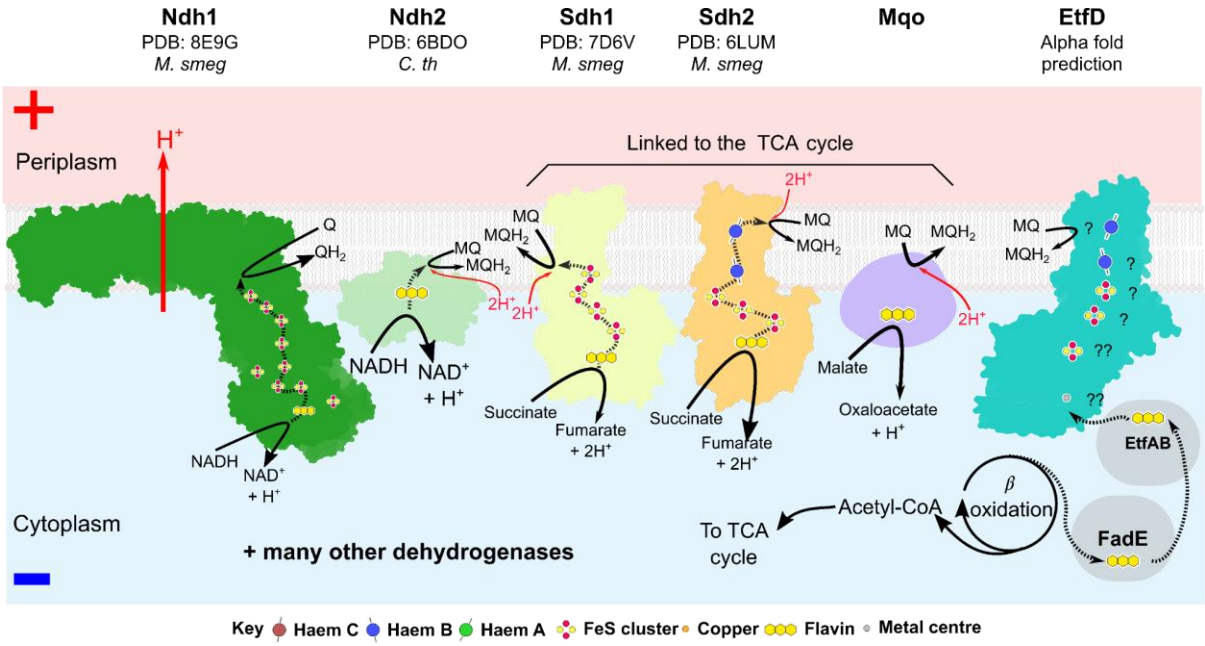

Figure 1.14 - The available structures of key mycobacterial dehydrogenases. *The sites of oxidation and quinol reduction are shown. Ndh1 is the proton-pumping NADH dehydrogenase (PDB:8E9G, Liang et al., 2023). Sdh1 is a class F succinate dehydrogenase (PDB: 7D6V, Zhou et al., 2021). Sdh2 is a class A succinate dehydrogenase (PDB:6LUM, Gong et al., 2020) There are no experimentally determined structures of mycobacterial Ndh2, Mqo, or EtfD. For Ndh2, the structure from C. th is shown instead (PDB 6BDO, Heikal et al., 2014). An alpha fold model of EtfD is shown with predicted cofactors based on homology.*

Mycobacteria have both of the two types of NADH dehydrogenases (ndh), the type I is encoded by the *nuo* operon and is not the major ndh in mycobacteria but appears to be used in carbon-limited conditions (Liang et al., 2023). Instead, the type II ndh is dominant in mycobacteria, often referred to as Ndh2. *M. smeg* only has one homologue but *M. tb* has two type-II dehydrogenases often distinguished as Ndh and NdhA (Beites et al., 2019).

Mycobacteria also have multiple succinate dehydrogenases, Sdh1 and Sdh2 (Pecsi et al., 2014). Sdh2 is a class A succinate dehydrogenase and is near essential in *M. smeg* where as Sdh1 is not (Pecsi et al., 2014). Sdh1 is the founding member of the class F succinate dehydrogenase (Hards et al., 2019) and it appears to be favoured in *M. tb* (Adolph et al., 2024) and is essential for *M. tb*'s survival in the stationary phase. Experiments with knockdowns of the succinate dehydrogenase in *M. tb* have demonstrated that the lack of one can be compensated by the other (Adolph et al., 2022). The structures of both succinate dehydrogenases have been determined (Gong et al., 2020; Zhou et al., 2021). Mycobacteria can have either Mqo, Mdh or both. *M. tb* has both whereas *M. smeg* only has Mqo (Harold et

al., 2022). Along with the succinate dehydrogenase, Mqo provides a direct link between the TCA cycle and the ETC in mycobacteria. There are several other dehydrogenases present in mycobacteria, typically supposed to be monotopic membrane proteins akin to Ndh2 and Mqo, for example, the glycerol-3-phosphate dehydrogenase (GDPH).

Concerning β-oxidation of fatty acids and its connection to the ETC, recent work has demonstrated that some of the enzymes are not conserved between mitochondria and mycobacteria (Beites et al., 2021). The acyl-dehydrogenase (FadE) and electron-transferring flavoprotein (EtfAB) appear to operate similarly and have similar structural architecture to their mitochondrial homologues. However, the mycobacterial Etf:quinol oxidoreductase (EtfD) is a transmembrane protein as compared to the mitochondrial enzyme which is monotopic. Upon inspection of the predicted alpha fold model of EtfD, (Jumper et al., 2021; Varadi et al., 2022) it appears that there are up to two sets of axial ligands that could coordinate haem groups (personal communication with Dr Morwan Osman). The biochemistry of this complex remains to be resolved: the exact composition of cofactors and the contribution to the generation of the Δp.

1.5.3.3 Mycobacterial terminal reductases and ATP synthase

Mycobacteria have two terminal oxygen reductases, the uniquely actinobacterial cyt *bcc:aa*$_3$ obligate respiratory supercomplex and the cyt *bd* quinol oxidase. Of the two oxidases, the supercomplex is more essential for the survival of the bacteria. Knockouts of components of the supercomplex severely hampered growth (Matsoso et al., 2005). The cyt *bd* quinol oxidase is upregulated in the absence of the supercomplex and under low oxygen tension (Kana et al., 2001). A second cyt *bd* is found in *M. Smeg* but not *M. tb* (Chauhan et al., 2022). The two cyt *bd*s found in *M. smeg are* akin to the two cyt *bd*s present in *E. coli* and are often distinguished by their operon names (Cyd and App). Throughout the rest of this thesis, I will refer to the Cyd cyt *bd* as simply cyt *bd* unless otherwise stated. The structures of the supercomplex (Gong et al., 2018; Mathiyazakan et al., 2023; Wiseman et al., 2018; Yanofsky et al., 2021) and the Cyd cyt *bd* (Safarian et al., 2021; Wang et al., 2021) have been determined.

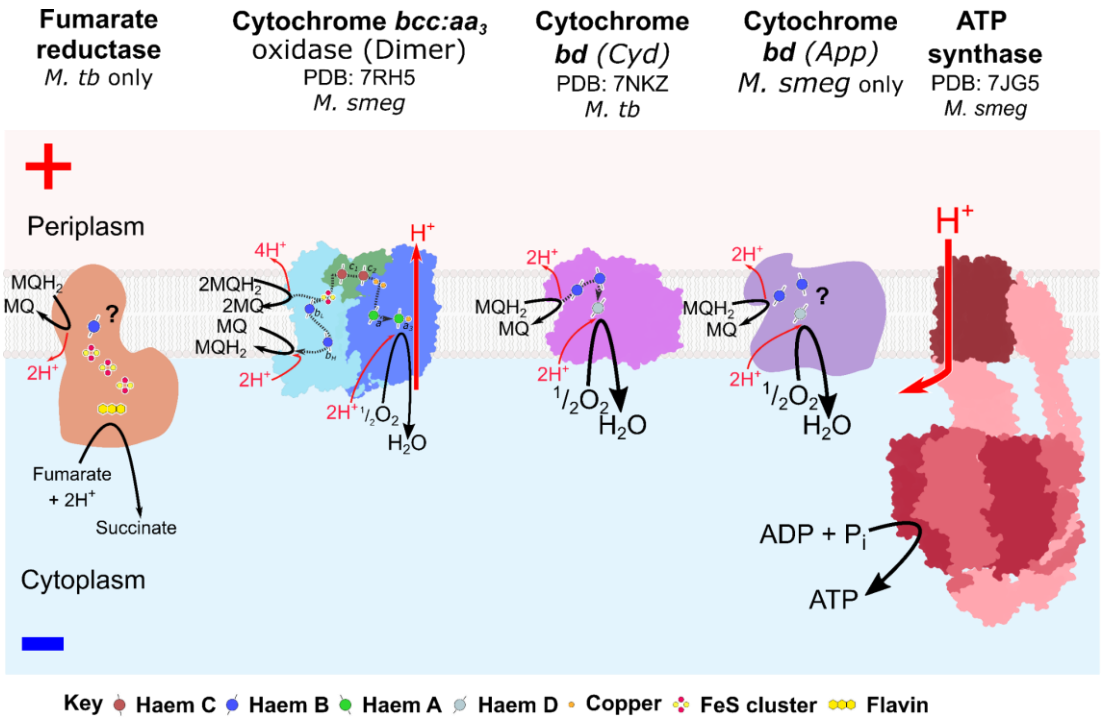

Figure 1.15 - The mycobacterial terminal reductases and ATP synthase. *The fumarate reductase is only present in M. tb, its structure has yet to be determined. The cyt bcc:aa₃ is an obligate supercomplex of a cyt bc type complex and HCO (PDB:7RH5, Yanofsky et al., 2021). The complex exists as a dimer, see Figure 1.16 A. Two cyt bd quinol oxidases are found in the mycobacterial genome. Only the Cyd cyt bd is present in M. tb (PDB:7NKZ, Safarian et al., 2021). The ATP synthase structure has been resolved (PDB:7JG5, Guo et al., 2021), and no oligomeric states have been observed.*

M. tb has an additional fumarate reductase not present in *M. smeg* that *M. tb* uses under anaerobic conditions to maintain the Δp by reducing fumarate to succinate (Watanabe et al., 2011). Its structure has not been resolved. The ATP synthase in mycobacteria is essential (Tran and Cook, 2005) and its inhibition is bactericidal (Andries et al., 2005). The full structure of the complex has been resolved with and without the inhibitor bedaquiline bound (Guo et al., 2021). A C-terminal extension of the α-subunit auto-inhibits the complex in the ATP hydrolysis direction (Guo et al., 2021).

1.5.3.4 Mycobacterial cytochrome *bcc:aa*$_3$ respiratory supercomplex

The cyt *bcc:aa*$_3$ supercomplex is a uniquely actinobacterial combination of a cyt *bc* type complex and a cyt *aa*$_3$ oxidase, overall catalysing the reduction of oxygen by menaquinol. A dimer of the cyt *bc* forms the core of the supercomplex, flanked by the cyt *aa*$_3$ oxidase on either side, Figure 1.16 A. The extension of the cyt *c* domain connects the cyt *bc* complex and cyt *aa*$_3$ complexes. Other subunits such as LpqE 'capping' the enzyme prevents

reduction of the cyt aa_3 by external cyt *c* (Gong et al., 2018; Megehee et al., 2006; Wiseman et al., 2018), reflected by the lack of soluble cyt *c* in the mycobacteria.

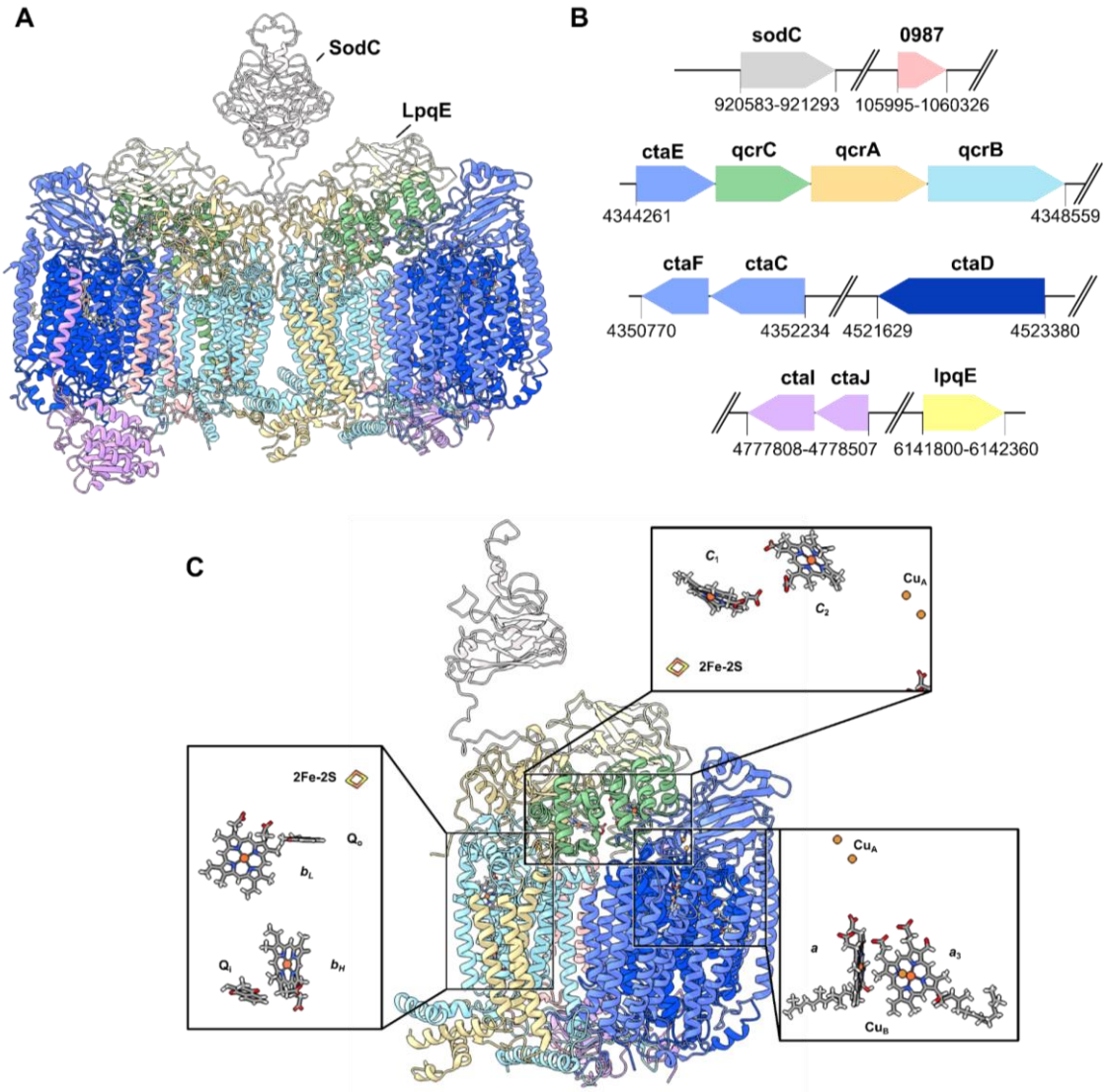

Figure 1.16 - The mycobacterial cyt bcc:aa$_3$ supercomplex. *(**A**) The structure of the dimer shows the SodC domain attached to the supercomplex and the LpqE subunit that sits on top of the cyt cc domain (PDB:7RH5, Yanofsky et al., 2021). (**B**) The genomic spread of the genes of the cyt bcc:aa$_3$ supercomplex in mc^{2}155 M. smeg. The density of MSMEG_0987 (Wiseman et al., 2018) has also been modelled as MSMEG_2575 (Gong et al., 2018; Yanofsky et al., 2021).*

The obligate nature of the supercomplex is reflected in the genomic organisation of the genes encoding for the supercomplex, Figure 1.16 B. *CtaE*, encoding a subunit of the cyt aa_3 is located within the *qcr* operon that encodes for the cyt *bcc* complex. Other subunits are spread across the genome, including several single transmembrane subunits, which are common in respiratory complexes. As the complex operates with menaquinol the redox potentials of the

redox cofactors are likely shifted more negatively as compared to the mammalian enzymes, as measured in the *C. glut* enzyme (Kao et al., 2016). The mycobacterial enzyme has a SodC-type superoxide dismutase (SOD) associated with the complex (Gong et al., 2018; Wiseman et al., 2018). Its exact role is unclear but it may neutralise the ROS produced by the cyt *bc* complex (Turrens et al., 1985).

1.5.4 The mycobacterial bioenergetic anti-TB agent target space

Mycobacterial bioenergetics has been a particularly fruitful new antimycobacterial target space. Bedaquiline, which targets F_1F_0ATP synthase (Andries et al., 2005), opened the bioenergetic target space as the first new TB drug in 50 years (Cox and Laessig, 2014; Mase et al., 2013). It has also been shown to be bactericidal on clinically important hypoxic nonreplicating populations of mycobacteria as they must maintain a *pmf* (Rao et al., 2008). It has now been licensed as part of the BPaL regimen for MDR-TB (Conradie et al., 2020). Clofazimine, previously used to treat leprosy (*Mycobacterium leprae*), has also recently been reinvestigated for MDR-TB regimens (Nunn et al., 2014). Clofazimine is thought to target Ndh2 resulting in reactive oxygen species (ROS) production (Yano et al., 2011). Other metabolic inhibitors are in clinical trials such as Q203 which targets the Q_o site of the cyt *bcc:aa*$_3$ supercomplex (Pethe et al., 2013). These demonstrate the fruitfulness of efforts in recent years to target bioenergetics.

The inherent flexibility of mycobacteria metabolism means that they can resist complete clearance by a single metabolic inhibitor. For example, the potency of Q203 is improved in either knockouts or combined with inhibition of the cyt *bd* quinol oxidase (Kalia et al., 2017; Lee et al., 2021). Surprisingly, early results from phase II clinical trials of Q203 have been positive in regimens without cyt *bd* inhibitions (Jager et al., 2020). This may be linked to observations that clinical strains of *M. tb* have lower expression levels of cyt *bd* than laboratory strains of *M. tb* (Arora et al., 2014).

TB treatments require multiple agents to prevent resistance from developing to a single mono-agent. Therefore when rationally designing regimens, the synergy of different agents is considered to maximise the effectiveness and shorten the length of the regimen. Along these lines, genetic screens have considered how interactions between the respiratory complexes could be exploited in treatment regimens (McNeil et al., 2022a). The other issue with current bioenergetic targeting agents is their associated side effects. Historically adverse events have been associated with bedaquiline, particularly cardiac events such as prolonged QT interval (Fox & Menzies, 2013). If the mechanism of action of agents such as bedaquiline can be clarified, then existing agents could be improved to reduce side effects and improve

efficacy. More tools are required to better understand mycobacterial bioenergetics as directly addressed by the work in this thesis.

1.6 Aims of this thesis

1. Adapt mammalian techniques for examining the mycobacterial respiratory chains, with a particular focus on non-invasively examining mycobacteria via multi-wavelength spectroscopy and oximetry measurement in the ‘bioenergetic chamber’ - Chapter 3
2. Build a spectral and thermodynamic model of the cyt *bcc:aa*$_3$ supercomplex to non-invasively measure $\Delta\Psi$ in live mycobacteria - Chapter 4
3. Isolate and begin spectral characterisation of other mycobacterial cytochromes, cyt *bd* quinol oxidase and the succinate dehydrogenase sdh2 - Chapter 5

Chapter 2 - Methods

2.1.1 Strains

Table 2.1 Strains of Mycobacterium smegmatis used in this work

Strain name	Genotype	Parent Strain	Source	Reference
mc^2155	'Wild-type' lab strain of mycobacterium smegmatis - electro-component	mc^26	Received from the Cook Lab	(Snapper et al., 1990)
JR128	Protein expression strain of *M. smeg* with a kanamycin cassette truncating the C terminus of GroEL1, T7 RNA pol	mc^24517	Received from Ma Miao, Luisi Lab	(Noens et al., 2011)
ΔcydAB	Markerless knockout of the *cydAB* operon (MSMEG_3233-MSMEG_3232)	mc^2155	Dr Zoe Williams & Dr Kiel Hards - Greg Cook Lab	(Lu et al., 2019)
ΔqcrCAB	Markerless knockout of the *qcrCAB* operon (MSMEG_4261-MSMEG_4263)	mc^2155	Dr Zoe Williams & Dr Kiel Hards - Cook Lab	(Chong et al., 2020)
Δsdh2	Markerless knockout of the Sdh2 operon (MSMEG_1672-MSMEG_1669)	mc^2155	Chen-Yi Cheung - Cook Lab	
3xFLAG *qcrB*	3xFLAG at the 3' end of the *qcrB* gene	mc^2155 (transformed with ORBIT plasmid)	Generated by Dr Morwan Osman	
3xFLAG *sdh2*	3xFLAG at the 3' end of the *sdhD* gene	mc^2155 (transformed with ORBIT plasmid)	Generated by Dr Morwan Osman	

2.1.2 Cell culturing

For culturing, Middlebrook 7H9 media was used as a base supplemented with 50 mM of glycerol and Tween 80, 0.05 % (v/v) unless otherwise stated. All media and supplements were autoclaved before use. For routine culturing, a glycerol stock was streaked on a 7H10 agar plate and left to grow at 37 ^{o}C until single colonies were visible. Single colonies from this plate were used to inoculate 50 mL starter cultures and were left to grow for ~3 days (250 mL flask, 37 ^{o}C, 200 rpm) to an OD_{600} of 1-3. These starter cultures were then stored at 4 ^{o}C until required and kept for a maximum of a month.

Typically, wild-type *mc^{2}155 M. smegmatis* was used apart from early experiments in the chamber or the native purifications of the cyt *bd* quinol oxidase, where JR128 was used. In this case, the starter cultures were supplemented with 30 μg.mL^{-1} of kanamycin before inoculation. For this strain, kanamycin LB agar plates were used instead of 7H10 to streak the glycerol stock for single colonies.

OD_{600} measurements were made in either a benchtop spectrophotometer or in the cuvette holder of the SpectraMax ABS Plus microplate reader (Molecular Devices). The measurement was made against a blank of Milli-Q H_2O and the culture was appropriately diluted if the OD_{600} was above 1.

2.1.2.1 Culturing for chamber experiments

Unless otherwise stated, cells used for experiments in the chamber were grown in 50 mL of media in a 250 mL Erlenmeyer flask. This was inoculated with the appropriate dilution of the starter to reach an OD_{600} of ~ 1 (early exponential phase) for the chamber experiment.

Initial growth experiments were performed in 1 L cultures in non-baffled 2.5 L culture flasks with 50 mM of either glycerol or succinate, no kanamycin was added to these large-scale cultures when JR128 was used. These were then harvested at the indicated time points during the growth. Subsequent variations in the culture volume are described in the text.

2.1.2.2 Bioreactors

The bioreactors were run with the help of Dr Jared Cartwright, head of the Protein Production Laboratory in the Technology Facility at the University of York Biology Department. Applikon mini bioreactor systems (500 mL) were autoclaved with 250 mL of Tween-80 containing media. Prior to inoculation, the bioreactor was warmed to 37 ^{o}C, and the V-control software was set to control & collect the pH, temperature, air input, and stir rate. The pH probe was calibrated with a two-point calibration. After the system was fully oxygenated, stirring at 300

rpm for 20 mins, the dO2 probe was set to 100 %. Drops of antifoam were added to each bioreactor to prevent excessive foaming.

A starter culture as described above was used to inoculate the bioreactor (1/200 dilution, 0.25 mL). The 2nd succinate culture, set to 40% dO2, was reinoculated with 2.5 mL of starter culture at ~ 23 hrs due to a lack of visible growth. The culture was then followed with the software-collected data, periodic OD_{600} measurements, and 5 mL samples examined with the bioenergetics chamber. The dO2 control loops were set to either 30 % or 40 %. The control loop operates such that the stir speed increases to maintain dO2 up to 550 rpm. Oxygen requirements beyond that stir speed are met by bubbling air through the culture. There was a delay in setting the control loop for the 40 % glycerol culture which did not begin until ~30 hrs into the run. The data collected by the system was extracted as a .csv and plotted via a Python script.

2.1.2.3 Culturing for the FLAG constructs

For expression of the 3xFLAG tagged supercomplex or the 3xFLAG tagged Sdh2 the media was supplemented with 50 µg/mL of Hygromycin (Filter sterilised). 50 mL (250 mL Erlenmeyer flask) fridge starter cultures were grown to a late exponential phase and kept at 4°C until required. These starter cultures were used to inoculate 1 L cultures in 2.5 L baffled flasks for expression of the 3xFLAG tagged constructs, typically a 1/200 dilution. These cultures were grown to an OD_{600} of ~ 0.8.

2.1.2.4 Culturing different strains of mycobacteria for spectral analysis.

The different strains were spread from glycerol stocks or agar stabs on 7H10 agar plates. From this starter cultures were grown as described above, depending on the strain this could take longer than the wild-type strain. From this starter culture, the 1L large-scale culture was inoculated (baffled 2.5 L flasks), again this was typically a 1/200 dilution. For the membranes isolated from cultures grown on Tryptic soy broth (TSB), Tryptic soy agar (TSA, Merck Millipore) was used to plate for single colonies. The cultures were grown on TSB (Merck Millipore) supplemented with 0.05% Tween.

2.2 Membrane Isolation

This is the protocol used for isolating membranes used in kinetic assays, for spectral characterisation of strains and in the purification of the FLAG-Tagged constructs.

The lysis buffer was either 50 mM Tris-SO_4 pH 7.4, 150 mM NaCl 1 mM EDTA or 50 mM potassium phosphate pH 7.4 depending on the downstream application.

The cells were harvested by centrifugation (5 k*g*, 20 mins, 4 ^{o}C, SLC-6000 rotor). The pellets were then resuspended in a chilled lysis buffer with 1 Roche protease inhibitor tablet per 50 mL) and lysed by 3 passes through the cell disruptor (Constant Systems limited) at 40 kpsi. The system was washed with water followed by pre-chilled lysis buffer prior to passes. Unbroken cells and debris were pelted by centrifugation (12 min, 48 k*g* spin, SS-34 rotor, 4 ^{o}C). The supernatant from this spin was filtered through a 0.5 µm filter before a longer ultracentrifuge spin to pellet the membranes (150 k*g*, 2 hrs, Ty45Ti rotor). The pelleted membranes were washed by resuspending and pelleting again (150 k*g*, 2 hrs, Ty45Ti rotor). The membranes were then resuspended and stored at -70 ^{o}C, small aliquot was taken to determine the protein concentration via bicinchoninic acid (BCA) assay.

2.3 Purification of mycobacterial cytochromes

2.3.1 Purification of 3xFLAG cyt *bcc:aa*$_3$ supercomplex

The buffer used throughout was either 50 mM Tris-SO_4, 150 mM NaCl or 50 mM potassium phosphate pH 7.4. The phosphate buffer system was tried over concerns of binding to the cyt *aa*$_3$ but no difference in behaviour was observed.

The membranes were thawed and diluted to 5 mg/mL, as determined by the BCA assay, and then incubated with 1 % n-dodecyl-β-D-maltoside (DDM) for 40 min at 4^{o}C with agitation (roller). Unsoublised material was then removed via ultracentrifugation (150 k*g* Type 70.1 Ti rotor, 4^{o}C). The anti-FLAG M2-affinity resin was washed twice and then resuspended in the binding buffer (buffer system, 0.02% DDM). The resuspended resin was then incubated with the solubilised membrane for 1 hr at 4 ^{o}C with agitation. The resin was then pelleted (300*g*, 2 mins) resuspended in the binding buffer and transferred to a gravity spin column (Pierce). The resin was then washed with the wash buffer (buffer system and 0.003% glyco-diosgenin (GDN)) to exchange detergent systems (3 washes with 4x resin volume), either by gravity or by centrifugation (50*g* 30s). The complex was then eluted off with the elution buffer (buffer system, 0.003% GDN and 150 µg/mL FLAG peptide), 3 times 1x resin volume, again either gravity or centrifugation. The elution was then concentrated with 300 kDa concentrators to remove the FLAG peptide and to the required concentration.

2.3.2 Purification of cyt *bd* quinol oxidase

2.3.2.1 Membrane isolation

An earlier version of the protocol was used to isolate the membranes. The lysis process was as before except the ultracentrifuge spin was replaced by a longer spin (48 k*g*, 3 hrs, SS-34,

4 °C) to pellet the membranes. A second longer spin (48 k*g*, 2-3 hrs, SS-34, 4 °C) of the supernatant was used to pellet a smaller membrane pellet. The membrane pellets from both spins were combined and resuspended in lysis buffer (Tris-Cl pH 7.4) and stored at -70 °C.

2.3.2.2 Sample preparation

Per purification, 3-4 mL of crude membranes were defrosted and resuspended. The best results were achieved when the membranes were then diluted to ~20 mL and incubated with DDM at 4 °C for 40 mins with agitation. The solution was then clarified by centrifugation at 48 k*g* for 20 mins (SS-34 rotor, 4 °C). The supernatant was then concentrated (vivaspin 30,000 MWCO concentrator) and filtered through a 0.2 µM filter before loading onto the sample loop.

2.3.2.3 Purification protocol

An ÅKTA system (Cytivia) was used for all purifications.

2.3.2.3.1 Buffers

Table 2.2 - Composition of buffers used during cyt bd purifications. Buffers were filtered and degassed before use.

Buffer	Composition
IEX buffer A	20 mM Tris-Cl pH 7.4, 10 % glycerol, 0.2% DDM
IEX buffer B	20 mM Tris-Cl pH 7.4, 10 % glycerol, 0.2% DDM, 1 M NaCl
SEC buffer	20 mM Tris-Cl pH 7.4, 10 % glycerol, 0.05% DDM, 150 mM NaCl

2.4.2.3.2 Ion exchange

HiTrap HP Q columns were connected in tandem and used for the purifications, typically 2 or 3 1 mL columns were used. The column volume (cv, 0.9 mL) of 1 of these columns was used as the cv for the method. A 5mL loop was used to apply the sample to the column. Before loading the sample, the system, loop, and columns were washed in MilliQ H2O, followed by equilibration in IEX buffer A at a flow rate of 1 mL.min^{-1}. The system was set to monitor the absorbances at 280 nm (protein), 420 nm (haem) and 650 nm (haem D) throughout the run. The sample in the loop was loaded onto the columns using buffer A. The columns were then washed with 20 cvs of buffer A. The flow-through for both stages was collected. The bound proteins were then eluted off with a NaCl gradient, with 0.5 mL fractions collected in a 96-well plate across the elution. The gradient was followed by high salt washes with a final wash at 100% buffer B.

2.4.2.3.3 Size exclusion

Small samples from the fractions intended for pooling were taken for spectra and gel samples (typically ~70 µL). The remainder of the fractions were pooled and concentrated to < 500 µL using a vivaspin 30,000 MWCO concentrator (4.4 k*g*, 10 mins runs). A 1 mL loop was used to apply the sample to the column (Superdex 200 increase 10/300 GL, Cytiva). Prior to loading the sample, the system, loop, and columns were washed in MilliQ H_2O, followed by equilibration in SEC buffer at a flow rate of 0.5 ml. min^{-1}. The system was set to monitor the absorbances as 280 nm, 420 nm, and 650 nm throughout the run. 0.5 mL fractions were collected during elution in 96 well plates with a 0.4 cv delay.

To note initially the absorbance at 625 nm was used to monitor the haem D content, however, this was later changed to 650 nm as it better reflected the haem D content.

2.4 Biochemical assays and gel electrophoresis

2.4.1 Kinetics

SpectraMax ABS Plus microplate reader (Molecular Devices) and accompanying software (SoftMax Pro 7.1) were used for both the BCA assay and the NADH oxidation assays.

2.4.1.1 Bicinchoninic acid (BCA) protein assay

The protein concentration was determined using the BCA assay as advised for a 96-well plate (200 µL of BCA working reagent to 25 µL sample). Membranes were diluted to allow concentration determination, typically 1/10, 1/25, 1/50, 1/100. Averages of triplicates were used to plot the BSA standard curve (0, 0.1, 0.2, 0.4, 0.5, 0.6, 0.8, 1 $mg.mL^{-1}$) and calculate sample concentrations.

2.4.1.2 NADH oxidation assay

Assay were performed in triplicate in a 96-well plate. The assay buffer consisted of Tris-SO_4 pH 7.4, 150 mM NaCl. Small aliquots of 100 mM NADH stocks were used in the assay and had been made up in the reaction buffer and stored at -20 ^oC before use. The stocks of pore-forming antibiotics Gramicidin D or Alamethicin made in ethanol at 1.88 $mg.mL^{-1}$ and 2 $mg.mL^{-1}$ respectively. For the assay membranes were diluted to 0.2 $mg.mL^{-1}$ with and without pore-forming antibiotics at required concentrations in 225 µL volumes. The plate was incubated for 10 minutes at 37 ^oC before adding 200 µL to the reaction well with 1.4 µL of 100 mM NADH to give a final concentration of 700 µM NADH. The reaction mixture was mixed via x10 pipetting with care not to introduce bubbles. NADH oxidation was followed for 10 minutes by the change in the absorbance at 340-380 nm using 4.81 $mM^{-1}.cm^{-1}$ as an

extinction coefficient for NADH. These rates were normalised to mg^{-1} based on the protein concentration determined with the BCA assay.

2.4.2 Gel electrophoresis

2.4.2.1 Blue Native-Polyacrylamide Gel electrophoresis (BN-PAGE)

3-12% Bis-Tris Native gels (Invitrogen) were run as recommended by the manufacturer's protocol. The running and cathode buffer contained 1X NativePAGE™ running buffer (Invitrogen). The cathode buffer contained 1X NativePAGE™ cathode additive. For 15 well gels, samples were prepared by mixing with 3 µL 4x NativePAGE sample buffer and 0.5 µL G250 additive and made up to the appropriate volume with MilliQ H_2O depending on the concentration of the sample. The 4xNativePAGE sample buffer was made in-house (200 mM BisTris, 24N HCl, 200 mM NaCl, 40% glycerol and 0.004% Ponceau S). The NativeMark™ Unstained Protein™ Standard (Invitrogen) was used as a ladder. For earlier gels during the purification of the cyt *bd* oxidase, size exclusion standards were used as markers instead.

10 µL aliquots of samples were then loaded into the wells and run at 150 V at 4°C for 60 mins, then voltage was increased to 250 V Constant for the remainder of the run (30–90 minutes) until the dye front had reached the end of the gel. The gels were then washed in milli-Q H_2O and stained with Coomassie dye. The gels were then left to destain overnight in fresh milli-Q H_2O to improve the contrast.

Table 2.3 - Molecular weight markers for cyt bd oxidase BN-PAGE

Molecular weight marker	Molecular weight (kDa)
Thyroglobulin	669
Alcohol Dehydrogenase	158
Conalbumin	75
Ovalbumin	45

2.4.2.2 High resolution - Clear native electrophoresis (hr-CNE) and In-gel activity assays

The protocols within (Wittig et al., 2007) were followed. The gels were run as for the BN-PAGE except for the cathode buffer 1X NativePAGE™ running buffer (Invitrogen), 0.02% DDM and 0.05% sodium deoxycholate. The samples were made up as for the BN-PAGE but

without the G250 additive. Once the gels had been run either the whole gel or sections of the gel were incubated in 50 mM potassium phosphate buffers (pH 7.4) with the agents of the specific assay. NADH dehydrogenase - 2.5 mg/mL Nitro Blue Tetrazolium and 150 µM NADH, 3-5 minutes was required to see staining. Succinate dehydrogenase - 2.5 mg/mL Nitro Blue Tetrazolium, 20 mM succinate and 202 µM phenazine methosulfate (PMS), 3-5 minutes was required to see staining. Quinol oxidoreductase - 0.5 mg/mL 3,3'-diaminobenzidine, 30 minutes to 1 hr was required to see staining. The staining was stopped by incubating with a fixing solution (50% methanol and 10 % acetic acid). The gel could then be stained by coomassie but often an additional gel was only stained with coomassie. For mass spectrometry, bands were excised and sent to the Technology Facilities' protein identification service.

2.5.2.3 SDS-PAGE

The BN-bands were excised and incubated with SDS buffer (5% 2- mercaptoethanol, 62.5mM Tris-HCl pH 6.8, 2% SDS, 10 mM Glycerol) for 20 mins at room temperature. Non-band samples were mixed with 4x SDS loading buffers. The samples & bands were then run on 12 % SDS gels (4% stacking) at 200 V for ~ 40 mins. A pre-stained BioRad ladder was used. Similar staining procedure as for the BN-PAGE gels, often with gels left in stain overnight.

2.5 Bioenergetic chamber system

The system has been described previously (Kim et al., 2011), what follows is a description of the system and any adaptations that have been made to measure mycobacteria.

2.5.1 Chamber specifications

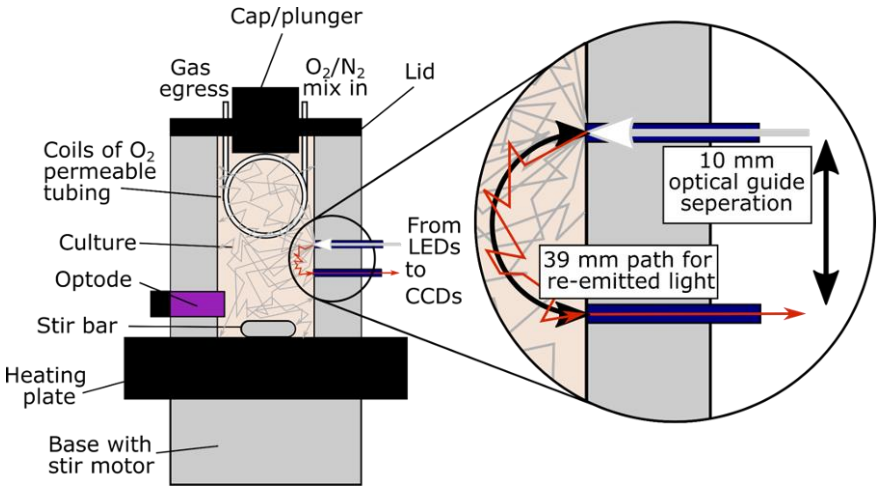

Figure 2.1- Diagram of the bioenergetic chamber.

A diagram of the custom-built chamber is shown in Figure 2.1. It consists of a 5 mL, 17 mm inside-diameter quartz crucible within an aluminium block. The block is maintained at the desired temperature (37 ^{o}C) by a thermoelectric element below the crucible. The culture or solution is kept homogeneously agitated via a glass stir bar and stir control unit (Rank Brothers Ltd) below the aluminium block, with seals' made of Viton by best respirometry practices (Haller et al., 1994). The chamber is sealed via a lid (with or without the gas ports with attached tubing). Several ports within the side of the chamber accommodate other aspects chamber as described below. The chamber is controlled by bespoke software (Palencia).

2.5.2 Oxygen measurement and culture oxygenation control

The oxygen concentration of the chamber was measured via an oxygen optode system with a phosphorescent membrane (Tau Theta Instruments, Boulder, CO) inserted in the side of the chamber. The optode sits within the culture to measure the oxygen concentration within the culture. The phosphorescent lifetime of the membrane is inversely proportional to the oxygen concentration. This is measured via the phosphorescent emission at 650 nm. The chamber is oxygenated or deoxygenated under the control of the blend on N_2/O_2 that passes through 120 mm of platinum-cured silicone tubing (Braintree Scientific), immersed in the chamber contents. This blend is controlled using a feedback loop within custom software that allows the chamber to maintain a constant set of oxygenation. No CO_2 is required in the tubing for the maintenance of mycobacteria. Oxygen consumption of the chamber was measured from the change in chamber oxygen concentration (VrO2) and the delivery of oxygen to the chamber, DgO2. The oxygen delivery rate was determined by the oxygen gradient across the tubing and the tubing permeability. The oxygen gradient was measured via a second oxygen optode at the exit port of the gases and the oxygen permeability was calibrated at the beginning of each run using a two-point calibration with the set oxygen varied from 100 µM to 150 µM.

2.5.3 Haem attenuation spectra - Remission spectroscopy

A warm white light-emitting diode (4000K-90 Luxeon-CZ at 300 mA) was used to illuminate the culture. The light was detected by optical fibre in remission spectroscopy, directly below the light source. The distance between the source and detector is 10 mm. Previously the differential path length has been measured as ~39mm (Kim et al., 2011) using the 2nd deferential techniques of the 740 nm absorption band of water (Matcher et al., 1994).

The collected light was detected by two separate CCD (charge-coupled device) spectrograph systems working in time-multiplexed mode at 50 Hz using 6 ms on and 4 ms off duty cycle.

Contiguous spectra were averaged to give a resolution of 0.5 s. Typically the CCDs were set to detect over the wavelength ranges and slit widths stated in Table 2.4.

For later experiments, 2 phases were used. One with LEDs on, one without. The second phase was subtracted from the first to remove a phosphorescent peak that would otherwise contribute to the spectrum at 650 nm, interfering with the wide CCD spectrum.

Table 2.4 - Typically settings used the CCDs

Parameter	Cytochrome/Narrow CCD	Wide CCD
Centre point (nm)	574.59	566.26
Wavelength range (nm)	508.62 - 639.93	430.51 - 701.37
Grating	600g/mm@500nm	300g/mm@500nm
Silt width (microns)	200	100

2.5.4 Calibrations

Wavelength calibrations were performed at the beginning of each day with Milli-Q water in the chamber. The specific intensity bands from a mercury lamp were used to calibrate the wavelengths of the spectra, slits set to 0 microns to improve band resolution.

Two types of oxygen calibration were used. When either of the optode membranes are replaced, 5% steps of oxygen from 0 to 100 %, are held for two minutes and used for a lifetime calibration. The chamber optode was routinely calibrated when a different buffer/media or temperature was used for experiments using a two-point calibration. Oxygenated point - the buffer is allowed to equilibrate with the atmosphere, the oxygen concentration at this point will depend on the temperature. Deoxygenated point - 0 µM oxygen upon the addition of sodium dithionite. Changes in temperature and salinity are inputted into the calibration interface for both the lifetime and 2-point calibration. Changes in the atmospheric pressure are also accounted for.

Prior to the addition of cells, an intensity calibration is performed with the buffer, silt width and LED intensity that will be used during the experiment. The permeability of the tubing was calibrated using two-point calibrations at the beginning of every run, as detailed in Figure 2.2.

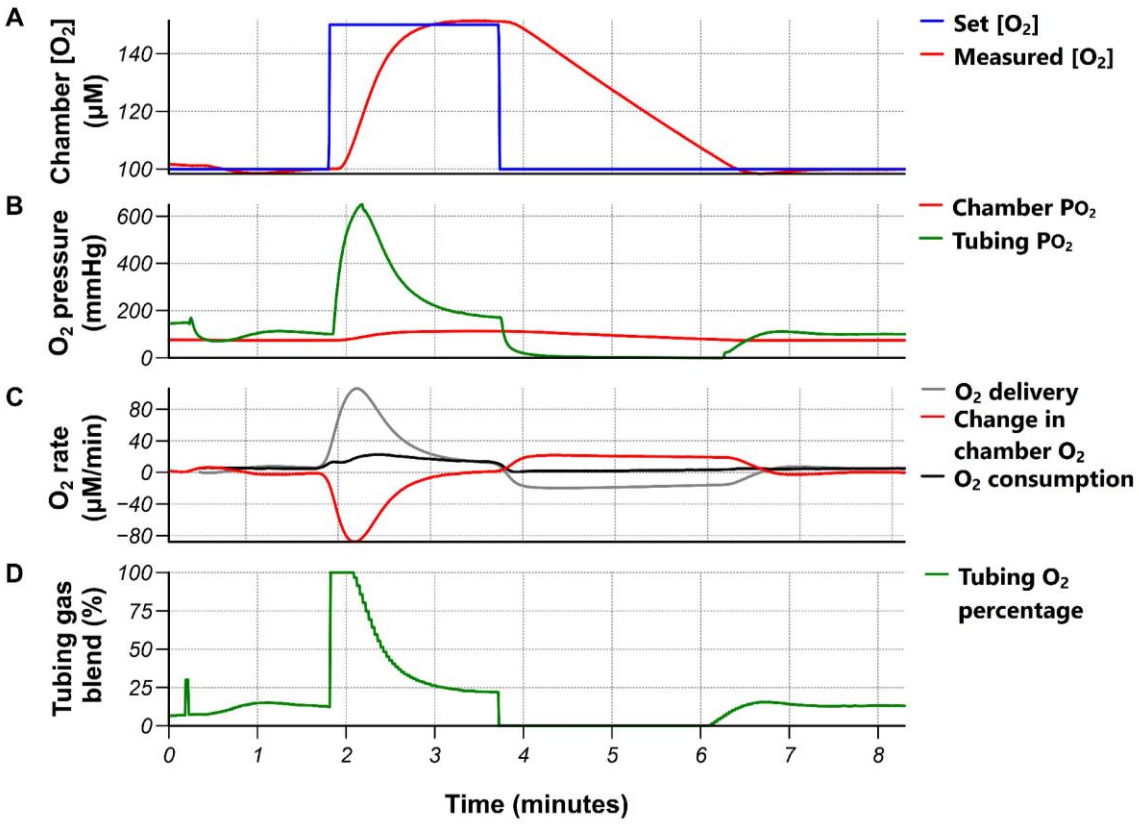

Figure 2.2 - Chamber oxygenation measurements, control and Top hat calibration *(A) Shows the set oxygen concentration, in blue, and the measured chamber oxygen concentration, in red, as measured by the chamber optode. (**B**) Shows the oxygen pressure of the chamber (chamber P_{O_2} in red) and in the tubing (tubing P_{O_2} in green). The tubing oxygen is measured via an optode in the exit port of the tubing. (**C**) Shows the changes in the oxygen rates during the calibration. O_2 delivery, in grey, demonstrates the oxygen delivery as calculated based on the difference in the oxygen pressure in the chamber and tubing. This was calibrated at the start of every experiment, using the top hat to determine the permeability of the tubing. Change in chamber O_2, in red, is the change in the oxygen concentration in the chamber over time, calculated from the gradient of chamber O_2, red in graph **A**. The overall oxygen consumption is shown in black and is the sum of the O_2 delivery and change in chamber O_2. (D) The tubing O_2 percentage, in green, shows the percentage of oxygen flowing through the tubing. This is under the control of a feedback loop to maintain the chamber at the set oxygen concentration.*

2.5.5 Haem fitting and spectra averaging

A spectral fitting algorithm employs a linear combination of model spectra from reference spectra to generate a plot of the concentration of oxidised haem over time. The collected Δ attenuation spectra were decomposed using spectral model 1 as described in Chapter 3

unless otherwise described. Other spectral models applied in later experiments are described in the text.

2.5.6 Cell prep for chamber/performing the runs

5 mL of culture with an OD_{600} ~1 was used for the chamber experiments. Before the experiment, the cells were pelleted (tabletop swing bucket centrifuge, 3.8 k*g*, 37 ^{o}C, 5 mins) washed once and resuspended in 5 mL of autoclave 7H9 media and 50 mM glycerol, that had been kept warm prior to using to resuspend the cells. As indicated in initial experiments the cells were instead resuspended in a buffer of 20 mM HEPES pH 7.4, and 150 mM NaCl.

2.5.7 *In vivo* ΔΨ and E_hQH_2 measurements.

The ΔΨ measurement was made as described in (Kim et al., 2012; Springett, 2015a) and is described in more depth in the text of Chapter 4. Briefly, the oxidised and reduced point of the *b*-haems were set based upon the addition of thioridazine to give the oxidised position and anoxia to give the reduced position. This gave the oxidation state of the two *b*-haems throughout the experiment. From the oxidation states the redox poise between the two *b*-haems can be used to calculate the ΔΨ based on Equation 2.1 (the same as Equation 4.3 in Chapter 4).

$$\Delta G^{b_L \rightarrow b_H} = -(E_h^{b_L} - E_h^{b_H}) + \beta \Delta\Psi \qquad \text{Equation 2.1}$$

Where $\Delta G^{bL \rightarrow bH}$ is the Gibbs free energy of the transfer of electrons from b_L to b_H, E_h^{bL} and E_h^{bL} are the redox potentials of b_L and b_H respectively, β is the fraction of the membrane that the electrons are transferred over and ΔΨ is the membrane potential. The transfer of electrons between the two *b*-haems is in a state of equilibrium as the centres are within 14 Å of each other, therefore the Gibbs free energy is approximately zero and so Equation 2.1 can be rearranged to calculate the $\Delta\Psi$. The redox potentials of the *b*-haems can be calculated from their redox state, using a thermodynamic model that accounts for the anti-cooperativity between the *b*-haems as detailed in (Springett, 2015a). This assumes that the *b*-haems are in equilibrium with the Q-pool so from their redox state the redox potential of the Q-pool can be measured.

2.6 Cuvette system

2.6.1 Cuvette system specifications

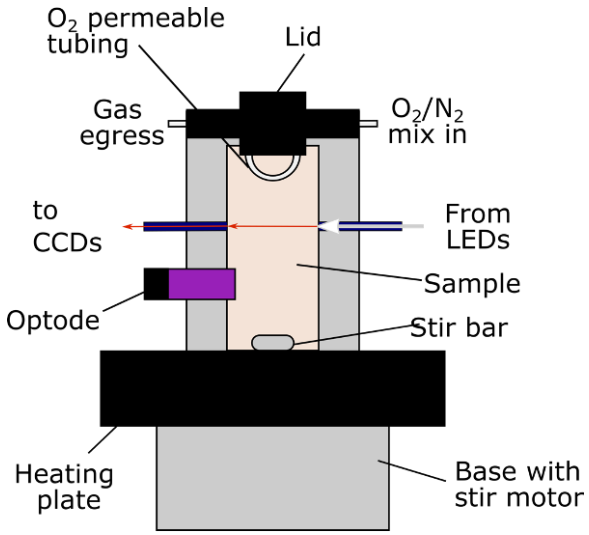

Figure 2.3 - The cuvette systems

The cuvette system is shown in Figure 2.3 and has a very similar design to the chamber system except that the spectroscopy geometry is transmission rather than remission. The cuvette holds 2.1 mL of volume and the optical fibres illuminating the contents are on the opposite side of the cuvette to the fibre collecting the light, with a path length of 1 cm. This can be connected to the same CCDs as the chamber system or to a single CCD system with the same wavelengths as the narrow cytochrome CCD. The vast majority of the experiments were performed with a single CCD configuration.

A considerably greater intensity of light is transmitted through the cuvette system. To avoid the CCD becoming saturated the LED (Luxeon CZ 4000K-90) was run at 25 mA and the slits were kept as narrow as the system allows for. The collected spectra were collected and decomposed using the spectral model as defined in the text, typically this was spectral model 1 or the final spectral model, this helped to judge which haems centres were being reduced as the experiment was being performed.

For delivering oxygen 26.7 mm of the tubing was used to control the oxygenation of the system. Other heating, stirring and oxygenation aspects of the system are as in the chamber system. The same calibrations as with the chamber system were performed with the appropriate buffers. Any detergent was not included in the oxygen calibration. If large volumes were added to the cuvette, i.e. for a protein sample, the same volume was taken out

prior to the sample addition so that the total volume remained constant. Other additions were kept below 20 µL to prevent dilution of the sample.

2.6.2 Cuvette experiments

The same buffering system for the protein purification was used for the cuvette experiments, either 50 mM Tris-SO_4 pH 7.4, 150 mM NaCl or 50 mM potassium phosphate buffer pH 7.4. 0.003% GDN was added to the buffer inside the cuvette to help stabilise the complex. Often set % of O_2 was supplied to the chamber rather than allowing the system to match a set O_2 concentration.

For the isolation of the cyt aa_3 and cyt *cc* spectral signals, 20 µL of 3xFLAG cyt *bcc:aa*$_3$ (at 5.6 mg.mL^{-1}, as determined by BCA assay) was added to the cuvette containing 50 mM Tris-SO_4 pH 7.4, 150 mM NaCl and 0.003% GDN. 20 µM of potassium ferricyanide was added to the cuvette and used to extract the cyt *aa*$_3$ spectrum as described in Chapter 4. A mixture of ascorbate and TMPD were then added to the cuvette to give a final concentration of 3 mM of ascorbate and 62.5 µM of TMPD. Simultaneously the oxygen was set to 0 µM. The cyt *cc*$_3$ spectrum was extracted as described in the text.

For the isolation of the mycobacterial b_L spectrum, 50 µL of 3xFLAG cyt *bcc:aa*$_3$ was added to the cuvette which contained 50 mM Potassium Phosphate pH 7.4, with 0.003% GDN, and 20 µM PES. The buffer had been deoxygenated under a nitrogen atmosphere in a glovebox prior to its addition to the cuvette. Initially, after the sample was added, the oxygen was set to 5% and 200 µM addition of NADH was used to transiently reduce the haem C and haem A centres. To reduce the haem B centres, 2 µL of concentrated dithionite was added and the oxygen was set to 0%. 2 µM of menadiol (20 mM stock in ethanol) was used to oxidise the sample. The oxygen was steadily increased from 0% to 1 % to 5%. The b_L spectrum was extracted as described in Chapter 4

2.7 Potentiometric redox titrations -

The titrations were performed by Petra Hellwig and Frederic Melin at the University of Strasbourg using a thin-layer electrochemical cell as described previously (Hellwig et al., 1999; Moss et al., 1990). The working electrode was a gold grid modified with a 1:1 solution of cysteamine and mercaptopropionic acid. A mixture of 19 mediators was added to purified 3xFLAG cyt *bcc:aa*$_3$ supercomplex (at ~0.194 mM of the monomer). This gave the mediators a final concentration of 50 µM. Aqueous Ag/AgCl 3M KCl was used and the reference electrode with a platinum contact as the counter electrode. This was coupled to a potentiostat to set the ambient voltage. Spectra were recorded using a Cary 300 spectrometer for 32

voltages spread across the titration range typically in 25 mV steps. 1 hour was given to allow for the equilibration of the system in between voltage steps before the spectrum was collected. In the oxidative direction spectra were recorded between -0.65 V and + 0.3, with the spectrum at -0.65 V being the reference. In the reductive direction, spectra were recorded between +0.3 V and -0.7 V with the spectrum at +0.3 taken as the reference.

2.7.1 Single wavelength data processing

For the initial analysis performed by Petra Hellwig and Frederic Melin. The differential absorbance at specific wavelengths was plotted against the ambient applied electrical potential. These were then fitted to a Nernst equation with one or two components. Voltages were then converted from vs AgCl/Ag by adding +208 mV to vs SHE (standard hydrogen electrode) determining the midpoint potentials of the haem cofactors.

2.7.2 Multiwavelength data processing

The data processing was implemented in a Python script using the NumPy, Scipy and Pandas libraries (Harris et al., 2020; McKinney, 2010; Virtanen et al., 2020). For fitting the spectral models, the titration data was compiled into a matrix, as described in Chapter 4 between 511-627 nm. The reference spectra in the spectral models were interpolated so that they had the same wavelength sampling as the titration data. Normalised background functions were also included to account for any changes in the background ($1+ 1/\lambda^2$).

The titration spectra were decomposed using Equation 4.7 described in Chapter 4. This is encoded by the defined function shown in Figure 2.4. Where Abs is the titration data, and S is the matrix containing the reference spectra, which can be amended depending on the number of reference spectra in the fit. C, a matrix of the concentration of each of the components in the S matrix at each of the measure voltages, is returned.

```
def decomposition(Abs):
    S = np.stack((haemC1,haemBH,haemBL,haemA,blank,scatter2),axis=1)#
    C = np.matmul(np.matmul(np.linalg.inv(np.matmul(np.transpose(S),S)),np.transpose(S)), (Abs))
    return C
```

Figure 2.4 - Python function used to decompose the spectra

The concentration of each of the haem components could then be plotted against voltage as a ‘haem redox titration curve’

The fitting of thermodynamic models was implemented using the SciPy curve_fit module (Vugrin et al., 2007). For each haem centre, the ‘Haem titration curve’ generated as a result of the decomposition was fitted to a specified thermodynamic model (single Nernst,

combination of Nernst, two Nernst centres interacting with an interaction between the two). The model parameters also included a gradient and constant value so that the curve could be normalised to the fraction reduced over time. For the *b* haem anti-cooperativity, the input data (the two *b* haem curves) had to be flatten, the 1st *b* haem curve directly followed by the 2nd *b* haem curve in a 1-D array, as the curve_fit function does not take 2-dimensional input data. The residual sum of squares (Σr^2) and standard error regression (SER) were calculated using equations 2.2 and 2.3 respectively, where i is the number of measurements during the titration and p in the number of parameters used to describe the thermodynamic model.

$$\sum r^2 = \sum_{i=1}^{n} (y_i - f(x_i)^2 \qquad \text{Equation 2.2}$$

$$SER = \sqrt{\frac{\sum r^2}{n-p}} \qquad \text{Equation 2.3}$$

A similar approach had to be employed for the simultaneous spectral and thermodynamic fitting. This was based on the approach in (Bloch et al., 2009). 'Stand in' reference spectra (arrays of zeros the length of the measured wavelength in the experiment) were used to compile the initial reference spectra matrix, which was then flattened to one dimension. The initial guess for the parameters in the described thermodynamic model (4 centres 1 interaction, 6 centres 3 interaction, 6 centres 3 interaction 4 observed centres) were appended to the flattened reference spectra matrix. This could then be passed at the first guess at the parameters of the model in the curve_fit function. Both the titration data and the theoretical titration data it was compared to were also flattened when they were passed to the curve_fit function. The Trust Region Reflective algorithm was used by curve_fit to determine the solution. The Python script for the 4 centre 1 interaction model is provide in appendix 1

2.8 Spectral measurements of mycobacterial membranes

The 50 mM Tris-SO_4 pH 7.4, 150 mM NaCl buffer system was used throughout.

2.8.1 Initial membrane difference spectra (Chapter 3 glycerol grown vs succinate)

2.8.1.1 Preparation of samples

Membranes were isolated as for the cyt *bd* oxidase preparation with the membranes resuspended in Tris-SO_4 pH 7.4 instead. On the day of the spectral measurement, 500 µL of the crude membranes were defrosted, carefully resuspended, and incubated with 1 % DDM for 40 mins (4 ^oC with agitation). The solution was then clarified by centrifugation at 16

k*g* for 15 mins (tabletop centrifuge, 4 ^{o}C). 100 µL of the clarified solution was then used to collect spectra (75 µL for the stationary glycerol sample).

2.8.1.2 Spectra collection

A Cary 100 UV-vis Spectrophotometer (Agilent Technologies), controlled via the Scan Application (CaryWinUV software version 4.20), was used to collect absorption spectra between 800-350 nm (scan rate: 200 nm/min, data intervals: 1 nm, 0.3 SBW: 4 nm). Baseline corrections were performed with an appropriate buffer (lysis buffer for crude membranes, SEC buffer for purified samples) in a 50 µL quartz cuvette (10 mm path length) before the addition of each sample. For the 'as prepared' spectrum, equal volumes of the buffer were removed, and the sample was added to the cuvette, this was then mixed with pipette. Spectra were regularly collected until the spectra stabilised. For the reduced spectrum, 1 µL of 1 M sodium dithionate (H_2O), made freshly on the day, was added to the cuvette, and mixed by pipette, with care not to introduce bubbles. As with the 'as prepared', spectra were collected until the spectra stabilised.

2.8.1.3 Spectra processing

The data collected was used to generate a .csv file with columns for: wavelength, average oxidised, average reduced, and reduced-oxidised (difference spectrum). A truncated portion of this data (500-800 nm) was then analysed by a Python script. To determine the concentration of the haem signals, the difference spectrum was fitted using a linear combination of Gaussian peaks and normalised background scatter functions ($1 + 1/\lambda + 1/\lambda^2$). The was performed by decomposition using Equation 2.2.

$$C = A(S^T S)^{-1} S^T \qquad \text{Equation 2.4}$$

Where **C** is a column matrix of the determined concentration of the components fitted **A** is the column matrix of the absorbance at each wavelength for the fitted difference spectrum. **S** is the matrix containing the specific absorbance of each component of the fit for the fitted wavelength range, i.e. a matrix of the reference spectra. The Gaussian function used to describe the haem peaks described by the Equation 2.3

$$y = e^{-\frac{(\lambda-\lambda_0)^2}{(\frac{\sqrt{2}}{2\sqrt{2ln2}}w)^2}} \qquad \text{Equation 2.5}$$

Where λ_0 is the wavelength maxima of the peak and w is the full width at half maximum. The $\frac{\sqrt{2}}{2\sqrt{2ln2}}$ is approximated at 0.6006. The values for λ_0 and w for each peak are described in

Table 2.5. As detailed in Chapter 3, haem D is accounted for by a combination of two Gaussians.

Table 2.5 - Parameters used to define the Gaussians modelling the haem peaks.

Component	λ_0 (nm)	w
Haem C	551.9	11.6
Haem B	563.1	9.2
Haem A	600.5	19.3
Haem D (anaerobic)	629	20.9
Haem D (aerobic)	654	20.9

2.8.2 Reduction of membranes by NADH or succinate.

The chamber was set up and filled with 5 mL of membrane resuspension buffer, left with the plunger off to reach temperature and oxygenate. 100 µL of membranes were then added such that the membranes were at ~0.2 mg/mL. The gas control system was then turned on and the plunger was placed on to seal the chamber. Typically the oxygen was set to 100 µM. The chamber was typically left for ~10 mins for the oxygen concentration and haem oxidation state to settle before beginning experiments. Substrates were added at indicated points through a port in the plunger.

2.8.3 Difference spectra of membranes isolated from different strains of mycobacteria.

A similar procedure was followed, again the chamber was filled with 5 mL of the resuspension buffer. Depending on the concentration of the membranes, between 50-200 µL of isolated membranes were added to the chamber containing the resuspension buffer such that the membranes were at ~0.2 mg/mL. The oxygen was set to 100 µM. Additions of 4 µM potassium ferricyanide were used to oxidise the sample, up to 16 µM. This was judged based on the presence of reduced features in the attenuation spectrum. Additions of concentrated sodium dithionite (~2-5 µL, made up in H_2O) prepared that day were used to reduce the sample. Typically 2-minute periods were averaged over for the oxidised and reduced spectrum.

Chapter 3 - Establishing a visible-wavelength bioenergetic chamber as a tool for mycobacterial bioenergetic research

3.1 Introduction

3.1.1 Non-invasive measures of bioenergetic systems within living organisms

A classical problem with measuring biological systems is that often to quantify or measure a property of the system, the system must be disrupted, affecting the process under measurement. This is particularly a problem in bioenergetics where the processes being studied are delicate balances of rapid redox reactions. That is not to say that experimental techniques that rely on the disruption of cells do not offer powerful insights into the function of bioenergetic processes, only that they will be affected by the disruption by an unknown amount. A good example of these experimental approaches that rely on the disruption of the cell is the various -omics approaches. Figure 3.1 B shows an overview of these different experimental approaches.

Non-invasive techniques offer one way to relate reductive observations on isolated enzymes back to the system of the cell or make original observations within the cellular context (Figure 3.1 A). Spectroscopy is the measurement of how molecules interact with electromagnetic radiation, either through absorbance or emittance. The distinct interactions of the molecule under study will be dependent on the wavelength of the electromagnetic radiation and relate to the physical and chemical properties of the molecule. For example, the wavelength of light that the molecule absorbs is represented by an absorbance spectrum. In spectroscopy, the nature of the signal that you are measuring is important. The signal needs to be of sufficient intensity to be distinguishable from the noise, for example in visible spectroscopy, absorbance peaks need to be distinguishable from the background scatter and noise. A signal also has to be distinct for the component of the system that it originates from, e.g. chemical shift of different inorganic phosphate at different pHs or the spectral differences between haem of different chemical types. Spectroscopy techniques will often result in complex mixtures of signals that require processing to separate the constitutive signals.

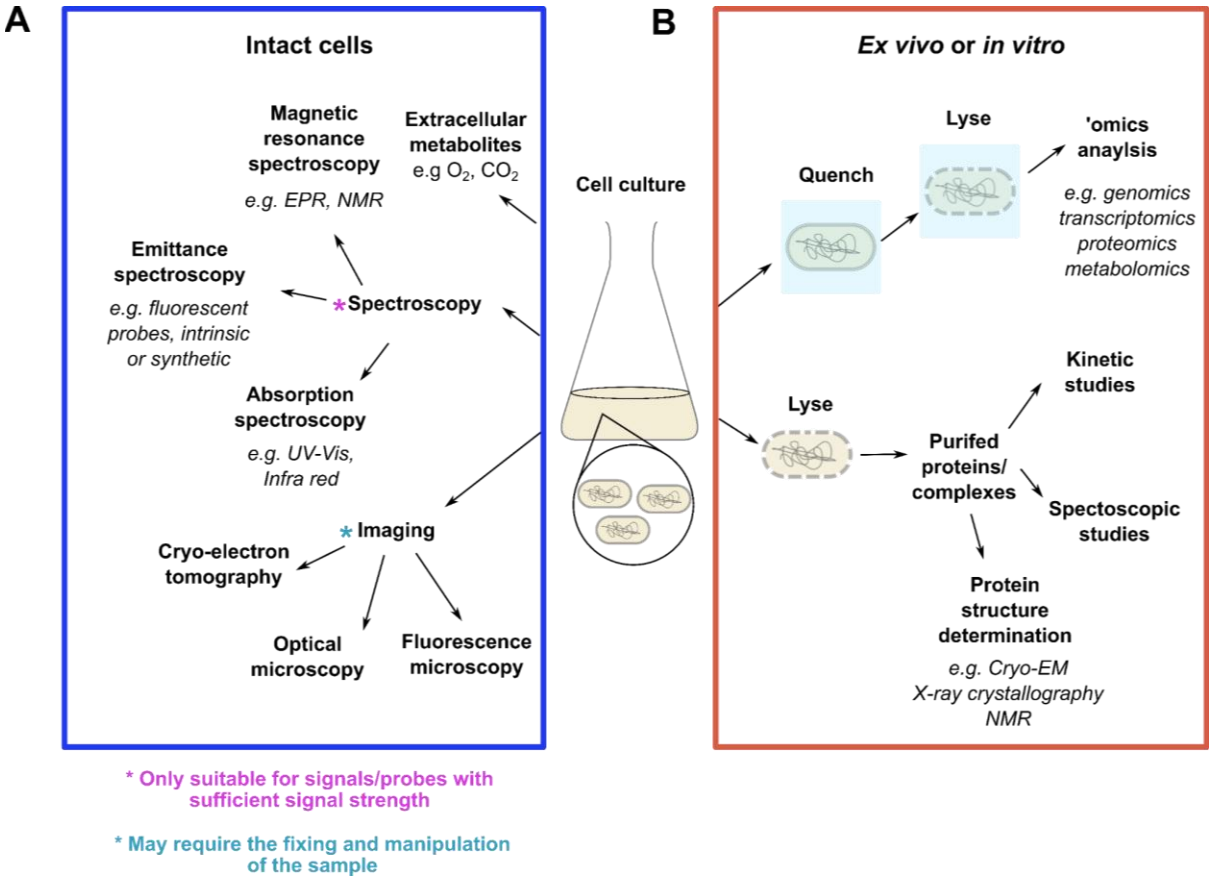

Figure 3.1 - A summary of the approaches that can be used to measure bioenergetic systems non-invasively and invasively *(**A**) Non-invasive approaches that do not require breaking open the cell or are minimally invasive. Broadly these approaches fall into spectroscopy and imaging. Changes in extracellular metabolites, excreted or quickly uptaken by the cell can be measured. (**B**) Invasive approaches, either characterising the population of a particular biological molecule or a reductionism approach, breaking down the system into its parts and individually characterising the parts.*

Applying spectroscopic techniques to intact cells is often accompanied by technical complexities. Some of this complexity is associated with keeping the cells in a live and 'happy' state so that making the measurement leaves the state of the cells unperturbed. Often this relates to combining this with the technical equipment for the spectroscopy with oxygenating the cells. The signal within the biological sample can often be at very low abundance compared to standard chemical measurement. This often means specialised equipment is required to detect the signal in the biological sample. The signal can be increased by making bulk measurements (cell culture). However, this does preclude its application on the single-cell level. Spectroscopic techniques are also applied with great utility to studying isolated components of the system (isolated protein complexes) or experimental levels in between

isolated complexes and intact cells, such as membrane vesicles. Understanding from these experimental levels is often required to make the most of the information in whole intact cells.

In relation to oxidative phosphorylation (OxPhos), haem spectroscopy and oximetry have been the dominant techniques to make non-invasive measurements. Haem spectroscopy is the use of visible-wavelength spectroscopy and specific data processing steps to measure the change in the redox state of haem groups that are integral to many OxPhos complexes. Oximetry covers the physical methods of measuring the change in oxygen concentration that occurs as aerobic cells respire. To a lesser degree fluorescence spectroscopy of NAD(P)H and ^{31}P NMR spectroscopy have also been used to non-invasively measure bioenergetic systems. Figure 3.2 A shows the aspects of the OxPhos system that these techniques can individually measure, in the context of mycobacteria.

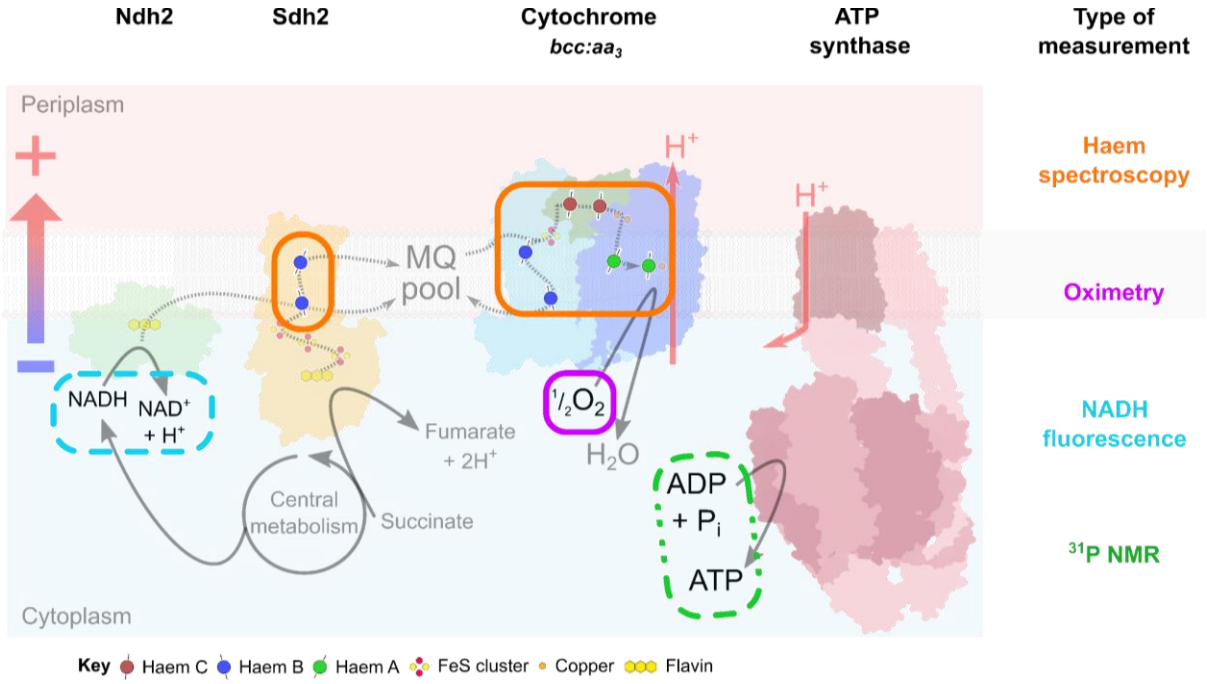

Figure 3.2 - Non-invasive approaches and which components of the mycobacterial oxidative phosphorylation system that the approach can be used to measure.

This chapter will specifically focus on haem spectroscopy and oximetry. I will cover the history of these measurements with particular reference to the suitability of these measurements to bacteria. I will also discuss the development of a system that combines both these measurements: the bioenergetics chamber. We have subsequently used this system to non-invasively study mycobacterial bioenergetics, the subject of this chapter. Using non-invasive techniques to study mycobacterial OxPhos may help to understand how the mycobacterium species adapt to their environment including those encountered in the context of human disease. Mycobacterial OxPhos has also been a recent success story in the anti-TB target

space. Bedaquiline, which targets ATP synthase, is now part of the BPaL drug regime that is the preferred option for treating multidrug-resistant tuberculosis (MDR-TB) (WHO, 2022). Improving our understanding of the action of OxPhos targeting compounds in a cellular context may offer direction for derivatives and synergistic drug combinations. More generally bacterial bioenergetics are less well understood than mammalian systems. This work should begin to bridge those gaps in understanding.

3.1.2 The history of oxygen consumption measurements

The oxygen consumption rate (OCR) is a key parameter that can be used to describe oxidative phosphorylation systems as under most circumstances, the oxygen consumption rate is tightly coupled to the rate of oxidative phosphorylation. Oxygen quantification allows the measurement of the overall function of the oxidative phosphorylation system, inferring the flux of electron transport down the chain and the rate of ATP synthesis. The physical and chemical properties of oxygen combined with its clear importance in respiration have meant that oxygen consumption measurements have been central to bioenergetics since the earliest days of the field. The respiratory control ratio (RCR) is a key parameter describing the ratio of the oxygen consumption rate when the ETC is coupled to the Δp or uncoupled. It can indicate the influence of backpressure on the flux through the ETC, estimating how coupled the Δp, and so ATP synthesis is to the operation of the ETC.

3.1.2.1 Manometers

Otto Warburg was one of the first to measure the rate of oxygen consumption associated with oxidative phosphorylation, and more generally the gases associated with metabolism. He utilised manometers, an instrument for measuring the pressure of a liquid or gas, that had previously been used to measure blood gases by Haldane & Barcorf (Barcroft and Haldane, 1902). Haldane & Barcorf's original manometer was configured to measure the volume of gas evolved from blood upon the addition of potassium ferricyanide, measuring the change in volume of gas as the pressure was kept constant. Brodie offered improvements to this setup (Brodie, 1910), by using a smaller sample flask more rigidly attached to the manometer allowing shaking of the whole equipment whilst keeping the volume constant. The flask could also then be submerged in a water bath keeping the temperature constant. The volume remaining constant meant that the pressure could instead be measured, hence the requirement of the water bath to keep the temperature constant.

Warburg further refined this apparatus to measure gases associated with metabolism, oxygen and carbon dioxide (CO_2). To distinguish between these two gases the CO_2 was

'trapped' in a central well full of water due to CO_2's solubility. This was later substituted by an alkali solution, neutralising acidic CO_2. Trapping the CO_2 meant that the change in pressure inside the closed system was only due to the consumption of oxygen, allowing the rate to be measured. Figure 3.3 shows an example of what is often known as a Warburg apparatus. Measurements of oxygen consumption rate allowed Warburg to measure the dramatic increase in the oxygen consumption rate of sea-urchin eggs post-fertilisation and to conclude that it was iron-containing respiratory ferment (atmungsferment) that was responsible for oxygen consumption (Warburg, 1925). It was for this work that he won the Nobel Prize in 1931 (Warburg, 1931). This respiratory ferment was later identified as cytochrome oxidase.

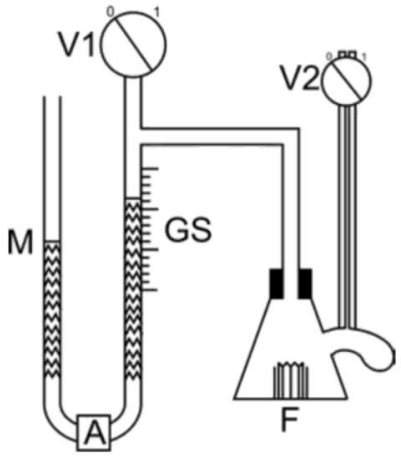

Figure 3.3 - 'Warburg' manometer. *The biological sample is placed in Flask F, with potassium hydroxide in a central well to absorb the evolved CO_2. Chemical additions to the experiment can be housed in the sidearm of the flask and added to the sample by tipping. The flask is connected to a manometer (M) that will sense the change in pressure caused by the consumption of oxygen by the sample. The graduated scale (GS) can be used to quantify the changes in pressure, as the meniscus of the manometer fluid moves. During the experiments, both valves remain closed, creating a fixed volume. The flask is submerged in a water bath to maintain a constant temperature. Taken from Lighton, 2018.*

3.1.2.2 Oxygen Electrodes

The next advance in oxygen consumption measurement came with the introduction of oxygen electrodes. In the late 19th century physical chemists determined that an electrochemical cell could be used to determine the oxygen concentration in a solution. In an electrochemical cell composed of two platinum electrodes, if sufficient voltage is applied, the current generated as the result of the reduction of oxygen to water is directly proportional to the oxygen concentration in the solution. In the early 20th century similar electrodes were used to measure oxygen concentration in several biological systems (Davies and Brink, 1942;

Petering and Daniels, 1938). However, these electrodes posed several issues for biological samples. The detection consumed the oxygen at a rapid rate, therefore fresh sample had to continually flow over the electrode. The bare electrode also could poison the biological sample or proteins/cells in the biological sample could block the electrode surface.

These issues were addressed by the designs of Clark (Clark et al., 1953). In this design, a semipermeable cellophane membrane was placed over the electrode that allows oxygen to diffuse across but at a slow rate. The electrode then measures the oxygen that has diffused across the membrane which will be proportional to the oxygen concentration of the sample. The diffusion of oxygen across the membrane measured by the electrode reduced the rate of oxygen consumption by the electrode and so reduced the sample requirement and errors introduced by the electrode to the oxygen consumption measurement. The cellophane membrane has subsequently been replaced by Teflon membranes.

The very wide application of Clark electrodes to live cells and mitochondrial preparations helped greatly to advance the understanding of bioenergetic systems. Chance and colleagues used oxygen electrodes to describe the different states of mitochondrial respiration and estimate the ADP/O ratio, adding known quantities of ADP and determining how much oxygen was consumed when different reducing equivalents were supplied (Chance and Williams, 1955). Clark electrodes are considerably more convenient than manometers and are still used today for measuring oxygen consumption rates. The main limitations of oxygen electrodes are:

- Oxygen is consumed as part of the measurement process, limiting the length of experiments that can be conducted. The oxygen concentration will also not be constant throughout the experiment.
- Measurements from the electrode tend to be noisy, meaning large sample volumes are required.
- Accurate measurements reflecting the oxygen concentration in the bulk solution are dependent on constant stirring so that the bulk solution > Teflon membrane > electrode solution > electrode equilibria are maintained.

3.1.2.3 Phosphorescent oxygen sensors

A number of optical sensors have been developed for measuring oxygen, pioneered by David Wilson and colleagues (Rumsey et al., 1988). These are typically phosphorescent sensors and work based on oxygen's ability to quench the phosphorescence of the sensor. The intensity of the phosphorescence peak will be inversely proportional to the concentration of oxygen; however, this will also be affected by the intensity of the excitation,

which is not always stable depending on the excitation source. A more stable measurement is the phosphorescence lifetime which is not affected by the intensity of the excitation source or photobleaching of the phosphorescence. The lifetime will be inversely proportional to the oxygen concentration, shorter when the oxygen concentration is higher, and longer when the oxygen concentration is lower. This relationship can be described by the Stern-Volmer equation (Eq 3.1).

$$I_0/I = \tau_0/\tau = 1 + k_q.\tau.[O_2] \qquad \text{Equation 3.1}$$

I_0 and τ_0 are the unquenched intensity and lifetime of the phosphorescent signal at zero oxygen. I and τ are the quenched intensity and lifetime at a specified oxygen concentration, $[O_2]$. k_q is the bimolecular quenching constant. In an ideal system, the relationship between oxygen concentration and the lifetime of the phosphorescence is linear. However, particularly close to the limit of detection, oxygen-sensing compounds can have a nonlinear relationship.

The wavelength required for excitation and the wavelength the phosphorescence is measured at is specific to the sensor molecule used. Platinum or palladium porphyrin complexes are typically used. The properties of the molecules are often balanced in choosing the best compound for the exact purpose. For example, octaethylporphyrin (OEP) complexes have a strong conversion of the excitation intensity to the emission intensity. This conversion ratio is often represented by ϕ. However, OEP complexes only have moderate photostability (Lee and Okura, 1997a). Tetrakis(pentafluorophenyl)porphyrin (TFPP) complexes in comparison are much more photostable (Lee and Okura, 1997b) but have lower ϕ, see Table 3.1. Their photostability is why TFPP complexes are more widespread for biological oxygen sensor systems, despite their reduced emission conversion. The range of oxygen concentration where the sensor can accurately measure the concentration will differ from sensor to sensor, which is also important to consider when choosing a probe for an application.

These phosphorescent oxygen sensors have been used across a range of biological samples (mL to µL), even the recent incorporation of an oxygen sensor into a microfluidics chip, for ‘micro-respirometry’ (Levitsky et al., 2019). The main advantage of phosphorescence oxygen sensors is the fact that they do not consume oxygen as part of their measurement processes. In practice interactions between the probe and oxygen can result in oxygen consumption, albeit at a much lower rate than oxygen electrodes and so is only an issue when trying to measure trace amounts of oxygen (Borisov, 2018).

***Table 3.1 - Oxygen sensing complexes/compounds**, compounds collated in Borisov, 2018 OEP - octaethylporphyrin, TFPP - tetrakis(pentafluorophenyl)porphyrin. [a] - In polystyrene at 25 [o]C, [b] - Max lifetime in a range of solvents, [c] - Values may be an underestimate*

Complex	Absorbance maxima (nm)	Emission maxima (nm)	τ_0 (µs)	ϕ (%)	Reference	Coordinating complex
Pd(II) OEP	395 547	669	1217[a]	19	(Koren et al., 2011)	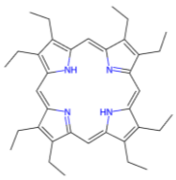
Pt(II) OEP	382 536	649	75	41	(Koren et al., 2011)	
Pd(II) TFPP	407 553	670	~900	3[c]	(To et al., 2013)	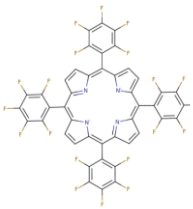
Pt(II) TFPP	394 540	648	60[b]	9[c]	(Lai et al., 2004)	

3.1.2.4 Modern commercial respirometry systems

There are several modern commercial systems for measuring oxygen consumption. The Seahorse and Oroboros systems encompass the different throughput scales and measurement approaches offered by commercial systems.

The Seahorse system uses a plate reader-style measurement system with a phosphorescent oxygen sensor to sample adherent cells in the bottom of a well (Wu et al., 2007). At time points during the experiment, the probe is lowered over the well to form a seal over a ~2 µL volume in the well. The oxygen consumption rate is measured by a phosphorescent oxygen sensor at the end of the probe and metabolic effectors can be added via a port in the probe. Extracellular acidification can also be measured with an additional pH-sensitive optical probe (Serrill et al., 2015), reflecting the export of acidic products of metabolism (lactic acid from glycolysis and carbonic acid from the TCA cycle). This system is a higher throughput measurement than a classical respirometry system due to its plate reader design. The approach's drawback is that the small volumes of the well can cause errors in the oxygen consumption rate measurements at low O_2 concentrations. The error in the measured oxygen consumption rate can be easily misinterpreted but with careful experimental design, this can be somewhat mitigated. The system is less suitable for bacteria as they do not adhere as well to surfaces as mammalian cells naturally do, meaning that they become dislodged during

the measurement process and so interfere with the consistency of the oxygen consumption rate measurement.

The Oroboros is much closer to a classical respirometry system. The consumption of oxygen is measured via oxygen electrodes in a closed system (Gnaiger et al., 2000). Metabolic effectors can be added via a port at the top of the chamber. There are two sample chambers so controls can be run simultaneously. Add-ons to the system allow the measurement of other parameters either via additional electrodes or fluorescent probes. Like classical respirometry systems, the Oroboros system has much higher sample volume requirements than required for individual wells in the Seahorse XF Analyzer. The setup also means that the throughput is much lower than the Seahorse. The closed nature of both systems, with no oxygen perfusion systems, limits the length of time that biological samples can be kept under physiological oxygen conditions. Neither system allows the maintenance of constant oxygen concentration which can alter the generation of reactive oxygen species, interfering with the oxygen consumption rate measurement. The higher oxygen consumption rates that are observed with bacteria particularly limit its application for studying their metabolism.

For mammalian cells and mitochondria, there are established protocols using metabolic effectors to probe the bioenergetic status of the cells. These metabolic effectors do not always have identical effects in bacterial systems. For example, oligomycin is a strong mitochondrial ATP synthase inhibitor but is known not to be as effective in bacterial systems as in mitochondrial systems (Perlin et al., 1985). It is generally more difficult to penetrate bacteria with metabolic effectors. There are several reasons for this. Firstly, the barrier to getting into a mammalian cell is much less complex than in a bacterial cell envelope. The multiple far less permeable layers of the bacterial cell envelope can pose an issue to transport. Secondly, bacteria tend to have more efflux pumps and like a grumpy toddler they will ‘throw’ many molecules away. Unfortunately, the specificity of these efflux pumps can often match the physical properties of compounds that target the membrane protein components of OxPhos.

Many of these differences between bacterial and mitochondrial/mammalian cells are due to the hostile environment that bacteria have to survive in. Metabolic effectors also generally have more well-characterised inhibition properties (affinity and specificity) for mitochondrial complexes compared to their bacterial homologues. Ideally one would wish to use nanomolar inhibitors to avoid off-target effects, but some bacterial systems require much higher concentrations to see any effect, likely due to the reasons described above. Therefore, the use of classical metabolic effectors requires considered thought when applied to bacterial oximetry experimental protocols.

3.1.3 History of haem spectroscopic measurements: Keilin, Chance, & Springett

3.1.3.1 The nature of cytochrome spectral properties

Cytochromes have distinctive and strongly absorbing spectral handles that make them ideal for non-invasive measurements. These spectral handles are due to their haem cofactors and change as the cytochrome performs the redox reactions. The haem cofactor is composed of a porphyrin ring coordinating an iron atom. The iron is found in either the (II) or (III) oxidation state. These two oxidation states allow for the transfer of electrons between haems and other redox cofactors.

Haems absorb specifically in two regions of the visible spectrum, in the Soret (B-band) region, 400-450 nm, and in the α/β (Q-band) region. The spectrum changes as the iron changes oxidation state, with the absorbance in the Soret region red shifting and the absorbance in the α/β region increasing. The spectrum in the ferric form (III) is referred to as the oxidised state and the ferrous (II) as the reduced state. Figure 3.4 E shows the spectra of oxidised and reduced isolated horse cyt *c*, showing the change in the spectrum of a single type of haem in the α/β region. Figure 3.4. F shows the oxidised and reduced spectrum of the mycobacterial cyt *bcc:aa*$_3$ supercomplex, showing the change in the spectrum of a mixture of haems in both the Soret region and the α/β region.

The location of the absorbance peaks is specific to the chemical nature of the haem centre and the protein environment of the haem centre. These differences in their spectra are more separable in the $\alpha\beta$ region however the intensity of the absorbance is stronger in the Soret region (Figure 3.4 G). The chemical nature of the different haem groups found in mycobacteria is shown in Figure 3.4 A-D. Haem B is a porphyrin ring with two distinctive propionate groups from two adjacent pyrrole rings and additional methyl and vinyl group substitutions on the ring. All the other haems are seen as modified versions of haem B, for example, haem C is covalently attached to the protein via cysteine residue. Haem A has an additional hydroxyethyl farnesyl group and a formyl group as compared to haem B. Haem C and Haem A require specialised pathways for their synthesis and incorporation into the cytochrome. In Haem D one of the pyrrole rings has been hydroxylated. This allows one of the propionate groups to form a spironolactone group with the pyrrole ring. This means that it is a partially hydrogenated porphyrin known as a chlorin which explains its different spectral properties to the other haem groups. Table 3.2 summarises the typical peak maxima in the difference spectrum for each different chemical type of haems.

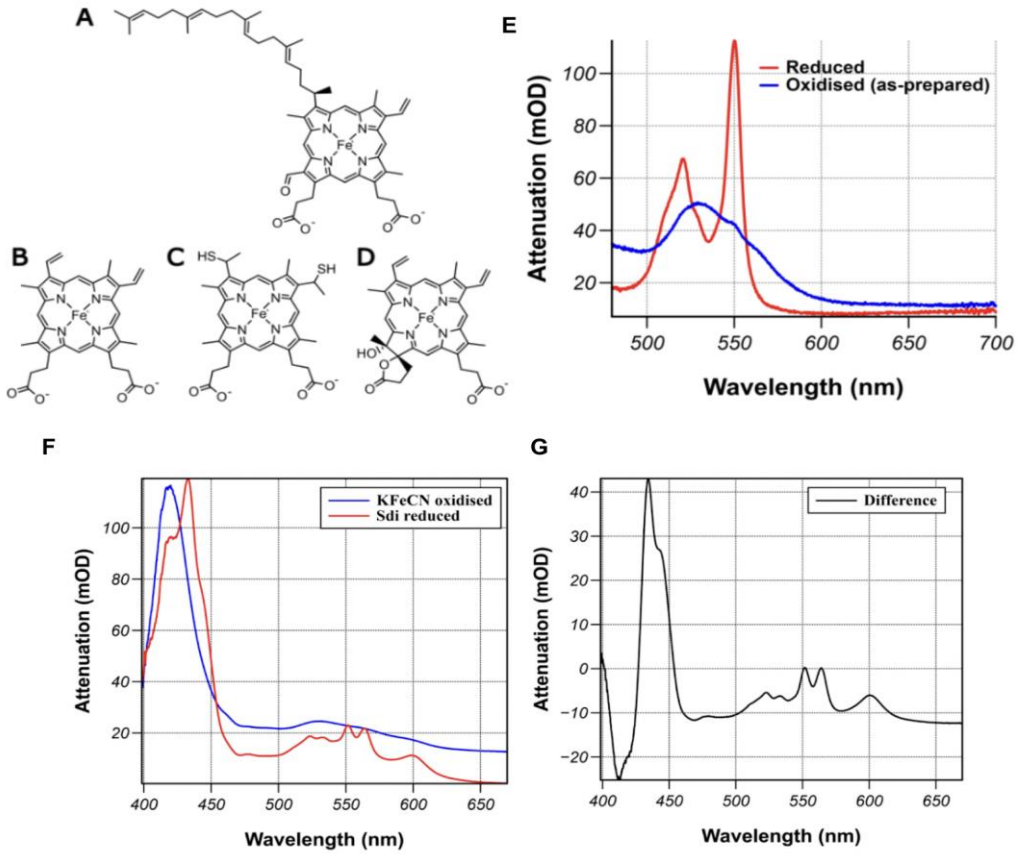

Figure 3.4 - The chemical structure of haems and their characteristic spectra *(**A-D**) The chemical structure of the haem present in mycobacteria. (**A**) Haem A, (**B**) Haem B, (**C**) Haem C, (**D**) Haem D. (**E**) The oxidised and reduced spectrum of bovine cyt c (Sigma) in the $\alpha\beta$* region*. The oxidised spectrum is 'as-prepared' and so is not fully oxidised as indicated by the small peak at 550 nm. (**F** & **G**) The total spectrum of the cyt bcc:aa$_3$ supercomplex, prepared as in Chapter 4, Fig 4.8 (**F**) oxidised and reduced spectrum (**G**) difference spectrum (reduced minus oxidised). **E**-**G** were measured using the bespoke cuvette described in Chapter 2, Section 2.6.*

Table 3.2 - Different chemical types of haem and their typical absorbance peaks. **The maxima of the spectrum when oxygen is bound to the reduced haem D, causing a trough in the difference spectrum.*

Chemical haem type	Soret peak maxima (nm)	α peak maxima (nm)
Haem C	415	550
Haem B	432	560
Haem A	445	600
Haem D	430	630 (650*)

3.1.3.2 The initial identification of cytochromes using visible light spectrometry

MacMann was the first to observe cytochrome with its distinctive absorbance pattern in muscle and other tissues of animals (MacMunn, 1886). At the time his observations were not widely accepted. This is in part due to confusion with haemoglobin which has an absorbance band in a similar region to cytochromes. MacMann originally termed these pigments myo- and histohaematin. Keilin re-discovered these pigments (Keilin, 1925), finding them in a broader range of species including unicellular organisms such as yeast. He renamed them cytochromes, 'cellular pigment'. Keilin was able to observe the absorbance bands appearing and disappearing depending on the aeration of yeast or the excitation of muscle tissue, helping to illustrate the pigment's links to cellular respiration. Keilin was also able to determine that the four 'bands' were three distinct pigments.

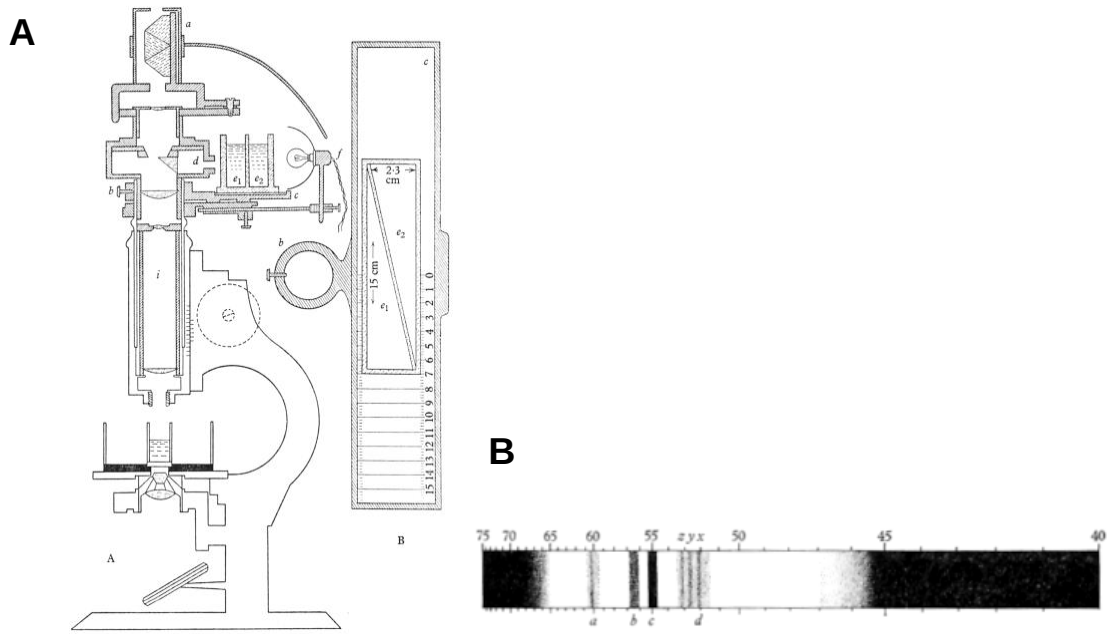

Figure 3.5 - Early spectral measurements of cytochromes *(**A**) Hartridge low dispersion spectroscope, used by Keilin in early measurement of cytochromes. (**B**) The absorbance bands of cytochromes as observed in the thoracic tissue of a bee. Scale in m x 10 $^{-8}$. Taken from Keilin, 1966.*

This early work was performed using a low dispersion spectroscope designed by Hartridge (Figure 3.5 A) fortuitously ensuring the haem absorbance band was sharp, and not diffuse in the background scatter. Keilin was also able to demonstrate that these cytochromes were not derivatives of haemoglobin by mixing yeast with sheep's blood. The yeast consumption of oxygen would result in the reduced form of the cytochrome signals and the deoxygenated form of the haemoglobin. By shaking the mixture with air the haemoglobin signal shifted,

whereas the cytochrome signal disappeared (Keilin, 1925), demonstrating their distinct natures. Figure 3.5 B shows an example of the cytochrome absorbance bands observed using the Hartridge spectroscope. Much of this work was performed on dissected insect muscle tissue, from Keilin's initial research interest in entomology, or using suspensions of yeast or bacteria. Subsequent investigation into the nature of these pigments determined that there were 3 distinct pigments contributing to these spectral bands, haem C, haem B and haem A.

Keilin and collaborators subsequently determined the effect of different compounds on the haem signals, such as KCN, demonstrating that Warburg's respiratory ferment was a cytochrome (Keilin and Hartree, 1939). Owing to its stability cyt *c* could be readily extracted and purified, with its first spectral characterisation in 1931 (Dixon et al., 1931). Keilin and Hartree determined that measuring the spectrum at low temperatures, using liquid nitrogen, improved the intensity and resolution of the cytochrome absorbance peaks (Keilin and Hartree, 1949). Low-temperature spectroscopy can also result in peak splitting and further removes the biological sample from physiological conditions. Many subsequent measurements were made on submitochondrial particles or mitochondria for experimental ease, again away from *in vivo* measurements.

The main issue with trying to measure cytochrome *in vivo*, or even in isolated mitochondria and membrane vesicles, is the contribution of scatter by the highly scattering nature of the biological samples. In normal absorbance measurements, the signal from the cytochrome is often difficult to distinguish from the scatter contribution. Britton Chance's advances in spectrophotometers offered a solution to this issue (Chance, 1954). Spectrophotometers developed in this era utilised a chopper to split the beam of light. This can either be between two samples (split-beam) or between two monochromators (dual-wavelength), as shown in Figure 3.5.

In the split beam spectrophotometer, the reference and sample are differentially reduced and a spectrum is taken using a monochromator to scan between two wavelengths. The generated difference spectrum then shows the effects of the reduction, not including the contribution of the scatter as both samples should have equal scatter. This is not always true as the act of manipulating a sample can sometimes cause a change in the scatter, due to the swelling or lysis of cells. In the dual-wavelength spectrophotometer, the beam transmitted through the sample is split between two monochromators, measuring at two wavelengths to capture the maxima of the peak and an isosbestic point that should not change in absorbance as the haem redox state changes. The dual-wavelength approach was more useful for tracking changes over time.

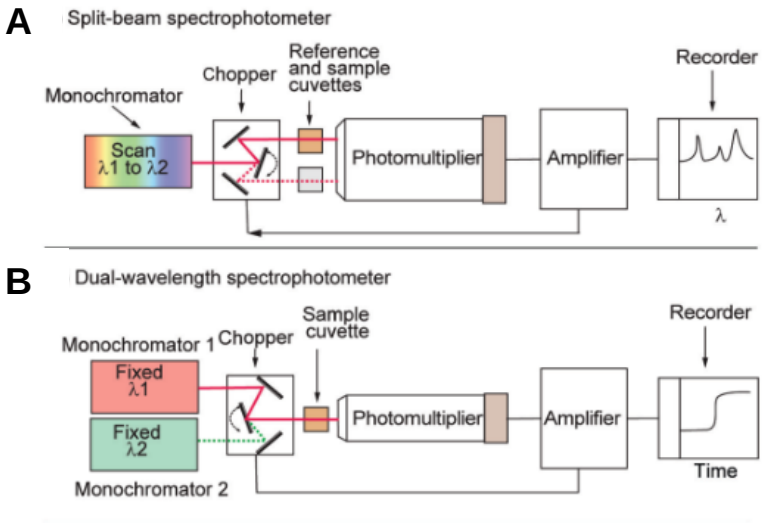

***Figure 3.6 - Chance's spectrophotometers**. (**A**) The split-beam spectrophotometer. A chopper is used to simultaneously scan a sample and reference generating a difference spectrum. (**B**) The dual-wavelength spectrophotometer. A chopper is used to simultaneously measure at two wavelengths. Taken from Nicholls and Ferguson, 2013.*

These initial spectrophotometers worked with analogue equipment to record the spectra or intensity at specified wavelengths. The spectrophotometers have subsequently been adapted to the digital age. The updates to the digital age negated some of the need for the split beam, as the reference spectrum can be stored in digital memory. Digital sensors can be used to directly measure the full spectrum at once without needing to scan through a wavelength range, avoiding the need to only measure at two wavelengths. One major advance in digital imaging was the introduction of charged-couple-device (CCD).

CCDs are arrays of coupled capacitors that are highly sensitive photon detectors. Each capacitor, which will cover a small segment of the image or spectrum (pixel), will convert photons of light that fall on that area to a build-up of charge proportional to the intensity of the light in that region. The charges from the specific capacitor will then be read out at the end of the measurement period and recorded. These CCDs work quickly allowing for measurements on a millisecond time scale. CCD require a cooling system to reduce the effect of 'background temperature' on the measurement but this cooling allows for measurements with a very high signal-to-noise ratio. Spectrographs where CCDs are used as the detectors, as is often the issue with the digital age, have increased the amount of data that can be collected in a short space of time. To make the most of the vast amount of data, innovations are needed for quick and computationally efficient methods to process the data.

3.1.3.3 Signal deconvolution via decomposition

A total haem spectrum will be a mixture of haem signals from the various haem centres present. Whilst dual-wavelength approaches can distinguish between haem centres of different chemical types, this approach is insufficient for distinguishing between haem centres of the same chemical type due to the overlap in their absorbance peaks. Instead, reference spectra can be used to deconvolute the total spectrum by decomposition, separating the mixture of spectral signals.

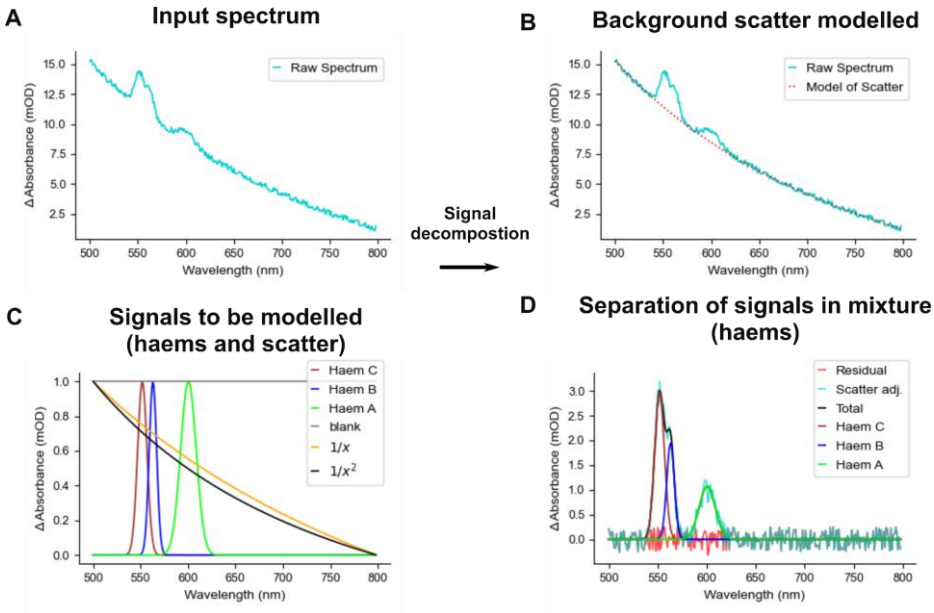

Figure 3.7 - An example of signal decomposition. *(**A**) An input spectrum will be a mixture of known signals, in this example haem signals and background scatter (**C**). Through signal decomposition, the contribution of each component can be determined, allowing their quantification (**B** – scatter and **D** – Haems).*

The approach is widespread beyond haem spectra for separating a mixture of known signals. The approach has been used in several bioenergetic publications demonstrating the power of the approach (Shinkarev et al., 2006a, 2006b). Ultimately this approach allowed the *in situ* measurement of cytochromes c_1 and c_2 kinetics in *Rhodobacter sphaeroides*, whose peaks only differ by 1.5 nm and had previously been indistinguishable (Shinkarev et al., 2006c). To do this, matrices were used to quickly and efficiently perform the simultaneous equations required. More details about this approach are provided in the results section.

3.1.3.4 Tackling the issues of highly scattering biological samples

In remission spectroscopy, rather than the light being transmitted through the sample, the light scattered off the sample is measured instead. This is sometimes referred to as diffuse

reflectance spectroscopy (Yodh and Chance, 1995). Because different wavelengths will be differentially diffracted upon scattering, the path length of the backscattered light will be different at different wavelengths but the right optics geometry can be used to manage this effect. If the sample illumination/light source and detection are in parallel the detected spectrum of light will be photons that have followed a banana-like path back to the detector, as shown in Figure 3.8 (Bender et al., 2022). Shorter wavelengths will be scattered more than longer wavelengths, taking a narrower/steeper route. In the right geometry (distance between the light source and the detector), this results in very similar path lengths across the measured wavelength range. In a visible wavelength spectroscopy remission set up the path length only varied by 3.3 ± 2.9 % across the measured wavelength range between (Hollis et al., 2003, 530-740 nm, a parallel source-detector separated by 3.2 cm).

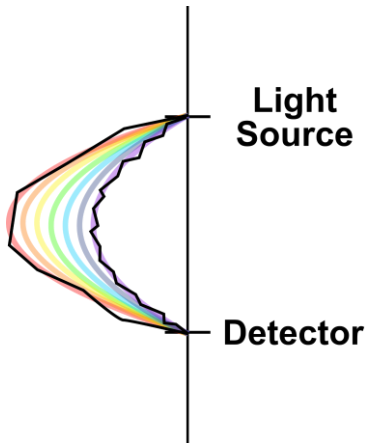

Figure 3.8 - Differential path length of remission spectroscopy. *In remission geometry shorter wavelengths (violet) are scattered more and so take a steeper path. Longer wavelengths (red) are scattered less and so take a shallower path. This means that given specific spectroscopic geometry, there is not a larger difference in the differential path length across the visible-wavelength region.*

Point light sources and detectors also help to reduce differences in the path length across a range of wavelengths. The 'average' path length can be approximated via two methods, time of flight to measure path length and using the absorption spectrum of water(Delpy et al., 1988; Matcher et al., 1994). These were calibrations developed for IR-Spectroscopy but applicable to visible wavelength spectroscopy. More generally this type of spectroscopy has been very powerful within medical biophotonics. Remission spectroscopy is used in blood oxygen sensors to spectrally measure the oxy and deoxy haemoglobin in blood vessels using sensors on the surface of the skin.

An integrating sphere is another method that has been used to improve the signal-to-noise ratio of haem spectroscopy measurements. Integrating spheres are highly reflective spheres,

which help to improve the intensity of the light that reaches the detector. The sample being examined is placed inside the sphere, the incident light will then be absorbed by the sample multiple times prior to it reaching the detector, increasing the signal intensity. An image and schematic of an integrating sphere is shown in Figure 3.9. However, because of this behaviour, it can be complex to determine the path length. Maintaining a biological sample in a physiologically relevant state inside an integrating sphere also poses a technical challenge but has been previously achieved including more recent examples (Chess et al., 2013).

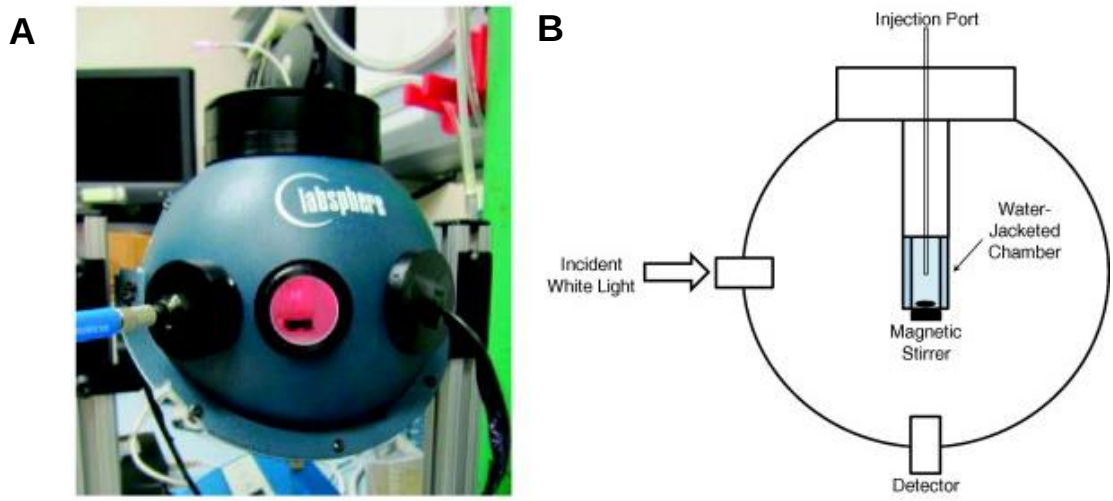

Figure 3.9 - Non-invasive spectroscopy using an integrating sphere *(**A**) Picture of the sphere, (**B**) Diagram of the sphere with an internal chamber to house cells or mitochondria. Taken from Chess et al., 2013.*

3.1.4 Other non-invasive methods for measuring bioenergetic systems

Several other methods have historically been used to examine other aspects of bioenergetics non-invasively.

3.1.4.1 ^{31}P NMR

There are several phosphorus-containing molecules important to bioenergetic systems. These include the bioenergetically important molecules of ATP, ADP & P_i. The [ATP]:[ADP] ratio or the phosphorylation potential is an indicator of the cell's energetic status, determining the potential energy for driving reactions requiring ATP hydrolysis. Phosphorus naturally has a non-zero nuclei spin making it measurable by nuclear magnetic resonance spectroscopy (NMR spectroscopy). NMR measures the transition between spin states when nuclei such as ^{31}P interact with an external magnetic field. Different local environments will cause the nuclei

to resonate at slightly different frequencies. This is termed the chemical shift and will be specific to nuclei in a particular chemical environment, allowing the identification of different molecules, i.e. distinguishing between ADP and ATP.

The chemical shift of the phosphate ion is also affected by the pH. This means that the ∆pH can be determined from the phosphate peaks observed in cells, internal and external (Nicolay et al., 1982). ^{31}P NMR is a non-invasive quantitative measurement, however, the signal from phosphorus is not strong and so requires a high density of cells for the measurement. The technical difficulties of keeping high densities of cells sufficiently oxygenated inside an NMR magnet poses an experimental challenge. This can be attested to by efforts to use ^{31}P NMR to measure *M. smeg* non-invasively by another PhD student within the group (Personal communication with Suzy Harrison).

3.1.4.2 NAD(P)H fluorescence

Nicotinamide adenine dinucleotide (NADH) is an important reducing equivalent within OxPhos. It is the main reducing equivalent that is produced by central metabolism that is then fed into the electron transport chain via NADH dehydrogenases, either directly or indirectly generating ∆p. NADH and NADPH, the additional phosphorylated NADH, both have fluorescent properties, absorbing at ~340 nm and emitting at ~460 nm. As only the reduced forms of both molecules are fluorescent, measuring this fluorescence peak will reflect the redox state of the NAD(P)H pool. The main issue with this is that the phosphorylated and unphosphorylated forms are indistinguishable. NADPH is involved in anabolic pathways compared to NADH's bioenergetic functions. However, this measurement can still be a useful indicator of the bioenergetic status of the cell. It is possible to measure the NAD(P)H oxidation state in mammalian cells (Ripple et al., 2013b). There have even been recent efforts to use NAD(P)H fluorescence as a way to image cellular redox state (Liu et al., 2018).

3.1.5 Integrating haem spectroscopy and oxygen consumption rate measurements: the Springett Device

The measurements of parameters like oxygen or cytochromes oxidation state on their own can provide powerful insights into the internal workings of bioenergetics systems. However, a single measurement can sometimes lack sufficient context to understand exactly what is happening in a system. A more comprehensive picture of the system can be built if these measurements are made simultaneously. (Hollis et al., 2003), developed a system that simultaneously measures oximetry measurements and multi-wavelength spectroscopy to measure the electron occupancy of the haem centres, Figure 3.10 A. This was combined with

a Nitric oxide (NO) sensor and allowed them to study the effects of NO on cytochrome redox state. The haems are measured via remission spectroscopy, measuring the reflected light backscattered from the suspension of cells. The change in attenuation (scatter and absorption) are then deconvoluted via decomposition to determine the contribution from each haem centre, based on reference difference spectra of the haem centres. These changes reflect changes in the electron occupancy of the haems centres.

The system was then further refined by Roger Springett to the bioenergetic chamber (Ripple et al., 2010, Figure 3.10 B). The main development was the addition of an oxygen perfusion system to keep the cells at a set oxygenation level. The oxygen is delivered by oxygen-permeable tubing submerged in the cell suspension. The perfusion system is controlled by a feedback loop that uses the measured concentration of oxygen in the chamber and the tubing, allowing the rate of oxygen delivery to be calculated and adjusted to maintain the desired oxygen concentration. To do this the oxygen electrode was switched to an optode, an optical oxygen sensor using the phosphorescence lifetime of a platinum porphyrin compound (platinum tetrakis(pentafluorophenyl)porphyrin, Pt-TFPP). The optode offered better temporal resolution of the measurements, improving the success of the feedback loop.

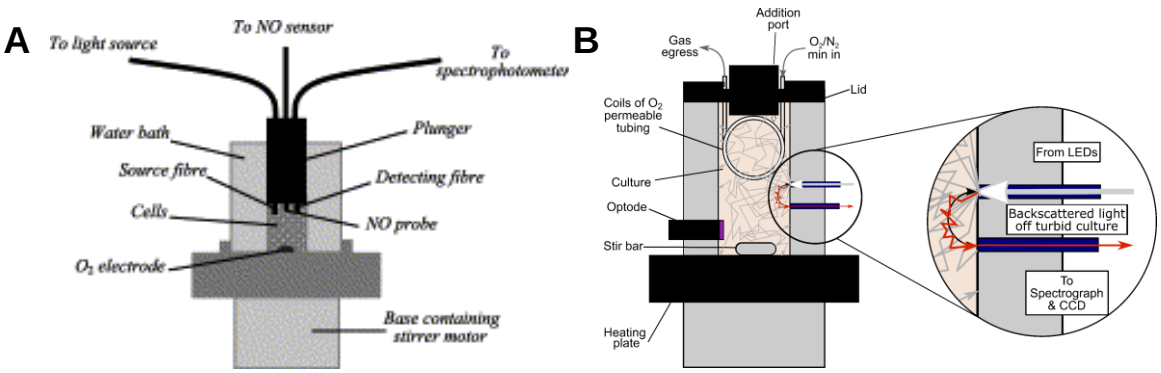

Figure 3.10 - Comparison of the original system and the current bioenergetic chamber *(**A**) The system used in Hollis et al. 2003, the oxygen is measured via an oxygen electrode in the base of the 1 mL chamber. The spectroscopy is in the lid of the chamber with a source-detector distance of 2.3 cm. A water bath around the chamber is used to maintain the temperature of the culture (**B**) The current 5 mL bioenergetics chamber. The oxygen electrode has been replaced with an optode in the side of the chamber rather than the base of the chamber. The oxygenation of the chamber can be controlled via an oxygen perfusion system using oxygen-permeable tubing submerged in the culture. The spectroscopy has been moved to the side of the chamber as well, with the source-detector distance shortened to 1 cm. A heating element in the base of the chamber is used to maintain the temperature of an aluminium block surrounding the chamber.*

The spectroscopy of the system was moved from the top of the chamber to the side. This spectroscopy system was later used to also measure the NAD(P)H oxidation state from its fluorescence (Ripple et al., 2013c). For the NAD(P)H fluorescent measurements a second CCD is required, with a narrower grating to diffract a wider spectrum onto the CCD. Figure 3.11 shows the mirror within the spectrograph that focuses the light onto the grating and then onto the CCD.

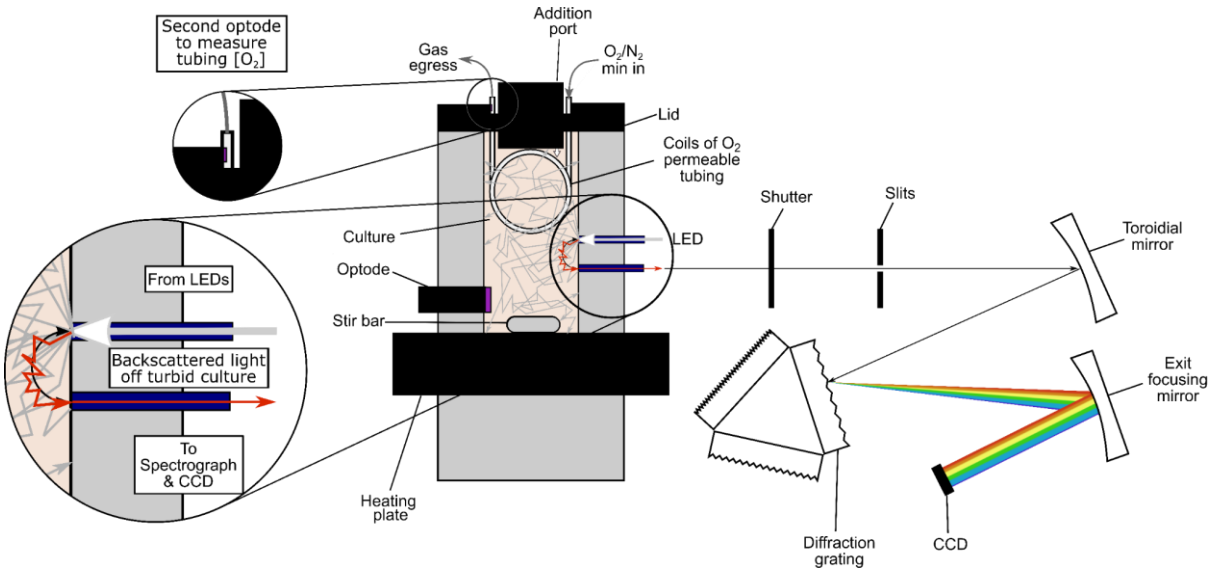

Figure 3.11 - A schematic of the bioenergetic chamber with aspects highlighted *The second optode in the exit port of the tubing, allows for the measurement of the oxygen delivery to the chamber. The shutter controls the exposure cycle of the CCDs and the slit width controls how diffuse the light is entering the spectrophotometer, improving the spectral resolution of the peaks. 3 gratings of different sizes allows for different sized wavelength ranges to be focused on the CCD allowing for a wider or narrower spectrum to be measured depending on what is required.*

The remission spectroscopy configuration means that there is no fixed path length. This means that the absolute concentration cannot be obtained from a single spectrum. However, if the haem are transformed completely from their oxidised to their reduced form, their redox state throughout the experiment can be obtained. The reduced state is achieved with anoxia and the oxidised state is achieved using specific inhibitors of the dehydrogenases of the ETC, preventing electrons from entering the ETC. The redox states of the haems can be used to derive bioenergetics parameters such as the $\Delta\Psi$ from the distribution of electrons in the chain (Kim et al., 2012 and Chapter 4 of this thesis).

The benefit of simultaneously measuring these parameters is the depth of information that can be collected. For a given oxygen consumption you know the ratio of different haem centres present in the cell and the distribution of electrons within these haems. As far as I am

aware, prior to this work none of these types of haem electron occupancy measurements have been made on intact mycobacteria.

3.1.6 ‘Haem spectroscopy’ in mycobacteria

Interest in mycobacterial OxPhos has grown in recent years, stemming from the discovery of a novel anti-TB agent that targets ATP synthase (Koul et al., 2007), suggesting mycobacterial OxPhos could be a novel and fruitful target space for new anti-TB agents (McNeil et al., 2022a). Arnold Brodie and colleagues did much of the initial characterization of the OxPhos in mycobacteria. This work was performed with the fast-growing mycobacteria, *Mycobacterium phlei*, including haem spectroscopy experiments on membrane vesicles from *M. phlei* (Asano and Brodie, 1964, Fig 3.12 A). From these early haem spectra, it was apparent that there were cytochromes containing haem C, B, and A present in mycobacteria. Brodie and colleagues observed differences in the haem B signal responses to succinate and NADH in membranes (Cohen et al., 1973, Fig 3.12 B). NADH showed a much greater reduction of the haem B than succinate did. The maxima of the haem B signal generated by the reduction of two different reductants also varied, suggesting multiple different haem B centres were present. They were also able to determine that the mycobacterial OxPhos used menaquinone-9 as its membrane-soluble electron carrier (Brodie et al., 1958; Gale et al., 1963).

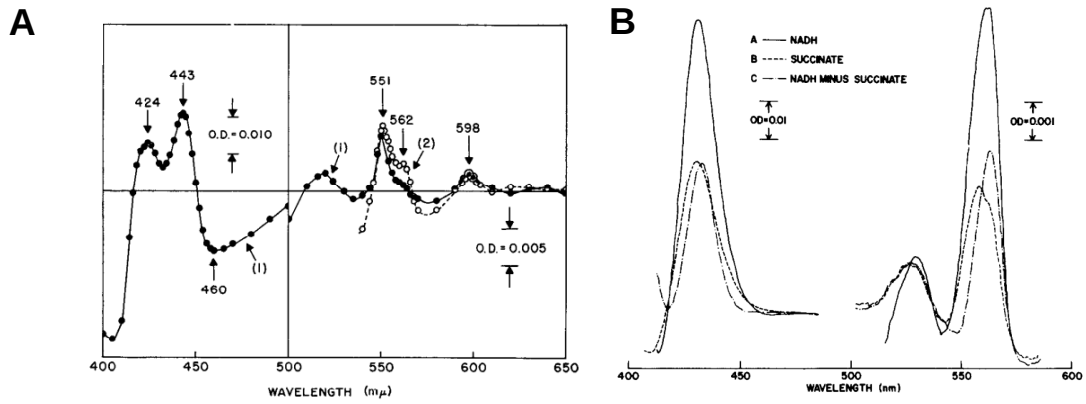

Figure 3.12 - Early haem spectra of the M. phlei. *(**A**) The reduction with succinate (dark circles) the reduction with dithionite and 2-n-nonylhydroxyquinoline N-oxide (open circles, a quinoline with the same head group has HQNO but a longer tail), from Asano and Brodie, 1964. (**B**) A comparison of the haem B species reduced upon NADH or succinate, taken from Cohen et al., 1973.*

The presence of a cyt *bd* quinol oxidase was not apparent until the sequencing of *Mycobacterium tuberculosis* (Cole et al., 1998), the presence of a cyt operon with homology

to the *E. coli* operon suggested the presence of a cyt *bd*. This was confirmed by cloning and membrane spectral characterisation in *M. smeg* (Kana et al., 2001). Increased expression was seen under low oxygen tension, matching the prevailing view that the cyt *bd* was used in these low oxygen tension as occurs in *E. coli.*

The development of strains that allow easier genetic manipulation in *M. smeg* by William Jacobs and colleagues (Snapper et al., 1990), and the broader development of genetic techniques for *M. tb* has moved the mycobacterial field away from *M. phlei*. Both *M. smeg* and *M. phlei* are faster-growing strains of mycobacteria with doubling times of ~2-3 hrs compared to the 24 hrs doubling time of *M. tb*, hence why these species have been used as laboratory model organisms for *M. tb.* Sequencing of the mycobacterial genomes has demonstrated that there is a high conservation of the OxPhos complexes across mycobacteria. Genome sequencing has also allowed the probing of the other likely components of the mycobacterial OxPhos systems. Many complexes of the OxPhos system have high conservation across mycobacteria, and similarity to OxPhos components in the wider actinobacteria genus, such as *Corynebacterium glutamicum (Kao et al., 2022)*. The exact number of complexes with shared enzymatic functions varies between species for example, at the succinate/fumarate junction. In *M. smeg* there are two succinate dehydrogenases, Sdh1 and Sdh2 (Pecsi et al., 2014) whereas *M. tb* has an additional fumarate reductase. Sdh2 is near essential in *M. smeg* (Pecsi et al., 2014), whereas Sdh1 is required for long-term survival in *M. tb* (Hartman et al., 2014).

With the advances in electron cryo-microscopy making determining the structures of membrane complexes more tractable and the interest in OxPhos as an anti-TB agent target space, the structures of the most well-described cytochromes in mycobacteria have been determined, predominantly from *M. smeg* (Gong et al., 2020, 2018; Guo et al., 2021; Montgomery et al., 2021; Wang et al., 2021; Wiseman et al., 2018; Zhou et al., 2021). Some respiratory complexes have also been determined for the *M. tb* enzymes (Mathiyazakan et al., 2023; Safarian et al., 2021; Zhang et al., 2024), showing very conserved structures. What has often been lacking within the field of mycobacterial OxPhos in recent years is the connection between the structure of these enzymes and their function within the chain. Spectroscopic properties of the complexes, beyond the total difference spectra of the purified cytochrome complexes, have also been neglected. The function of a complex can be inferred from its structure but this now needs to be brought back into a complex function within the OxPhos system as a whole and most importantly, how it functions within a cellular context. There have been oxygen consumption measurements using the Seahorse (Lamprecht et al., 2016) and Oroboros (Kalia et al., 2023) made in intact mycobacteria but to my knowledge.

3.2 Aim and objectives for this chapter

Aim:

To adapt existing methods to mycobacterial bioenergetics, with a particular focus on non-invasive methods to understand the composition of their respiratory chain under different growth conditions and the response of the oxidative phosphorylation system to perturbation by metabolic effectors.

Objectives of this chapter

1. Determine growth and experimental conditions for *M. smegmatis* that are compatible with the bioenergetic chamber, adapting existing techniques used for mammalian systems.
2. Applying accessible spectral models (combinations of Gaussian peaks and adapted mammalian spectral models) for the decomposition of mycobacterial spectra and assessing their utility.
3. Determining the response of *M. smegmatis* to classical metabolic effectors, working towards being able to fully transform its haem signals in order to facilitate quantitative thermodynamic analysis.
4. Assess the benefits and limitations of the bioenergetic chambers as a tool for understanding mycobacterial bioenergetics.
5. Use the bioenergetic chamber and other techniques to study mycobacterial membrane vesicles to understand the contributions of the various mycobacterial cytochromes to the overall spectrum.

3.3 Results

3.3.1 Characterising the cytochrome content of *M. smegmatis* under different growth conditions.

Current understanding of how mycobacterial species utilise their flexible respiratory chains is predominantly built upon evidence from genetic techniques and more limited extent *in vitro* biochemical characterisation. There have been several studies looking at the transcriptional response to different growth conditions and the effect of knocking out key respiratory complexes. Whilst some of this work has been performed in slower-growing mycobacterial species, including attenuated strains of *M. tuberculosis* (mc^2 6230 - M. tb H37Rv Δ*panCD* &

mc^2 6206 - M. tb H37Rv Δ*panCD* Δ*leu*), the majority of understanding has come from the faster growing *M. smegmatis*. The shorter doubling time of *M. smeg* makes it a much more genetically tractable organism.

The key mycobacterial respiratory complexes have good sequence conservation between *M. smeg* and *M. tb*, including the known cytochromes (cyt *bcc:aa*$_3$ supercomplex, cyt *bd* quinol oxidase & Sdh2). It is, however, important when using *M. smeg* as a model for *M. tb* to bear in mind that the two organisms are not equivalent. There are differences in the number and variety of respiratory complexes between *M. smeg* and *M. tb*. For example, *M. tb* has two Type-II NADH dehydrogenases (Ndh, NdhA) whereas *M. smeg* only encodes one (Ndh). The difference in doubling time likely means that there is a difference in energy demand between the two species and so differences in how their bioenergetic machinery is utilised. Given the ease of working with *M. smeg* in terms of safety precautions, time, and scale as compared to attenuated *M. tb* (BSL-2) *M. smeg* was chosen as the model organism to begin working with.

The group acquired the bioenergetic chamber approximately 6 months into beginning my PhD. Before this, I had been working to characterise the cytochrome content under different growth conditions using isolated mycobacterial membranes. Growing under different conditions will result in different complements of respiratory enzymes. If one can find robust conditions that favoured the different oxidases, their respective roles can be inferred from their presence or absence. This can give different results to transcriptomic approaches, by observing the presence of a cytochrome rather than inferring its presence from the increased expression of its associated genes. The two often correlate but may not be equal due to translation regulation or complex stability. Robust conditions favouring a particular respiratory complex also offer opportunities for downstream applications such as purifying the complexes (Chapters 4 and 5). The next section encompasses this initial work which was then used to inform the growth conditions that were then used as a starting point within the bioenergetic chamber.

3.3.1.1 The development of a protocol to isolate mycobacteria membranes

Isolated membranes have been a historically powerful system for understanding bioenergetic systems. Examining the spectrum of membranes provides an easy way to determine which cytochromes are present in the cell. There are a number of existing protocols for isolating membranes from mycobacterial (Dunn et al., 2014; Koul et al., 2007). Because of the nature of the mycobacterial membrane, gentler approaches such as traditional enzymatic lytic cocktails do not successfully lyse the cells. Instead more physical methods, bead-beating, French press, and cell disruption are required.

An initial protocol was developed during my MBiochem project using a cell disruption and differential centrifugation, which was further refined during my PhD. The cell disruptor uses shear forces to break open the cells and is compatible with the scale required for downstream processes such as protein purification. Once the cells had been broken, differential centrifugation was used to isolate membranes. Initially, after a cell debris spin, membranes were isolated by a spin at 48 k*g*. In subsequent preparations, this was increased to 100 k*g* to reduce time and improve the yield of membranes. From parallel work in the group on *Bacillus*, a second membrane wash spin was added. From Cryo-EM images of membrane samples, the initial spin pellet contained a high concentration of ribosomes (personal communication with Dr. Pooja Gupta and Beth Hardman). The concentration of ribosomes could be reduced by washing the membranes. A scheme of the refined mycobacterial membrane isolation protocol is shown in Figure 3.13.

3.3.1.2 Haem content in different growth conditions from membranes

3.3.1.2.1 Growth of *M. smeg* with two carbon sources, glycerol and succinate

With an established protocol for isolating membranes, I could then use it to examine the change in the cytochrome context during the growth of *M. smeg* and the effect of growing on different carbon sources. *M. smeg* was grown in either glycerol or succinate. Historically glycerol has been added to mycobacterial growth media but there is literature to suggest that glycerol up-regulates the expression of the cyt *bd* quinol oxidase as compared to other carbon sources (Kalia et al., 2019). I also wished to see if the expression of other mycobacterial cytochromes could be increased or decreased. Succinate was chosen to see if the expression of Sdh2, which contains two haem B centres, could be increased.

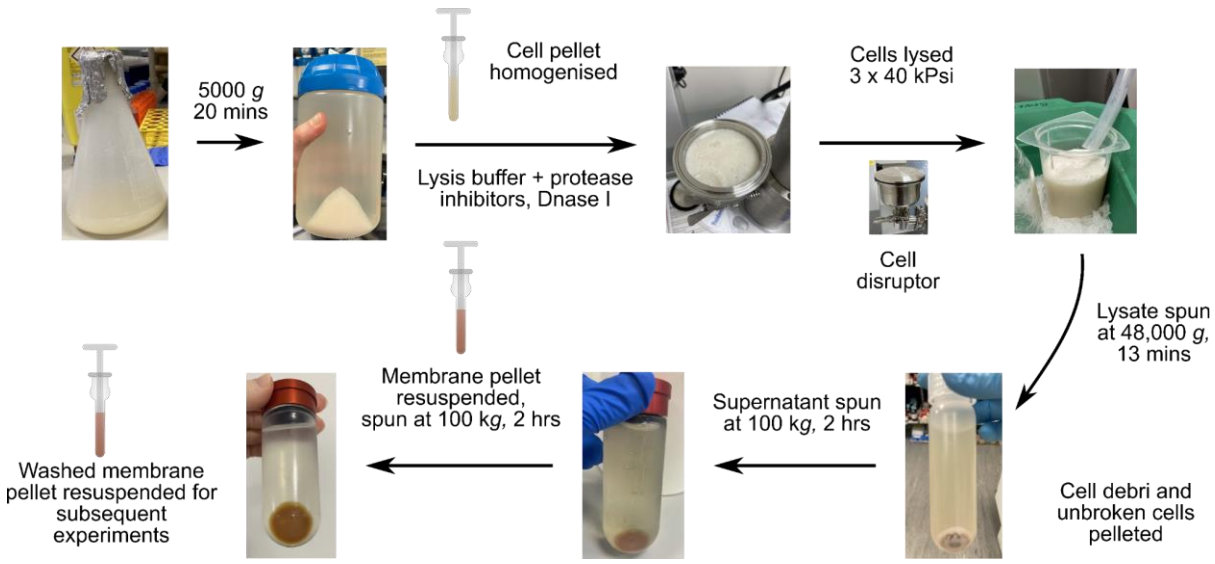

Figure 3.13 - A schematic of the optimised membrane isolation process

The growth under the two carbon sources was monitored by OD_{600} and membranes were isolated at the indicated points during the growth (Fig 3.14) to have membranes from mid-exponential phase cells, late exponential growth and stationary phase cells. The growth in glycerol was initially faster than succinate, succinate appeared to sustain more growth by stationary phase. This is only based upon OD_{600} which is not always a good approximation of biomass particularly in later stages of growth where morphological changes in growth can affect the measurement.

Visible-wavelength oxidised-reduced absorbance spectra were then used to quantify the relative abundance of the cytochrome-containing respiratory enzymes in the isolated membranes. Here the absorbance spectrum of the oxidised membranes has the absorbance spectrum of the chemically reduced enzymes subtracted to provide the distinctive haem-specific peaks while avoiding problems with background signals. In this case, the 'as-prepared' enzyme was assumed to be oxidised. Cytochromes can also be oxidised by using agents such as potassium ferricyanide. The difference spectrum was spectrally decomposed using a python/NumPy script modelling the haem components as Gaussian peaks providing the ratio of the signal from *d* haem (specific to the cyt *bd* quinol oxidase) compared to the signal from *a* haem and *c* haem (specific to the cyt *bcc:aa*$_3$ supercomplex).

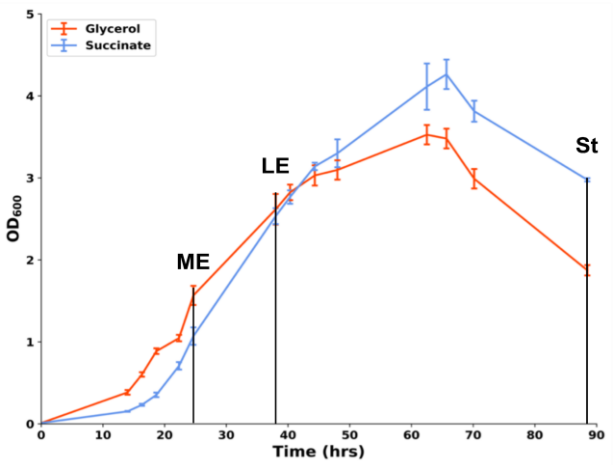

Figure 3.14 - Glycerol vs Succinate growth curves*: Average of the three cultures left to stationary for each carbon source, time point exponential phase cultures were harvested is indicated. ME – mid-exponential (24 hrs), LE – late-exponential (38 hrs) (likely more a transition point between late exponential and stationary), St – Stationary (88 hrs) given the change in OD_{600} there may be a morphological change in the cells occurring.*

3.3.1.2.2 Decomposition using matrices

In the case of spectral decomposition, I am referring to the breaking down of a total spectrum into its component parts using the mathematical technique of decomposition. In this form of

decomposition, a matrix is factorised into a product of matrices. This mathematical approach is also used within Palencia, the software associated with the chamber system. For the membrane spectra, the fitting was implemented in my own Python script, with the aid of an online tutorial within the online textbook 'A pragmatic introduction to signal processing'(O'Haver, 2021). I implemented these in the accessible programming language Python (Van Rossum and Drake, 2009) using the NumPy libraries (Harris et al., 2020).

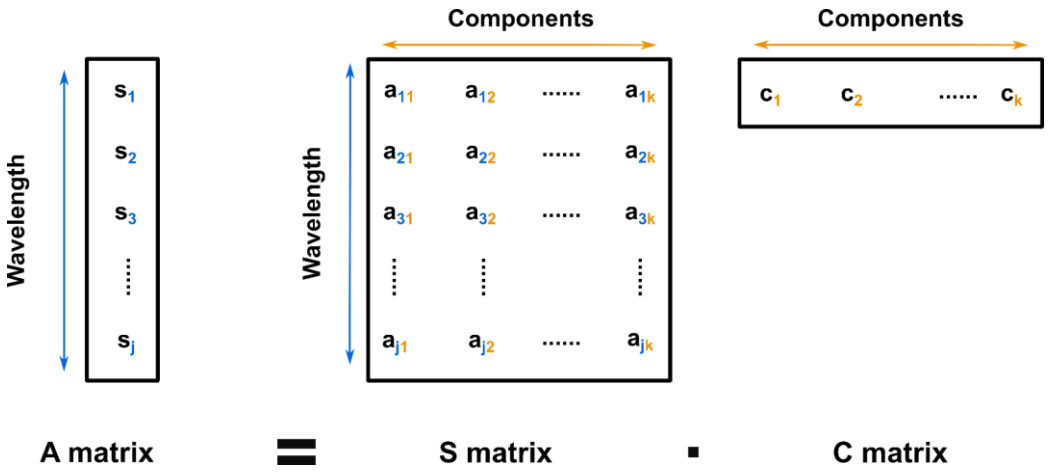

Figure 3.15 - Matrix and vectors described in Eq. 3.2

Fig 3.15 and Eq. 3.2 illustrates the matrices that can be used to describe the input spectrum and its relationship to the concentration of known components:

$$\mathbf{A} = \mathbf{S.C} \qquad \text{Equation 3.2}$$

For *k* number of components measured over *j* number of wavelengths. **A** is a *j* vector of the absorbance at each wavelength. Given the Beer-Lambert law, **A** is the product of **S** and **C** where **S** is a *j* x *k* matrix of the known specific absorbance at each wavelength for each component, (i.e. a matrix of the reference spectra) and **C** is a *k* vector of the concentration of each component in the spectrum. Usually for the Beer-Lambert law, **A** would be divided by **S** in order to solve for **C**. However, a matrix or vector cannot simply be divided by another matrix. Therefore, the inverse matrix ($\mathbf{S^{-1}}$) and the transposed matrix ($\mathbf{S^{T}}$), where the columns and rows of the matrix are switched have to be utilised.

As :

$$\mathbf{S^{-1}.S} = \mathbf{I} \qquad \text{Equation 3.3}$$

Where **I** is the identity matrix and equivalent to multiplying by 1. This means that multiplying by $\mathbf{S^{-1}}$ is equivalent to dividing by **S**. In the case of square matrices, where there are an equal number of columns and rows this is simple; however, when the number of columns and rows

is not equal the transposed matrix has to be used. This is because to multiply one matrix by another, the first matrix must have the same number of columns as the number of rows in the second matrix. Taking these matrix laws into consideration in order to rearrange Eq. 3.2 for **C**, both sides are multiplied by $(\mathbf{S}^T\mathbf{.}\ \mathbf{S})^{-1}\mathbf{.}\ \mathbf{S}^T$ (Eq. 3.4). This will simplify to Eq. 3.5 as $(\mathbf{S}^T\mathbf{.}\ \mathbf{S})^{-1}\mathbf{.}\ \mathbf{S}^T\mathbf{.}\ \mathbf{S}$ will be equal to the identity matrix.

$$(\mathbf{S}^T.\ \mathbf{S})^{-1}.\ \mathbf{S}^T.\ \mathbf{A} = (\mathbf{S}^T.\ \mathbf{S})^{-1}.\ \mathbf{S}^T.\ \mathbf{S}\ \mathbf{C} \qquad \text{Equation 3.4}$$

$$\mathbf{C} = (\mathbf{S}^T.\ \mathbf{S})^{-1}.\ \mathbf{S}^T.\ \mathbf{A} \qquad \text{Equation 3.5}$$

Therefore Eq. 3.5 can then be used to find **C** given **S** and **A**. In Python using the NumPy module Eq. 3.5 is coded by,

```
C=np.matmul(np.matmul(np.linalg.inv(np.matmul(np.transpose(S),S)),np.transpose(S)), (A))
```

If C, S and A are NumPy arrays of the matrices shown in Fig 3.14.

3.3.1.2.3 The haem content of the membranes as determined by spectral deconvolution

Using the developed Python script, the haem content of membranes isolated from each of the growth phases for the two carbon sources was determined. The haems were modelled by Gaussians. The Gaussian centred at the haem type typically absorbance with some adjustment for a reasonable fit across all of the membrane samples. Scatter components were also fitted to account for the background scatter in the spectra. An example of this fitting process is shown in Figure 3.16. For the *d* haem signal, a combination of a positive Gaussian and negative Gaussian was fitted to account for the typical sinusoidal feature in the difference spectrum as a result of its unusual spectral features in the anaerobic form. The fits of the six membrane spectra are shown in Figure 3.17.

Consistently, there was substantially more of the *d* haem signal in the glycerol cultures at every growth phase as compared to the succinate cultures. This is particularly apparent from the ratio of *d* haem signal to *c* haem or *a* haem signal. In both carbon sources, the *d* haem signal also increased as the culture grew, with the most *d* haem seen in the stationary phase. Improvements to this would either require reference spectra from a cyt *bd* homologue or the spectral characterisation of isolated mycobacterial cyt *bd*. The cytochrome origin of the *b* haem signals is difficult to determine with this Gaussian peak decomposition approach as it could have originated from multiple different cytochromes (cyt *bcc:aa*$_3$ supercomplex, cyt *bd*, Sdh2 or other unknown cytochromes). However, it can be inferred from the relationship between the *c* haem and *d* haem signals. In the glycerol cultures the increased amount of *b* haem signal is likely due to the presence of cyt *bd*, based upon the increase in the amount

of *d* haem. In comparison in the succinate cultures the additional *b* haem signal is likely from increased expression of Sdh2.

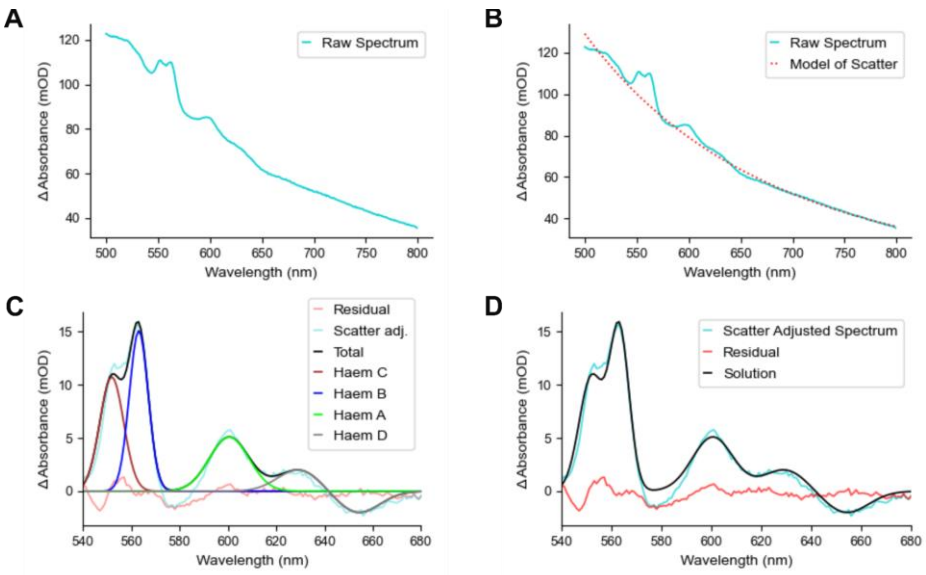

Figure 3.16 – Example of the membrane spectrum fitting *(**A**) The raw difference spectrum (**B**) The modelled scatter of the difference spectrum built from y = 1, y = 1/x and 1 = 1/x^2 (**C**) The size of each of the haem signals in the raw spectrum as determined by the decomposition. This is shown with the scatter-adjusted spectrum. (**D**) The sum of the signals can be compared to the raw spectrum to give the residual, indicating areas where the solution deviates from the data, in this case, shown as scatter-adjusted spectrum and solution for clarity.*

Table 3.3 – Haem ratios for membranes grown under different conditions: *d haem signal is specific to the cyt bd quinol oxidase and c haem and a haem signal is specific to the cyt bcc:aa$_3$ supercomplex.*

Sample	D : C ratio	D : A ratio
Glycerol Mid Exponential	1 : 5.3	1 : 2.5
Glycerol Late Exponential	1 : 4.0	1 : 1.9
Glycerol Stationary	1 : 2.5	1 : 0.9
Succinate Mid Exponential	1 : 102.7	1 : 38.5
Succinate Late Exponential	1 : 26.5	1 : 8.4
Succinate Stationary	1 : 7.3	1 : 1.7

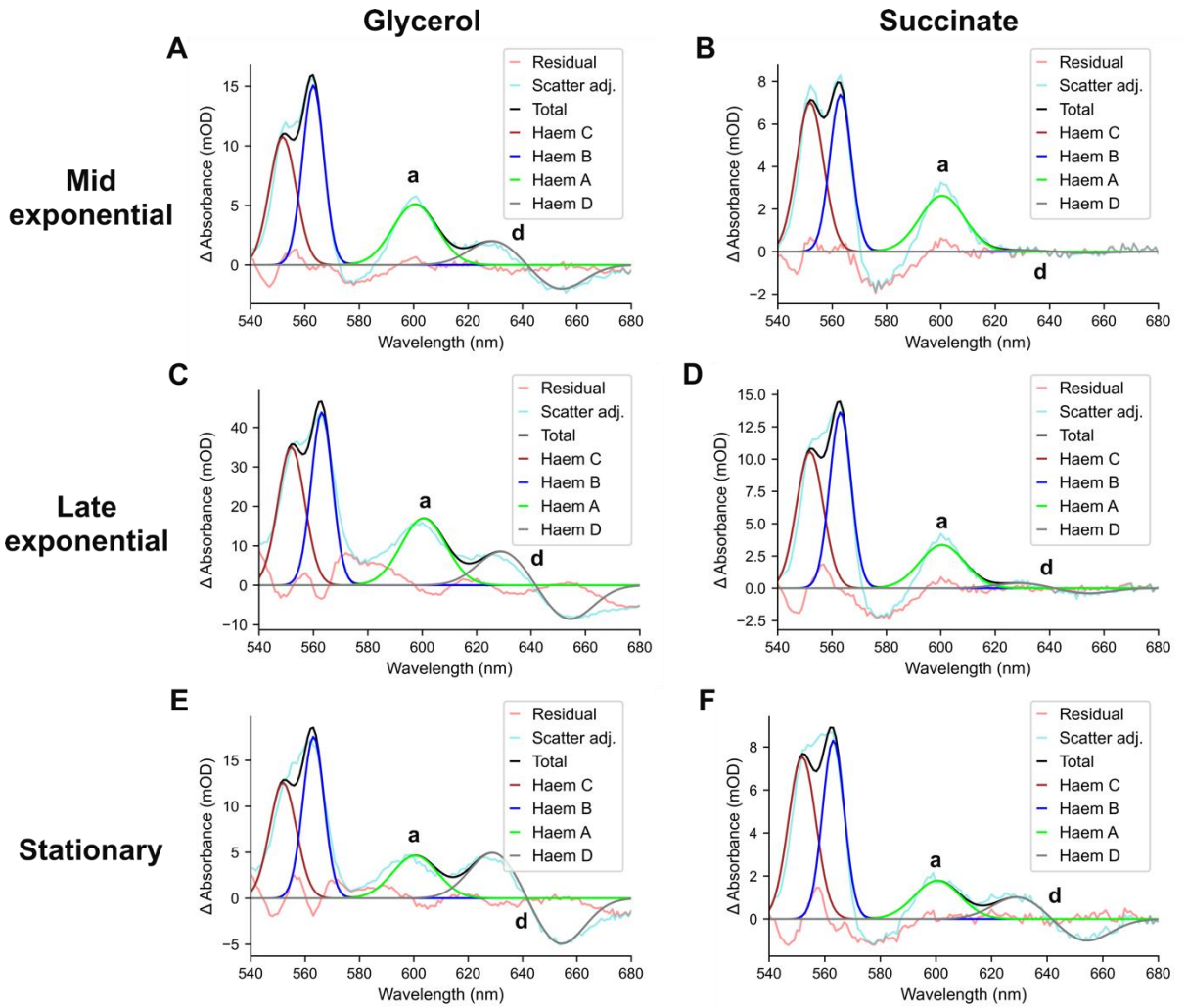

Figure 3.17 - Haem spectra of membranes isolated from the two cultures at different stages*: Membranes were isolated from 1 L of cells from each of the three-time points with the two carbon sources. A difference spectrum for each was collected and processed. The peaks corresponding to a haem signal (specific to the cyt bcc:aa$_3$) and d haem signal (specific to the cyt bd) are indicated.*

Overall, from the total spectra it appears that the cyt *bcc:aa*$_3$ is the dominant cytochrome in *M. smeg* during exponential phase growth. This matches with previously published work, that Δ*qcrCAB M. smeg* had particularly stunted growth during the exponential phase (Matsoso et al., 2005). However, at least under these growth conditions, there is more cyt *bd* quinol oxidase present early in the growth phase than expected.

3.3.1.3 Mycobacterial porphyrin production

As this experiment was carried out I observed that the glycerol cultures began turning reddish (Figure 3.18 A) as their growth approached the stationary phase (after 65 hrs). This colour appeared to be in both the cells and the growth media, judging by the appearance when the

cells were harvested (Figure 3.18 B). This colour change has been reported previously (Berney and Cook, 2010; Nikitushkin et al., 2016). The colour change appears to be due to a pigment, that was identified as free porphyrins (tetramethyl coproporphyrin and octamethyl uroporphyrin esters), which was both in extracts from the cells and excreted into the media (Nikitushkin et al., 2016). Subsequent purification fractions had very similar absorption spectra to the absorbance spectra of chloroform extract pigment from Nikitushkin et al. (Figure 3.18 C & D). This absorbance spectrum did not change upon the addition of reducing agents, supporting the idea that this is attributable to a free porphyrin and not a cytochrome. It is unclear what the exact role of the production of this pigment is.

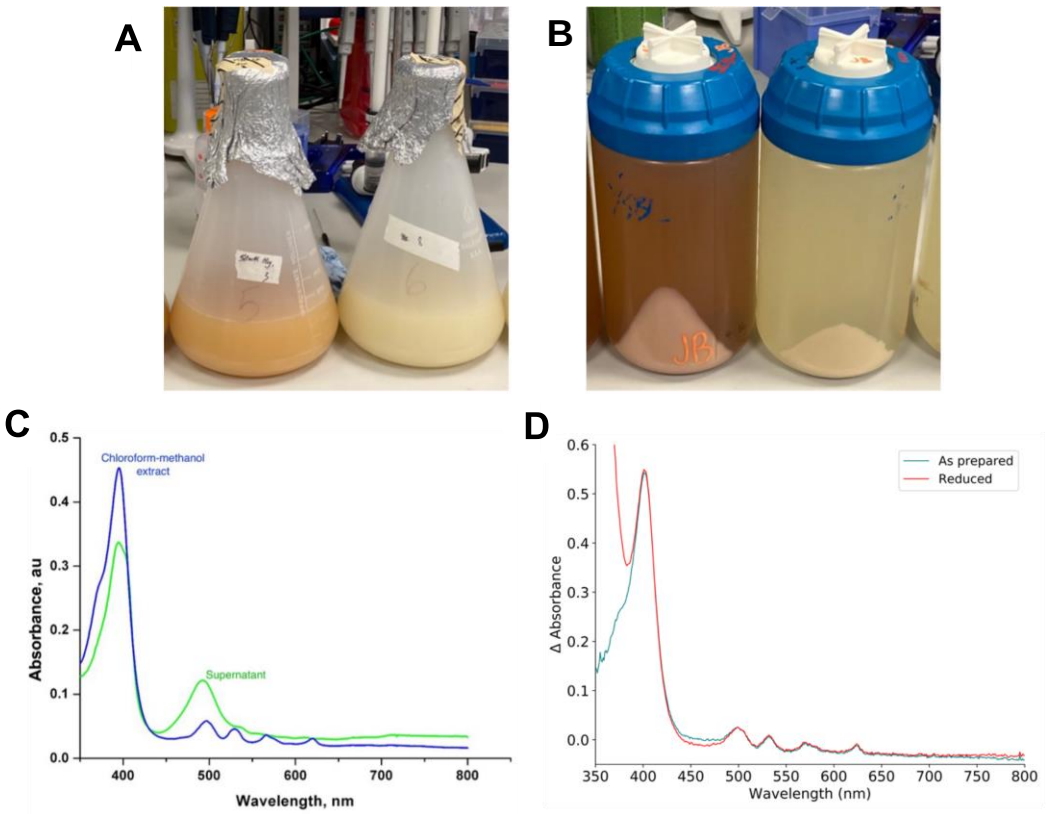

Figure 3.18 - Mycobacterial coproporphyrin pigment: *(**A**) Culture colour – Cultures after 65 hrs of growth, glycerol on the left, succinate on the right, this colour was the same for all cultures grown on the same carbon source. (**B**) Pigment location – The cultures post harvesting, glycerol on the left and succinate on the right. The red pigment is seen in both the pelleted cells and the growth media of the glycerol cultures but not the succinate culture. (C) Figure from Nikitushkin et al., 2016 showing the absorbance spectra of supernatant (green) and a chloroform-methanol extract (blue) from pigment-producing M. smeg. The chloroform-methanol extract was later determined to be a mixture of free porphyrins and their methyl esters by NMR and MALDI. (D) An absorbance spectrum from an anion exchange*

chromatography fraction as prepared (red) and after the addition of the reducing agent sodium dithionite (blue). (See Chapter 5 - from a fraction eluted ~40 mL in Figure 5.4)

The observation of this pigment is important for subsequent spectral experiments as it may interfere with any haem spectra measurements. Its spectral features are in the same wavelength region as the distinct spectral handles of cytochromes (500 - 650 nm) due to the chemical relationship between porphyrins and haems. These growth conditions provided a starting point for chamber experiments that appear to not produce the pigment, early in the growth phase and when the cells are grown on succinate. We also have some idea of what complement of cytochromes is to be expected under the specific growth conditions.

3.3.2 Trialling the bioenergetic chamber for examining mycobacteria, initial experimentation

As introduced previously, the bioenergetic chamber allows simultaneous oxygen consumption and haem electron occupancy measurements on live intact cells. Using the same setup as for the mammalian systems to measure *M. smegmatis* posed several issues that had to be dealt with initially. These were:

- Sufficient oxygen delivery to match *M. smeg* higher oxygen demand as compared to mammalian cells.
- Interference from a mycobacterial coproporphyrin pigment present in certain growth conditions.
- Spectral interference from the optode phosphorescence in the 650 nm region where the *d* haem signal is present.
- Mis-fitting using the standard set of mammalian haem reference spectra.

The next section details how these were dealt with.

3.3.2.1 Maintaining oxygenation and measuring oxygen consumption rate

The chamber is oxygenated via oxygen-permeable tubing submerged in the cell suspension with a blend of nitrogen and oxygen flowing through it. This blend of gases is under the control of a feedback loop through the chamber acquisition software, Palencia. From the first experiments with *M. smeg* it was apparent that the current rate of oxygen delivery was insufficient to maintain a constant oxygen concentration in the chamber. To address this the length of tubing used was increased from 80 mm to 120 mm. 120 mm was sufficient to supply *M. smeg* at an OD ~1. Figure 3.19 shows a run where the oxygen consumption rate of the cells was ~ 100 µM/min. 100 µM/min of oxygen appears to be the oxygen delivery capacity

of the system with 120 mm of tubing as shown by the length of time it takes the chamber to return to 100 µM oxygen. This is important to consider for experiments where the oxygen consumption rate could increase during the run, say upon the addition of an uncoupler. Due to the nature of how this tubing is fitted into the chamber, increasing the tubing length by any more runs the risk of coming out of its coil during the experiment and interfering with the spectroscopy.

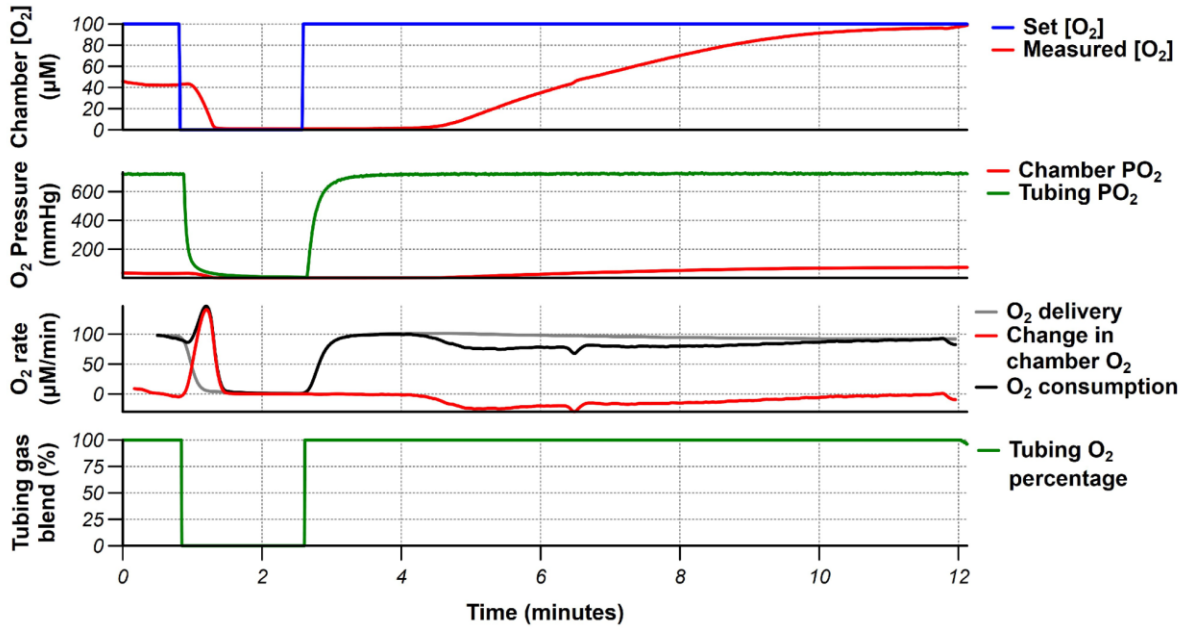

Figure 3.19 - Maintaining the oxygen concentration in the chamber. *(A) Shows the set oxygen concentration, in blue (Set [O_2]), and the measured chamber oxygen concentration, in red (Measured [O_2]), as measured by the chamber optode. (**B**) Shows the oxygen pressure of the chamber (Chamber P_{O2} in red) and in the tubing (Tubing P_{O2} in green). The tubing oxygen is measured via an optode in the exit port of the tubing. (**C**) Shows the changes in the oxygen rates during the calibration. O_2 delivery, in grey, demonstrates the oxygen delivery as calculated based on the difference in the oxygen pressure in the chamber and tubing. This is calibrated at the start of the run using the top hat to determine the permeability of the tubing. Change in chamber O_2, in red, is the change in the oxygen concentration in the chamber over time, calculated from the gradient of the chamber [O_2], red in graph **A**. The overall oxygen consumption is shown in black and is the sum of the O_2 delivery and change in the chamber [O_2]. (D) The tubing O_2 percentage, in green, shows the percentage of oxygen flowing through the tubing. This is under the control of a feedback loop to maintain the chamber at the set oxygen concentration.*

This density of cells was sufficient to measure distinct haem signals. It was not possible to either increase the density of the cells or increase the length of the tubing to accommodate

more cells as the oxygen perfusion system was unable to match the oxygen demand. Subsequent experiments in the chamber with *M. tb* by other members of the group determined that *M. tb*'s oxygen demand per OD_{600} of cells was less than that of *M. smeg* (personal communication with Suzy Harrison and Dr Morwan Osman). This means that the density of the *M. tb* cells can be increased 7-10 fold for experiments in the chamber.

3.3.2.2 Observing mycobacterial haem spectral signals in the chamber, adapting the mammalian fit to give sensible interpretation

Using the growth conditions established prior to having the chamber, haem spectra were measurable in *M. smeg* grown with either glycerol or succinate as the carbon source. Figure 3.20 shows the anoxic-aerobic difference spectra collected by the chamber. These will not be identical to the difference spectra from membranes (Figure 3.17) as under aerobic conditions the cells will be respiring and so a fraction of the haems will be reduced in the aerobic spectrum. Despite this, the general haem content should be observable. Two different wavelength ranges were collected, with a wider spectrum set to encompass beyond 600 nm with the hope of observing the *d* haem signal.

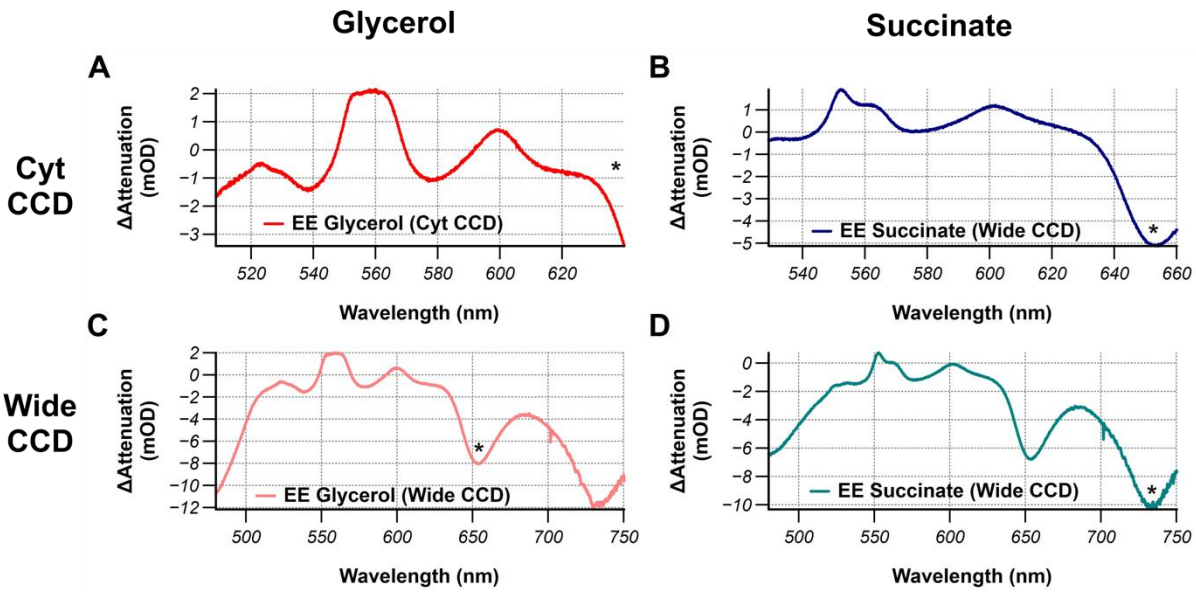

Figure 3.20 - Haem spectra of mid-exponential phase (24 hrs) M. smeg grown in glycerol or succinate. *(**A** & **C**) anoxic-aerobic haem spectra of the glycerol culture, from the narrower 'cyt CCD' (**A**) and the wider 'wide CCD' (**C**) (**B** & **D**) anoxic-aerobic haem spectra of the succinate culture, from the narrower 'cyt CCD' (**B**) and the wider 'wide CCD' (**D**). All the spectra were generated using 1 minute averages of the collected spectra. The trough at 650 nm (*) is an artefact generated by the phosphorescence of the optode.*

The difference spectra demonstrate that there is sufficient signal to measure the haems at this density of *M. smeg.* The peaks in the difference spectrum corresponding to signals from *c* haem, *b* haem and *a* haem were distinguishable in both carbon sources. However, the phosphorescence of the optode created a trough in the difference spectra at 650 nm that prevented the observation of the *d* haem signal. Despite these caveats these difference spectra broadly match previous observations with the early exponential phase membrane spectra, with more *b* haem siganl in the glycerol grown than succinate grown.

The acquisition software, Palencia, performs a similar deconvolution by decomposition as I had applied to the isolated membranes. As this is a mathematically 'inexpensive' set of calculations it can be done as the software acquires the data, meaning the haem traces can be followed in real-time. Reference spectra for each of the haem components present in the mammalian cells had previously been measured or taken from the literature by Roger Springett and incorporated into a spectral model that could be used to fit the collected data in Palencia (Kim et al., 2012). Figure 3.21 A & B shows the cytochromes present in the mitochondria compared to the cytochromes thought to be present in mycobacteria. Figure 3.21 C shows the spectral model previously used to decompose the mammalian spectra and the reference spectra of those that contribute to the overall spectrum.

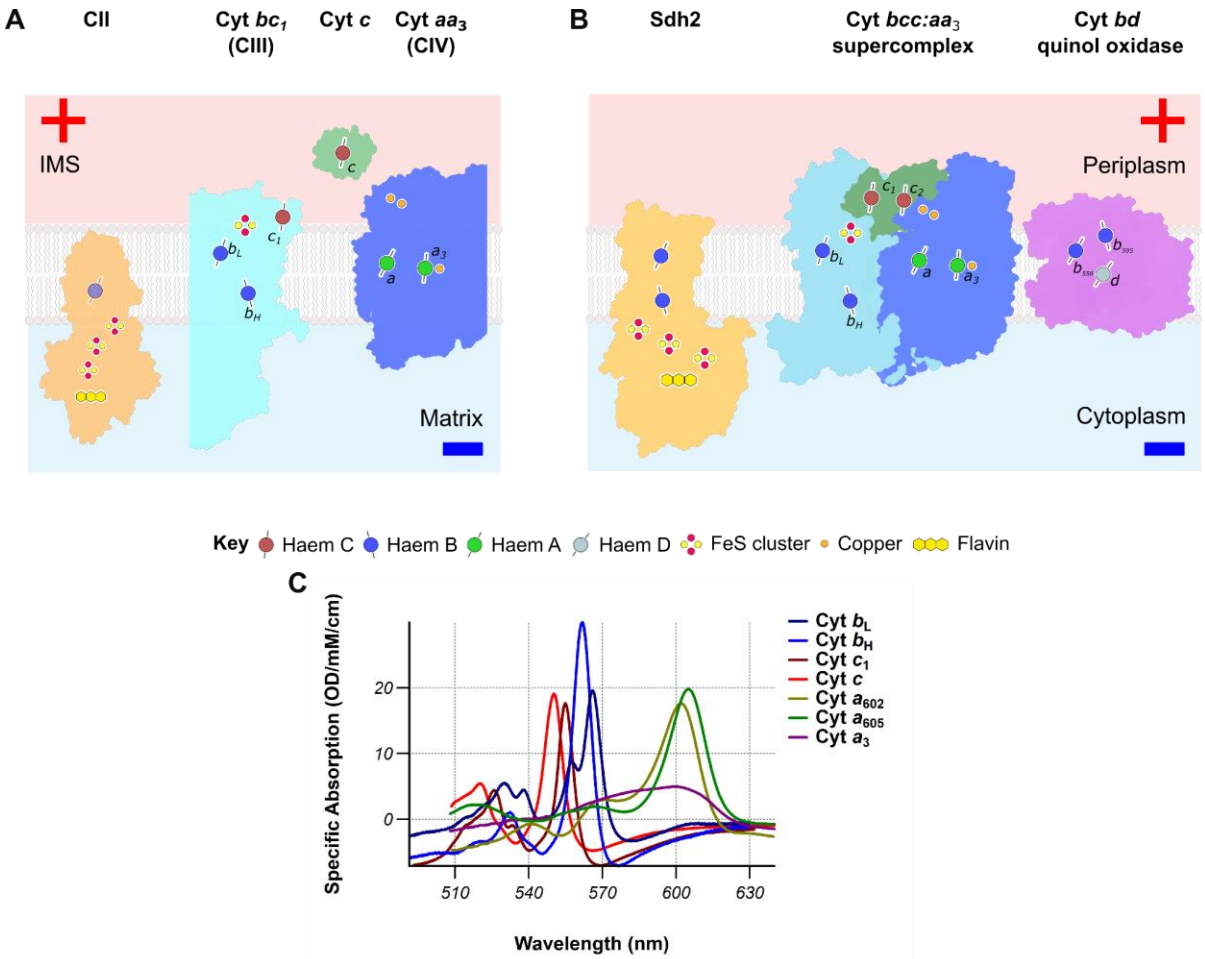

Figure 3.21 - Comparing the mammalian and mycobacterial cytochromes and their haem spectra *(**A**) The mammalian cytochrome, complex II (CII), the cyt bc_1 (CIII), soluble cyt c and the cyt aa_3 cyt c oxidase (CIV). Complex II, the succinate dehydrogenase in the mammalian ETC, does contain a b-type haem, however, it is not directly involved in the electron transfer pathway of the enzyme and it has a more negative E_m than the other centres. Therefore, it was decided not to include its spectrum in the spectral model. (**B**) The mycobacterial cytochromes, Sdh2, cyt $bcc:aa_3$ supercomplex and cyt bd. (**C**) The mammalian reference spectra that make up the spectral model for decomposing mammalian haem spectra.*

The decomposition is performed on the Δattenuation, change in scatter and absorbance as compared to the start of the run, reducing the contribution of the background scatter of the cells. This then gives a change in the 'concentration' of the oxidised species of each haem centre present in the spectral model. Because the path length is not fixed, an absolute concentration cannot be calculated, however, an approximation can be made using the average path length of 3.9 cm (Kim et al., 2011). The change in the 'concentration' of the oxidised species is plotted against time as a haem trace. An example of the mammalian fitting

applied to a run with *M. smeg* is shown in Figure 3.22. Downward deflection indicates reduction of the haem and upward deflection the oxidation of the haem. The un-altered mammalian fit was not perfect however for the initial experiments it was sufficient to begin exploring the established growth conditions, providing at a glance a sense of how the haems were behaving during the run without having to generate difference spectra.

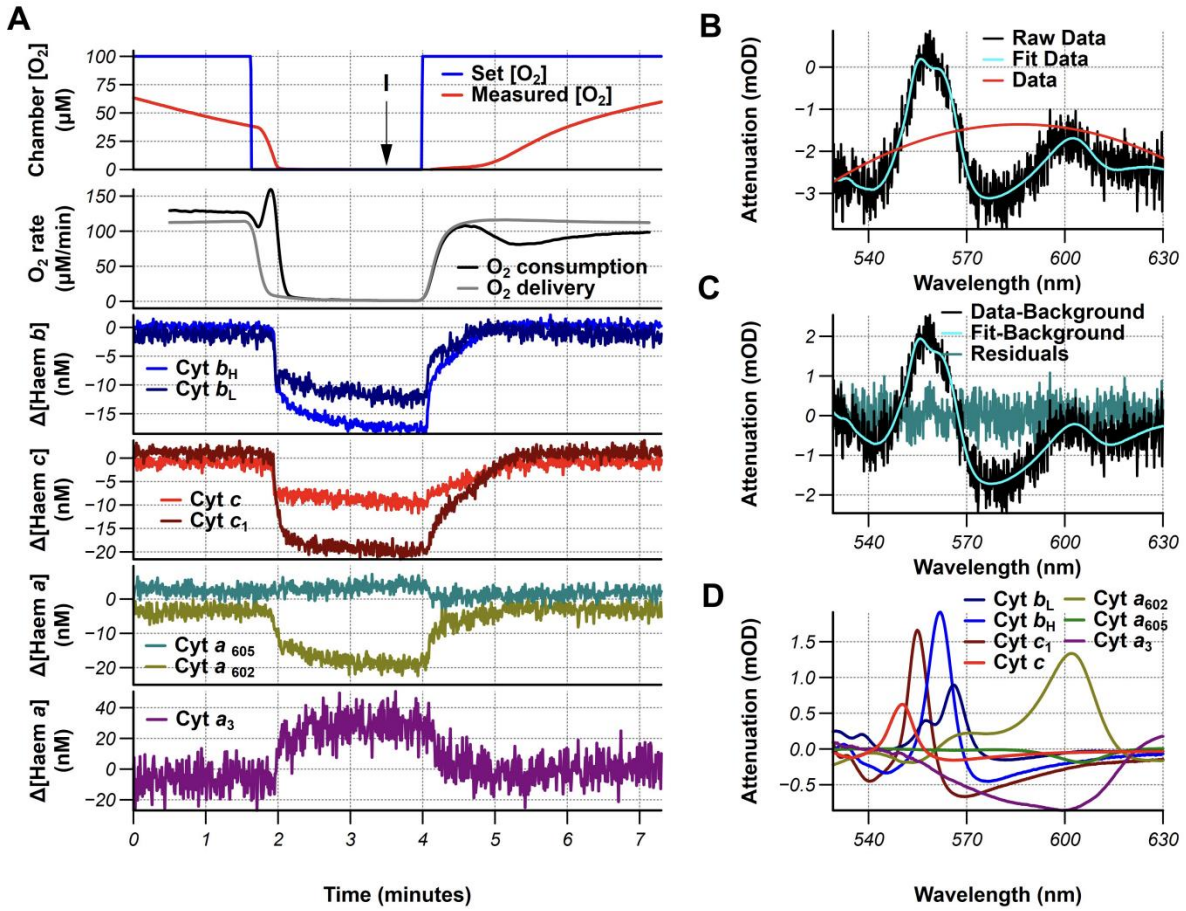

Figure 3.22 - Example of the mammalian fit on M. smeg succinate culture at 48 hrs *(**A**) Experimental traces as the cells were taken anoxic (**B**- **D**) Example of the fitting at point I. (**B**) The raw data, fit generated by the decomposition using the original mammalian fit and the background function fit. (**C**) The background-subtracted data and fit. The residual difference between the data and the fit is shown in teal. (**D**) The size of the haem components fit during the anoxia period. Mis-fitting by the a_3 signal can be seen in this case.*

3.3.2.3 Appearance of interfering coproporphyrin pigment during routine culturing

Mid-exponential phase culture grown on glycerol or succinate showed a dramatic difference in the haem traces. The glycerol-grown cultures had a ‘drifting baseline’ in its haem traces (Figure 3.23 A). This was the result of a prominent pigment in the absorbance spectrum (Fig. 3.23 B) that matched the previously seen coproporphyrin pigment. As before, this absorbance

did not change under reducing conditions(anoxia). At 10 minutes when the cells were taken anoxic, the drifting stopped and it did not continue to drift when the culture was taken aerobic again allowing the generation of the difference spectrum shown in Fig 3.20 A & C. The appearance of the pigment in the chamber was from cultures at a much earlier time point (24 hrs) than previous culture colour change (60 hrs). However, the pigment was more prominent in older cultures (Figure 2.23 C).

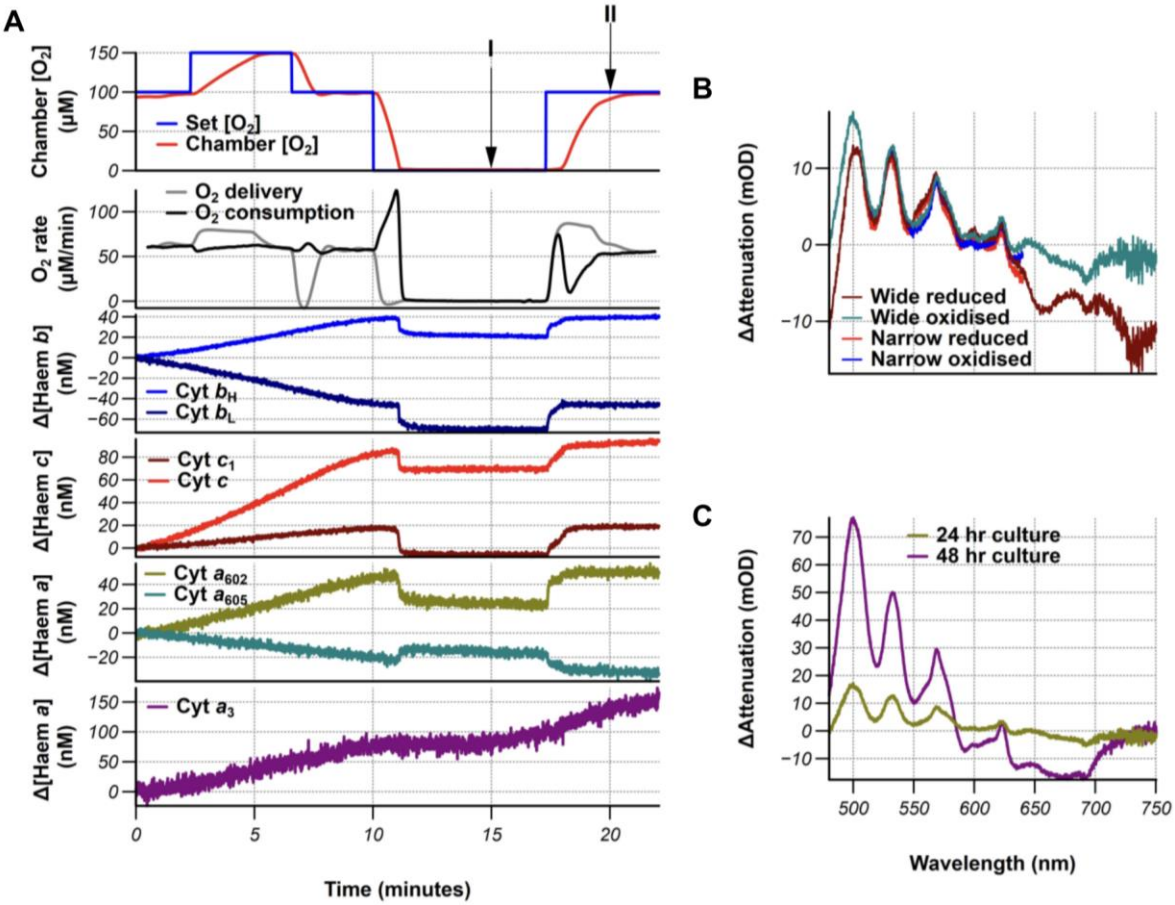

Figure 3.23 - Interference of the coproporphyrin pigment in the haem traces *(**A**) Experimental traces from 1 L glycerol at 24 hrs, OD_{600} ~ 1. The drift in the haem traces experiment is likely due to an increase in the coproporphyrin pigment over the course of the experiment. The cells were taken through the 'top-hat' (oxygen concentration change from 100 μM to 150 μM, back to 100 μM, anoxic (0 μM) and finally back to 100 μM). (**B**) reduced/anoxia spectrum (~15 mins, I) and oxidised spectrum (~20 mins, II) from the narrow and wide CCD. The coproporphyrin pigment is visible in both spectra with absorbance peaks at 500, 533, 569, and 623 nm. (**C**) Average attenuation spectrum from the first 30s and at 11 mins into the experiment, demonstrating an increase in the coproporphyrin pigment over the course of the experiment. Taken from a 1 L glycerol culture after 48 hrs of growth.*

Unlike 1 L glycerol cultures, 1 L succinate cultures did not have the coproporphyrin pigment when placed in the chamber (Fig. 3.24). Interestingly smaller glycerol cultures typically used as starter cultures to inoculate the larger cultures also did not produce this pigment (Fig 3.25).

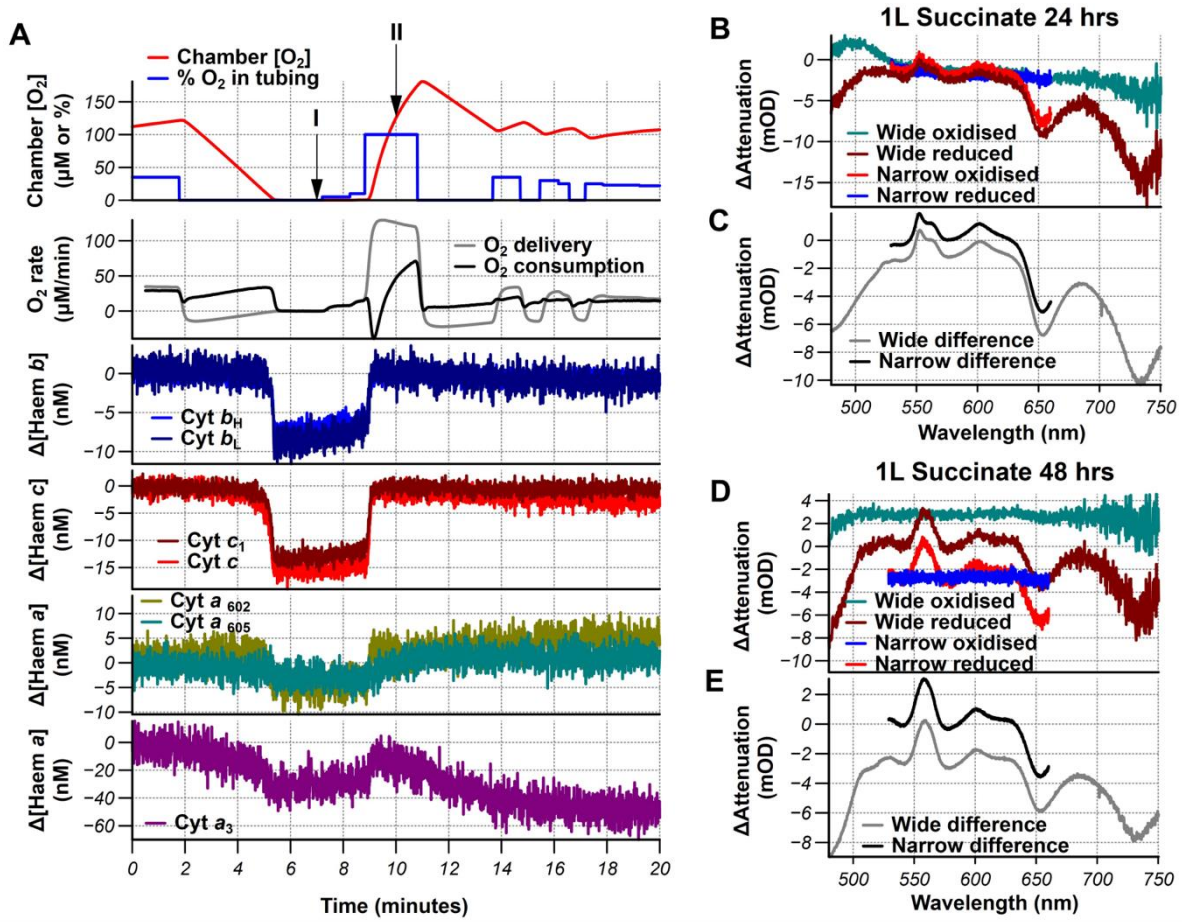

Figure 3.24 - Lack of coproporphyrin pigment in succinate cultures *(**A**) Experimental traces from 1 L succinate at 24 hrs, OD_{600} ~ 1. Some drift particularly in the a-haem traces, but not to the same degree as for the 1 L glycerol cultures. (**B**) Anoxia spectrum (~7 mins, I) and aerobic spectrum (~10 mins, II) from the narrow and wide CCD. Absorbance attributed to coproporphyrin pigment is not visible in the difference spectrum (**C**) Difference spectrum generated from spectra in (**B**), again shows a similar haem composition to previously isolated membranes. (**D** & **E**) 1 L succinate at 48 hrs, OD_{600} ~ 2. (**D**) Anoxia spectrum and aerobic spectrum from the narrow and wide CCD.*

3.3.2.4 Reassessing the oxygenation of the cultures, using bioreactors to demonstrate oxygen limitation in 1L flask growth conditions

It was also observed that if the flask containing the culture was left out of the bench, no longer being aerated, the culture appeared to get redder, similar to the colour change seen at around

60 hrs. From this observation, it was hypothesised that the current culturing setup was oxygen-limited, particularly when glycerol was the carbon source. This would also explain why more cyt *bd* oxidase had been seen in the glycerol conditions than expected, given the association between the cyt *bd* oxidase and lower oxygen tension. The initial setup had 1 L of culture in plastic non-baffled flasks with a foam bung covered in foil. Given the density that mycobacteria can grow in detergent, it is conceivable that the current setup does not allow for sufficient oxygen diffusion for the cultures grown on glycerol.

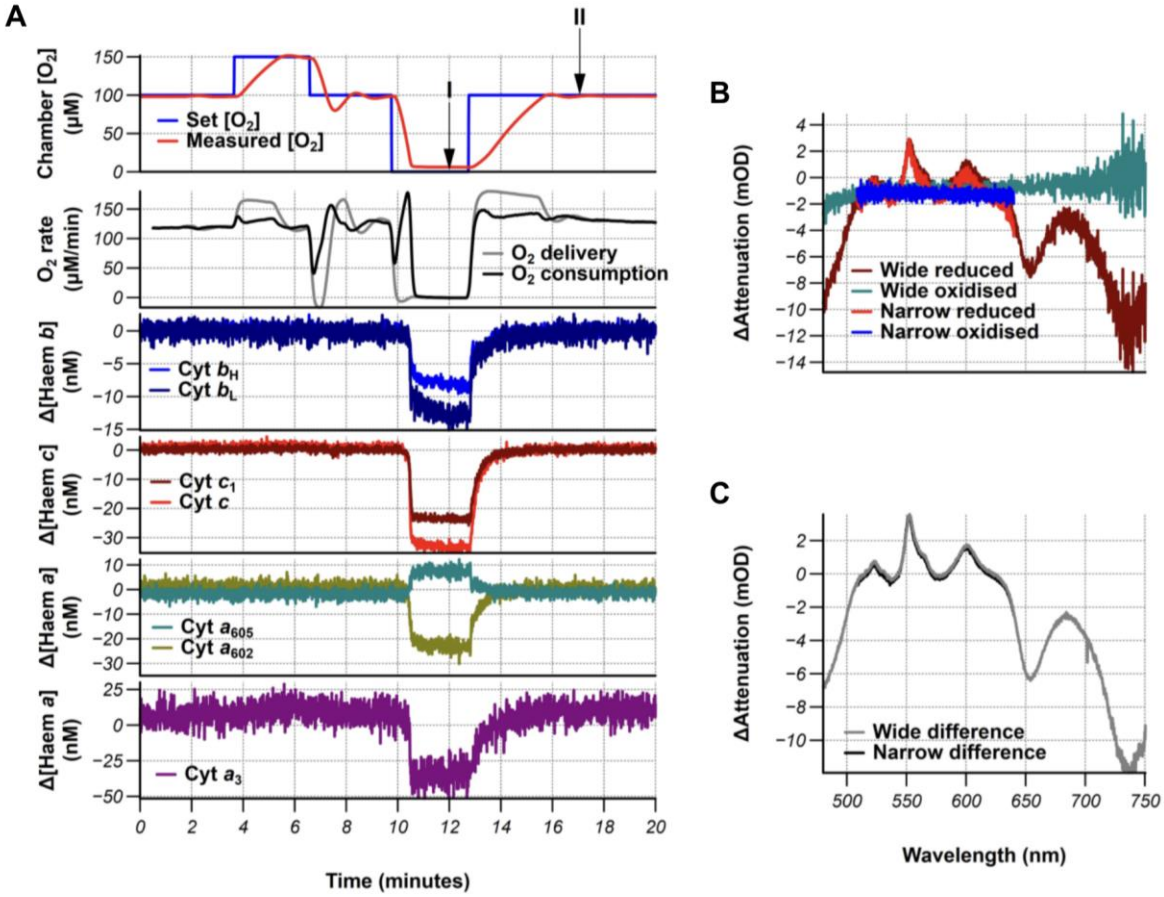

Figure 3.25 - Haem trace and spectra of small 50 mL cultures. *(**A**) Oxygen concentration, oxygen consumption rate and haem traces during the experiment as the cells were taken through the 'top-hat'. (**B**) ΔAttenuation spectra from **I** - reduced and **II –** oxidised, as indicated points for both the wide and narrow CCDs spectrum (**C**) The difference spectrum generated from the reduced minus oxidised spectra in **B**.*

To further explore this, succinate and glycerol-grown cultures were grown in bioreactors where the O_2 concentration could be controlled. Four bioreactors were set up to grow cultures of either glycerol and succinate with a set dissolved oxygen concentration of either 30 % or 40 %. Samples taken from both carbon sources in the exponential phase growth did not contain or generate the pigment in the chamber (Fig. 3.26 C & D). Alongside these

experiments, cultures with half the volume (0.5 L) were grown in the same flasks as previously. These also did not generate/contain the pigment (Fig. 3.26 A & B).

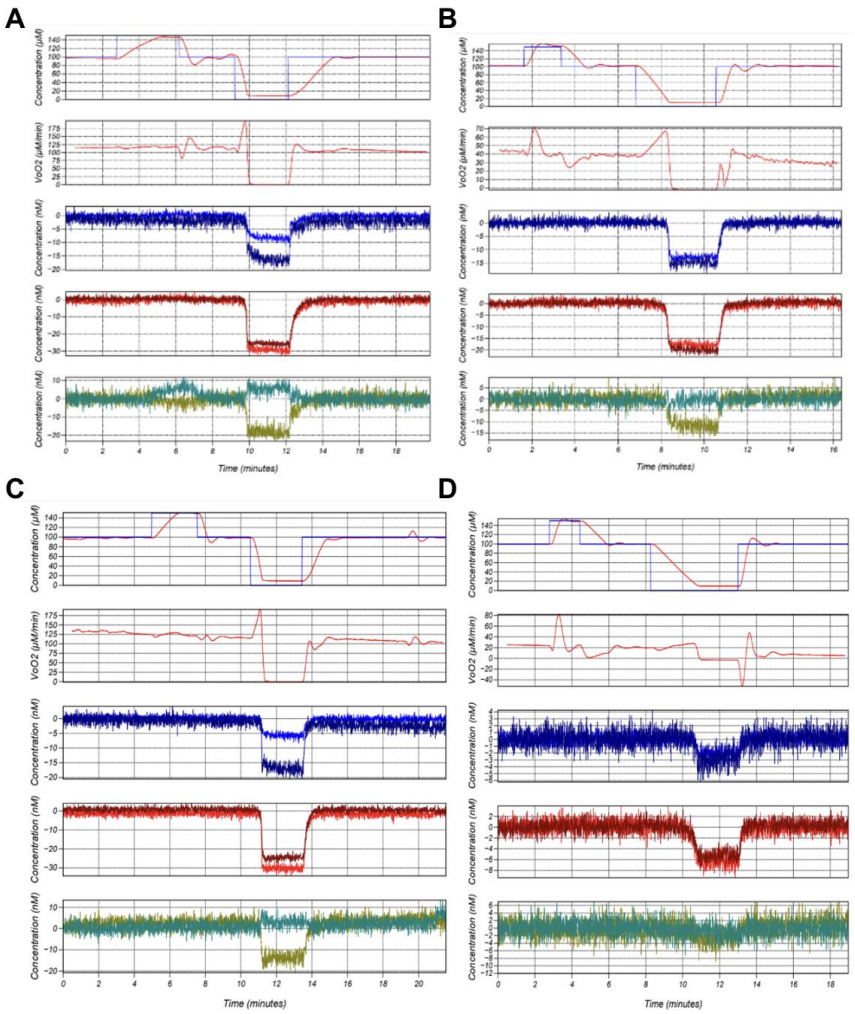

Figure 3.26 - Lack of coproporphyrin pigment interference in either 500 mL cultures or cultures grown in the bioreactors with both glycerol and succinate as the carbon source *(**A**) Experimental traces from the 500 mL glycerol culture showing a relatively stable haem trace, with a slight deviation at ~ 6 mins. The oxygen consumption slightly drops over the course of the run. OD_{600} ~1.4. (**B**) - Experimental traces from the 500 mL succinate culture. Again the oxygen consumption slightly drops over the course of the run. OD_{600} ~1.31. (**C**) Experimental traces for a sample from the glycerol bioreactor culture (30% dO_2, OD_{600} ~2). The oxygen consumption noticeably drops over the course of the run. (**D**) Experimental traces for a sample from the succinate bioreactor culture (30% dO_2, OD_{600} ~0.4). The oxygen consumption noticeably drops over the course of the run. None of the traces show evidence of the coproporphyrin and the associated drifting baseline.*

In these new conditions in both the 0.5 L flask and in the bioreactors the glycerol cultures reached their peak OD_{600} quicker (Fig. 3.27 A & B). This may further support the hypothesis that the original 1 L conditions were oxygen-limited. The comparison of the colour of the 0.5 L and 1 L cultures grown on succinate or glycerol showed a slight pinkness of the 1L glycerol cultures as compared to the other cultures. (Fig. 3.27 C).

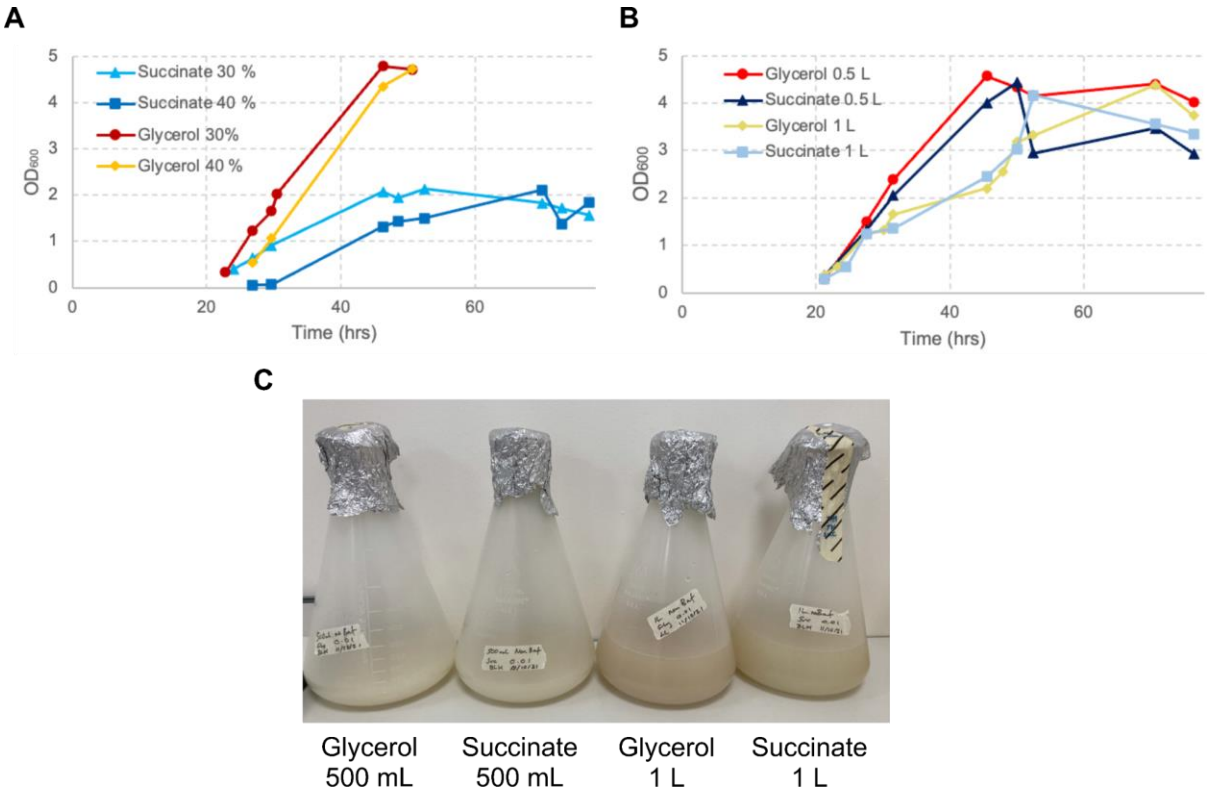

Figure 3.27 - Comparing growth rates for flasks and bioreactor conditions *(**A**) OD_{600} growth curves for flask conditions comparing culture volume (0.5 L vs 1 L) and primary carbon source (glycerol vs succinate). (**B**) OD_{600} growth curves for bioreactor experiments comparing set dissolved O_2 (30 vs. 40 %) and primary carbon source (glycerol and succinate). The succinate cultures appear to have stunted growth which coincides with an increase in the pH from ~7 to 9.5 (green trace in Fig 3.26 C & D). This stunted growth is not seen in the flask conditions with succinate. (**C**) An image of the 500 mL cultures compared to the 1 L cultures showing the difference in the colour of the cultures.*

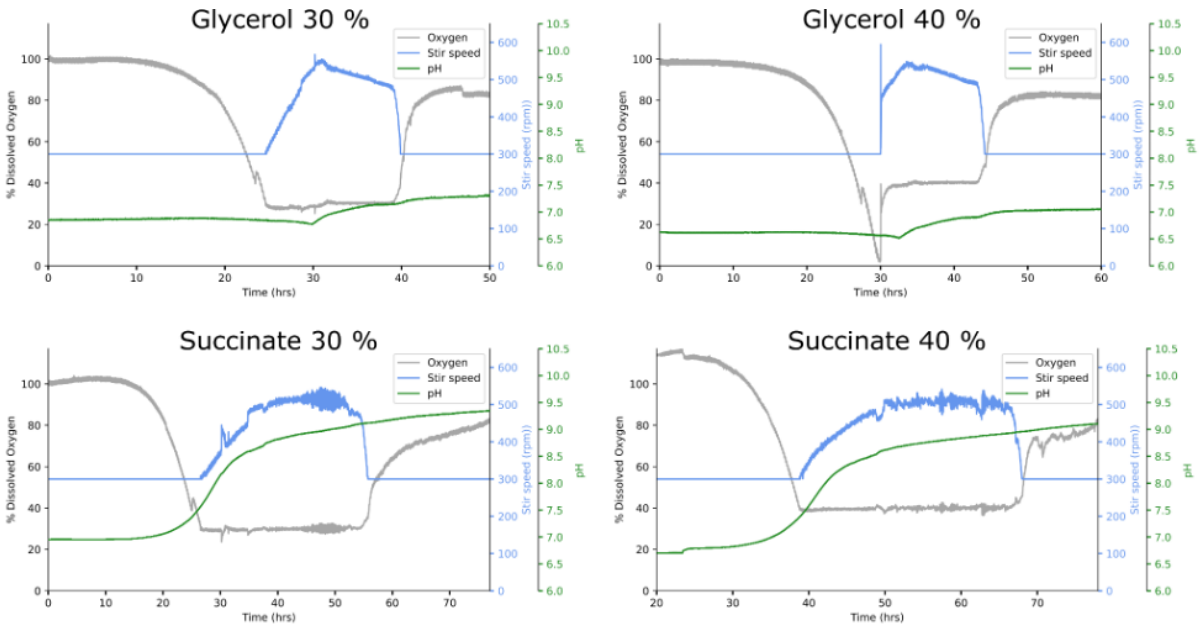

Figure 3.28 - Oxygen demand and pH of cultures grown in the bioreactor. *Plots of the monitored variable (dissolved oxygen, pH and stir speed) of the four bioreactors with two primary carbon sources (succinate or glycerol) and two set dissolved oxygen points (30 or 40 %) as indicated. The grey lines are the % dissolved oxygen (dO-$_2$) as measured by a Clark electrode of each culture. The green lines are the pH. Unlike the glycerol cultures, where pH only increases slightly, the succinate cultures show an increase from a pH ~7 to pH ~9. The blue lines are the stir speed (rpm). The control loop increases the stir speed to maintain the dO-$_2$ at the set point. The increase in the oxygen and decrease in the stir speed roughly corresponds to when the culture reached the maximum OD$_{600}$ (Fig. 3.26 B).*

Moving forward in order to avoid coproporphyrin pigment, the cells were grown in oxygen-replete conditions. As only 5 mL of culture is required for the chamber, going forward for experiments in the chamber, cells were cultured in 50 mL of media in 250 mL flasks. These conditions appear to be as oxygenated as the 500 mL cultures and are a more economical use of media. In subsequent experiments, I also observed that the culture colour change could be reduced by increasing the Iron content of the media (data not shown). Other members of the group working with attenuated *M.tb* have subsequently also observed the same coproporphyrin pigment in older cultures (personal communication with Suzy Harrison). This may be a result of the static growth conditions that *M. tb* is grown in.

3.3.2.4 Succinate cultures contain more *b* haem signal than glycerol cultures

The succinate 0.5 L flask also reached its peak OD$_{600}$ quicker than the original 1 L cultures. However, the succinate bioreactor cultures did not follow a similar pattern, appearing to show stunted growth with a max OD $_{600}$ of ~2 at 50 hrs (Fig. 3.28 B). The pH was monitored

throughout the run and increased from a pH of 7 to 9 (green trace in Fig. 3.27 C & D), which may offer some clue to the stunted growth. It is not clear why the stunted growth occurred in the bioreactors but not the culture flasks.

The difference in the oxygenation of the original culture conditions (1L) to the new culture conditions also altered the haem composition of the cells. In well-oxygenated conditions the glycerol cultures appeared to have less *b* haem signal than the succinate cultures (Fig. 29). This apparent loss in *b* haem signal in the glycerol cultures may be due to the lack of cyt *bd* now that the cultures are well oxygenated. The comparatively larger amount of *b* haem signal in the succinate cultures is likely due to an increased amount of sdh2. As the well-aerated glycerol conditions appeared to contain predominantly the cyt *bcc:aa*$_3$ supercomplex, it was decided to focus on this condition. This cytochrome content matches the current mammalian reference spectra the best and so should be the easiest to approximate.

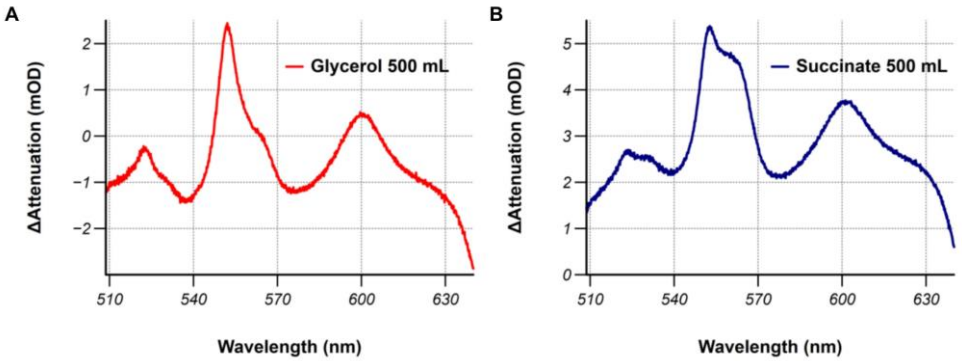

Figure 3.29 - Difference in the b haem signal of aerobic culture grown on glycerol or succinate - *Difference spectra from the 500 mL cultures **(A)** glycerol culture from Fig. 3.26A and **(B)** succinate culture from Fig. 3.26 B. The relative amount of b haem to c haem signal is higher in the succinate cultures than in the glycerol cultures. The amount of b haem signal in the glycerol cultures is less than previously seen in the 1 L oxygen-limited cultures.*

3.3.2.5 Adapting the mammalian reference spectral model for mycobacteria

As shown above, the un-altered mammalian/mitochondrial reference spectra performed reasonably well in deconvoluting the mycobacterial spectra, with the haem traces generally reducing as the chamber was taken anoxic. Figure 3.30 shows an example of the data output in Palencia including the haem traces and an example of the fit is shown for when the cells were reduced at 10 mins, at the point **I** indicated on the chamber [O_2] graph. From the residual of the fit, it also appeared that the reference spectra accounted for the total observed spectrum well. There did appear to be some mis-fitting occurring with the mammalian fit.

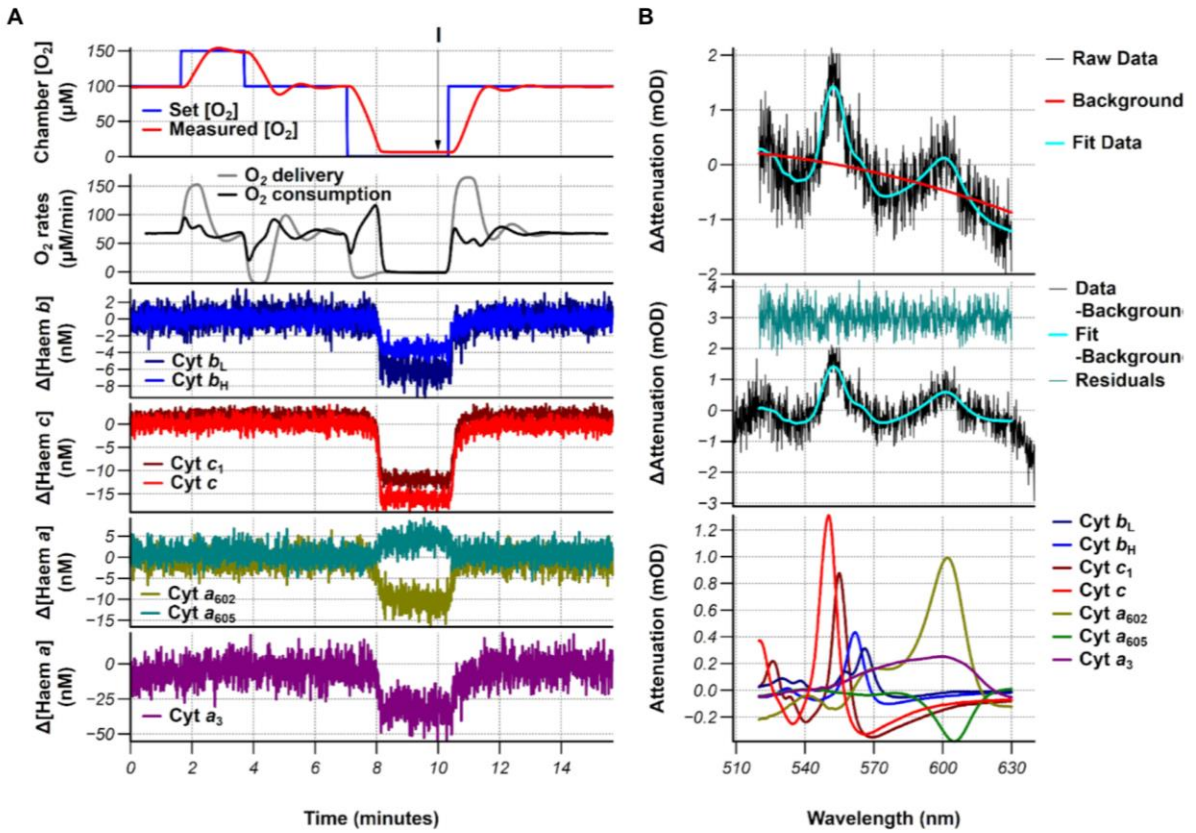

Figure 3.30 - Example of the original mammalian fit to aerobic glycerol grown wild type M. smeg *(**A**) The oxygen concentration, oxygen consumption rate and haem traces as the cells were taken through a 'top-hat' (**B**) An example of the quality of the fit at anoxic, as indicated by point I. The solution is not a bad match for the data but the signals for the a-haems are fitting in the opposite direction.*

The *a* haem not in the binuclear site of the oxidase is accounted for by two signals in the mammalian spectral fit. This relates to a blue shift that is observed in this haem signal as the ΔΨ is uncoupled with the peak centre shifting from 602 nm to 605 nm and has been observed in living cells and detergent solubilised oxidase (Kim et al., 2011; Rocha and Springett, 2018). The extent of this peak shift has been disputed by other groups, based on measurements made using an integrating sphere rather than a remission set-up (Covian et al., 2024). No matter the wavelength maxima of the two species, the presence of two signals for this haem causes mis-fitting in the mycobacterial spectrum. As can be seen from the fitting example shown, the two signals are fit in opposite directions causing a total peak at ~ 600 nm where it appears the mycobacterial haem A maxima is. Efforts to move two peaks to try and avoid this were unsuccessful. From studying the protonation site around the haem pocket in the mycobacterial cyt aa_3 oxidase there are sufficient differences that could explain this different behaviour between mycobacteria and mammalian *a* haem signals (personal communication with Roger Springett). The haem a_3 signal accounts for the haem A in the binuclear site of

the aa_3 oxidase. It has a much broader spectral signal than the other haem signal. Whilst in some experiments it would behave as expected, often it would account for changes in the background scatter rather than the haem centre, confusing the fit.

From this original mammalian fit, an adapted 'mycobacterial' fit was developed, using the aerobic glycerol conditions where it appeared that the cyt *bcc:aa*$_3$ was the dominant cytochrome component of the cells. All but one *a* haem signal was removed as this prevented the mis-fitting that occurred with multiple spectral signals. This *a* haem signal was centred at 600 nm reflecting the peak in the mycobacterial spectrum. The *c* haem signals were adjusted to reduce the residual around them. Two c_1 type signals better account for the observed spectrum, these were adjusted until they both had a similar concentration. These were assumed to account for the two different haem Cs present in the cyt *bcc:aa*$_3$ supercomplex. The *b* haem signals were left as they were with the assumption that the haems had similar spectral features in the mammalian and mycobacterial enzymes. The application of this adapted mammalian fit to *M. smeg* cells is shown in Figure 3.31. This fit was used for subsequent experiments and is referred to as spectral model 1 in Chapter 4.

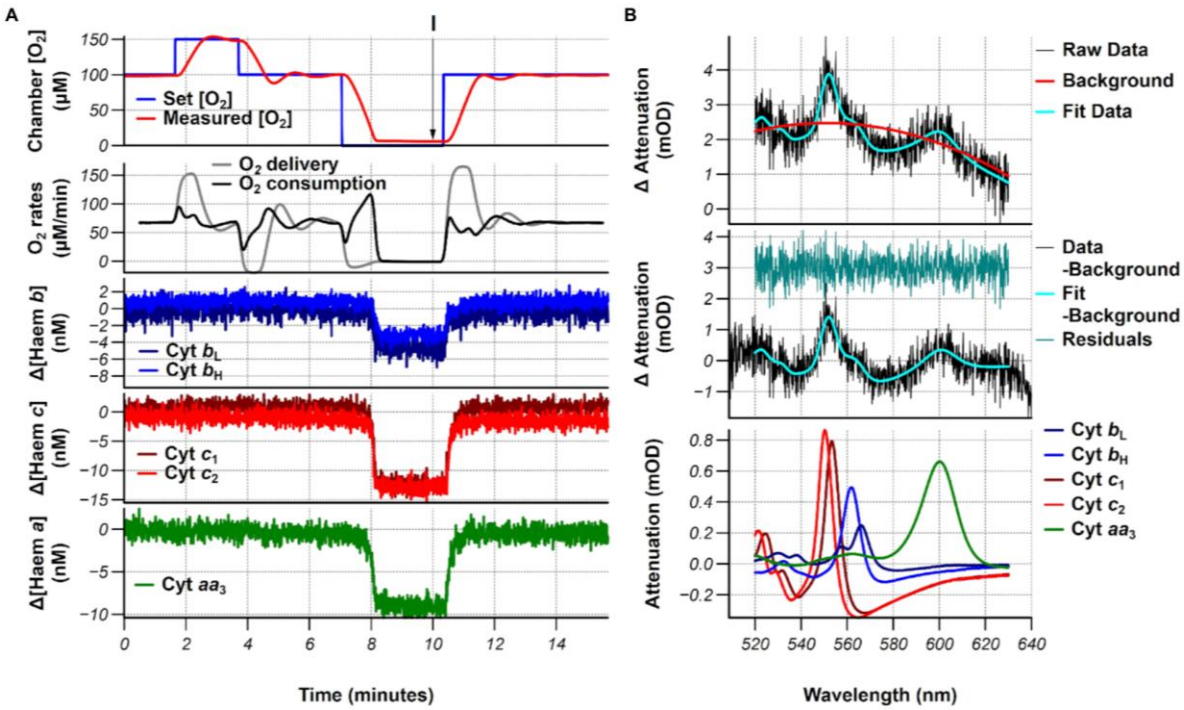

Figure 3.31 - Example of the adapted mammalian fit/spectral model 1 to aerobic glycerol grown wild type M. smeg *(**A**) The oxygen concentration, oxygen consumption rate and haem traces as the cells were taken through a 'top-hat' (**B**) An example of the quality of the fit under anoxic conditions, as indicated by point I.*

3.3.2.6 Removing spectral interference for the optode

The optode emission at ~650 nm significantly interferes with identifying the presence or absence of cyt *bd* in the cells due to the overlap with cyt *bd* spectral features. To remove its contribution Roger Springett designed a CCD collection-cycle to remove the optode contribution. The cycle is similar to how NAD(P)H fluorescence measurements had previously been made using the system. The cycle is split into two phases as shown in, Figure 3.32. In phase I, the LED is on and so a spectrum of the haem absorbances and optode emission is collected. In phase II the LED is switched off, this allows for the measurement of the optode emission alone. The subtraction of phase I by phase II then gives an absorbance spectrum with no interference from the optode.

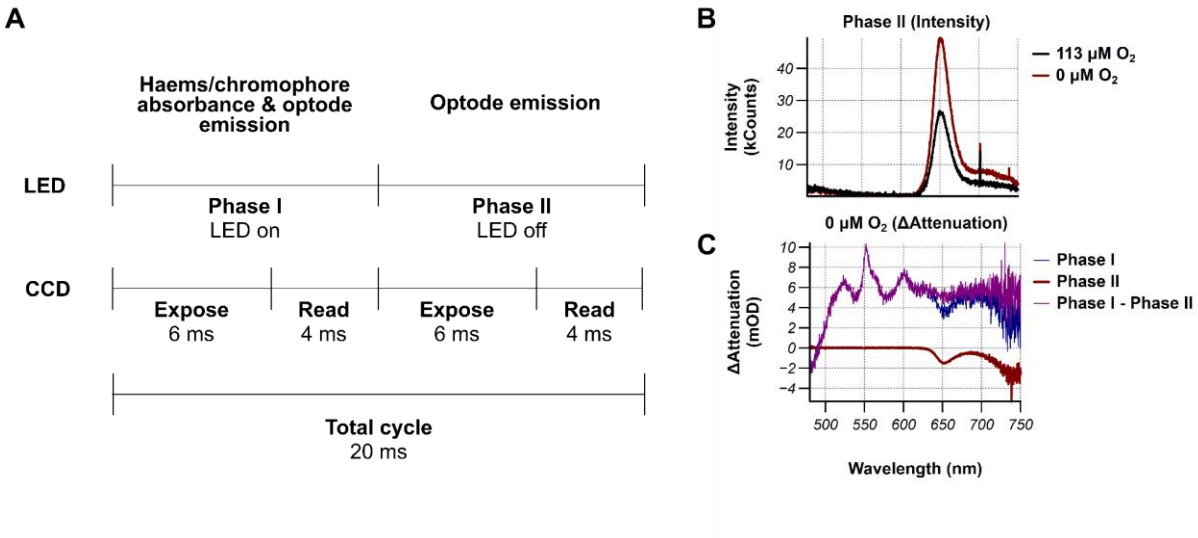

Figure 3.32 - Removing the contribution of the phosphorescence peak. *(**A**) The adjusted collection cycle for the CCDs. To remove the optode phosphorescence peaks, as shown in **B**, Phase II was subtracted from Phase I. (**C**) The impact of the phase subtraction on the collected spectrum, The trough at 650 nm is significantly reduced, and reflects the contribution from cyt bd in the phase subtracted spectrum.*

As can be seen in Figure 3.32 C, the subtraction of the phases removed the larger trough, making it possible to discern the presence of a small amount of cyt *bd*. As compared to the *a* haem signal from the cyt *bcc:aa*$_3$ supercomplex the *d* haem signal is a much lower intensity making it somewhat difficult to distinguish it from the noise. Figure 3.33 shows an example of a run and the contribution of the optode to the spectra. Because the spectra are fitted to the ∆attenuation, there is very little contribution of the optode when the oxygen concentration is similar to the starting point (T1). However, when the oxygen concentration is different than the starting point a trough at 650 nm can be seen (T2). In the narrower range that the mammalian cytochromes had previously been fitted to (510 - 640 nm), the optode does not

seem to alter the attenuation spectrum. The degree of contribution is only apparent in the wide spectrum (480- 750 nm), which has a greater overlap with the phosphorescence peak.

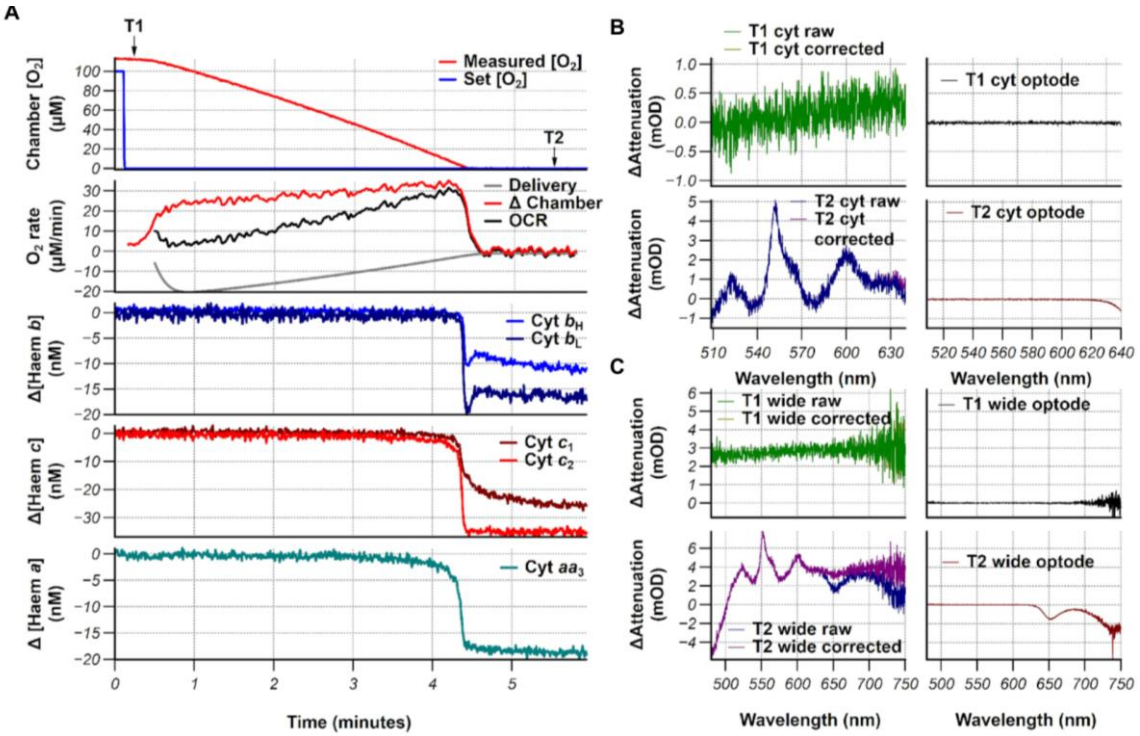

Figure 3.33 - The contribution of the phosphorescence peak to the two different ranges of wavelength collected. *(**A**) The experimental traces as cells were taken from 100 μM O_2 to anoxic. Two time points are indicated, T1 - aerobic, and T2 - anaerobic (**B**) The impact of the phosphorescent peak in the narrow spectrum is minimal with a slight contribution at the longer wavelengths. (**C**) The impact of the phosphorescent peak in the wide spectrum, minimal, large trough at around 650 nm. The greatest difference in the phosphorescence peak is seen at the most different oxygen concentration to the starting point, (T2 in this case).*

3.3.3 Examining membranes to further understand the mycobacterial cytochromes

Now that properly oxygenated growth conditions have been obtained, I returned to membranes as an easier experimental system for understanding what is present in the ETC and validating the choice of spectral model. The bioenergetic chamber can also be used for measuring the oxygen consumption and haem spectra of membrane vesicles. Membrane vesicles and mitochondria have been a classic experimental system for bioenergetic studies. Their benefits of less cellular complexity and less stringent oxygenation requirements make performing well-controlled experiments easier. It is also easier to increase the concentration

of the chromatophores in the sample, increasing the signal-to-noise ratio. Whilst not non-invasive, given that the cells have to be broken to obtain the material, membrane vesicles are informative for spectral measurements of the cell. Membranes were isolated from cells grown under the oxygenated conditions to the early exponential phase, OD_{600} ~1. The aim was to develop these membranes as a system for examining mycobacterial OxPhos and help validate the choice of spectral model.

Inverted membrane vesicles (IMVs) can form during cell lysis and have an inverted membrane orientation (Fig. 3.34B) compared to intact cells or right-side-out vesicles (Fig. 3.34A). Cell lysis will produce a mixture of both vesicle types however previous work with IMVs or equivalent particles in other species has demonstrated that the method of lysis can impact the properties of the vesicles produced. Several procedures have been published for generating mycobacterial IMVs (Dunn et al., 2014; Koul et al., 2007). These protocols informed the development of my membrane preparation protocol. What was now required was a way to characterise the properties of these membranes.

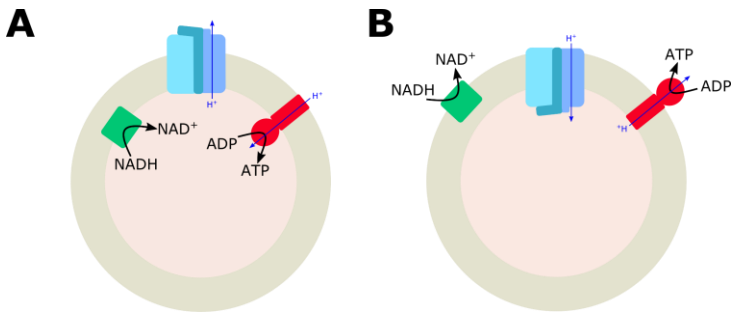

Figure 3.34 – Membrane vesicles *(**A**) Right-side out vesicle – Membrane proteins are orientated as in intact cells with the normally periplasmic side facing the bulk solvent and the cytoplasmic active sites (NADH oxidation, ATP synthesis) facing the interior of the vesicle (**B**) Inverted vesicle – Inverted in reference to intact cells with the normally cytoplasmic side facing the bulk solvent and periplasmic side facing the interior of the vesicle. Ndh2 in green, cyt bcc:aa$_3$ supercomplex in blue/purple and ATP synthase in red. The direction of proton movement by complexes is shown with blue arrows.*

For different experimental studies with IMVs different catalytic properties are important and should be considered when preparing the vesicles. The respiratory control ratio (RCR) is a measure of how coupled the catalytic rate of the chain is to the Δp, an imperfect measure of how 'leaky' the vesicles are. This can be measured by comparing the catalytic rate with and without the Δp present, achieved using uncouplers. The fraction inverted is a ratio of the two vesicle orientations. This can be made by comparing the catalytic rate of uncoupled vesicles to those where reductants have access to the intravesical active sites. This can be achieved

using pore-forming molecules such as alamethicin. Right-side-out vesicles have the potential to have complicating scatter and buffer effects in optical spectroscopy, whilst 'in theory' being catalytically silent.

3.3.3.1 Determining RCR and fraction inverted in isolated glycerol-grown mycobacterial membranes

The rate of NADH oxidation is one way to assess the catalytic activity of a membrane preparation. As NADH has a significant absorbance at 340 nm which is not present in NAD+, its oxidation can be easily monitored spectroscopically. For measuring the RCR, gramicidin can be used to collapse the Δp. Gramicidin is a channel-forming ionophore with poor selectivity between protons, monovalent cations and NH_4^+ (Nicholls and Ferguson, 2013). However, gramicidin also has inhibitory effects at higher concentrations potentially before the system has been fully uncoupled. Therefore, the optimum concentrations of gramicidin needed to be determined for this assay.

Figure 3.35 A shows the NADH oxidation rate at a range of gramicidin concentrations with membranes isolated from aerobic glycerol-grown cultures. Of the tested concentrations the greatest rate was seen at 1 µg ml-1 of gramicidin, which when compared to the rate with no gramicidin equated to an RCR of 1.10 and so not a particularly coupled preparation. However, given the limited concentrations tested it is difficult to determine if the gramicidin concentration was at the optional point for uncoupling the vesicles.

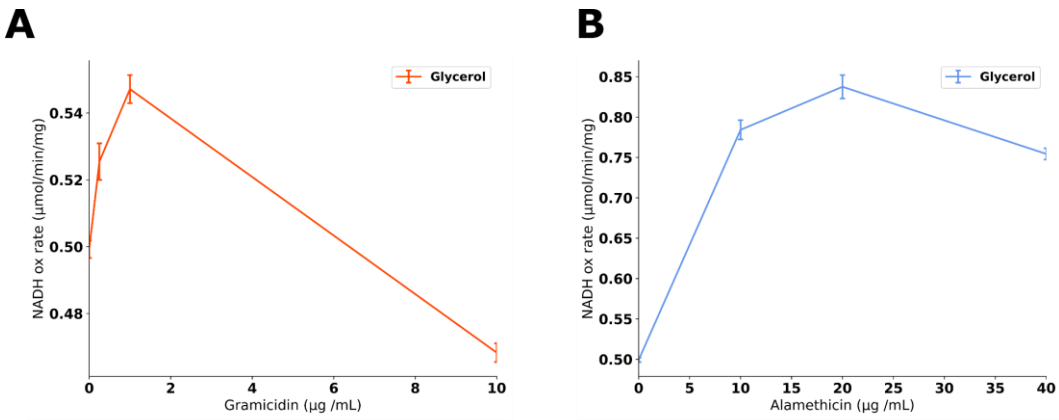

Figure 3.35 - NADH oxidation rates at a range of concentrations of pore-forming molecules (**A**) Gramicidin (**B**) Alamethicin

To assess the fraction of the membrane vesicles that were inverted alamethicin, an antibiotic that forms pores in membranes larger enough for NADH (Gostimskaya et al., 2003), was used to access the active site in the interior of vesicles. This was performed at a range of alamethicin concentrations to determine the maximal increase in the rate (Figure 3.35 B).

Based on the max NADH oxidation rate with gramicidin and max alamethicin rate the vesicles are 65.3 % inverted (Table 3.3). This value has some caution given the uncertainty over gramicidin's effectiveness at uncoupling these vesicles. The fact that a reasonable NADH oxidation rate can be measured at least suggests that this preparation is active, if not particularly coupled. This provides a membrane preparation for further spectroscopic investigation.

Table 3.3 - NADH oxidation rates used to calculate the RCR and % inverted for mc²155 (wild type) grown on glycerol *The NADH oxidation rate has been calculated as µmol of NADH oxidised per minute per mg of protein in the membranes, as determined by a BCA assay.*

Strain	Average NADH oxidation rate (μmol min^{-1} mg^{-1})			RCR	% inverted
	Nothing	Gramicidin	Alamethicin		
mc^{2}155 (Wild type)	0.499 ± 0.003	0.547 ± 0.005	0.837 ± 0.021	1.10 ± 0.011	65.3 ± 2.63

3.3.3.2 Wild-type membrane preparation gives a greater haem reduction in response to NADH than succinate

NADH and succinate are two key reductants of the respiratory chain via NADH dehydrogenase and succinate dehydrogenase respectively. As discussed above, in *M. smeg* Sdh2, which contains two b-type haems, is near essential (Pecsi et al., 2014). Hypothesising that it then is likely present in the membrane, the question is whether this is at a high enough concentration to contribute to the overall spectrum considerably. Therefore it was reasoned that the extent of Sdh2 *b*-haems contribution to the overall spectrum would be apparent by comparing the response of the membranes to succinate and to NADH. What must be considered is the difference in the redox potential of the succinate/fumarate couple as compared to the NADH/NAD$^+$ couple. Retrospectively it would be better to perform these experiments anaerobically to reduce the effect of the difference in their redox potentials. It would have allowed for the 'maximal' reduction of the chain with the different reductants without a 'hole in the bottom of the bucket' - electrons leaving the chain via the oxidases.

This was initially performed with membranes isolated from aerobically grown glycerol cultures, placed in the bioenergetic chamber. Membranes, like cells, can have a high background scatter that can sometimes interfere with interpreting spectral measurements. Using the chamber helped to reduce the contribution of the scatter and allow the control of the oxygenation of the membranes. In response to succinate, a slight reduction of the chain

was seen (Figure 3.26 A & B) and no noticeable change in the oxygen consumption rate. The haem reduction appeared to be made up of signals from *c*, *b* and *a* haems but the noise made this difficult to distinguish. The haem reduction was increased with a 10x addition of succinate, with the haem peaks more distinguishable. However, when NADH was added a much greater reduction of the chain was seen and a noticeable increase in the oxygen consumption rate. Both reductants only partially reduced the available haems, as demonstrated in comparison to the anoxic-oxidised spectrum. The order of the reductant was then changed with NADH added first and then succinate. Minimal haem reduction was seen upon the addition of succinate if NADH had already been used to reduce the membranes (Figure 3.37). In both these responses there did not appear to be extra *b* haem signal reduction upon succinate reduction as compared to NADH, suggesting Sdh2 is not at a sufficient concentration in these cultures to significantly contribute to the overall spectra changes.

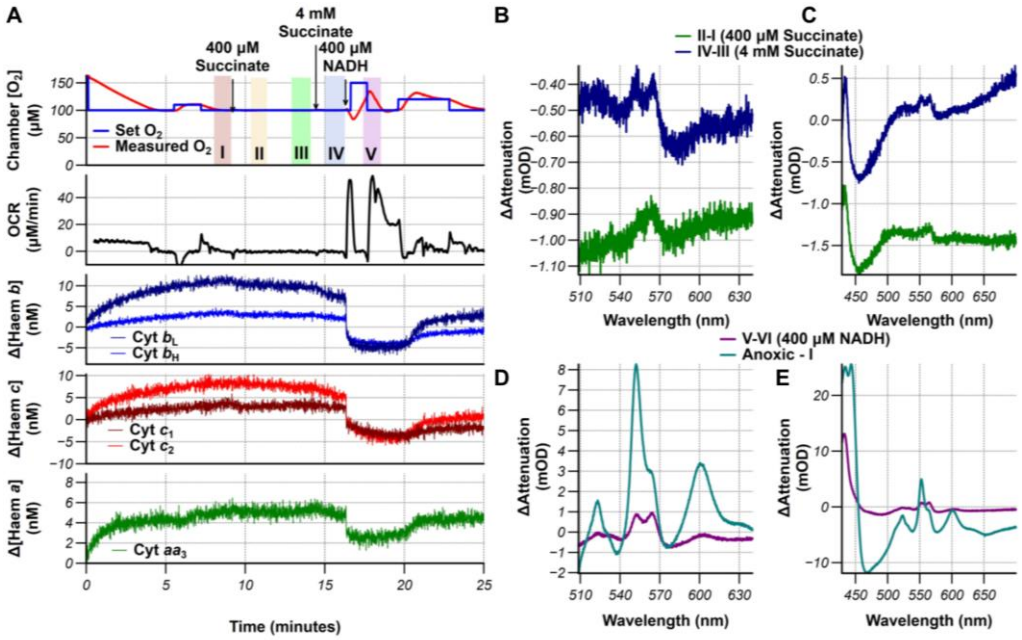

Figure 3.36 - Oxygen consumption and oxidation state of b-haems in response to succinate and then NADH. *Membranes isolated from aerobically glycerol-grown cultures at OD_{600} of ~1. (**A**) The oxygen consumption (2nd panel) and change in haem electron occupancy (bottom 3 panels) upon the addition of NADH and then succinate. This was performed under aerobic conditions, as shown by the top panel (**B** & **C**) Changes in the spectra after the addition of succinate (400 µM (II-I) in green and 4 mM (IV-III) in dark blue) (**D** & **E**) Changes in the spectra after the addition of NADH (teal (V-IV)). The difference spectrum of the membrane under anoxic condition minus the most oxidised potion in the run*

(I) The time periods that the spectra were averaged from are shown by the shaded section in the top panel of A

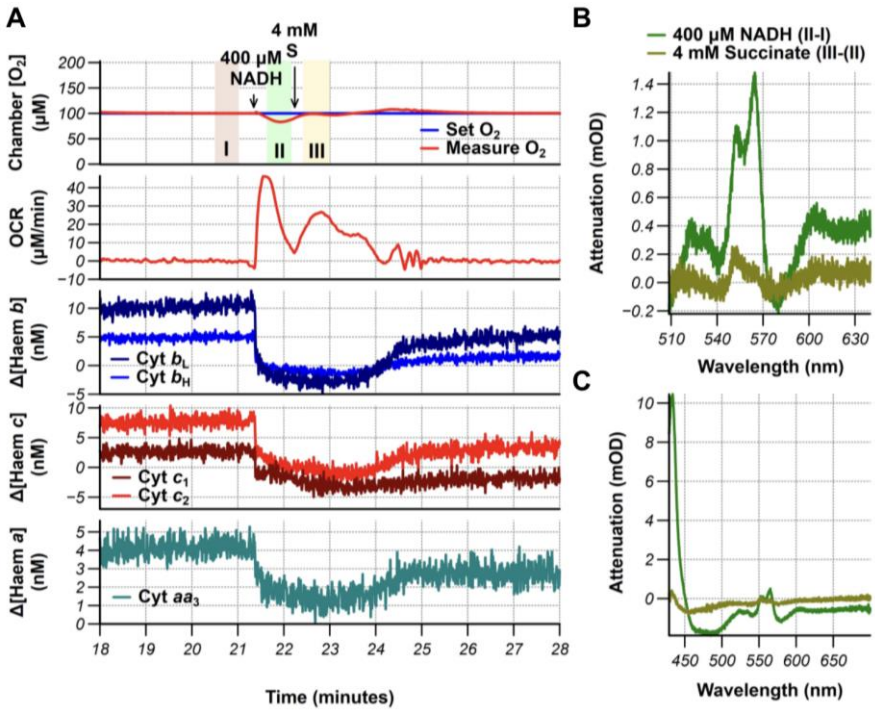

Figure 3.37 - Oxygen consumption and oxidation state of b-haems in wild-type M. smeg membranes in response to NADH and then succinate *Membranes isolated from aerobically glycerol-grown cultures at OD_{600} of ~1. (**A**) The oxygen consumption (2nd panel) and change in haem electron occupancy (bottom 3 panels) upon the addition of NADH and then succinate. This was performed at 100 µM [O_2] (**B** & **C**) Changes in the spectra after the addition of NADH (green) and succinate (gold). The time periods that the spectra were averaged from are shown by the shaded section in the top panel of A*

Membranes from aerobically grown succinate cultures were then examined (Fig 3.38). Again a greater response to NADH was observed but this time the response to succinate was predominantly a *b* haem signal rather than a mixture of haems. This suggests that there is a higher concentration of Sdh2 in these membranes that significantly contributes to the total haem spectrum of mycobacteria.

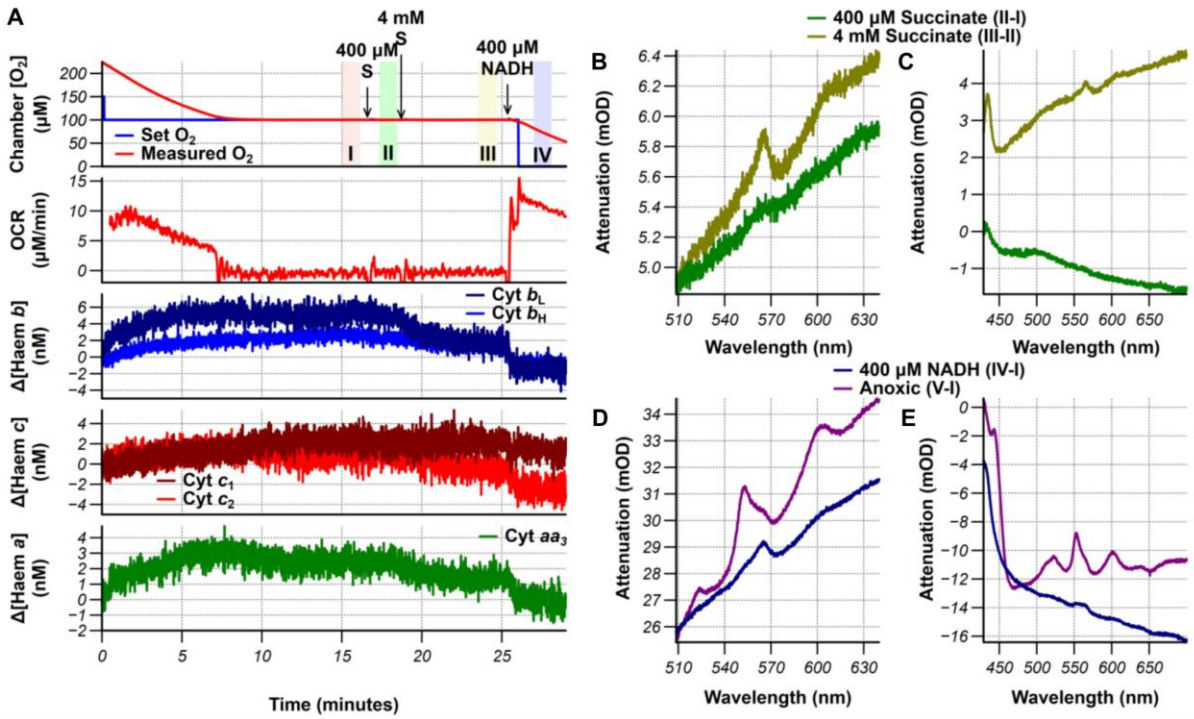

Figure 3.38 - Oxygen consumption and oxidation state of b-haem in wild-type M. smeg membranes in response to succinate and then NADH *Membranes isolated from succinate-grown cultures at OD_{600} of ~1. (**A**)The oxygen consumption (2nd panel) and change in haem electron occupancy (bottom 3 panels) upon the addition of NADH and then succinate. This was performed at 100 µM [O_2]. (**B** & **C**) Changes in the spectra after the addition of succinate (400 µM - green, 4 mM - gold). (**D** & **E**) Changes in the spectra after the addition of NADH (blue) and when the membranes were taken anoxic. The time periods that the spectra were averaged from are shown by the shaded section in the top panel of A.*

3.3.3.3 Characterising *Δ*cydAB membranes preparation

To simplify the possible cytochrome present in the chain, it was then explored if knockout strains could be used to simplify the complement of cytochromes present in the cells. The cyt *bcc:aa*$_3$ supercomplex appears to be the dominant cytochrome in the membrane and growth is severely hampered without it (Matsoso et al., 2005). Focusing on the cyt *bcc:aa*$_3$ would also allow for the measurement of ΔΨ from the redox poise of the cyt *bcc b*-haems (Kim et al., 2012). One way to reduce contamination of non-cyt *bcc:aa*$_3$ components (Sdh2 and cyt *bd*) would be to use a strain where these additional cytochromes have been genetically knocked out.

A Δsdh2 strain has been produced by Chen-Yi Cheung in Greg Cook's group (personal communication with Chen-Yi Cheung) and is examined in Chapter 5. However, this strain has a slower growth phenotype and so seems to be very attenuated. It is therefore not an

ideal candidate for routine use in the chamber as it would be difficult to determine what relates to the genetic background and what was the effect of the manipulation of the strain. In contrast, a strain with the cyt *bd* knockout Δ*cydAB* has a near-normal growth phenotype and so may be suitable for routine chamber use. This strain is a markerless knockout of the *cydAB* operon MSMEG 3233-3232 (Lu et al., 2019), which encodes the dominant cyt *bd* quinol oxidase in *M. smeg*. There is an additional cyt *bd* oxidase operon in the *M. smeg* genome, encoded for by the *appCB* operon (MSMEG 5605-5606), but it is unclear what role this *bd* oxidase plays in mycobacteria. This *appCB* operon is not present in the *M. tb* genome.

Figure 3.39 compares the difference spectrum of wild type and Δ*cydAB* and shows a reduced *d*-haem signal in the Δ*cydAB* membranes. On examination of these ΔcydAB membranes no evidence of the Sdh2 b-type haems could be seen as the spectral response to both succinate and NADH looked like cyt *bcc:aa*$_3$ spectrum (Fig 3.40)..

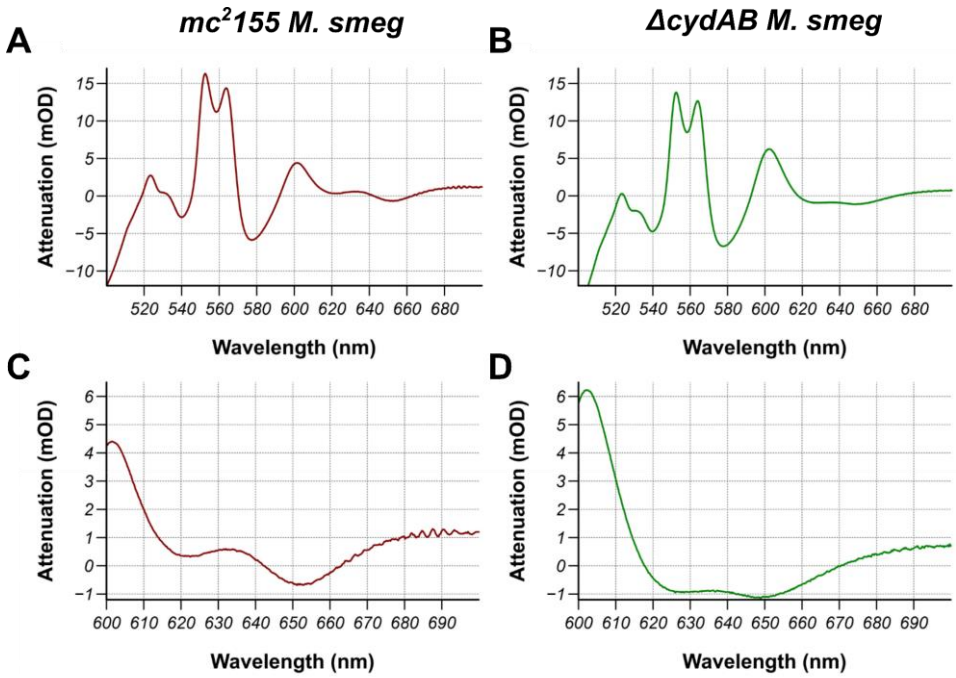

Figure 3.39 - Difference spectra of wild-type and ΔcydAB membranes. *(**A** & **C)** The difference spectrum of wild-type membranes, with a focus on the haem D spectral region (**C**). (**B** & **D)** The difference spectrum of ΔcydAB membranes, with a focus on the haem D spectral region, demonstrates a less prominent d haem peak (**D**). This figure is part of a figure that was prepared for a paper with the help of Dr Morwan Osman.*

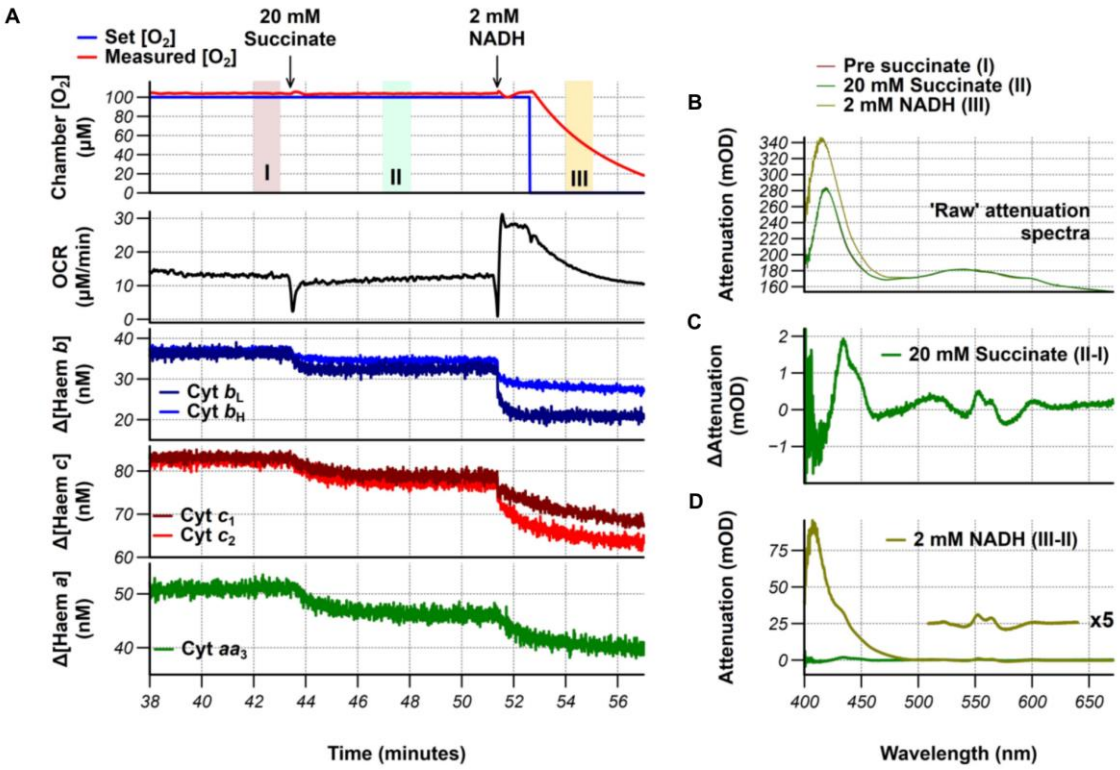

Figure 3.40 - Spectral examination of ΔcydAB membranes reduced with Succinate and NADH *(**A**) The oxygen concentration during the experiment (top panel) and the oxygen consumption (2nd panel) and change in haem electron occupancy (bottom 3 panels) upon the addition of NADH and then succinate. (**B**) The 'raw' attenuation spectra at the indicated points in the experiment by the shaded areas in the oxygen concentration graph. (**C**) The difference spectra upon reduction with succinate (**D**) The difference spectrum upon reduction with NADH, the haem region is highlighted (x5).*

3.3.3.4 Native PAGE and in-gel activity assays of mycobacterial membranes

Native gel polyacrylamide electrophoresis (native - PAGE) has been a historical method for separating and analysing large membrane complexes and their oligomeric states. In blue native PAGE (BN-PAGE), the anionic Coomassie dye is added to the cathode buffer. The binding of the Coomassie to the protein complexes gives them a negative charge that allows them to migrate to the anode. A gradient polyacrylamide gel then facilitates the complexes to separate approximately based on size. In-gel assays are one way to determine the nature of the bands on the gel. This has somewhat been superseded by mass spectrometry however it is still a quick and relatively inexpensive way to highlight bands of interest. The basis of these in-gel assays is to incubate the gel with the substrate of a specific complex and a colourific redox dye. The complex reacts with the substrate reducing the redox dye causing it to change colour. For example, NADH dehydrogenase activity can be assayed by NADH

and Nitro blue tetrazolium (NBT), the NBT changes from yellow to a blue precipitate as it is reduced. (Figure 3.41 Aii). Succinate dehydrogenase can be stained for using a similar assay where NADH is substituted by succinate, Figure 3.41 Aiii).

The Coomassie dye in BN-PAGE can interfere with the binding of the redox dye or the observation of this specific change in colour. For this reason, Wittig et al. developed high-resolution clear native gels, hrCN-PAGE (Wittig et al., 2007). In hrCN-PAGE the Coomassie is replaced by the anionic detergent, sodium deoxycholate and the non-ionic detergent DDM. This facilitates the migration of the protein complex through the polyacrylamide gels in a similar pattern to BN-PAGE. This is not always true, particularly for proteins with a pI higher than 5.5. The advantage is that the hrCN gel is then compatible with other in-gel assays, such as the staining for cyt *bc* and oxidases. For example, both complexes can be assayed for by the oxidation of 3,3'-diaminobenzidine (DAB) which forms a brown precipitate (Figure 3.41 Aiv).

Figure 3.41 A & B shows a hrCN-PAGE gel of mc^2155 and ∆*cydAB M. smeg* membranes that have then been stained for NADH dehydrogenase activity, succinate dehydrogenase activity, and stained with DAB. Both membranes had very similar staining patterns for all of the stains. A prominent band ran at ~750 kDa in both samples and is consistent with the cyt *bcc:aa*$_3$ supercomplex. This band and another band running at a higher molecular weight (~1000 kDa) were stained by DAB. In the Coomassie-stained gel, this corresponds to a double band. Subsequent mass spectrometry (MS) analysis of equivalent BN-PAGE bands found that the ~750 kDa band contained all the subunits of cyt *bcc:aa*$_3$. Figure 3.41 D shows the distribution of qcrA in the bands as a representation of the location of the cyt *bcc:aa*$_3$ subunits. Interestingly the higher bands contained EtfD. This was originally annotated as an iron-sulphur cluster-binding protein (MSMEG 0690) and so it was not obvious until it was brought to my attention by Dr Morwan Osman, that this is a putative cytochrome and so may also be contributing to the spectra.

For the succinate dehydrogenase assay, the mediator PMS is also added (Zerbetto et al., 1997). However, when I used PMS it resulted in quite significant staining of the gel. This is likely due to non-specific staining potentially of other dehydrogenase present in the membrane. On subsequent MS analysis, a band in this region did contain all the subunits of Sdh2 apart from SdhF, a small single TMH subunit. In all the MS results for the bands, there were several hits for other respiratory proteins including glycerol-3-phosphate dehydrogenase, malate:quinol oxidoreductase, type-II NADH dehydrogenase, and ATP synthase. Overloading of the gel and general smearing in the lanes is likely responsible for this poor separation of these smaller complexes on the gel. The NADH dehydrogenase

activity staining showed a smear at ~250 kDa and a band at ~200 kDa. It was difficult to determine the corresponding band in the Coomassie-stained gel.

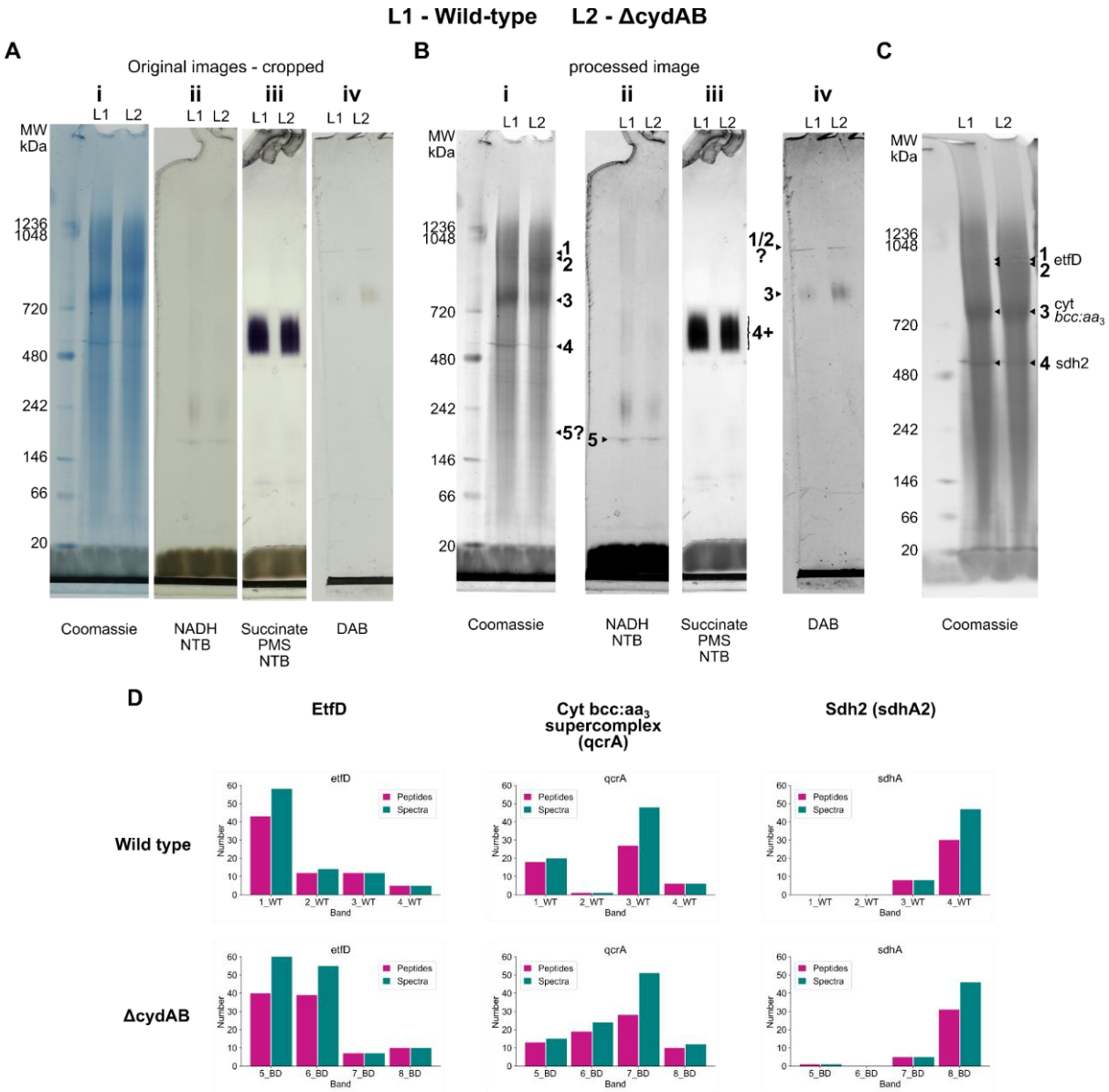

Figure 3.41- In-gel activity staining of hrCN-PAGE and results from Mass spectrometry of excised bands *(**A**) Original colour images of the hr-CN-PAGE stained with Coomassie (i) for NADH dehydrogenase activity (ii) succinate dehydrogenase activity (iii) and with 3,3 - diaminobenzidine. (**B**) processed images of the same gel slices to improve the contrast. (**C**) Equivalent hr-CN PAGE slice to A(i) that bands were excised from for mass spectrometry. (**D**) Plots of the number of peptides and spectra in each band for the two strains (Wild type/ mc²155 M. smeg and ΔcydAB). QcrA and sdhA2 were used to represent the distribution of the cyt bcc:aa₃ supercomplex and Sdh2 respectively. Graphs produced using a Python script initially developed by Dr. Morwan Osman*

3.3.4 Inhibiting the chain to fully transform the haem signals

The prior work in this chapter established that the cyt *bcc:aa*$_3$ supercomplex is the dominant contributor to the overall haem spectrum in aerobic conditions with glycerol as the carbon source. It also demonstrated that the adapted mammalian spectral model behaves reasonably well and is sensible given the response of the membranes to succinate and NADH. The focus could now be returned to measurements on intact cells. To advance the analysis of the haem spectra collected in the chamber a way to quantify the signals was required.

By the nature of the spectroscopy approach, there is no fixed path length of the light that is backscattered off the culture and detected by the CCD. However, if the signals are fully transformed from their reduced state to their oxidised state, the oxidation state of the haem centres during the run can be determined. The quantification/determination of the oxidation states allows the measurement of key bioenergetic parameters like the $\Delta\Psi$ (Kim et al., 2012). This measurement is based upon the redox poise of the *b*-haems in the cyt *bc*$_1$ complex, offering an intrinsic non-invasive measurement of $\Delta\Psi$, as covered in Chapter 4. Therefore, the aim of this next section was to establish conditions to achieve these fully oxidised and fully reduced states with the overarching aim of using these conditions to measure $\Delta\Psi$ in intact mycobacteria.

Previously to fully transform the signals from the oxidised to the reduced state in mammalian cells required the use of anoxia (reduced conditions) and inhibitors of complex I, rotenone, and complex II, 3-nitropropionic acid (Kim et al., 2012). This collection of conditions will not necessarily be suitable for fully transforming the signals in mycobacteria. For example, the mycobacterial homologue of mammalian complex I is not highly expressed under oxygen-replete conditions in the mycobacterial chain, instead the type II non-pumping NADH dehydrogenase, Ndh2, is highly expressed. Rotenone does not inhibit Ndh2. However, compounds that are part of the phenothiazine class of molecules are thought to inhibit Ndh2 (Weinstein et al., 2005). Figure 3.42 shows some of the complexes that make up *M. smeg*'s OxPhos system. Compounds that have been demonstrated to inhibit the individual complexes, or that have been demonstrated to inhibit homologous complexes in other species are indicated.

The next section of work aimed to explore combinations of inhibitors that might achieve the full transformation of the signals in mycobacteria. These experiments were performed with another PhD student in the group, Suzy Harrison, who is also working on studying mycobacterial bioenergetics. Together we explored the effects of classical uncouplers and

various metabolic effectors that are thought to inhibit different components of the mycobacterial respiratory chain to try and achieve the oxidised spectrum and to explore their effects on mycobacteria, both the electron occupancy of their haems and their oxygen consumption rate. This work also illustrates the utility of the bioenergetic chamber for examining the mechanism of action of compounds. The chamber could be a powerful tool in aiding anti-TB agent drug discovery, helping to clarify the mechanism of action in the intact cell. Suzy has subsequently expanded on this work to clarify the mechanism of action of bedaquiline in intact live cells and has shown that the cyt *bd* acts as a relief valve to prevent hyperpolarisation (draft publication in progress).

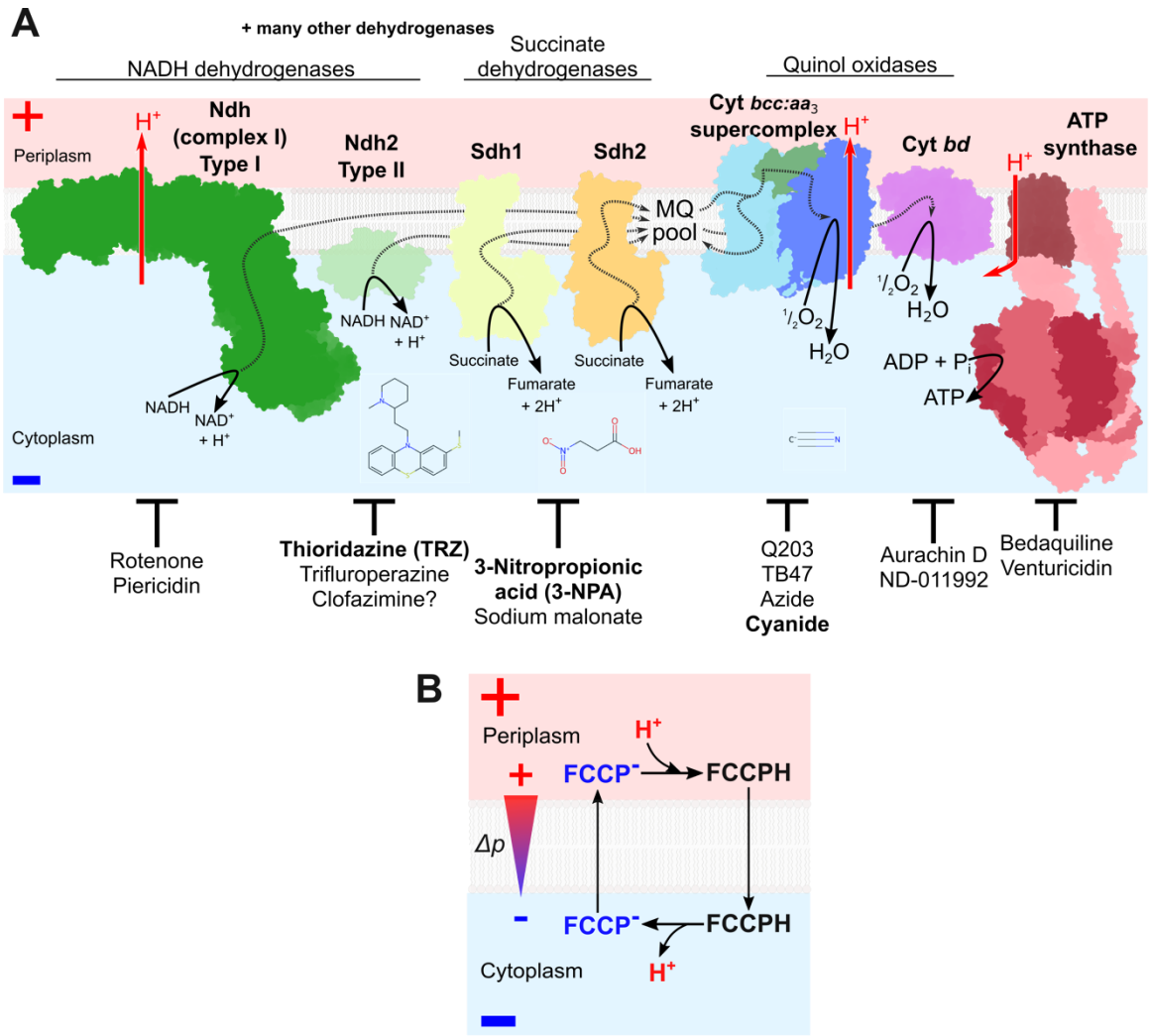

Figure 3.42 – Effectors of components of the mycobacterial oxidative phosphorylation system. *(**A**) Inhibitors of the chain. The compounds explored in this thesis are in bold and the chemical structures of the molecules are shown. The protein complex structures are as previously shown in this thesis. (**B**) Protonophore cycling by uncouplers, FCCP in this example.*

3.3.4.1 The effect of uncouplers and the need to wash the detergent off the cells

We first began by exploring the effect of the classical uncouplers, CCCP and FCCP. These are protonophores that will dissipate the Δp by transporting protons across the membrane. This occurs as these molecules can permeate the membrane both in the protonated form and the anionic form. This is because both CCCP and FCCP have an extensive π-orbital system that allows the delocalisation of the charge when the protonophore is in the anionic form. This means that the molecule remains lipophilic and therefore can cross the membrane. Faced with a Δp, the protonophores will shuttle protons across the membrane dissipating the Δp and uncoupling ATP synthesis from the function of the electron transport chain.

For a well-coupled chain, the addition of an uncoupler should lead to an increase in the oxygen consumption rate as the back pressure experienced by the ETC (the Δp slowing the action of proton pumping complexes) is released, increasing the flux through the ETC. It should also lead to the oxidation of the *b*-haems. This is for two reasons. Firstly, as the flux through the ETC increases, the pools of the reducing equivalents and subsequently the quinone pool will oxidise. This will mean that the ambient redox potential experienced by the *b*-haems will become more positive leading to the oxidation of the *b*-haems. Secondly, as described in more detail in Chapter 4, the presence of $\Delta\Psi$ will make the reduction of b_L more favourable than indicated by its mid-point potential. This is due to its position within the membrane and the operation of the cyt *bc* complex. Any decrease in the $\Delta\Psi$ will decrease the favourability of reducing b_L.

We initially observed the effect of adding µM amounts of CCCP to *M. smeg* (Fig 3.43). Only small changes in the oxidation state of the *b*-haems were seen. This oxidation occurs because of the location of the *b*-haems in the membrane and the influence of the redox state of the quinone pool. As described in more detail in Chapter 4, the presence of a $\Delta\Psi$ makes the reduction of b_L more favourable and therefore the dissipation of the Δp, including the $\Delta\Psi$, will lead to the oxidation of b_L. Given the relatively high concentration and unexpectedly small response, we considered if there were factors that may be reducing the concentration of CCCP that was able to penetrate the *M. smeg* cells.

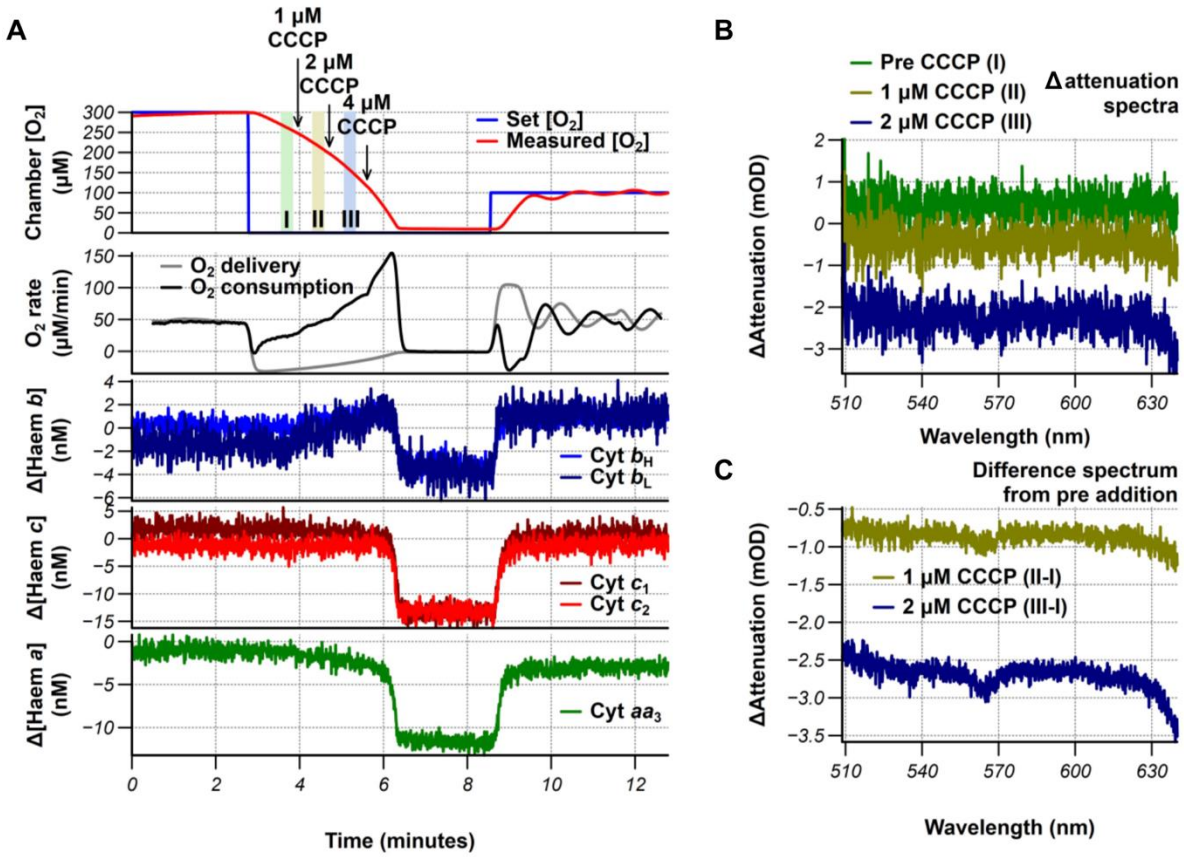

Figure 3.43 - The response of M. smeg grown in 0.05% Tween 80 to CCCP. *(**A**) Oxygen and haem response upon the addition of CCCP (**B**) The Δ attenuation spectra at the indicated points (The system did not have the correct intensity calibration use the raw attenuation spectra) (**C**) The difference spectra upon CCCP addition, showing minor oxidation of the b-haems.*

M. smeg and other mycobacterial species are prone to clumping. To avoid this, the standard growth media includes detergents such as Tween 80 or Tyloxapol to reduce clumping and allow the cultures to reach a much higher density. For our cells, this was 0.05% Tween. We wondered if the lipophilic CCCP was instead partitioning into the Tween rather than penetrating the cells. To examine this we grew *M. smeg* in 0.01% Tween 80 and examined the response of this culture to the same concentrations of CCCP (Fig 3.44). At the same CCCP concentration, a much greater response was seen. In this response the *b*-haems oxidised again but the *c*-haems and *a*-haems reduced. Presumably, this is because of increased flux through these haems as the backpressure is removed.

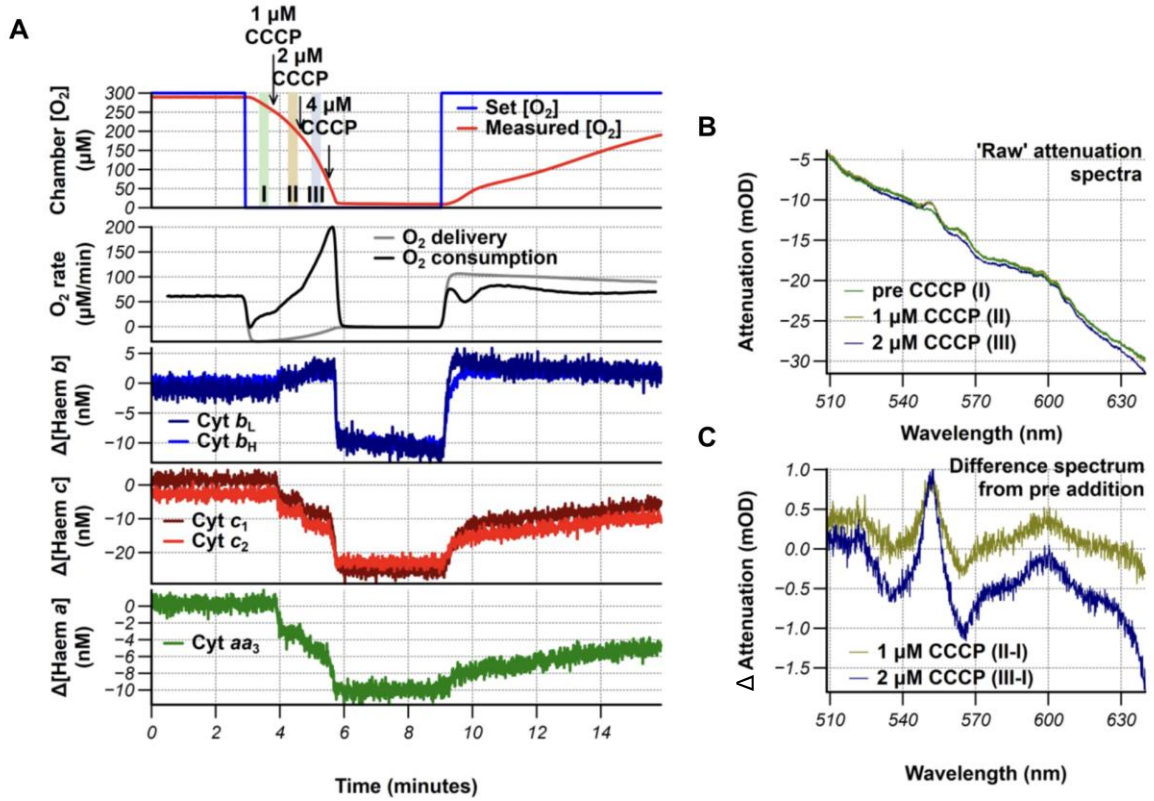

Figure 3.44 - The response of M. smeg grown in 0.01% Tween 80 to CCCP. *(**A**) Oxygen and haem response upon the addition of CCCP (**B**) The raw attenuation spectra at the indicated points (**C**) The difference spectra upon CCCP addition, showing oxidation of the b-haems and reduction of the c-haems and a-haems.*

As a result of these experiments, it was deemed sensible to wash the cells prior to examining them in the chamber. This way standard culture conditions could be used, and the effects of metabolic effectors could be examined at more reasonable concentrations, removing the interferences of the detergent. Altering the standard culture conditions would likely change the behaviour of the cells in a not easily quantifiable way and would reduce the compatibility of our results to other published results. For the washing step, we settled on two cycles of pelleting and resuspending in either butter or media based on when we could see a response to an exogenously added carbon source, glycerol in this example (Fig 3.45). This experiment also gave a nice example of the change in haem occupancy that occurs when the flux down the chain is increased, by the addition of a carbon source. This washing procedure was followed for all subsequent experiments with the cells in the chamber.

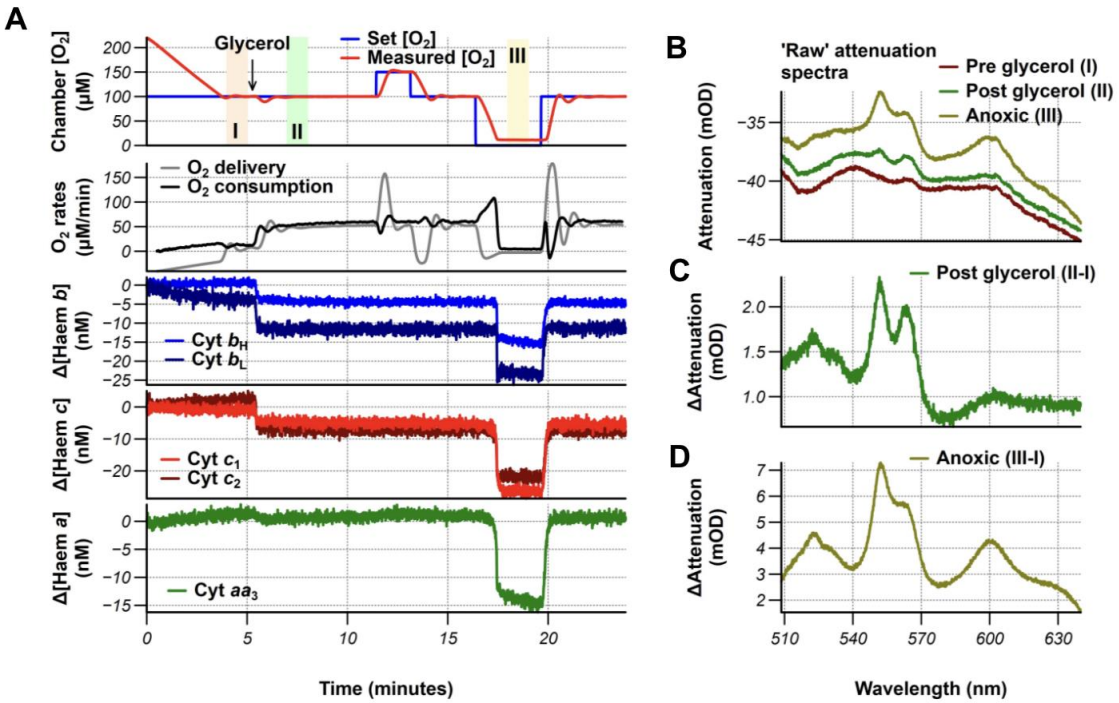

Figure 3.45 - The response of washed M. smeg to glycerol and anoxia *(**A**) Oxygen and haem response upon the addition of glycerol and anoxia (**B**) The raw attenuation spectra at the indicated points (**C**) The difference spectrum upon glycerol addition, showing a reduction of the c- haems, b- haems, and a- haems. (**D**) The difference spectrum (anoxia-pre glycerol). These cells were washed into a buffer of 20 mM HEPES pH 7.4, and 150 mM NaCl.*

We also examined the effect of FCCP and found that it has effects at lower concentrations than CCCP. Figure 3.46 shows an example of a run where the oxygen consumption rate was properly examined. At lower concentrations (0.1 to 0.5 μM FCCP) the *b*-haems oxidised and the oxygen consumption rate increased. Interestingly at higher concentrations (1 to 1.5 μM), the oxygen consumption rate decreased which was accompanied by the oxidation of the *c*-haems and *a*-haems. It is not clear why this occurs but potentially at higher concentrations, FCCP is inhibiting electrons entering the chain. This highlights the care that has to be taken with classical metabolic effectors in mycobacteria. This same behaviour was observed with higher concentrations of CCCP (data not shown).

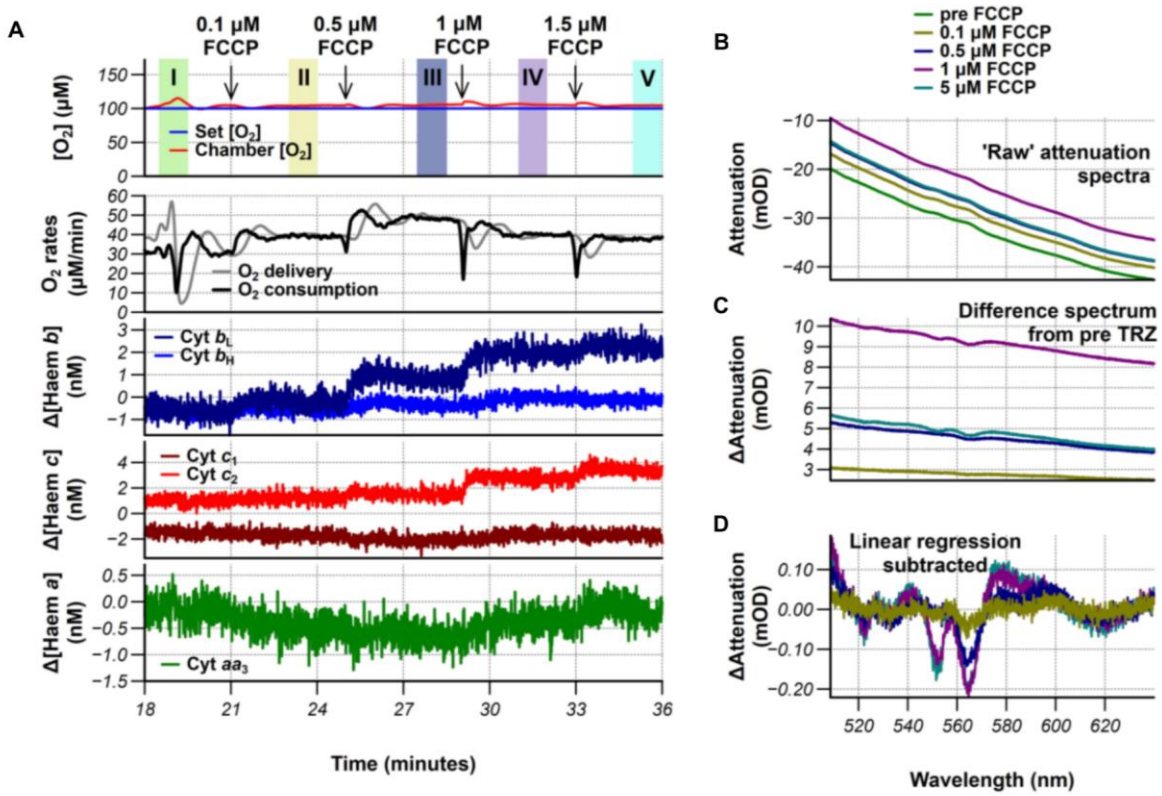

Figure 3.46 – The effect of FCCP (EtOH) on washed ΔcydAB M. smeg *(**A**) Oxygen and haem response upon the addition of FCCP (**B**) The raw attenuation spectra at the indicated points (**C**) The difference spectra upon FCCP addition (**D**) A linear regression was subtracted from the spectra in **C** to allow for the observation of the haem signals showing oxidation of the b-haems initially. At higher concentrations, all of the haems oxidised. This is a small section of the run presented in Fig 3.53*

3.3.4.2 The mixture of effects of thioridazine on mycobacterial haems.

As discussed above the phenothiazine class of molecules has been shown to inhibit type II NADH dehydrogenases. To explore this in the bioenergetic system we observed the effects of thioridazine (TRZ) on *M. smeg*. Unexpectedly, at lower concentrations of TRZ, we saw an increased reduction of the haems centres and an increase in the oxygen consumption rate. At higher concentrations, the expected response of oxidation of haems and a decrease in the oxygen consumption rate was observed. The fitting had to be carefully interpreted for additions of thioridazine as it appeared to cause a large change in the background scatter even if the haem signals were changing on top of this. This highlighted the common pitfall of just following the haem traces as what appeared to be large amounts of oxidation could sometimes be the result of an increase in the background scatter instead.

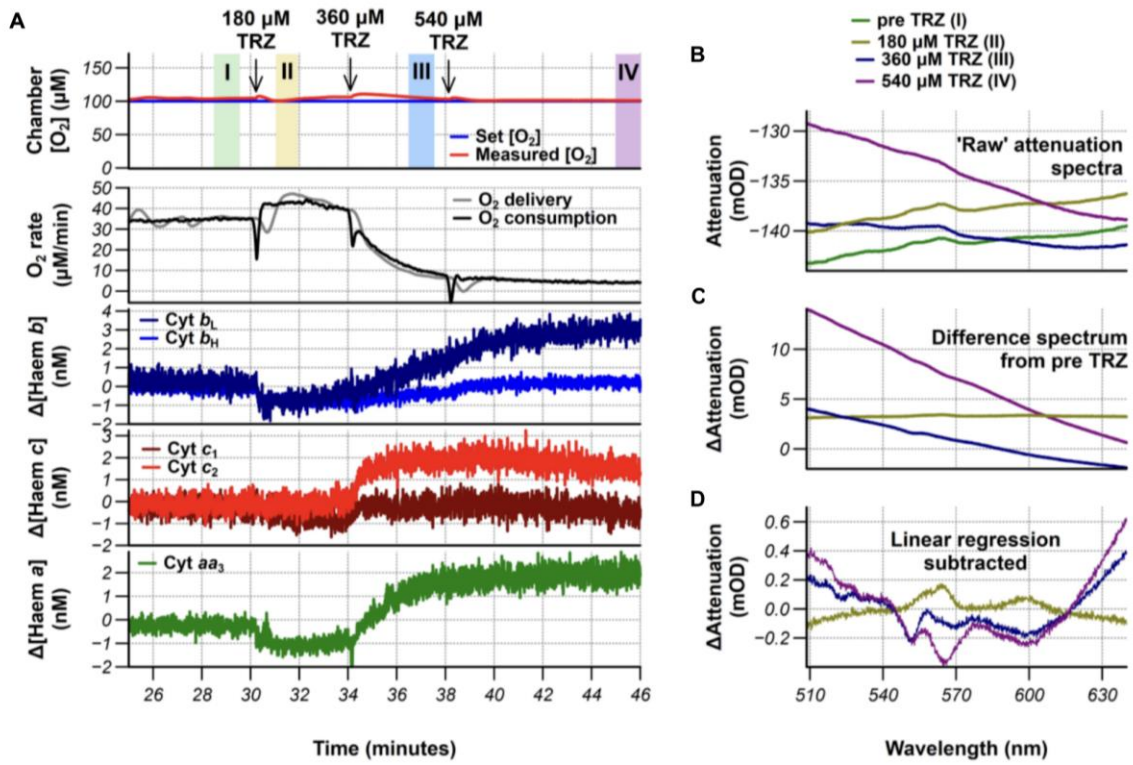

Figure 3.47 - The effect of TRZ (H_2O) on washed wild-type M. smeg *(**A**) Oxygen and haem response upon the addition of TRZ (**B**) The raw attenuation spectra at the indicated points (**C**) The difference spectra upon TRZ addition (**D**) A linear regression was subtracted from the spectra in **C** to allow for the observation of the haem signals the initial reduction of the haems at lower concentrations and oxidation of the haems at higher concentrations. This is a small section of Figure 3.51.*

We reasoned that the observed difference in the effect of thioridazine at different concentrations was potentially the result of two modes of action of TRZ (Fig 3.48). At lower concentrations TRZ was acting as a redox cycler, increasing the rate of transfer of electrons to the cyt *bcc:aa*$_3$ supercomplex, and so increasing the oxygen consumption rate and increasing the electron occupancy of the haems. At higher concentrations TRZ was inhibiting the function of Ndh2 and potentially other dehydrogenases resulting in a decrease in the electron flux to the cyt *bcc:aa*$_3$ supercomplex, explaining the decrease in oxygen consumption rate and oxidation of the haems. Another phenothiazine, trifluoperazine, showed similar behaviour. Redox cycling has been hypothesised as a mechanism of action of clofazimine which is used to treat leprosy which is also caused by a mycobacteria species (Lechartier and Cole, 2015). Whilst not a phenothiazine, clofazimine has a similar conjugated ring system.

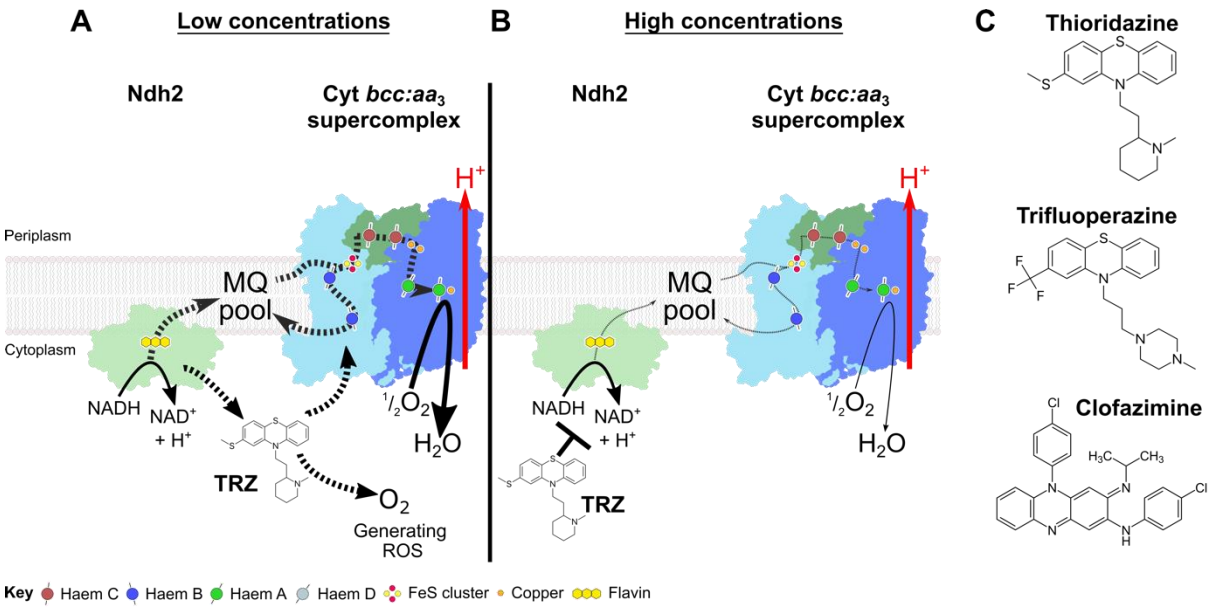

Figure 3.48 - Two proposed mechanisms of action of TRZ at different concentrations. *(**A**) At lower concentrations, TRZ acts as a redox cycler reducing the chain and increasing the oxygen consumption rate. (**B**) At higher concentrations, TRZ inhibits Ndh2 preventing the reduction of menaquinol, oxidising the chain and decreasing the oxygen consumption rate. (**C**) Chemical structures of phenothiazines: Thioridazine & Trifluoperazine, and the anti-mycobacterial agent Clofazimine.*

3.3.4.3 Further exploration of NADH dehydrogenase and succinate dehydrogenase inhibitors

We then explored the effect of a mixture of inhibitors including the classical type-I NADH dehydrogenase inhibitor, rotenone and two different succinate dehydrogenase inhibitors, sodium malonate and 3-nitropropionic acid (3-NPA). Neither rotenone nor sodium malonate showed any effect on the haem spectra or the oxygen consumption rate (Fig 3.49). TRZ oxidises the haem signals after these additions. This suggests that neither rotenone nor sodium malonate was able to prevent the reduction of the chain. We then substituted sodium malonate with 3-NPA (Fig. 3.50). We observed an unexpected reduction of the haem and a decrease in the oxygen consumption rate. We later realised that the 3NPA stock was very acidic which may explain the odd result.

The increasing amounts of TRZ added, again showed the oxidation of the haem centres alongside a large increase in the background. This oxidation was apparent if the spectrum from the TRZ addition was subtracted from the previous TRZ spectrum. An additional subtraction of a linear regression line fitted to the spectrum allowed the observation of the haem signals. The additional layer of the spectrum process illustrates the large change in the

background upon TRZ addition. It is unclear if this background is due to the spectrum of TRZ itself, the change in another chromatophore, with a broad absorption or just changes in the attenuation spectrum caused by changes in the scatter.

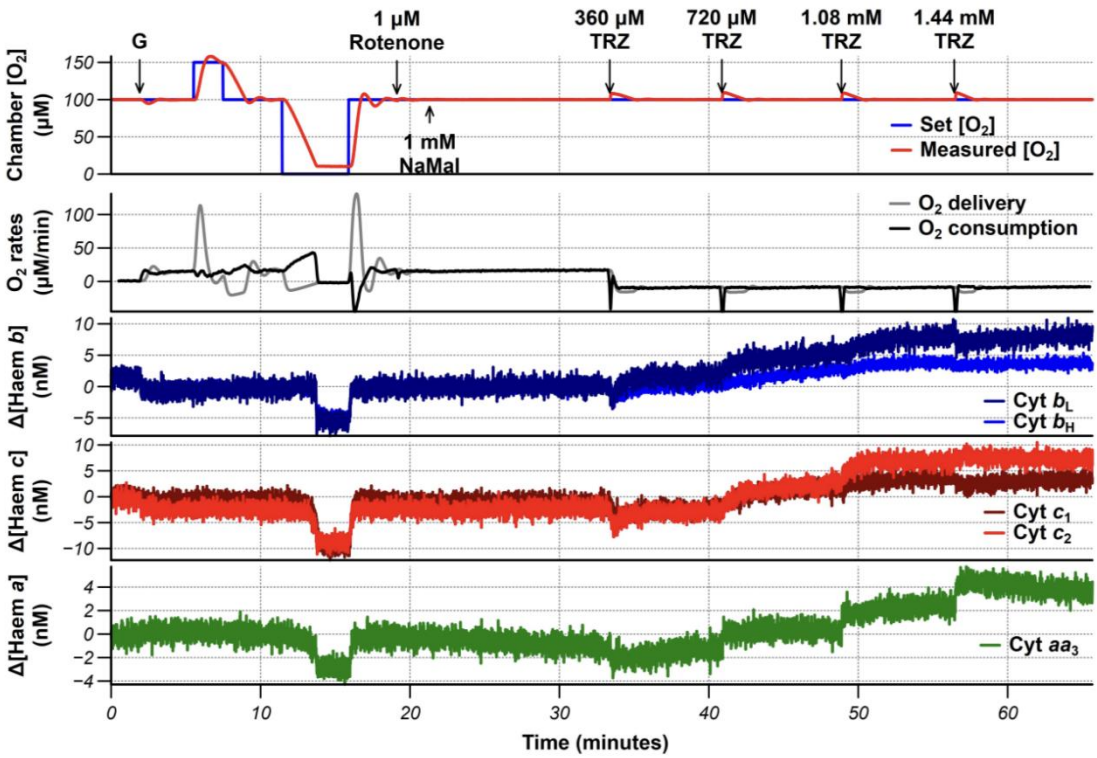

Figure 3.49 - Expanded run to explore the effects of rotenone and sodium malonate of wild-type M. smeg (Glycerol grown). *The oxygen concentration, oxygen consumption rate and haem traces are shown as before. No effect on the haems or oxygen is seen upon the addition of Rotenone or sodium malonate (NaMal). TRZ behaves as before. These cells were washed into a buffer of 20 mM HEPES pH 7.4, and 150 mM NaCl.*

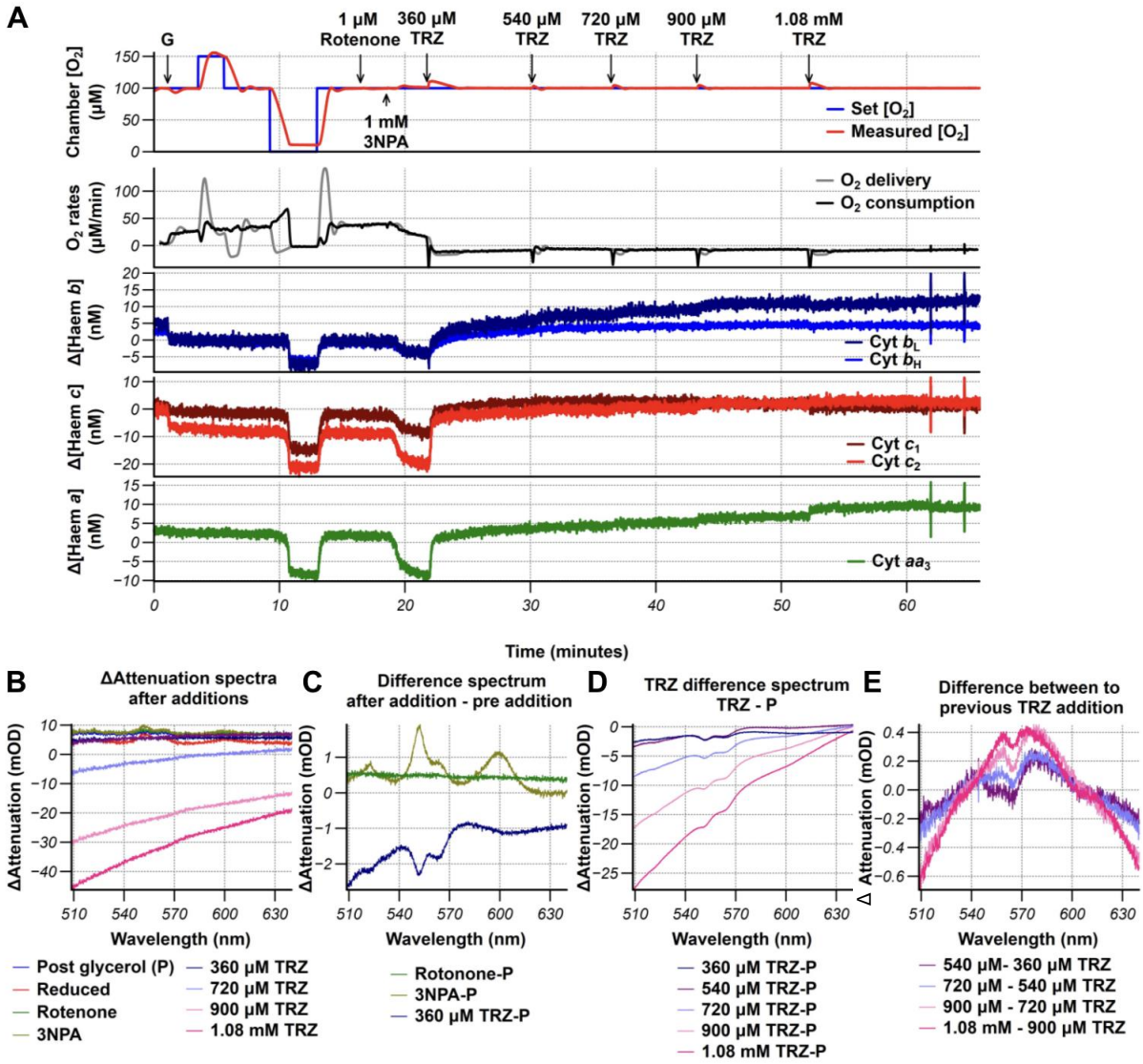

Figure 3.50 - Expanded run to explore the effects of rotenone and 3 nitropropionic acid of wild-type M. smeg (Glycerol grown). *(**A**) The oxygen concentration, oxygen consumption rate and haem traces are shown as before. No effect on the haems or oxygen is seen upon the addition of Rotenone, 3-nitropropionic acid (3-NPA) decreases oxygen consumption rate and reduces the haems (**C**), but this may be related to the acidity of the drug stock. TRZ behaves as before. (**B**) All the raw attenuation spectra at the time points indicated in the run. (**C**) The difference spectrum for the additions of rotenone, 3-NPA and the first TRZ addition. (**D**) The difference spectra from the TRZ addition, a large change in the background scatter is seen. (**E**) Linear regressions are subtracted from the spectra in D to show the oxidation of the haems, drowned out by the changes in the background. These cells were washed into a buffer of 20 mM HEPES pH 7.4, and 150 mM NaCl.*

3.3.4.4 Sodium dithionite

We had previously presumed that anoxia was sufficient to reduce all the haems. However upon further reading and work with the isolate cyt *bcc:aa*$_3$ supercomplex, it became apparent that the *b*-haems of the cyt *bcc* complex are very negative ($E_m^{b_L}$ = -291 mV, $E_m^{b_H}$ = -163 mV - Kao et al., 2016). These values are nearly 150 mV more negative than values for the mammalian homologue (Kim et al., 2012; Shinkarev et al., 2001). Fully reducing either membranes or isolated protein required a concentrated sodium dithionite and a considerable length of time, particularly for a slow *b* haem signal to reduce. An insufficiently reduced *b* haem signal would be a source of error for the ΔΨ measurements. We then considered if anoxia alone was sufficient to reduce the haem groups in the cells. At the end of the TRZ experiment presented in Figure 3.47, concentrated dithionite was added (Fig 3.51). This did result in an additional reduction of the *b*-haems as compared to anoxia alone. The addition of dithionite did not always cleanly reduce the haem signals as a drift in the baseline background through the run could lead to mis-fitting upon the addition of dithionite, either because of the dithionite itself or the addition of other compounds.

Additionally, despite the manipulation of the cells during the experiment, it does not appear that the haem signals have been fully transformed. The red spectrum in Figure 3.51 C shows the raw attenuation spectrum after dithionite with a linear regression subtracted. The larger *b* haem signal as compared to the difference spectra does suggest that the current difference spectrum (dithionite reduced - TRZ oxidised) underestimates the *b* haem content. In this case, I believe this was due to insufficient oxidation of the *b*-haems in the TRZ oxidised spectrum.

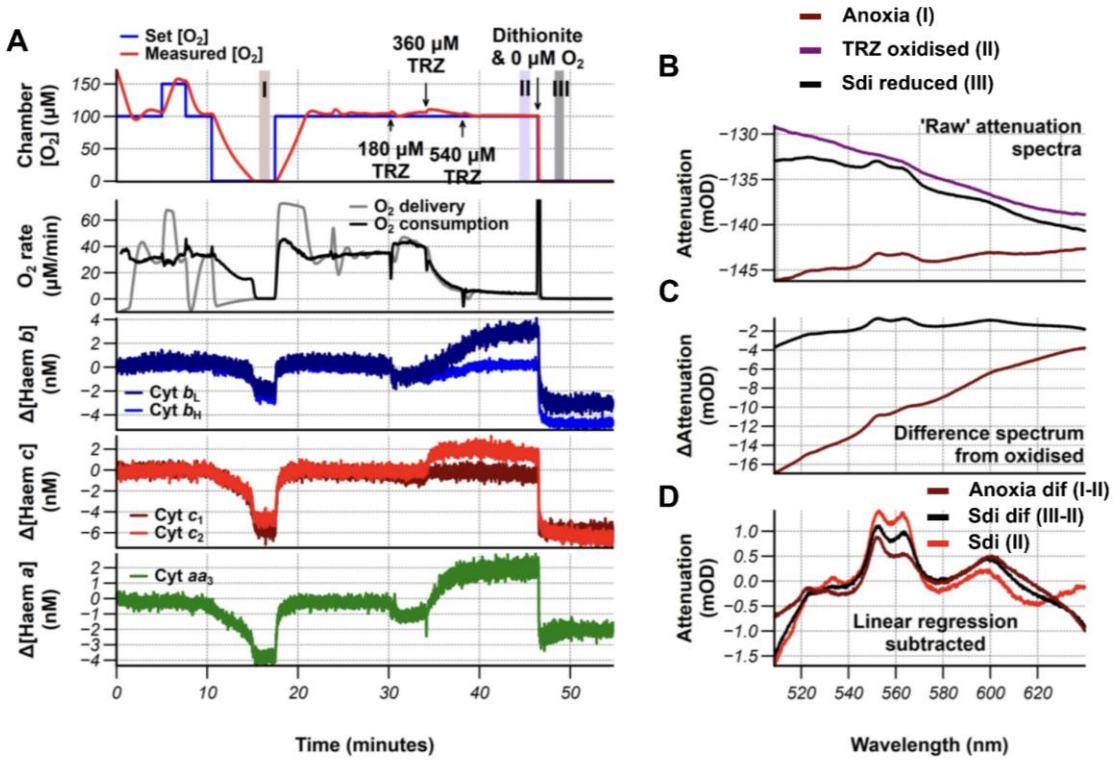

Figure 3.51 - The extra reduction provided by the sodium dithionite to wild-type M. smeg. *(**A**) Oxygen and haem response upon the addition of TRZ and dithionite (**B**) The raw attenuation spectra at the indicated points (**C**) The difference spectra upon anoxia or the addition of dithionite to the TRZ oxidised spectrum, as indicated during the run (**D**) A linear regression was subtracted from the spectra in **C** to allow for comparison of the haem signals, demonstrating that dithionite increases the reduction of the b-haems. The remaining imbalance in the intensity of b haem and c haem signals is likely caused by incomplete oxidation. In red in the 'raw' dithionite reduce spectrum with a linear regression subtracted, showing higher b haem content than the dithionite difference spectrum.*

3.3.4.5 Example of an ideal experiment to achieve the fully oxidised and fully reduced

All of this work informed an ideal run. Anoxia and sodium dithionite were used to try to achieve the reduced position and the inhibitors TRZ and 3-NPA were used to try and achieve an oxidised position. This was performed both on wild-type *M. smeg* and Δ*cydAB M. smeg* (Fig 3.52 and 3.53). Unfortunately, the dithionite caused too great a change causing mis-fitting, instead anoxic would have to serve as the reduced point. The TRZ behaved as expected, oxidising the chain. The addition of 3NPA did not appear to change the oxidation state of the haems. Distinct changes were seen in the oxidation of the *b*-haems upon the addition of FCCP which should be suitable for measuring the ΔΨ. It was decided to move forward with measuring ΔΨ with the ΔcydAB strain to avoid potential interference from the *b*-haems of the

cyt *bd* oxidase with the cyt *bcc* haem fitting. Any mis-fitting caused by the signal from the cyt *bd* oxidase would interfere with the ΔΨ measurement. This run is used in Chapter 4 as an example run for translating the ΔΨ measurement into *M. smeg* and to test the new spectral model developed from the characterisation of purified cyt *bcc:aa*$_3$.

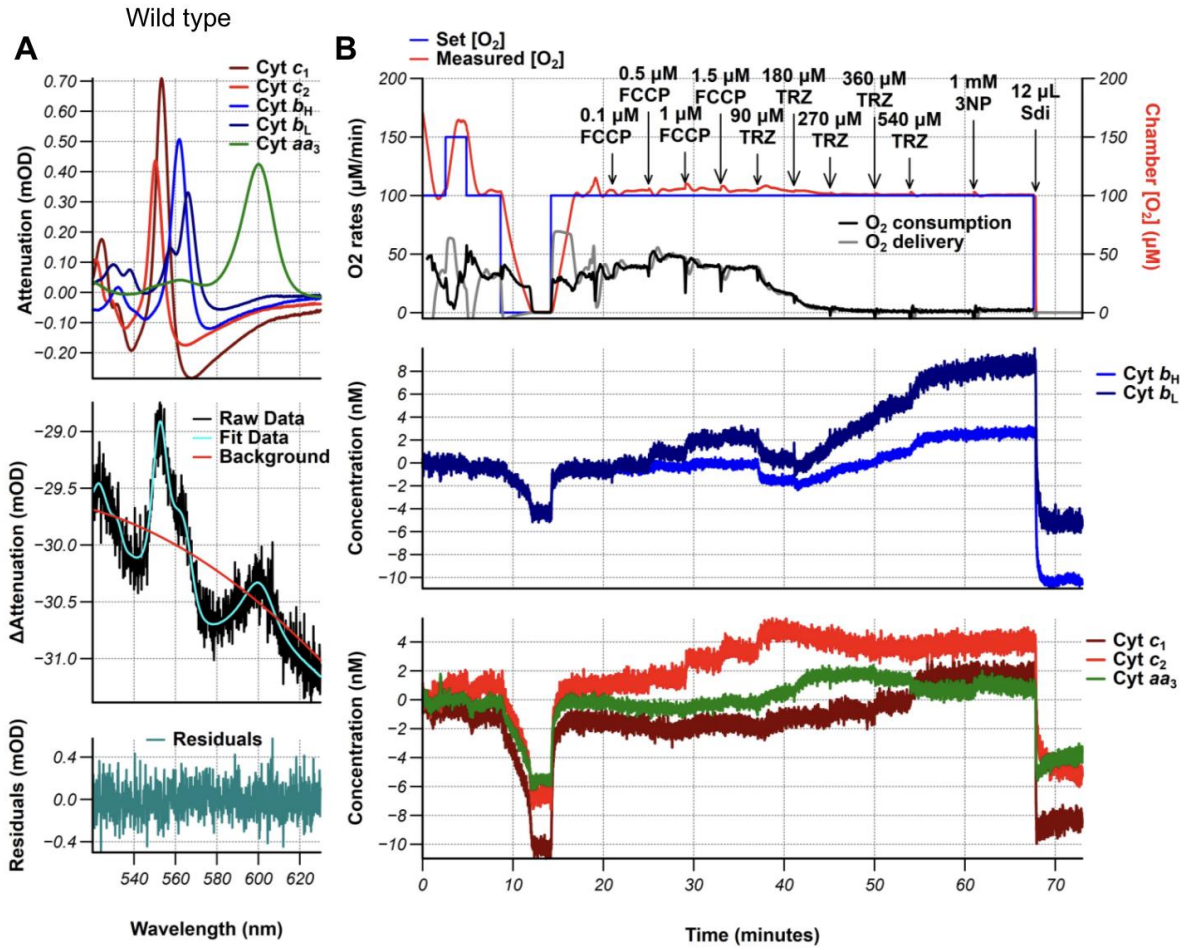

Figure 3.52 - Wild-type M. smeg with haem signals 'fully/partially' transformed to allow for ΔΨ measurement. *(**A**) Example of the quality of the fit at anoxia (**B**) The oxygen concentration, oxygen consumption rate and the haem traces over the course of the run as FCCP was titrated in, followed by the oxidation of the chain by TRZ. 3-NPA and dithionite were added to improve the oxidised and reduced point respectively.*

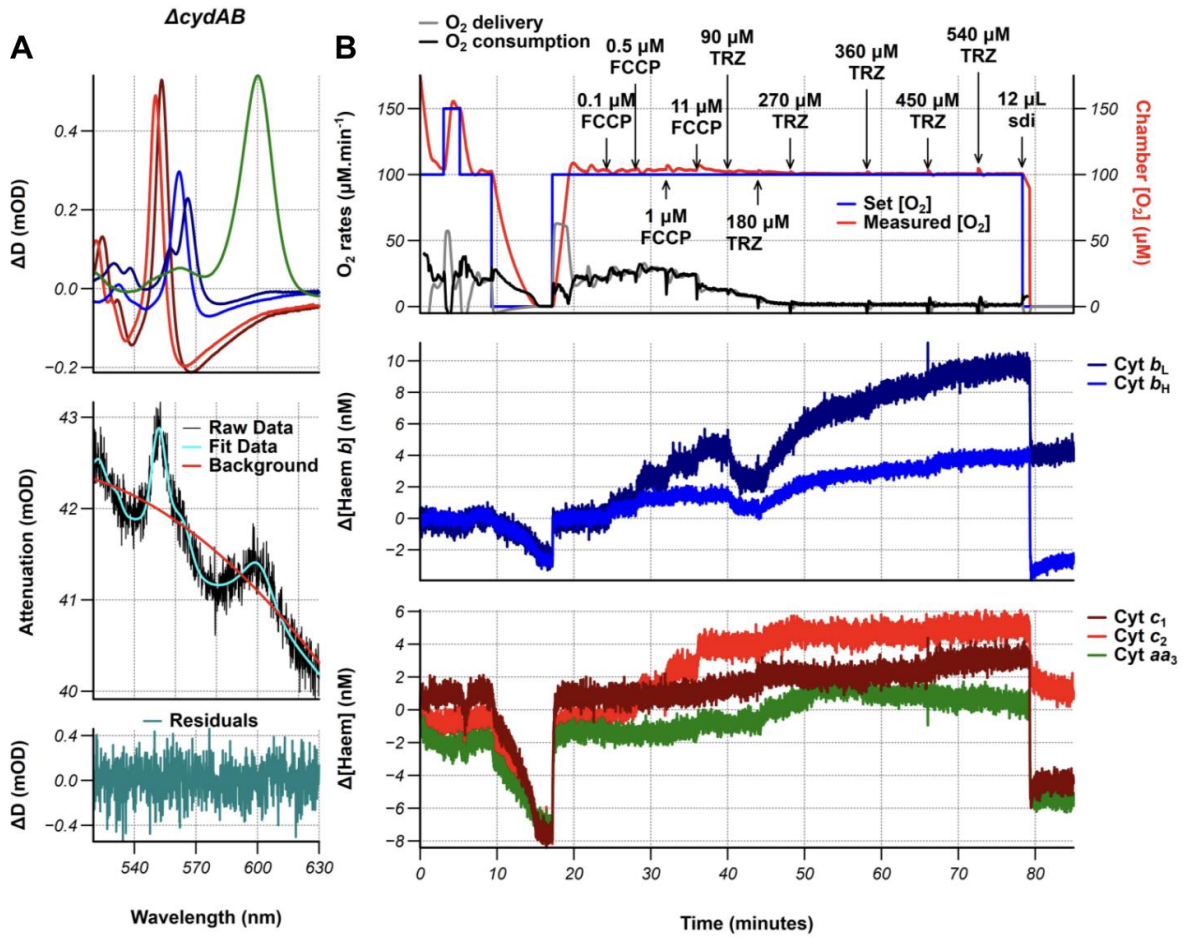

Figure 3.53 - ΔcydAB M. smeg with haem signals 'fully/partially' transformed to allow for ΔΨ measurement. *(**A**) Example of the quality of the fit at anoxia (**B**) The oxygen concentration, oxygen consumption rate and the haem traces over the course of the run as FCCP was titrated in, followed by the oxidation of the chain by TRZ. Dithionite was added to improve the reduced point.*

3.4 Discussion

3.4.1 Strength and weakness of using the bioenergetic chamber to examine mycobacteria.

As hopefully demonstrated in this chapter the bioenergetic chamber offers a powerful way to probe the bioenergetic function of cells. Applying this tool to mycobacteria offers the expanding field of mycobacterial bioenergetics an insight into the operation of the ETC in intact cells, allowing results on isolated proteins to be translated to living cells. Not only does the chamber provide a powerful window into bioenergetic function *in vivo*, but it also avoids

processes that generate aerosols, which are incompatible with safe working with a respiratory pathogen. The chamber could therefore be a powerful platform for both determining the mechanism of anti-TB agents that directly target the OxPhos system but also the effect of other anti-TB agents on the bioenergetic processes in *M. tb*

3.4.1.1 Mammalian spectra, thermodynamics, and mechanistic information do not simply translate to mycobacteria.

The main limitation of the chamber's application to mycobacteria is the incompatibility of some aspects of techniques developed in mammalian systems to mycobacteria. From the initial experiments, it is apparent that the haem signals present in mycobacteria differ from the much better-characterised mammalian equivalents. There are also potential haem signals present in mycobacteria that have no equivalent in mammalian systems. To improve this and make maximal use of the data produced by the chamber will require careful spectral characterisation of the mycobacterial cytochromes, the subject of the rest of this thesis. Firstly, it was decided to focus on the spectral contribution of the cyt *bcc:aa*$_3$ supercomplex (Chapter 4), but it is likely that other cytochromes may also be contributing, the focus of Chapter 5.

The spectral characterisation of the complement of cytochromes present in the mycobacteria chain under different growth conditions has been key to determining which cytochrome was the most important to focus on spectrally first, the cyt *bcc:aa*$_3$ given its prominace within the toal spectrum. However, there remains the possibility that other cytochromes or other chromatophores are contributing to the overall spectra of the cells that have been missed. For future work, it would be worthwhile considering more in-depth proteomic analysis of the membranes combined with bioinformatics approaches to search for possible cytochromes present in the cells at a sufficient concentration to contribute to the overall spectra.

Most likely, each different species placed in the chamber will present at least minor differences. Importantly, while these differences can be frustrating, they are the underlying bioenergetic biology: exploring them, as I do in subsequent chapters, offers biological and chemical insights that are often interesting in themselves.

3.4.1.2 The divergent responses to classical effectors and the lack of established chemical tools in mycobacteria.

The other limitation of the application of the bioenergetic chamber to mycobacteria is the lack of specific inhibitors of the mycobacterial oxidative phosphorylation system. In this chapter, I believe I have demonstrated that classical metabolic effectors do not always behave as

expected in mycobacteria. Further simultaneous work by Suzy Harrison in the lab on the mechanism of action of bedaquiline illustrates this well. Upon its addition, an increase in oxygen consumption is seen, which conflicts with its supposed ATP synthase inhibition activity which should decrease oxygen consumption rate as ATP synthase is blocked and back-pressure increases as observed with the classical mammalian ATP synthase inhibitor oligomycin (Ruas et al., 2016). This anomalous behaviour led previous work to conclude that it could be acting as an uncoupler (Hards et al., 2018). Suzy was able to demonstrate that the haem signals were reduced upon bedaquiline addition, matching the direct ATP synthase inhibition mechanism better. The initialling confusing increase in the oxygen consumption rate is instead caused by the cyt *bd* oxidase becoming activated, which may help to relieve the backpressure caused by the blocking of ATP synthase. In this case, the extra context that the haem spectra provided to the function of the chain, clarified confusing results from oxygen consumption rate measurements alone. With Suzy's work complete, bedaquiline can now be used as a tool like oligomycin but with the proviso that the corresponding change in the oxygen rate response does not match yeast or mammals.

Thermodynamic analysis requires that the haem centres are fully transformed during the chamber experiment, from the oxidised to reduced. To fully reduce the haems, starving the cells oxygen and adding a strong reducing agent can achieve this. To achieve better oxidation of the haems would require more well-characterised inhibitors of the mycobacterial dehydrogenases than currently available. By the nature of a common substrate, e.g. quinol binding sites, often metabolic effectors can target multiple different complexes. For achieving the oxidised spectrum, this may be working in our favour, preventing a wide range of dehydrogenases of contributing electrons. However, the current concentrations at which we are adding TRZ cause large background changes. Specific inhibitors should be effective at lower doses, reducing these effects. More specific inhibitors will also provide the opportunity to tease apart the conditioning of different complexes to the function of the chain. The plasticity of bacterial chains generally is much harder to tease apart as compared to the relatively simple mammalian chains. It does, however, demonstrate how different types of respiratory complexes are used to survive under a range of conditions.

3.4.1.3 The interference caused by background scatter

Broader changes in the background also seem to be a greater issue in mycobacteria than previously seen in mammalian systems. This could either be from the drug additions themselves, changes in chromatophores other than haems that have much broader peaks, or changes in the morphology of the bacteria leading to changes in the scatter. Changes in the scatter of bacteria would not be entirely unexpected as they are known to change their

morphology in response to stress or could simply be more likely to lyse. It would be worth exploring approaches to model greater changes in the scatter to aid the fitting of the haems signals. One way would be to combine the decomposition with non-linear regression analysis modelling the scatter as Eq 3.6 describing the contributions of the scatter to the Δattentuation (ΔD_s) as a function of the wavelength, λ, where a and b are parameters to be determined based on the collected data.

$$\Delta D_s = a\lambda^b \qquad \text{Equation 3.6}$$

This approach is similar to an analysis approach applied to redox titrations in Chapter 4. This may offer a way to account for changes in the background during the run. Careful consideration would have to be given to whether these changes in the scatter could cause a significant change in the average path length used to approximate the concentration of the haems.

3.4.2 Considerations of bacterial culture oxygenation

It is often assumed that shaken bacterial cultures are not oxygen-limited. It is then remarkable that halving the volume of the cultures in the same flasks changed the behaviour of mycobacteria. The initial culture conditions were in non-baffled flasks so it probably should have been more obvious that these cultures were oxygen-limited but it does indicate how fine that balance can be in standard laboratory culturing conditions. It also highlights the difficulty with scaling cultures whilst retaining the same oxygenation conditions. Smaller 50 mL cultures behaved like the 500 mL aerobic conditions than the 1 L conditions.

The production of the coproporphyrin pigment appears to be related to poor oxygenation of the cultures. It has previously been associated with cells entering a dormant state but it is unclear what purpose if any it serves (Nikitushkin et al., 2016). The link to iron availability is interesting particularly given that the coproporphyrin also is excreted in the media. Iron acquisition is important to the pathogenicity of M. tb as they are starved of Iron during infection (Rodriguez et al., 2022). Its presence in the cells does poses some issues to exploring these conditions as the pigment interfers with the measurement of the haem signals. However, from some brief experimentation with the fitting, it was possible to add a spectrum of the coproporphyrin to be able to distinguish between its spectrum and the haem signals (data not shown).

3.4.3 Coupleness of bacterial membranes?

The respiratory control ration (RCR) measured for the wild-type membranes was much lower than values that have previously been measured for mammalian systems, typically closer to ~3 (Jones et al., 2016; Pryde and Hirst, 2011). This may be due to the inhibitor effects of gramicidin. It would be worth exploring the effect of other uncouplers on the NADH oxidation rate. It could also be that physical disruption methods, required for isolating mycobacterial membranes, lead to more leaky membrane preparations. Collaborators in Newcastle and Birmingham have been working towards a BugBuster™-like cocktail of glycosidic hydrolases that would allow for osmolysis of mycobacteria (Personal communication with Dr Elizabeth Lowe and Joe Manion). Their aim for this is to improve the extraction of genomic DNA from mycobacteria but this could also be translated for isolating membranes. The main limitation of this would be the scaling up required to be able to lyse a sufficiently large quantity of cells in order to isolate membranes from. The difference in the measured RCRs could also reflect a genuine difference in the coupleness of the bacterial chain compared to the mitochondrial chain.

3.5 Conclusions

The cytochrome content of the initial growth condition was assessed by examining the spectra of isolated membranes, finding that the cytochrome content depended on the growth phase and the carbon source. The growth conditions were then adapted for use with the bioenergetic chamber. In the process, it was determined that the original conditions were not as oxygenated as previously thought. From in-cell spectroscopy, membrane spectroscopy and native gels, it is apparent that the cyt *bcc:aa*$_3$ is the major cytochrome present in cells in the early exponential phase well-aerated cultures. Comparing the reduction of membranes by NADH or succinate demonstrated that succinate is a poor reductant of the isolated mycobacterial membrane vesicles likely because of its unfavourable redox potential in relation to menaquinone. We were able to determine the effect of several classical metabolic effectors on mycobacteria. Using these effectors, it is possible to fully transform the *a* haem signal from its reduced to its oxidised form, allowing for subsequent determination of other bioenergetic parameters, such as $\Delta\Psi$.

Chapter 4 - Measuring flux, thermodynamics, and △Ψ in living mycobacteria using a bioenergetic chamber

4.1 Introduction

4.1.1 Why measure △Ψ

The *pmf* is central to bioenergetics (see Chapter 1). It is constantly maintained by cells to power themselves through ATP coupling and define themselves through active transport. Despite the importance of *pmf*, methods that accurately, easily, or quickly measure it are lacking. Being able to measure *pmf* offers insight into the potential energy governing oxidative phosphorylation as well as transport in and out of the cell.

Different organisms have different tolerances to dissipation of *pmf*. Mammalian cells can sustain mitochondria in a constantly energised state through homeostasis. In bacteria, the cytoplasmic and energy-transducing membranes are the same. This means that the *pmf* of their energy-transducing membrane is much more vulnerable to external insult. Mycobacteria appear to prefer to maintain a more constant *pmf* (Rao et al., 2001, 2008). However, some bacteria can tolerate a degree of dissipation of their *pmf* which may help to tolerate some antibiotics (Verstraeten et al., 2015). The *pmf* is also linked via the ETC to the turnover of key pools of important molecules, NADH, and TCA cycle components. Any dysregulation of the *pmf* is detrimental to the health of the cell. A depolarised cell will lack the potential energy to drive essential processes, and a hyperpolarised cell is more at risk of damage from reactive oxidative species, ROS (Korshunov et al., 1997).

To completely quantify *pmf* one would need to measure both components, ΔΨ and ΔpH. Typically the ΔΨ is the larger component of the *pmf* in most energy-transducing membranes (chloroplasts being the exception) even though energy-transducing processes are often described in terms of proton movement. Therefore, measuring ΔΨ will indicate the total *pmf*. Typically changes in ΔΨ are also reflected by similar changes in ΔpH (Nicholls, 1974; Nicholls and Ferguson, 2013). However, it is important to consider when interpreting changes in ΔΨ that the ΔpH may not follow the same pattern.

Measuring ΔpH in cells is possible but technically hard and prone to systematic error. Exogenous dye-based approaches for measuring ΔpH, similar to those subsequently described in this chapter for measuring ΔΨ, have been previously published (Blumwald et

al., 1984; Teuber et al., 2001), however, these suffer from the same artefacts as dye-based to an even worse degree than ΔΨ sensitive dyes due to the common pH-dependent aggregation of these probes. ^{31}P NMR can be used to measure ΔpH. The intracellular and extracellular inorganic phosphate populations will have a different chemical shift as a result of their respective pH (Nicolay et al., 1982). However, keeping a cell oxygenated, and so alive, inside an NMR machine poses a practical experimental challenge, which is being actively worked on within the York Bioenergetics Lab by Suzy Harrison but currently without interpretable results (personal communication, Suzy Harrison)

4.1.2 Using lipophilic cations to estimate the ΔΨ

Traditionally, lipophilic cations have been used to measure components of the *pmf*. This has been determined from the accumulation of an appropriate ion across the energetic membrane. For measuring ΔΨ, given the orientation of the membrane potential for respiratory membranes, cations will accumulate inside (bacterial cell, N-side of membrane). The Gibbs free energy of 1 mol of cation transported down a charge gradient of ΔΨ (mV) from a concentration of $[X^{m+}]_{out}$ to $[X^{m+}]_{in}$ can be described by Eq. 4.1

$$\Delta G = -mF\Delta\Psi + RT\ ln\ \{\frac{[X^{m+}]_{in}}{[X^{m+}]_{out}}\} \qquad \text{Equation 4.1}$$

This demonstrates how ΔΨ can drive a difference in ion concentration across a membrane. If this ion distribution across the membrane is at equilibrium (i.e. $\Delta G = 0$), Eq 4.1 can be rearranged for $\Delta\Psi$ (Eq 4.2)

$$\Delta\Psi = \frac{RT}{mF}\ ln\ \{\frac{[X^{m+}]_{in}}{[X^{m+}]_{out}}\} \qquad \text{Equation 4.2}$$

The ion must cross the membrane via passive charge transport. To do this the cation must have some way to shield or delocalise the charge to allow it to cross the membrane. This accumulation can then be measured by the decrease in the cation's concentration outside the cell, giving a rate of uptake. Monitoring over time allows the response to perturbations of the system to be measured. The internal volume also has to be calculated in order to calculate the internal concentration of the cation. This can sometimes prove complex due to swelling of cells or mitochondria when the *pmf* is altered. It is also assumed that the concentration of the probe being used is small enough that it does not alter the membrane potential.

The change in concentration of the probe can be measured in several different ways:

- Specialised compound-specific electrodes
- Changes in scintillation count for isotopically labelled lipophilic cations

- Fluorescence for fluorescent lipophilic cation

4.1.3 The history of methods for ΔΨ calculation

Some of the first attempts to measure the *pmf* and ΔΨ were made by Mitchell & Moyle (Mitchell and Moyle, 1969) using pH and K^+ sensitive electrodes on rat mitochondria. These experiments used valinomycin to allow the equilibration of K^+ ions across the membrane, as valinomycin is a potassium ionophore. The K^+ uptake could then be used to calculate ΔΨ using a K^+ sensitive electrode. A range of ΔΨ values were measured depending on the initial [K^+] that the mitochondria were incubated with prior to the measurement. Later work by Nicholls used $^{86}Rb^+$ instead of K^+ to measure cation uptake (Nicholls, 1974). Using $^{86}Rb^+$ avoided changes in the K^+ gradient, due to K^+/H^+ transporters present in the mitochondrial membrane, altering the measurement of ΔΨ. The limitation of both these approaches is the use of valinomycin which will partially clamp the ΔΨ at the level dictated by the Nernst equilibrium of the pre-existing K^+ or other cation gradients across the membrane. Subsequent changes in the ΔΨ, say upon the addition of an effector, will not be observable because of this clamping of cation gradients at a fixed position.

Subsequent work since the 1980s mainly used synthetic lipophilic cations such as TPP^+ or $TMRM^+$ (Fig 4.1). These cations have delocalised charges across the molecule allowing them to cross the membrane and so do not require valinomycin to equilibrate across the membrane. TPP^+, like $^{86}Rb^+$, can be measured isotopically or with specific electrodes. These cations do have caveats as they do not always accumulate exclusively based on the Nernst equation. Some of these errors are accounted for by measuring the accumulation of TPP^+ in the cell when the ΔΨ = 0. This is taken from measurements of TPP^+ accumulation when cells have been treated with valinomycin or uncouplers like CCCP, giving a value for non-specific binding (Ghazi et al., 1981; Rao et al., 2001). There are justifiable questions about how well this accounts for any non-specific binding. Lipophilic cation measurements in bacteria pose a particular issue due to the number of possible transporters present in the bacterial membrane. These transporters then may result in non-Nernstian transport of these lipophilic cations (Jindal et al., 2019).

In recent years the use of isotopic probes has been overtaken by fluorescent probes for *pmf* measurement. Several fluorescent-based probes have been developed including $DiSC_3(5)$, Safranin, and Oxonol VI. Fluorescence has the advantage over radioactivity in terms of safety and regulations. Fluorescent probes suffer from the same assumption that the probe is only accumulating according to the Nernst function and nothing else. The advantage of isotopic probes over fluorescent probes is in their value for absolute measurements, measurements

of isotopic probes will always be sensitive and directly proportional to the concentration of the probe.

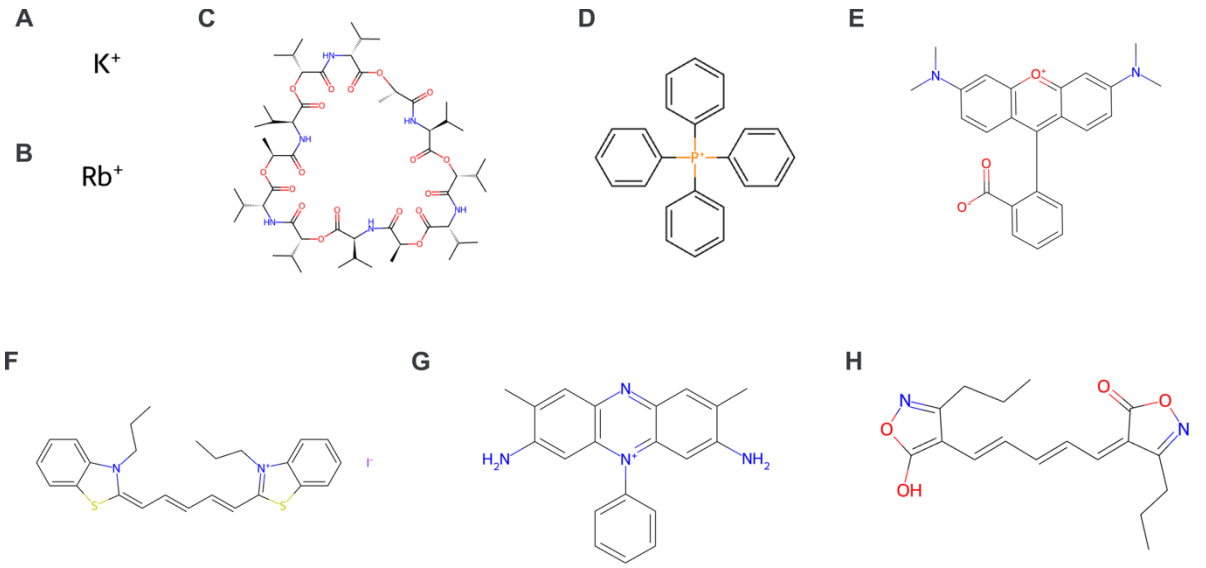

Figure 4.1 - Lipophilic cations used to measure/estimate ΔΨ (ChemSpider) *(**A** & **B**) potassium and rubidium ions, (**C**) Valinomycin, (**D**) tetraphenylphosphonium cation (TPP+), (**E**) tetramethylrhodamine (TMRM$^+$), (**F**) 3,3'-dipropylthiadicarbocyanine iodide (DiSC3(5)), (**G**) safranin, (**H**) oxonol VI*

4.1.4 Uses of fluorescent probes for measuring ΔΨ

Fluorescence is widely used within the biological sciences as a powerful means of imaging biological samples or detecting the presence of a specific molecule. These molecules, often composed of aromatic groups, can absorb a photon and then emit a photon at a longer wavelength, following Stoke's shift. Voltage-dependent fluorescent probes can be used in combination with several fluorescent techniques (flow cytometry and fluorescence microscopy) to measure ΔΨ based on their transport in or out of the cell. Depending on the experimental design the fluorescent probes can be used under quenching or non-quenching conditions.

Quenching conditions utilised the fact that at high concentrations, such as when the dye accumulates in the cell, the dye's fluorescence will be self-quenched. As the cell conditions are altered, any depolarisation will cause the release of the fluorescent dye, resulting in increased fluorescence in the media (as the dye is now at a lower concentration). These experiments cannot give absolute values but do offer a way to observe qualitative changes to the polarisation of the membrane (Buttress et al., 2022).

In non-quenching conditions, the probe is used at lower concentrations. This is to avoid aggregation of the probe or the self-quenching of its fluorescence as it accumulates inside the cell. The difference in the concentration between the inside and outside of the cell as measured by the intensity of the fluorescence can then be used to estimate the ΔΨ (Lo et al., 2007). Again for this calculation, the volume of the cell has to be known or measured. However, this is subject to the conditions inside the cell never inducing quenching of the probe fluorescence, either by the concentration of the probe or by other elements within the cell.

Both conditions assume that the uptake of the probe is only Nernstian. Many common probes, including $DiCS_3(5)$, have also been suggested to be substrates for bacterial transporters (Jindal et al., 2019), potentially resulting in non-Nernstian transport. A number of the fluorescent probes have also been demonstrated to be toxic to the cell, which can be exacerbated by the higher concentration inside the cell as the probe accumulates (Kadigamuwa et al., 2016).

4.1.5 Levels of the experimental system and the distance from cellular reality

Up until now, I have discussed measuring the *pmf* in terms of an intact whole cell, however, measuring this comes with experimental difficulties. Eukaryotic cells pose an extra layer of complexity as they have additional membranes, plasma membrane and outer mitochondrial membrane, over which a probe has to cross before reaching the energy-transducing membrane, the inner mitochondrial membrane (Ritchie, 1984). Some bacteria, such as *E. coli*, have an outer membrane that limits the ability of probes to reach the interior of the cell, requiring the use of compounds, such as EDTA, to increase the permeability of the outer membrane and so increase the accumulation of the probe in the cell (Lo et al., 2007). These compounds can potentially alter the observation itself. The general lack of experimental control in biological 'messy' cells leads to the choice of other more well-controlled experimental systems.

As discussed in Chapter 3, when cells are lysed, membrane vesicles form spontaneously. The nature of these vesicles can be modified by the conditions of lysis (method, temperature, and buffer composition). The vesicle formation process can expose cytoplasmic active sites to the bulk solvent, known as inverted membrane vesicles (IMVs). When formed from mitochondria, this is often referred to as submitochondrial particles, SMPs. This is ideal for exploring the role of substrates that do not naturally cross the membrane, such as NADH, as

shown in Fig 4.2. Vesicles orientated the other way, right-side out vesicles, are catalytically silent to substrates such as NADH however their haems are still spectroscopically visible. Vesicle systems have been an essential part of historical ΔΨ measurements, Mitchell and Moyle's experiments were on isolated mitochondria. Key experiments showed that mitochondria accumulated cations and SMPs hydrolysing ATP accumulated anions (Liberman et al., 1969). These experiments helped to provide evidence towards the chemiosmotic theory. A number of the *pmf* probes are better suited to vesicle systems. Excluding measuring *pmf* they have also been key to understanding energy transducing systems.

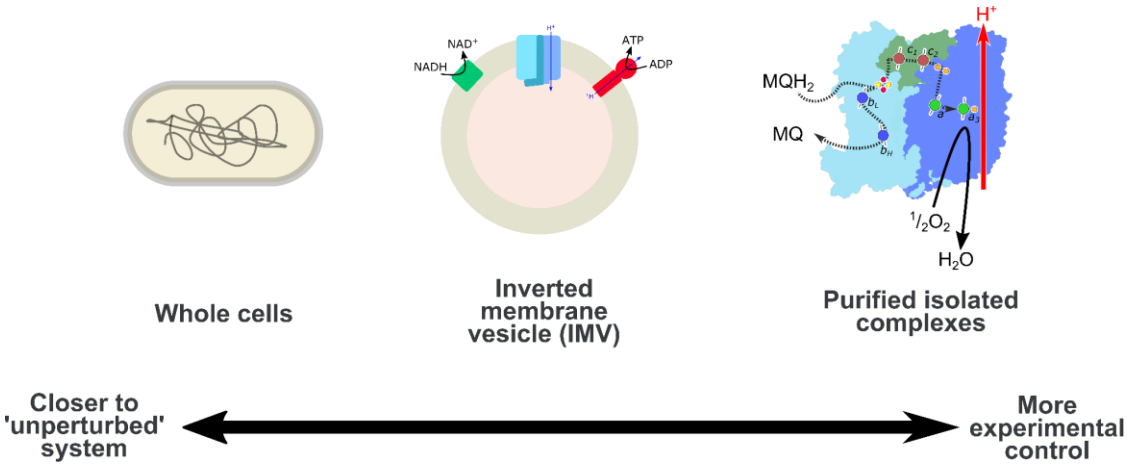

Figure 4.2 - Different levels of experimental systems in bioenergetic research

Beyond vesicles, purified complexes can be characterised by structural or enzymatic techniques. Purifying the often delicate membrane complexes that make up the bioenergetic system is not trivial, particularly whilst retaining the native activity of the complex. Being able to purify the component of any bioenergetic system is powerful, however, the end purification product is in an aqueous environment, which can pose technical challenges for highly hydrophobic substrates such as quinol species. A purified complex can be reconstituted along with other complexes into proteoliposomes, creating artificial vesicles. This requires the purification of each of the components and the ability to control or account for the orientation of the complexes. The advantage of this is much greater experimental control over variables such as stoichiometry of complexes, combination of complexes and substrates and access to cytoplasmic sites within a membrane environment.

Unfortunately, the complexity within a cell often is directly tied to the very phenomena that the experimentalist is trying to understand. It is therefore important that the correct experimental system is selected for the question being asked. Where possible, translating findings between the different levels of experimental systems can offer the assurance that a phenomenon can be recreated in several systems.

4.1.6 Alternative approaches to measuring ΔΨ

There are a variety of alternatives to lipophilic cations, which have been summarised in a recent review (Lo et al., 2024). One of these alternatives is using an electrode to directly measure the ΔΨ. This technique, often referred to as patch clamping, was pioneered by Hodkin and Huxley measuring the actional potential of giant axons from squids (Hodgkin and Huxley, 1939) which were later refined by Sakmann and Neher, where the electrodes form a seal with the membrane rather than directly disrupting the membrane. This can be used to measure ΔΨ in a voltameter-type set-up, where one electrode is directly attached to the energy-transducing membrane, and another is ground in an ionic solution matching the composition of the cytoplasm/mitochondrial matrix. Patch clamping had been historically limited to large cells due to the size of the microelectrode and pipettes used for the process, excluding measurements in bacterial cells. To circumvent this size barrier, spheroplasts of giant *E. coli* cells were examined this way and matched indirect measurements made using lipophilic cations (Felle et al., 1980). The caveat to these measurements is the perturbation required to generate these spheroplasts and how these perturbations may have altered the cell's physiology.

Some approaches use the intrinsic properties of the cell to measure the ΔΨ. These are limited to the specific cell type that contains these voltage-sensitive components. Carotenoids have been used in photosynthetic energy-transducing membranes as an indicator of ΔΨ. Carotenoids are long-chain aliphatic pigments that both protect against oxidative damage and aid in light harvesting. A series of conjugated isoprene units at the central hydrophobic region of the carotenoid molecule is responsible for their characteristic visible spectrum. This absorption spectrum shifts in response ΔΨ (Jackson and Crofts, 1969). The response is relative and so has to be calibrated to calculate ΔΨ. The shift will also only reflect their immediate environment, rather than specifically ΔΨ of bulk solution. The proton concentration in the immediate vicinity of the membrane will be higher than the bulk solution as a result of the fixed negative charge of the phospholipid. Likely due to this, carotenoids tend to give higher estimates of ΔΨ than other techniques.

Several groups have been designing systems to use the flagella of bacteria, like *E. coli* as a method of measuring ΔΨ (Krasnopeeva et al., 2021). Flagella rotation is driven by ion gradients, proton or sodium depending on the bacterial species. A variety of methods can be used to determine the rate of flagella rotation, including tracking the flagella via attached beads (Krasnopeeva et al., 2021). This rotation rate appears to have a linear relationship to this ion gradient driving the pump, although this relationship could be non-linear under conditions such as very high load. Relative changes in ΔΨ are then reflected by changes in

the rotation rate, and if this can be calibrated by orthogonal techniques the absolute ΔΨ could be measured. This technique is also dependent on the bacteria using flagella; some growth conditions, such as the stationary phase, have fewer motile cells and so may not have flagella present in their membranes (Cremer et al., 2019).

Using flagella or other intrinsic voltage-sensitive components as a method to measure ΔΨ is only applicable in cell types that naturally contain these voltage-sensitive components. This can be augmented by synthetic biology approaches via the introduction of non-native intrinsic voltage-sensitive components, such as recombinantly expressing a voltage-sensitive fluorescent protein (Jin et al., 2023; Kralj et al., 2011). Whilst expressing a voltage-sensitive fluorescent protein will circumvent the issue of transport of extrinsic dyes in and out of the cell, their fluorescence is likely to be quenched by non- ΔΨ related factors such as protein aggregation. One can also envisage non-fluorescent methods where synthetic biology could widen the range of applicable species.

4.1.7 Redox poise of *b*-haems of the cyt *bc* complex to measure ΔΨ

Another intrinsic approach, and the focus of this chapter, was first described by Kim, Ripple and Springett (Kim et al., 2012). This approach uses the distribution of electrons in the cytochrome bc_1 complex to measure ΔΨ (Springett, 2015b). As described in Chapter 3 the Springett chamber system can be used to measure the electron occupancy of different haem centres within the respiratory chain. Specifically for this approach, the two *b*-haems within the cyt *bc* complex are key to the measurement. These two haems (b_L and b_H) are situated across the membrane, and as part of the normal function of the enzyme, electrons move from b_L to b_H working against ΔΨ. The Gibbs free energy change of this electron transfer can be described by Eq. 4.3.

$$\Delta G^{b_L \rightarrow b_H} = -(E_h^{b_L} - E_h^{b_H}) + \beta \Delta \Psi \qquad \text{Equation 4.3}$$

Without the presence of ΔΨ, electrons would be distributed just based on the difference in the redox potentials of the two haem centres ($E_h^{b_L}$ & $E_h^{b_H}$). In mitochondrial enzymes, the E_m of b_L is -100 mV and the Em of b_H is +50 mV. Given their respective redox potentials, this would favour the distribution of electrons to b_H. However, b_H is closer to the negative side of the membrane so electrons transferred from b_L to b_H will have to do work against the ΔΨ as they will be repulsed by the negative side of the membrane (Fig 4.3 & Fig 4.4).

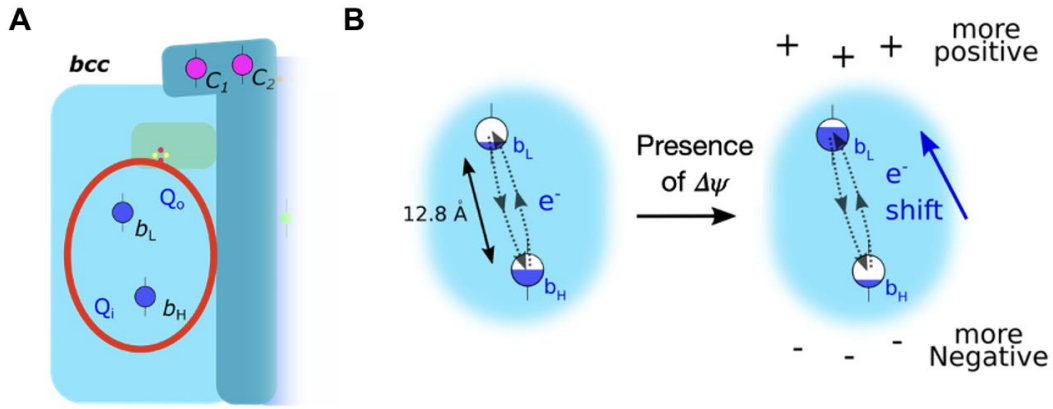

Figure 4.3 - Measuring the ΔΨ using the redox poise between the b-haems in cyt bc complexes *(**A**) A cartoon representation of the mycobacterial cyt bcc complex, component of the mycobacterial cytochrome bcc:aa$_3$ obligate supercomplex. The redox centres are shown, including the b-haems. (**B**) The effect of the ΔΨ on the redox poise (Left) A representation of the distribution of electrons (redox poise) between the two b-haems if there was no ΔΨ. As the b-haems are within 14 of each other electrons will transfer between the centres very quickly, in a state of equilibrium. The reduction state of the haems is shown by how 'full' the haem centres are. b$_H$ would be more reduced than b$_L$, given it's more positive E$_m$. This gives a redox poise (**Right**) Redistribution under ΔΨ. Given that b$_H$ is closer to the more positive side of the membrane and electrons are negatively charged, electrons moving towards b$_H$ will have to do work against ΔΨ proportional to the distance they move. This will shift the redox poise such that b$_L$ is more reduced than it would be without ΔΨ.*

This work will be scaled according to the fraction of the membrane that the electron is transferred across, known as the dielectric distance (β), which can be approximated to 0.5. An increase in the ΔΨ will then favour the distribution of electrons more onto b$_L$ despite the less favourable redox potential. Given that the two haems are under 14 Å away from each other, the electrons transfer between the two haems can be assumed to be in a state of equilibrium and so the Gibbs free energy change will be approximately zero. Eq. 4.3 can therefore be rearranged to solve for ΔΨ (Eq. 4.4).

$$\Delta\Psi = \frac{(E_h^{b_L} - E_h^{b_H})}{\beta} \qquad \text{Equation 4.4}$$

This means the distribution of electrons between the two haems can be used to measure ΔΨ, referred to as the redox poise. The 'hidden' potential energy (ΔΨ) in the system holds the redox poise of the *b*-haems in an unexpected position. The redox potentials of the *b*-haems are determined by their oxidation state, using a model to account for their anti-cooperativity

(Springett, 2015b). This relies on the *b*-haems being in equilibrium with the Q-pool but means that the E_h of the Q-pool is measured by the same modelling.

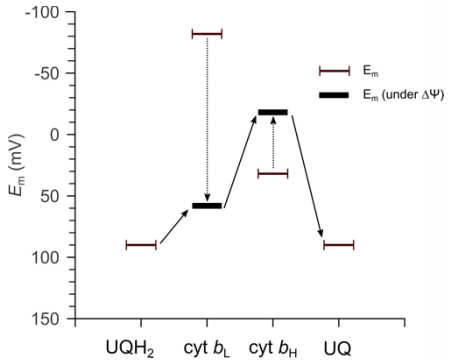

Figure 4.4 - The effect of ⊿Ψ the energy landscape on the cyt bc₁. *The ΔΨ Causes the E_m of the two b-haems to be closer together, a decrease in the E_m of b_L as it becomes more favourable to reduce.*

As demonstrated in Chapter 3, the Springett chamber system can be used to measure the haem signals from intact cells of the model species *Mycobacterium smegmatis.* Distinctive haem signals from the different haem types (under particular growth conditions) are present. These signals also respond to classical metabolic effectors, mainly in a predictable fashion. These have allowed us to perform experiments where we can transform the haem signals fully from their reduced form to their oxidised form allowing the calculation of their concentration. This is important in allowing the calculation of the ratio of oxidised and reduced haem for each centre. The E_h of each centre can then be calculated from this ratio and so used to calculate the ΔΨ.

The main limitation of this approach is the specialised hardware required for the spectral measurements and the prerequisite knowledge about the cyt *bcc* enzyme required for the calculation. Assuming that all homologues of the cyt *bc* enzyme operate in a similar fashion, i.e. the transfer of electrons from b_L to b_H do work against ΔΨ, one also requires a complete spectral and thermodynamic model of the enzyme. By this, I mean isolated difference spectra for all the components and E_m values to describe the redox potential of the *b*-haems. It also requires that the cyt *bcc* is abundant enough in the membrane of the cell to be able to detect it in the total haem spectrum. If the cyt *bcc* is the dominant cytochrome in the membrane, it would help to prevent mis-fitting as the result of other cytochrome complexes. This coule be the result of choice of growth conditions or by genetic manipulation or both.

4.1.8 Mycobacterial cyt *bcc* vs canonical cyt bc_1 complex

The cytochrome *bcc:aa*$_3$ supercomplex is the dominant spectral component of mycobacterial membranes, particularly in the exponential phase of growth (see Chapter 3). This supercomplex is made up of a homologue of cyt bc_1 (complex III) and a homologue of cyt aa_3 (complex IV). In mycobacterial species where the operon encoding the cyt *bcc*, *qcrCAB* operon, has been knocked out or knocked down, growth is considerably slower than wild-type strains (Matsoso et al., 2005; McNeil et al., 2022b). The dependence on a cyt *bc* type complex during growth may be unusual for bacteria. Whilst cyt *bc* type complexes appear to be present in several other bacterial species, they do not appear to be as dependent on the complex for growth as in mycobacteria. A *qcrA* knockout in *B. subtilis* showed no change in growth rate (Yu et al., 1995). It is unclear what conditions *B. subtilis* utilised a cyt *bc* type complex but it may be used to conserve reducing equivalents when nutrients are scarce (Mueller and Taber, 1989).

Other bacterial species appear to be more reliant on quinol oxidase. These quinol oxidases are part of either family of oxidases (Haem-Copper Oxidases type or cyt *bd* type). What does have to be considered is that most laboratory growth conditions favour rapid growth. This may favour bacterial growth to the detriment of maximising the *pmf* generated by carbon sources. The large protein complexes associated with respiratory chains that have energy-demanding biosynthesis processes may present too great a cost particularly when bacteria are aiming to grow as quickly as possible (Basan et al., 2015). Several bacterial species have no cyt *bc* type complex such as *E. coli,* however, *E. coli* does have a nitrate reductase with some homology to the cyt bc_1 complex. This does not necessarily rule out a similar ΔΨ measurement approach for bacteria that do not have a cyt *bc* type complex present in great abundance. Any intra-complex transfer of electrons where the electrons move across the membrane will result in either work against or with the ΔΨ. The advantage of the cyt *bc* complex is that it has already been used to measure the ΔΨ inside intact mammalian cells and so the thermodynamic model underlying the measurement is already understood.

Importantly for translating this ΔΨ measurement from mammalian to mycobacterial cells the spatial arrangement of the *b*-haems is conserved between the species. The fold of the membrane portion of the cyt *bc* complex is conserved between the mycobacterial and mitochondrial homologs as well as other cyt *bc* type complexes (Fig 4.5). This includes cyt b_6f complexes in photosynthetic organisms and cyt b_6 from the *Bacillus* genus. The main point of difference between the mycobacterial and mitochondrial homologue is in the cyt *c* chain/high potential chain. It appears that the mycobacterial ISP head domain cannot move from the cyt *b* position to the cyt *c* position, (Kao et al., 2022; Yanofsky et al., 2021) as

happens in the mitochondrial homologue (Zhang et al., 1998). This is due to non-conserved subunits, LpqE, of the mycobacterial supercomplex that block this movement. It is unclear why this is different between the homologs but based on distance would result in a slower rate of electron transfer from the FeS cluster to the first *c* haem (Kao et al., 2022; Riepl et al., 2024).

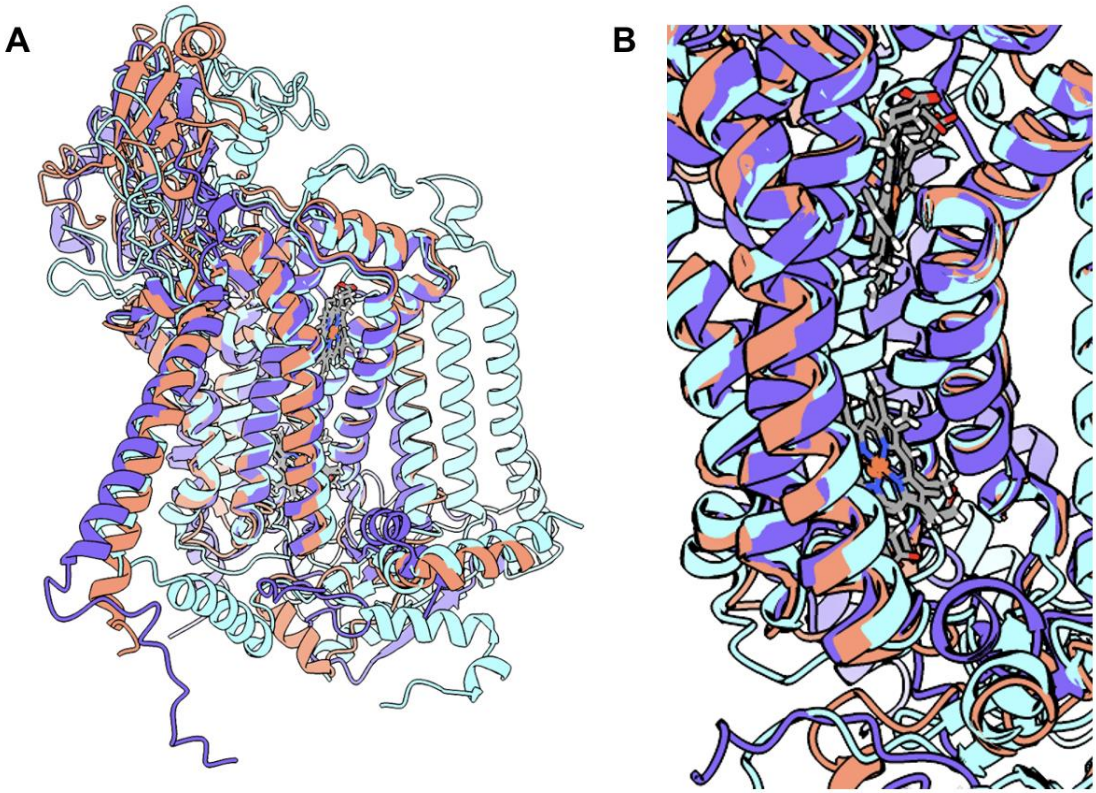

Figure 4.5 - Fold conservation of the cyt bc type complexes *(**A**) Global conservation of the membrane portion of the cyt bc type complexes, Light blue is the mycobacterial cyt bcc complex (PDB 7RH5, Yanofsky et al., 2021), purple is the bovine cyt bc_1 (PDB 1NTZ, Gao et al., 2003), and in red is the R. sp cyt bc_1 (PDB 8ASI, Swainsbury et al., 2023) (**B**) Focused view on the conservation of b-haems positions. Despite some global differences in the cyt bc type complexes the spatial arrangement of the haems and surrounding protein fold is very conserved.*

The conservation in the membrane portion of the cyt *bc* complex means that measuring the redox poise of the *b*-haems should be a tractable way to measure ΔΨ in live intact mycobacterial cells. To realise this ambition, what first has to be determined is how 'wrong' the model of the mitochondrial cyt bc_1 is for the mycobacterial homolog.

4.2 Aim and objectives for this chapter

Aim:

Develop methods to measure ΔΨ in the bioenergetic system of living mycobacteria as it powers the cell and changes in response to external stimuli.

Objectives of this chapter:

1. Apply a 'tweaked' spectral and pre-existing thermodynamic model of the mammalian cyt bc_1 enzyme to mycobacteria to measure ΔΨ and assess its validity and shortcomings
2. Use the purified cyt *bcc:aa*$_3$ supercomplex to measure mycobacterial spectral components and estimate their E_m values
3. Build a thermodynamic model for the mycobacterial supercomplex, incorporating redox anti-cooperativity between *b*-haems to create a mycobacterial spectral and thermodynamic model.
4. Apply the model for the mycobacterial supercomplex developed in objectives 2 and 3 and assess its validity and utility.
5. Make recommendations for where there are 'missing pieces' that future research could address.

4.3 Results

4.3.1 First estimations of ΔΨ in *M. smegmatis* using the mitochondrial bc_1 model

To assess the feasibility of measuring ΔΨ in live mycobacterial cells the mitochondrial model described in Kim et al. 2012 was used (Fig 4.6). This mitochondrial model includes mitochondrial reference spectra that have been adapted to the total spectrum from mycobacteria cells as described in Chapter 3. The model also includes a thermodynamic model of the mitochondrial cyt bc_1, including the E_m values accounting for anti-cooperativity between the *b*-haems.

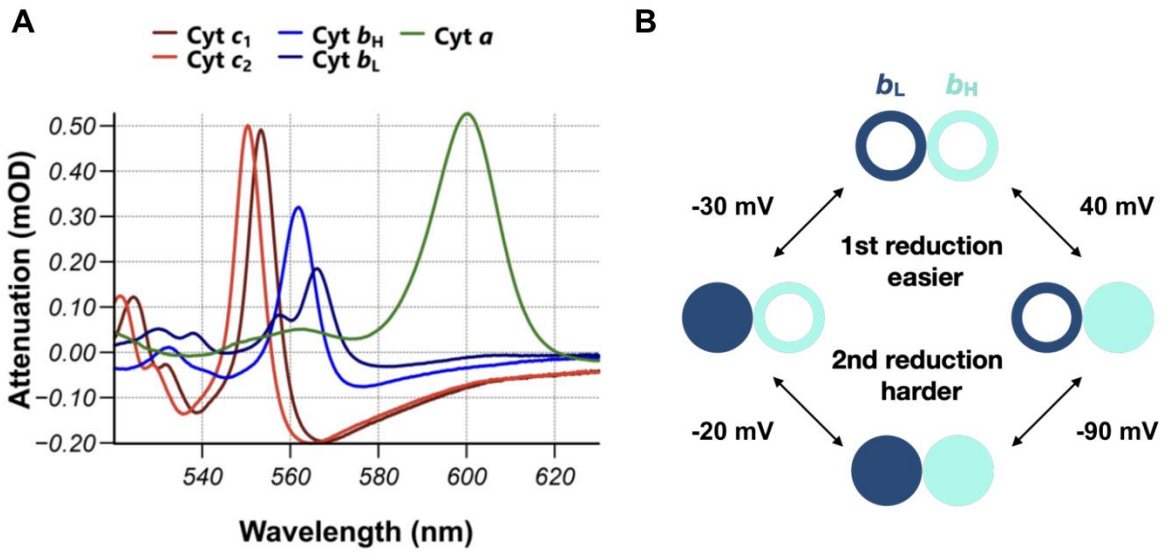

Figure 4.6 - Mammalian/Mitochondrial model used to 'first estimate' ΔΨ in mycobacteria *(**A**) Reference spectra of the mammalian cytochromes, Adapted from Kim et al. 2012 & Kim et al., 2011), adjusted as discussed in chapter 3 to account for the observed signals within mycobacterial cells. (**B**) Thermodynamic model of the b-haems of the cyt bc_1 complex**.** Used to calculate the Eh of the b-haems. The two different E_m values for each b haem (b_L: -30 mV & -90 mV, b_H: 40 mV & -20 mV) represent the anti-cooperativity between the two haem centres (~ 60 mV, as estimated in Shinkarev et al., 2001 and used in Kim et al., 2012). This makes reducing either centre harder when the other is already reduced.*

The trial experiment/run shown in Fig 4.7 (previously shown in Chapter 3) was used to examine the effect of the classical uncoupler FCCP on mycobacteria. A *ΔcydAB* strain of M. smeg was used, where the cyt *bd* oxidase has been knocked out. Using this strain limits the *b*-haems of the cyt *bd* interfering with the accounting for the cyt *bcc b*-haems signals. As described in Chapter 3 the lack of fixed pathlength in chamber systems means that concentration cannot be determined for the haems. The only way to obtain the oxidation state required for the ΔΨ measurement is to fully transform the haems from their oxidised to their reduced state. This approach works for redox enzymes in the respiratory chain that must switch between their oxidised and reduced states readily. In Kim et al. 2012 this was achieved with Rotenone and 3NPA (oxidised) and anoxia (reduced). This protocol has had to be adapted for mycobacteria, due to different sensitivities to metabolic effectors or conditions as addressed in Chapter 3.

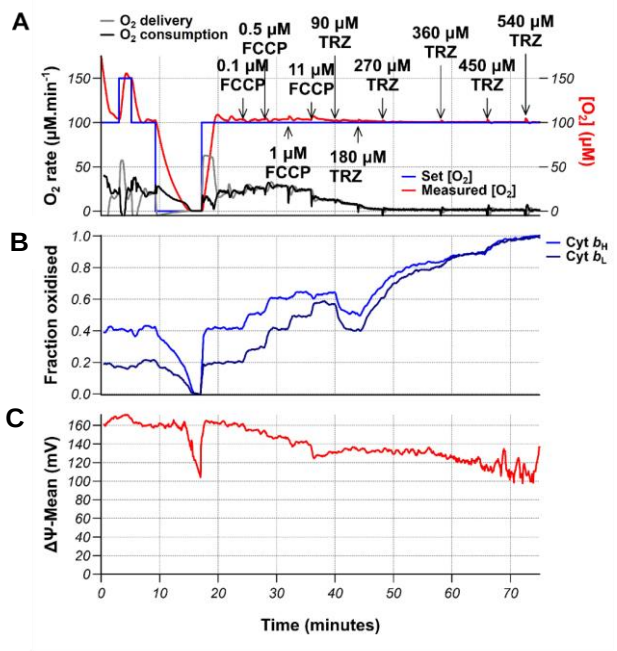

Figure 4.7 - First estimate of ΔΨ in mycobacteria *(**A) Oxygenation and oxygen consumption during the run,** ΔcydAB M. smeg, Set and measured oxygen consumption are shown in blue and red, respectively. Oxygen delivered by the tubing and oxygen consumed by the cells is shown in grey and black respectively. Effector addition points are indicated with arrows. FCCP (classical uncoupler) TRZ - thioridazine (hypothesised ndh2 inhibitor & redox cycler). Run previously shown in chapter 3 (Fig 3.53)* ***(B) Haem traces for b_L b_H & c_1 transformed to show oxidation state during the run*** *Haem traces produced from decomposed the total spectrum with Fig 4.6A have their oxidised point and reduced point set, giving the oxidation state of each centre throughout the run. The oxidised point is at 74 mins and the reduced point is at 16 mins.* ***(C) Calculated ΔΨ during the run*** *Using the derived oxidation states (middle panel) and the thermodynamic model in (Fig 4.6 B) the ΔΨ during can be calculated using Eq 4.4. For clarity, this has been contiguously averaged (1 min period every 0.1 min)*

The calculated ΔΨ is shown in Fig 4.7 C showing the expected decrease in ΔΨ upon the addition of the uncoupler FCCP. Interestingly this decrease continues at a concentration of FCCP (1 µM and above) after the oxygen consumption rate has peaked.

4.3.2 Caveats with the mitochondrial bc_1 model: 'when the answer is right but the working is wrong'

This data suggests that it is at least feasible to try to make ΔΨ measurements on mycobacteria, particularly given the expected decrease in ΔΨ is seen upon the addition of FCCP. The main issue is that we do not know how wrong the mammalian model is for mycobacteria given that the cyt bc_1 (mam) and cyt *bcc* (myco) are not identical. There are issues with both the spectra and electrochemical components of the mitochondrial model used.

Briefly, there are potentially unknown differences in the mycobacterial haem spectra to the known mitochondrial haem reference spectra. Within this, there could be differences in spectral components of the mycobacterial cyt *bcc* complex compared to the mitochondrial cyt bc_1 complex, as well as additional mycobacterial cytochromes with b-type haems. Both these factors could lead to mis-fitting of the spectra and so miscalculation of the ΔΨ. We also do not know how different the energy landscape of the mycobacterial cyt *bcc* complex is from the mitochondrial cyt bc_1 complex. This again could lead to miscalculation of the individual E_h and therefore the ΔΨ.

4.3.3 Mycobacterial haem reference spectra

The first of these issues to address would be the cyt *bcc* complex reference spectra. The exact spectral contribution of each of the haem cofactors for the mycobacterial enzyme has yet to be characterised. Therefore, it is difficult to determine how different these are from the known reference spectra from mitochondrial cyt bc_1 complexes. The major α-peak of individual haems will broadly reflect the chemical type of haem, Haem C - 550 nm, Haem B - 560 nm, Haem A - 600 nm, Haem D - 630 nm (reduced) but will then be further modified in shape and peak by the protein environment around the haem group.

To address this, I set out to directly measure mycobacterial haem reference spectra. Apart from being able to measure the ΔΨ inside live mycobacterial cells, it would also allow us to see how the electron occupancy is altered for each centre in response to metabolic effectors. If this was in combination with reference spectra for other cytochrome components of the mycobacterial respiratory chain it would help the interpretation of how these metabolic effectors are perturbing the chain. Given the interest in the mycobacterial OxPhos system as an antituberculosis target space, this could help in drug and combination regime design.

4.3.4 Purifying the supercomplex

The mycobacterial cytochrome *bcc:aa*$_3$ supercomplex, which contains the cyt *bcc* complex, has previously been structurally characterised by several groups via electron cryo-microscopy (Gong et al., 2018; Wiseman et al., 2018; Yanofsky et al., 2021). Yanoksky et al. utilised a chromosomal 3xFLAG tag to purify the whole cyt *bcc:aa*$_3$ in a one-step process. My colleague Dr Morwan Osman used the same phage-based recombination system (Oligonucleotide-mediated Recombineering followed by Bxb1 Integrase Targeting, ORBIT, (Murphy et al., 2018)) to reproduce the qcrB-3XFLAG strain as in Yanofsky et al.

This 3xFLAG tag can be pulled down using an antibody-based agarose resin which has a specific and high affinity for the FLAG epitope. Previous multi-step purifications of the cyt *bcc:aa*$_3$ have shown that it can result in the loss of subunits (Yanofsky et al., 2021), specifically a additional size exclusion step. The instability of the complex appears to be dependent on the detergent used to some degree. It has been reported that the cyt *bcc:aa*$_3$ did not lose subunits if it was solubilised in GDN rather than DDM (Król et al., 2022). However, GDN is poor at extracting proteins from membranes. Using GDN, to extract sufficient amounts of protein Król et al. solubilised the membranes overnight. To balance this and concerns that a long period of solubilisation may decrease the activity of the complex, I chose to extract with DDM for a short period of time. Whilst the complex was immobilised on the resin, the wash and elution buffer contained GDN instead, hopefully exchanging the detergent solubilising the complex. Based on spectral and BN-PAGE characterisation this was a pure cyt *bcc:aa*$_3$ preparation, Fig 4.8. As such a single FLAG tag purification step gives a pure intact supercomplex sufficient for the characterisation I wished to pursue. The profile of the elution run on an SDS-PAGE matches the previous publication including 2 bands at ~ 35 kDa, corresponding to CtaC and SodC.

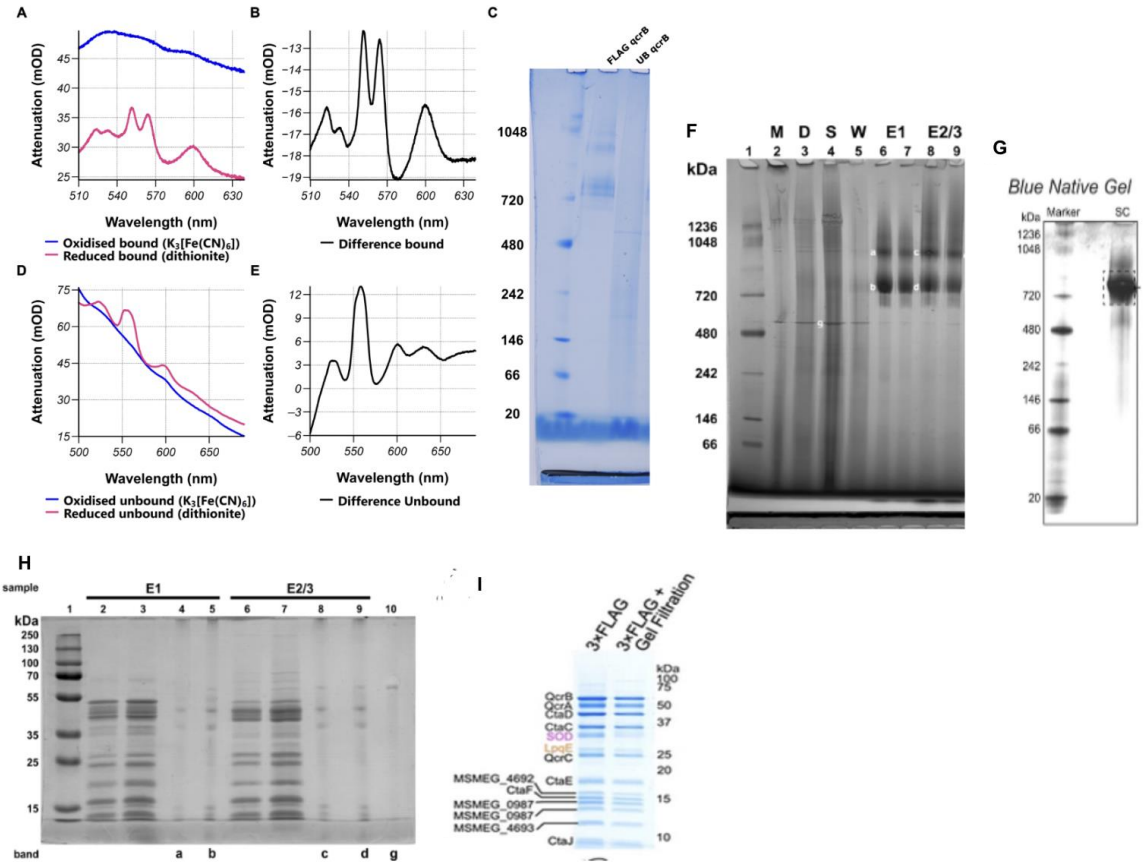

Figure 4.8 - Purification of the mycobacterial cytochrome bcc:aa₃ supercomplex*, (**A** & **D**) Oxidised and reduced spectra of the bound and unbound fraction from optimised purifications, Potassium ferricyanide oxidised (Blue) and sodium dithionite reduced (magenta) (**B** & **E**) Difference spectrum of bound and unbound fraction from optimised purifications (**C**) Blue native-PAGE of the bound and unbound fraction. The double band at around 720 kDa is consistent with the previous purification of the supercomplex. (**F**) BN-PAGE of early purification of cyt bcc:aa₃, M - un-solubilised membranes, D - after DDM solubilisation, S - supernatant from resin binding, W - elute from wash of the resin, E1 - 1 column volume (CV) elution with FLAG peptide, E2/E3 - pooled CV 2 and 3 elution with FLAG peptide. (**H**) SDS-PAGE of elutions off the resin plus SDS incubated BN-PAGE bands as indicated in F. (**G**) (Wiseman et al., 2018) and (**I**) (Yanofsky et al., 2021) BN-PAGE and SDS-PAGE from supercomplex purifications in the literature that have similar patterns of bands. In early purifications, it appears that the resin was overloaded, given the presence of supercomplex in the unbound/supernatant sample.*

Interestingly there are bands at higher molecular weights in the pure cyt *bcc:aa*$_3$ preparation (bound). Previous BN-PAGE of pure cyt *bcc:aa*$_3$ had a smear in this region (Wiseman et al., 2018, Fig 4.8 G). Factors other than the complexes's molecular weight can alter the distance

it will run on during PAGE, particularly native gels. However, it does match a pattern of banding seen in gels from membranes. The unbound samples appeared to contain spectral features from other cytochromes (distinctive cytochrome *bd* oxidase *d* haem signal) and some features from the cytochrome *bcc:aa*$_3$ supercomplex, Fig 4.8 E. The *a* haem signal is exclusive to the cyt *bcc:aa*$_3$ in mycobacteria. Given no full-size supercomplex could be seen on the BN-PAGE of the unbound fraction of the optimised purification, Fig 4.8 C, the *c* haem and *a* haem signal may originate from supercomplex that had fallen apart (cyt *aa*$_3$ component that had separated from the cyt *bcc* component) or overloading of the resin with intact supercomplex but at a concentration below the limit of detection of the BN-PAGE.

4.3.5 Assessing the suitability of mitochondrial reference spectra for the mycobacterial enzyme.

With a spectrally pure preparation of the supercomplex, the adapted mitochondrial fit could then be tested and its appropriateness determined. The purified supercomplex was run in a similar system to the chamber, however, in this system the light is collected in transmission mode for this system rather than remission (like a traditional cuvette). The oxygenation system is retained which allows some control over the oxygenation of an experiment. In a partially deoxygenated buffer, the enzyme was first oxidised with potassium ferricyanide ($K_3[Fe(CN)_6]$). This oxidises *a* haem and *c* haem which appear to be partially reduced in the 'as prepared' enzyme. Typically, more time or more additions of potassium ferricyanide were required to oxidise the haem *a* signal that the *c* haem signal. The *b* haem signal appeared to be oxidised in the 'as prepared' enzymes. The enzyme was then reduced with sodium dithionite. This resulted in the reduction of all the haem signals, *a* haem signal and *c* haem signal very quickly and then *b* haem signals much more slowly. The adapted mammalian fit developed in Chapter 3 was then applied to the spectra collected during the run (Fig 4.9).

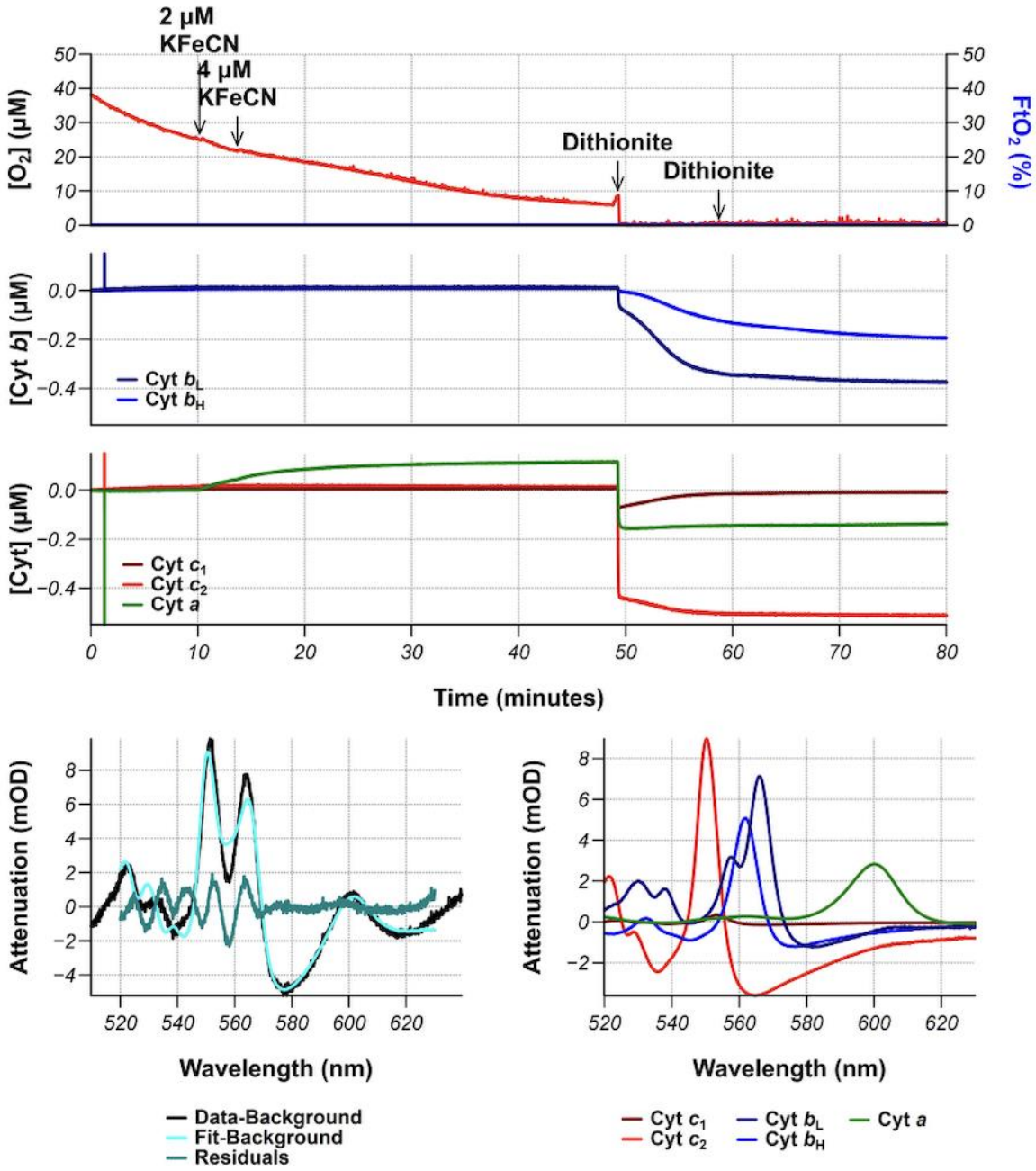

Figure 4.9 Decomposition of purified cyt bcc:aa$_3$ spectra with mammalian fit *Top panel - oxygen concentration during the experiment inducing any addition of oxidants or reductants. Middle two panels - haem traces from the decomposition of the spectra using spectral model 1 (as shown in Fig 4.6 B). Bottom panels - an example of the fit of the spectral model. The distinct features in the residuals (turquoise))demonstrate the mis-fitting. The labels indicate the final concentration in the cuvette. A concentrated stock of dithionite (~1 M) was used, typically with 2 µL additions.*

The purified supercomplex allows for experiments with a much greater signal-to-noise ratio. From this, it is apparent that the adapted mitochondrial fit does not match the purified supercomplex, as seen in the clear deviations in the residual (Fig 4.9 bottom panel). There

are several features in the residual, particularly around the 550-570 nm region indicative of mis-fitting. Interestingly, from the haem traces it appears that it would be more appropriate to fit the *c* haem signals as one peak (Fig 4.9 central panel, red and brown haem traces). Slightly strangely it appears that the mitochondrial b_L signal reduces before the b_H signal (Fig 4.9 second panel, blue traces). One would expect the centre with a more negative E_m, b_L, to reduce after the centre with the more positive E_m, b_H. This appears to be the opposite of what is observed with the haem traces, where the b_L trace is nearly fully reduced by 60 mins whereas the b_H signal is still partially oxidised. The ratios of the different haems also do not match what would be expected, however, given the features in the residual it is difficult to tell if this is because of an inappropriate extinction coefficient or just as a result of the mis-fitting.

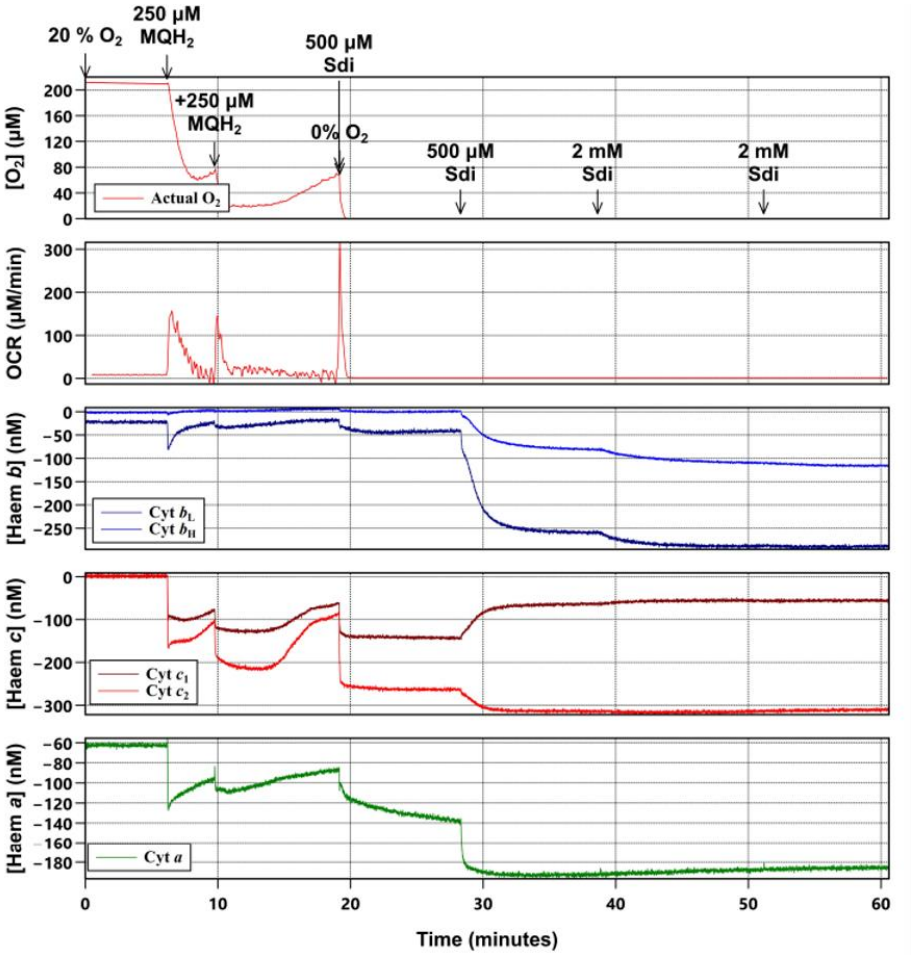

Figure 4.10 - The response of isolated cyt bcc:aa₃ to reduced menadiol, *The change in oxygen consumption (second panel) and spectral response to the addition of chemically reduced menadione to purified cyt bcc:aa₃ supercomplex. The collected absolute attenuation spectra were decomposed using the spectral model 1 (lower 3 panels).*

To demonstrate that the purified complex was active, chemically reduced menadione was added to the complex. Oxygen consumption was monitored and the protein was monitored

spectrally, using the mammalian-derived spectral fit (Fig. 4.10). Again the same mis-fitting is observed. Interestingly, the reduced menadione easily reduced the *c* haems and *a* haems but struggled to reduce the *b* haems. The initial rate of oxygen consumption was 154 uM.min^{-1}, equating to 52 e/s/complex, Table 4.1. This value is slightly lower than published values for the isolated complex (Riepl et al., 2024), but much lower than an approximate rate from cells of 238 e/s/complex, using values from the experiment in Fig 4.7.

Table 4.1 - Preliminary rates of the cyt bcc:aa3 supercomplex, purified complex compared to in cell, *concentration of complex determined by haem A concentration,*

Condition	Oxygen consumption (μM.min^{-1})	[Cyt *bcc*:*aa*$_3$] (nM)	Volume (mL)	Turnover rate (e/sec/mol)
Purified protein	155	200	2.1	52
In cell	25	7	5	238

4.3.6 Haem reference spectra: Building a spectral model that accounts for the signals from isolated cyt *bcc:aa*$_3$

It is apparent that improved reference spectra were required to properly fit the mycobacterial supercomplex spectra. To separate these haem signals the different centre's properties had to be exploited. One property is their E_m. Chemical oxidants or reductants could be used to selectively reduce or oxidise one centre at a time whilst the others are kept allowing their spectral contribution to be isolated. For scenarios where the midpoints are too close, using the spatial separation of the signal (by the wavelength of the peak centre), may offer a strategy for spectrally separating them.

Other properties that can be used are specific inhibitors of the various components of the mycobacterial supercomplex. Blocking certain substrate sites may be able to lock a centre in a particular oxidation state. Chemical oxidants/reductants could then be used to change the state of other centres allowing for their spectral separation. This relies upon the inhibitors working very specifically on the mycobacterial complexes. The mitochondrial homologues complexes are where the most information about the behaviour of inhibitors is known. However, the interest in mycobacterial OxPhos as an anti-TB target space has introduced several new inhibitors of components of the mycobacterial supercomplex. In terms of separating the spectral components, the mammalian system has also benefited from the fact that the complexes exist in distinct separatable complexes. The mycobacterial supercomplex, unlike some other supercomplexes, is obligate. This means that the cyt *bcc* or the cyt *aa*$_3$

components on their own are not competent enzymes and native activity cannot be reconstituted without the other complex. Even if it was possible to reconstitute the native activity of the individual complexes of the supercomplex, there would also be concerns about whether all necessary components had been retained during the purification process. It would be difficult to determine if any missing components would result in changes in the haem centre's protein environment that contribute to its specific spectral properties.

4.3.6.1 Determining reasonable models for *a* haem and *c* haem

The signals from haem A and haem C centres were the easiest to characterise by exploiting the response of different haems centres to oxidising and reducing agents. For the *a* haem signal, an initial addition of potassium ferricyanide ($K_3[Fe(CN)_6]$) oxidised all haems bar apart a small fraction of the *a* haem. This small fraction of *a* haem signal could be oxidised by a second addition of potassium ferricyanide Fig 4.11 B & C. The difference between the before and after this second addition gave a spectrum dominated by a peak at 600 nm, indicative of haem A, if noisy (Fig 4.11 D). This signal was assigned to both haems present in the complex, as it was not possible to distinguish the contribution of the two at this stage. In the mitochondrial cytochrome oxidase, a homolog of half of the supercomplex, the haem a_3 in the binuclear active site, has a broader spectrum than the other haem A centre (Liao and Palmer, 1996 and see mammalian reference spectra in Chapter 3, Fig 3.21).

The *c* haem signal proved more difficult to isolate. The addition of ascorbate would reduce the haem A and haem C centres but not the haem B centres. The rate of this could be increased by the redox mediator TMPD. Care had to be taken as TMPD interfered with the spectrum as its oxidised species has a spectrum which overlaps with the region of interest. The cuvette was kept anoxic by bubbling nitrogen gas through the system to prevent the TMPD oxidising and so interfering spectrally. The difference spectrum from before and after TMPD/ascorbate addition had both features from both haem A and haem C. Subtracting the *a* haem reference spectrum did not completely remove the haem A feature. To fully separate the *c* haem signal, a hybrid of the mitochondrial and mycobacterial *c* haem spectra was generated by combining the ascorbate spectrum from 510-554nm with the mammalian cyt c_1 reference spectrum from 554-630 nm Fig 4.11 F). The mitochondrial cyt c_1 spectrum had been aligned with the ascorbate spectrum to facilitate this as their peaks did not fully align (Fig 4.11 E). Given the separation of the *c* haem and *a* haem signals, whilst an imperfect solution it was sufficient for our purposes.

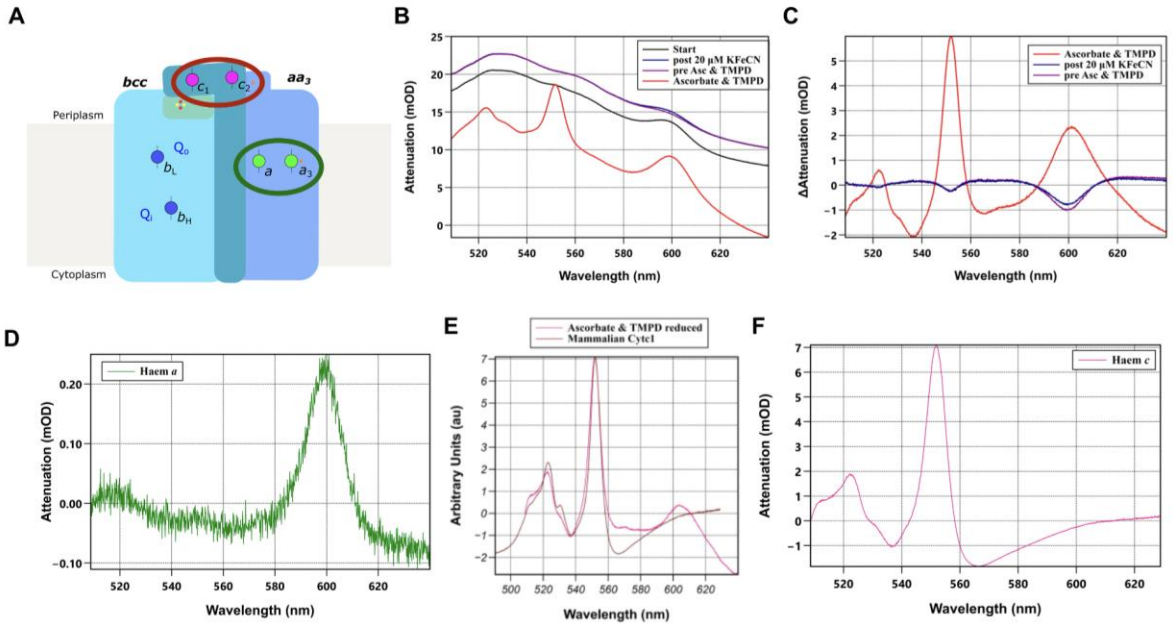

Figure 4.11 - Isolation of the mycobacterial a haem and c haem signal, *(**A**) Cartoon of the cyt bcc:aa$_3$ supercomplex with the haem C and haem A cofactor highlighted. (**B**) Average spectra at a specified point during the experiment: start, immediately after 20 µM K$_3$[Fe(CN)$_6$] addition, pre-ascorbate addition/ the most oxidised point of the run, post-ascorbate addition (**C**) These spectra with the starting spectrum subtracted. (**D**) Isolated a haem signal from the difference between immediately after 20 µM K$_3$[Fe(CN)$_6$] and the most oxidised point in the run, pre-ascorbate addition. (**E**) Alignment of the ascorbate reduced spectrum and mammalian cyt c$_1$ spectrum (**F**) Isolated c haem signal from the combination of the ascorbate reduced spectrum and mammalian cyt c$_1$ spectrum.*

4.3.6.2 Determining spectra for the *b*-haems: reasonable success for b_L but not b_H

To separate the spectral contribution of b_L, its more negative redox potential had to be utilised. Reducing the sample with NADH using phenazine ethanosulfate (PES) as a mediator could not reduce the B haem centress and only transiently reduced the C haem centres. All of the haems could be reduced if dithionite was added. Consistently it was observed that there was a very slow-to-reduce *b* haem signal, presumable b_L. Initially, I attempted to isolate the b_L signal by comparing the spectrum of the initial reduction to the spectrum of later reduction. b_L should be the last cytochrome to be reduced and so spectra of the latter portion of the reduction were compared (between 75 min (II) and 110 min (III). This often had contamination from an *a* haem signal, potentially because the ambient redox potential was not well equilibrated across the system. The cuvette is only kept anoxic by a N_2 line that may have small amounts of O_2. Performing this within a glove box or adding KCN would be a more

successful approach to preventing this inference. I had tried to avoid using any more mediators due to concerns over their spectral contributions.

Instead, the oxidative direction was used. Once the enzyme had been fully reduced by several additions of sodium dithionite, oxidised menadione was added. The addition of menadione resulted in the oxidation of this slow-reducing *b* haem signal (III compared to IV) which was aided by the addition of a small amount of oxygen (1%). Without the addition of menadione, similar oxidation of the enzyme resulted in both the *b* haem signals oxidised simultaneously, precluding their separation. This is presumably because both haems' oxidation states change too quickly to separate. The isolated b_L signal is shown in Fig 4.12. Using this signal, the mitochondrial b_H could be adjusted to account for the rest of the *b* haem signal in a total difference spectrum of the isolated protein. Interestingly the oxidation state of *c* haem and *a* haem did not recover to a fully oxidised state as at the beginning of the run.

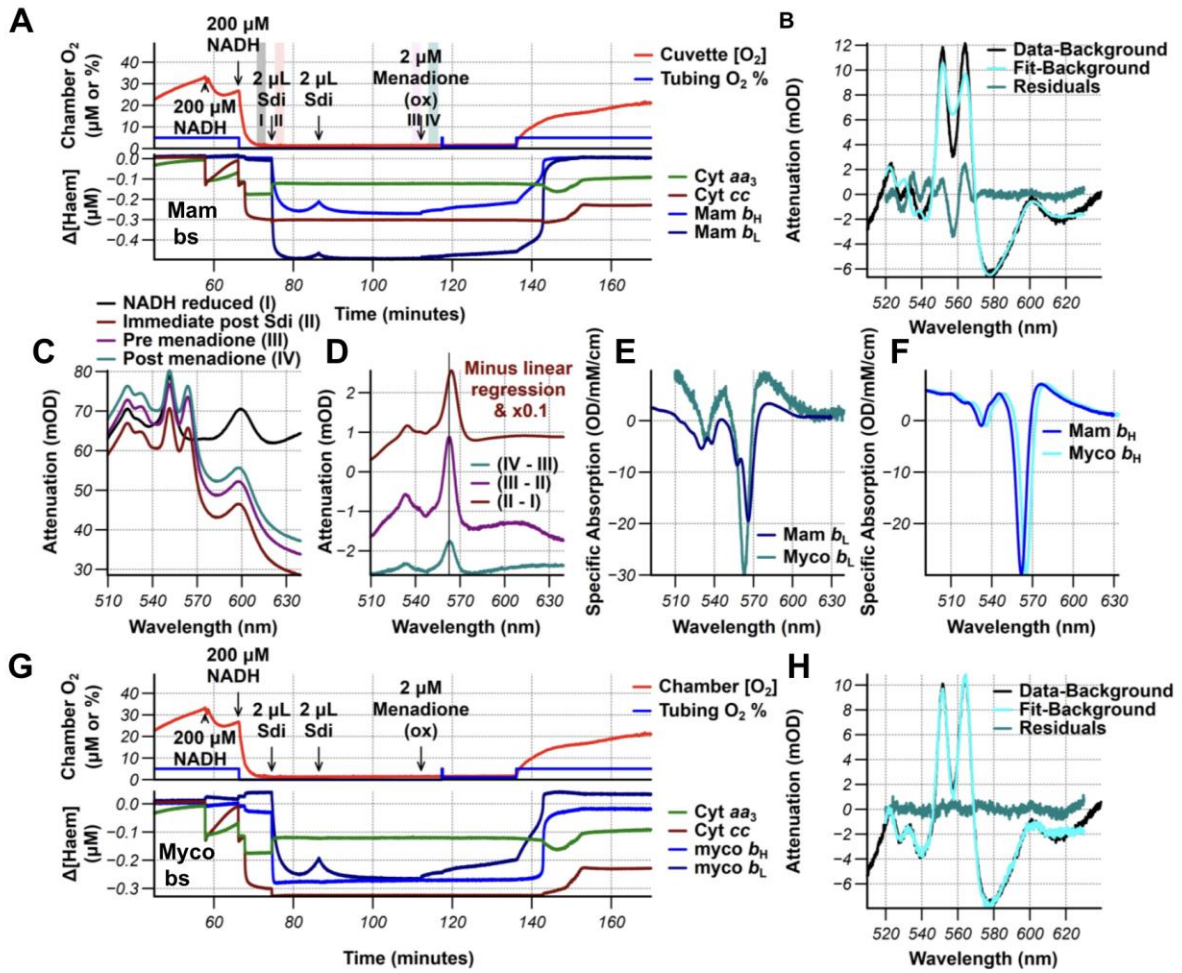

Figure 4.12 - Isolation of the mycobacterial b_L signal *(**A**) Purified cyt bcc:aa$_3$ supercomplex with PES, reduced with NADH, dithionite, and then oxidised with menadione and oxygen, cuvette oxygenation (top panel), decomposition of the spectrum using the isolated mycobacterial cyt aa$_3$, cyt cc and the mammalian b-haems (**B**) Example of fitting (mammalian bs) (**C**) Averaged spectra from time points during the run, I – NADH reduced complex, II – Immediately post dithionite reduction, III – At most reduced point pre menadione addition, IV- post menadione addition. Areas spectra average over indicated by shaded section in the top panel of **A**. (**D**) (**E** & **F**) Original mammalian reference spectra compared to new mycobacterial b_L and b_H. (**G**) Same cuvette experiment as in **A** except decomposed by new spectral model, cuvette oxygenation (top panel), decomposition of the spectrum using the isolated mycobacterial haems (**H**) Example of fitting (mycobacterial bs)*

4.3.7 Applying the mycobacterial reference spectra to purified cyt *bcc:aa*$_3$: a reasonable spectral model but without thermodynamic information

This new set of 'mycobacterial' reference spectra was applied to the previous run in section 4.3.6 (Fig. 4.13). This demonstrates that the new reference spectra are a much better fit for the data. The extinction coefficients were based upon those derived for the mammalian homologues of the respective enzymes and are described in Table 4.2. The mammalian c_1 extinction coefficient was doubled to reflect the two haem centres that the cyt *cc* signal is accounting for. It was judge best to use the mitochondrial b_H extinction coefficient for both mycobacterial *b*-haems as the spectral shapes matched the mitochondrial b_H best.

Table 4.2 - Initial mammalian mode (Spectral model 1) compared to the mycobacterial spectral model*, The Kim et al., 2011 spectra were measured by Roger Springett & Torsten Merbitz-Zahradnik. *For the minima, the value in the brackets represent the extinction coefficient at that value. This is reflected in the extinction coefficient values.*

Component	Sample origin	α - region maxima (nm)	α - region minima (nm)*	Extinction coefficient ($mM^{-1}cm^{-1}$)*	Reference
c_1	B. taurus	552.9	~530(-4.8)	(17.6+4.8)	(Kim et al., 2011)
b_H	B. taurus	561.95	~545(-5.2)	(30+5.2)	(Kim et al., 2011)
b_L	B. taurus	557.5, 566.1	-545(0)	20	(Kim et al., 2011)
aa_3	B. taurus	605.1	539(-3.3)	(23.3+3.3)	(Liao and Palmer, 1996)
c_1	M. smeg & B. taurus	553.3	~530(-9.6)	(35.2+9.6)	This work
b_H	B. taurus shifted + 3.5 nm	565.45	~545(-5.2)	(30+5.2)	(Kim et al., 2011)
b_L	M. smeg	563	~545(-5.2)	(30+5.2)	This work
aa_3	M. smeg	600.2	~539(-3.3)	(23.3+3.3)	This work

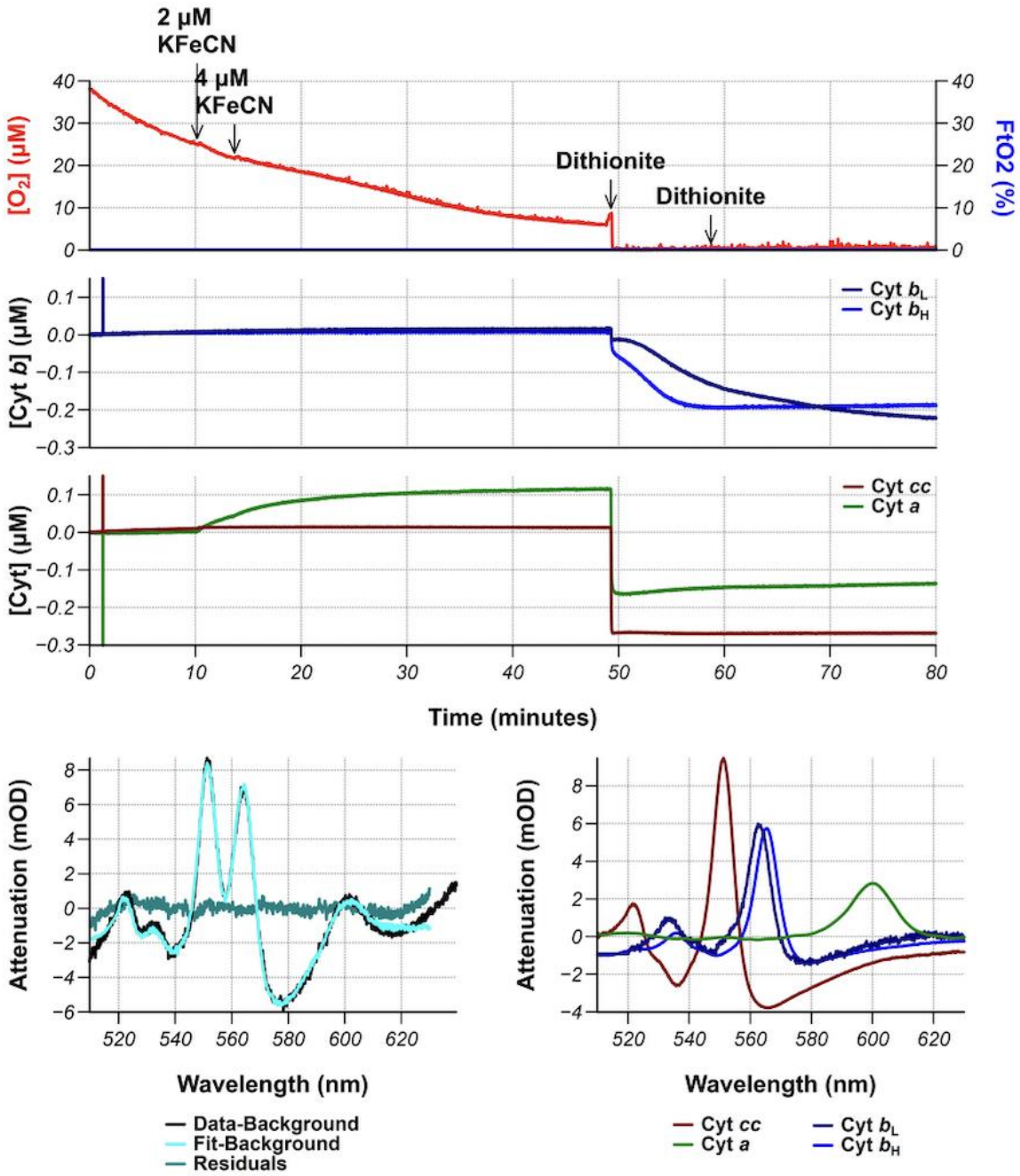

Figure 4.13 - Decomposition of purified cyt bcc:aa$_3$ spectra with mycobacterial fit (Final spectral model) *Same experiment as in Fig 4.9 with the new fit, Top panel - oxygen concentration during the experiment inducing any addition of oxidants or reductants. Middle two panels - haem traces from the decomposition of the spectra using spectral model 1 (as shown in Fig 4.6 B). Bottom panels - an example of the fit of the spectral model. Additions are as for Fig 4.9*

4.3.8 Determining the redox potentials of the *b*-haems in mycobacterial cyt *bcc*: a brief methodology

With an improved spectral model for the mycobacterial supercomplex, the next step was to characterise the E_m of the cyt *bcc* complex allowing for the accounting of the electrostatic interaction between the *b*-haems. One of the key differences between the mitochondrial cyt bc_1 and the mycobacteria cyt *bcc* is the quinol species that donates electrons to the complex. Like several other bacteria, mycobacteria use menaquinol as their membrane-soluble electron carrier. This is different to the ubiquinol that mitochondria use. Menaquinol has an E_m of -74 mV compared to ubiquinol's E_m of +100 mV, a significantly more negative redox potential. This means that electrons donated to the two homologs of the complex are at very different redox potentials.

Previously published work on the closely related corynebacterial cyt *bcc:aa*$_3$ demonstrated that the redox cofactors (including the haems) are tuned to reflect the substrate's more negative E_m values 17/02/2025 13:03:00. Logically the pattern of cofactors E_m tuning to match substrate E_m is broadly conserved for other related *bc* complexes that use menaquinol as a substrate (Bergdoll et al., 2016). It is likely that given the homology between the *C. glut* supercomplex and the mycobacterial cyt *bcc:aa*$_3$ the redox potentials of the cofactors will be broadly conserved.

4.3.9 Potentiometrically poising the mycobacterial cyt *bcc:aa*$_3$ for spectroscopic analysis

Prior work on the actinobacterial supercomplex only characterised the apparent E_m value of the redox centres. Given the need to more fully characterise the behaviour of the *b*-haems, we worked with Petra Hellwig and Frederic Mellin to replicate these potentiometric titrations for the mycobacterial supercomplex again. They performed this titration using a thin layer optical redox potentiometric system, Fig 4.14. This is a thin-layer electrochemical cell that has a working and reference electrode that allows the measurement of spectra during a different set of ambient redox potentials.

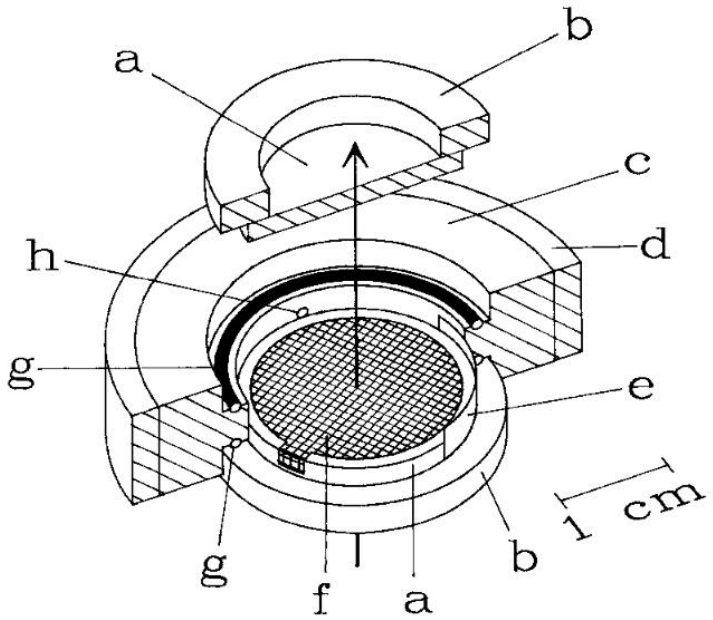

Figure 4.14 – Technical diagram of the thin layer spectroelectrochemical cell*, taken from (Moss et al., 1990) (a & b) Calcium fluoride window mounted on a plexiglass ring. (c & d) Teflon body with steel surround, encasing the cell. I platinum counter electrode, (f) gold mesh working electrode, (g) rubber O-ring (h) capillary connection to the reference electrode (Ag/AgCl 3 M KCl). The sample (volume ~8 µL) is placed in between the working electrode and the calcium fluoride window. As the titration is performed the spectra are collected through the optical axis (arrow) by a Cary 300 spectrometer coupled to a potentiostat. This setup results in a path length of ~ 10 µm.*

The measured titration in the oxidative and reductive direction are shown in Fig 4.15. Unfortunately, the oxidative titration was noisy, particularly around the regions associated with haem A (600 nm). This precluded some of the subsequent analysis with the oxidative direction. Whilst this titration set up provided a large amount of data, it had demanding sample requirements, ~10 µL at ~0.2 mM. Concentrating the supercomplex to this concentration, resulted in issues with precipitation, and ~5 times the amount of material required for the experiments performed in the cuvette.

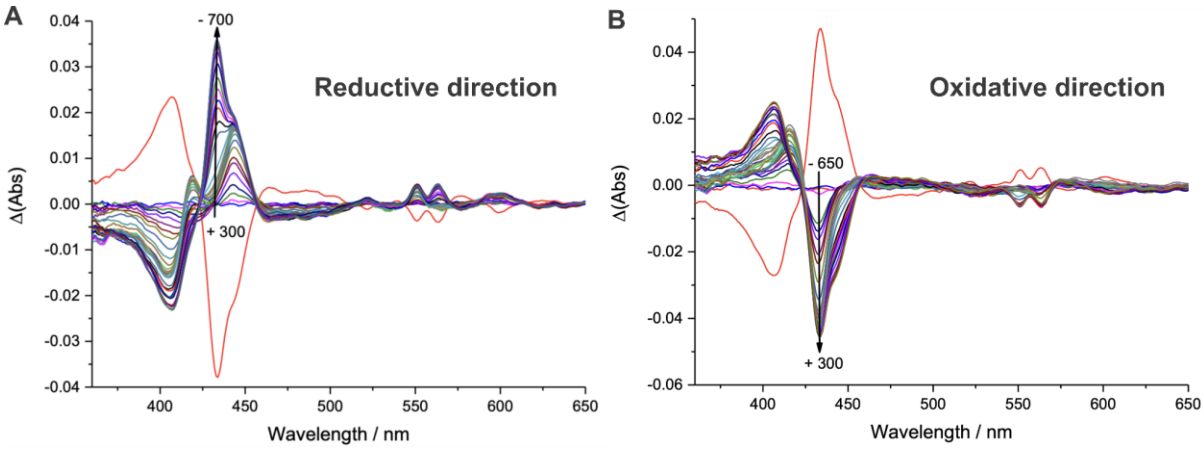

Figure 4.15 - Spectra collected during the reductive and oxidative titration experiments *(**A**) Reductive direction (**B**) Oxidative direction.*

4.3.10 Single wavelength determination of the redox potential of the mycobacterial cyt *bcc:aa*$_3$: a straight-forward initial analysis to build on

The classical approach to analysing potentiometric redox titrations, as in Kao et al. 2016, is to fit a Nernst equation for each redox centre observed (Eq. 4.5).

$$E_h = E_m + \frac{RT}{nF} ln \left(\frac{[Oxidised]}{[Reduced]}\right) \qquad \text{Equation 4.5}$$

Eq. 4.5 described how the ratio of the oxidised and reduced species of the redox centre ($\frac{[Oxidised]}{[Reduced]}$) related to the ambient redox potential (E_h). This is determined by the midpoint of the observed centre (E_m), where $[Oxidised] = [Reduced]$. *R*, *T*, & *F* are the gas constant, temperature (K) and Fara'ay's constant respectively.

As already discussed, the haems distinct spectral handles allow their redox state to be measured using UV/vis spectroscopy. Typically the normalised change in absorbance at a specific wavelength is used as a measure of the concentration of the reduced species so the fraction reduced can be calculated. Simple fitting procedures can then be used to calculate the E_m values based upon the Nernst equation. For circumstances where more than one centre of the same chemical type is present, two Nernst equations can be fitted. This approach does not give information about the degree of anti-cooperativity between haem centres in close proximity, for example, the two *b*-haems. This will be addressed later in this chapter.

As part of their initial analysis, Petra and Frederic performed this type of analysis of the collected data. The values of this closely match the values previously measured for the *C.*

glut supercomplex showing that the energy landscape is very similar and our preparation is behaving as expected. Fig 4.16 shows an example of Nernst fitting to the changes in absorbance at 551 nm (haem C), 563 nm (haem B), and 600 nm (haem A). All of the calculated E_m values are presented in Table 4.3.

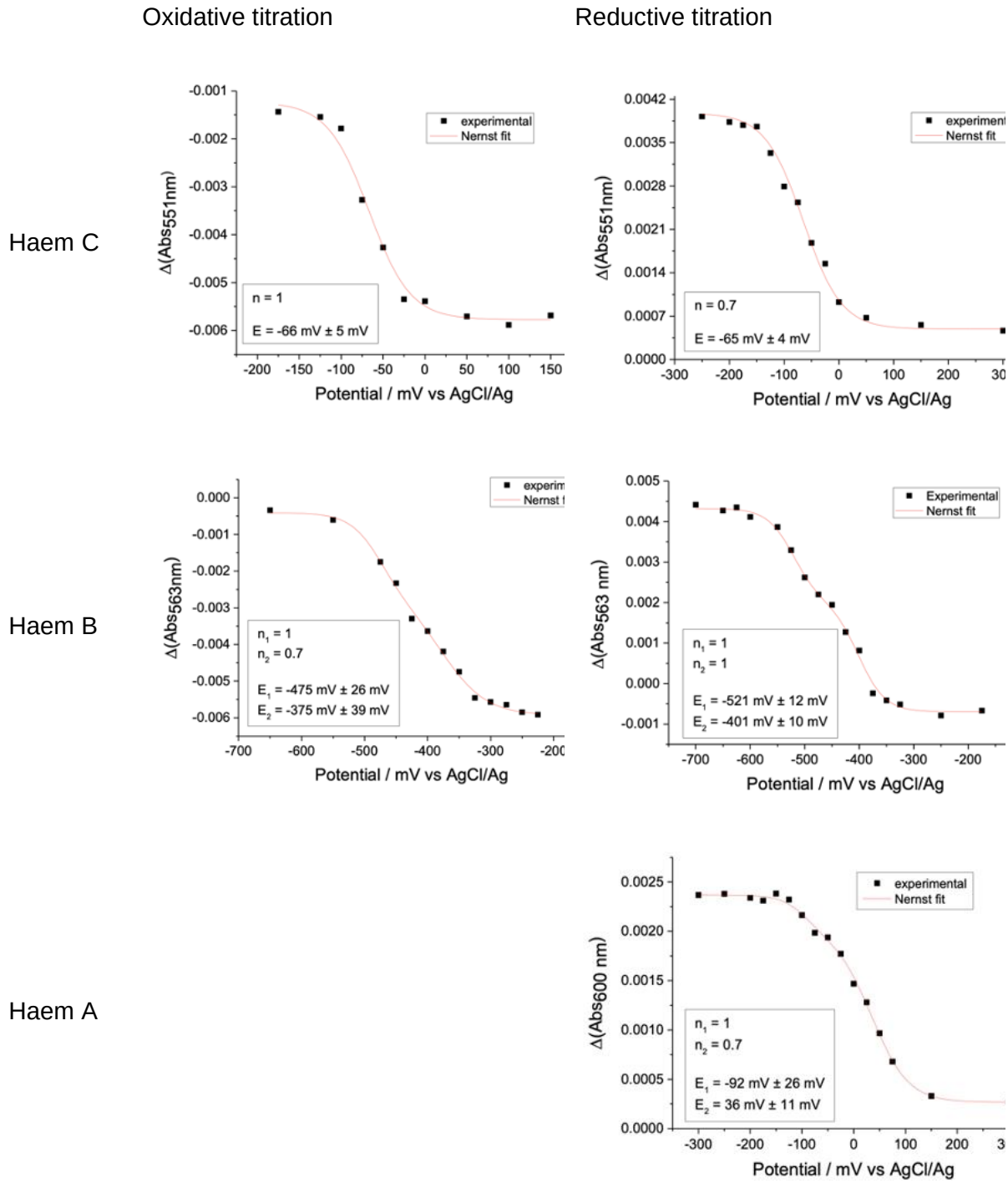

Figure 4.16 - Selection of the titration curves, *as collected and modelled by Petra Hellwig and Frederic Mellin*

Table 4.3 - E_m for the haem centres, *as determined by Petra Hellwig and Frederic Mellin*

Haem centre	Wavelength	Oxidative titration	Reductive titration	Average
a/a_3 (low E_m)	445 nm	155 mV ± 7 mV	176 mV ± 18 mV	166 mV ± 30 mV
	600 nm	Too noisy!	116 mV ± 26 mV	
a/a_3 (high E_m)	445 nm	333 mV ± 13 mV	276 mV ± 12 mV	305 mV ± 40 mV
	600 nm	Too noisy!	244 mV ± 11 mV	
b_L	432 nm	-312 mV ± 24 mV	-329 mV ± 7 mV	-320 mV ± 30 mV
	563 nm	-267 mV ± 26 mV	-313 mV ± 12 mV	-290 mV ± 40 mV
b_H	432 nm	-179 mV ± 14 mV	-188 mV ± 5 mV	-183 mV ± 20 mV
	563 nm	-167 mV ± 39 mV	-193 mV ± 10 mV	-180 mV ± 40 mV
c	551 nm	142 mV ± 5 mV	143 mV ± 4 mV	143 mV ± 5 mV

This titration data and analysis reaffirm the observation that menaquinone using enzymes has redox centres with more negative E_m to accommodate the more negative substrate. It could even be argued that ubiquinone-using enzymes have adapted the redox potentials of their redox centres to a more positive substrate given that it is likely during the evolutionary history of these enzymes, it is likely menaquinol was used prior to ubiquinol. The current analysis does not give information on the degree of anti-cooperativity between the centres. From the apparent E_m values of the two centres, one could assume that the same degree of anti-cooperativity exists as in the mitochondrial enzyme. This could then be used to generate a model of the anti-cooperativity as in Fig 4.6 B. However because of the importance of this behaviour to the ΔΨ calculation we wished to examine this further.

4.3.11 Fitting a unified spectral-thermodynamic model for the cyt *bcc:aa*$_3$: explanation of the approach and introduction to the mathematical and programming tools needed

Underlying a titration is the transformation of a signal from one form to another. In the case of redox titration between the oxidised and the reduced form, or vice versa depending on the direction of the titration. The transformation of the signal is dependent on the independent variable that is being changed during the titration, in this case, the ambient redox potential

(E_h). Properties such as the E_m will dictate how this signal shall change as a function of the dependent variable (E_h). This transformation is made more complex by behaviour such as anti-cooperativity between haem centres.

In this section, I will describe the behaviour of the haem signals in the cyt *c* oxidase as an example to illustrate the complexity that anti-cooperativity introduces to understanding the E_m of haem centres. I will then illustrate how the spectrum from the titration can be decomposed to better determine the E_m of haem centres rather than just by following the change in absorbance at one wavelength. I do this with a set of spectral models that build towards the final spectral model made up of the extracted difference spectrum from the mycobacterial enzyme. This allows the assignment of an E_m to the spectra in this final spectral model. This then builds towards a unified spectral-thermodynamic model to describe the properties of the cyt *bcc:aa*$_3$ supercomplex determined simultaneously from fitting to the titration data. This characterisation may demonstrate where there are issues with the extracted spectra. All of this analysis will provide the information needed to be able to measure $\Delta\Psi$ from the redox poise of the *b*-haems in the mycobacterial cyt *bcc*.

Examining this titration data in more depth requires mathematical tools, namely decomposition and least squares parameter estimation. I implemented these in the accessible programming language Python (Van Rossum and Drake, 2009) using the NumPy and SciPy libraries (Harris et al., 2020; Virtanen et al., 2020).

4.3.11.1 Decomposition using matrices

I have previously described spectral decomposition in chapter 3, see section 3.3.1.2.2. A similar set of matrices can be used to describe the titration. Fig 4.17 and Eq. 4.6 illustrates the matrices that can be used to describe the titration and their relationship:

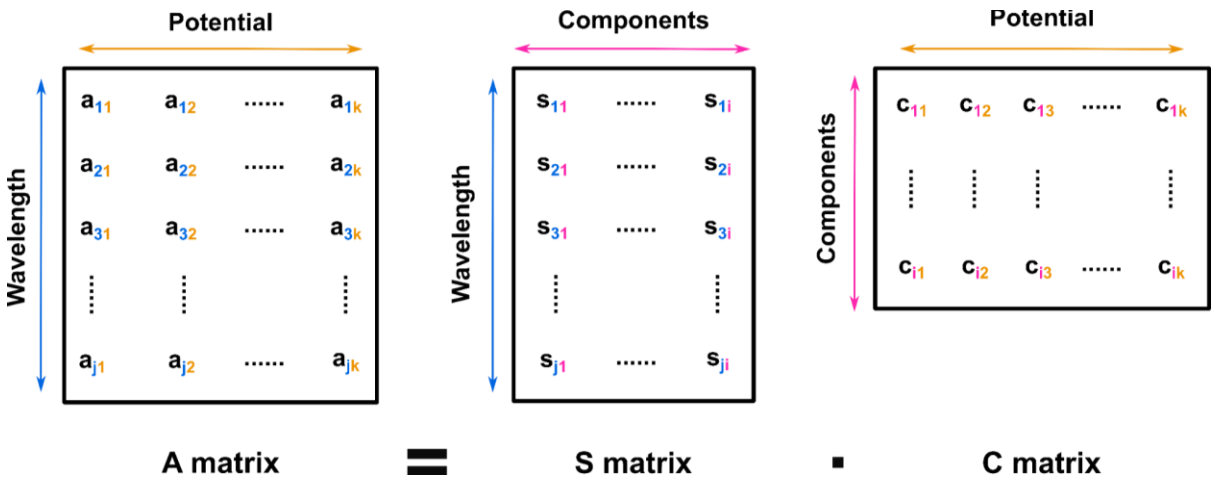

Figure 4.17 - Matrices described in Eq. 4.16

$$\mathbf{A} = \mathbf{S.C} \qquad \text{Equation 4.6}$$

For *i* number of components measure over *j* number of wavelengths at *k* number of voltages. **A** is a *j* x *k* matrix of the absorbance at each wavelength at each voltage measured i.e. a matrix of the titration spectra. Given the Beer-Lambert law, it is the product of **S** and **C,** where **S** is a *j* x *i* matrix of the known specific absorbance at each wavelength for each component, (i.e. a matrix of the reference spectra) and **C** is a *i* x *k* matrix of the concentration of each component at each wavelength for each voltage measured. To solve for **C** Eq. 4.7 can be used, which can be coded for in NumPy as described previously.

$$\mathbf{C} = (\mathbf{S}^{T}.\ \mathbf{S})^{-1}.\ \mathbf{S}^{T}.\ \mathbf{A} \qquad \text{Equation 4.7}$$

4.3.11.2 Least squares parameters estimation and optimisers

Least squares parameters estimation is a form of regression analysis used in data fitting. It is based upon the minimisation of the sum of the squared residuals, where the residual is the difference between the data and the predicted model (Eq. 4.8). Squared residuals are used so that negative differences become positive and are weighted equally with the positive differences.

$$\chi^2 = (y(obs) - y(pred))^2 \qquad \text{Equation 4.8}$$

Optimisers use an iterative process to fit nonlinear equations, such as Nernst functions. For a set of input values, a function is evaluated, the fit with the data calculated, and the difference scored, typically using a least squares approach. That creates a landscape of inputs and their fit and the optimiser finds a minima. The minima are the parameters of the object function where the difference score is as small as possible. Typically the process has a stop value so that it avoids searching for ever finer accuracy beyond that which the data can provide, which is called overfitting. Optimisers have been intensively developed over centuries and most modern implementations rely on intensive work carried out in the 1970s and 80s to develop the MINPACK and LINPACK libraries for FORTRAN subroutines (Dongarra et al., 1979; More et al., 1980); in many cases, these are still used directly.

SciPy's optimize module allows the implementation of several algorithms in order to do this process. For the fitting described in this chapter, I utilised the curve_fit function (Vugrin et al., 2007). For functions within this module, an objective function has to be defined describing the expected behaviour of the data that one wishes to fit. Optimize functions such as curve_fit, take this objective function, the xdata (independent variable over which the data was measured) and the ydata (the dependent variable) and use it to estimate the parameters for

the data. An initial guess of the parameters for the object function can be included, as well as bounds on these variables. This is coded by:

curve_fit(object_function, xdata, ydata, p0, bounds = (lower_bounds, upper_bounds)

The output of this function is an array of the optimised parameters and a covariance matrix, where the diagonals of this matrix are the variance of each parameter. The curve_fit function can utilise 3 different algorithms to approach nonlinear problems, the Levenberg–Marquardt algorithm (LM), the Trust Region Reflective algorithm (TRF) and the Dogleg algorithm (dogbox). In curve_fit, the default is the Levenberg–Marquardt algorithm (sections 4.3.12 - 4.3.13) unless bounds are given, in which case the Trust Region Reflective algorithm is used, (section 4.3.14, this shortened the run time and did not appear to alter the outcome).

4.3.12 Redox anti-cooperativity and spectroscopic data fitting pitfalls: cytochrome *aa*$_3$ simulations as a case study

When two charged centres are in close proximity there will be some degree of anti-cooperativity between their affinity for electrons due to Coulombic repulsions i.e. reducing a redox centre when a nearby centre is already reduced will be harder than if the nearby centre is oxidised. This means that the apparent Nernstian E_m will be different to the actual E_m of the centres, i.e. if one were able to measure the E_m of each centre individually (for example if one of the centres had been removed via purification or mutation). This type of anti-cooperativity behaviour has been thought about more in-depth for the haem centres within mammalian cyt *c* oxidase (a member of the haem copper oxidase family) and these studies present a case study in data fitting pitfalls. The case study was helpful for me to develop simulation approaches using the mathematical and programming tools introduced above. This package will be used later for studying mycobacterial supercomplex.

Early titrations of mammalian cyt *c* oxidase showed an *a* haem signal titrating as in Fig 4.18 A, with two deflection points. This signal could be fitted to two Nernst functions corresponding to two E_m of ~ 360 mV & ~ 220 mV. Further investigation found that these two Em values did not correspond to the different centres, but instead two centres both with a high E_m of ~340 mV (Nicholls and Petersen, 1974) with a strong anti-cooperative interaction of ~ -100 mV (Krishtalik, 1985). To demonstrate how from single wavelength titrations, these two models are indistinguishable I have simulated the two scenarios in Fig 4.18 B. The input data in panel A was fitted to either a model using two Nernst functions or two Nernst functions with anti-cooperativity introduced between them. It can be seen that the two models cannot be distinguished by fitting alone as in both cases a reasonable fit to the haem signal is achieved.

In this case, it was only orthogonal data from biochemical experiments that demonstrated there was strong anti-cooperativity between the centres.

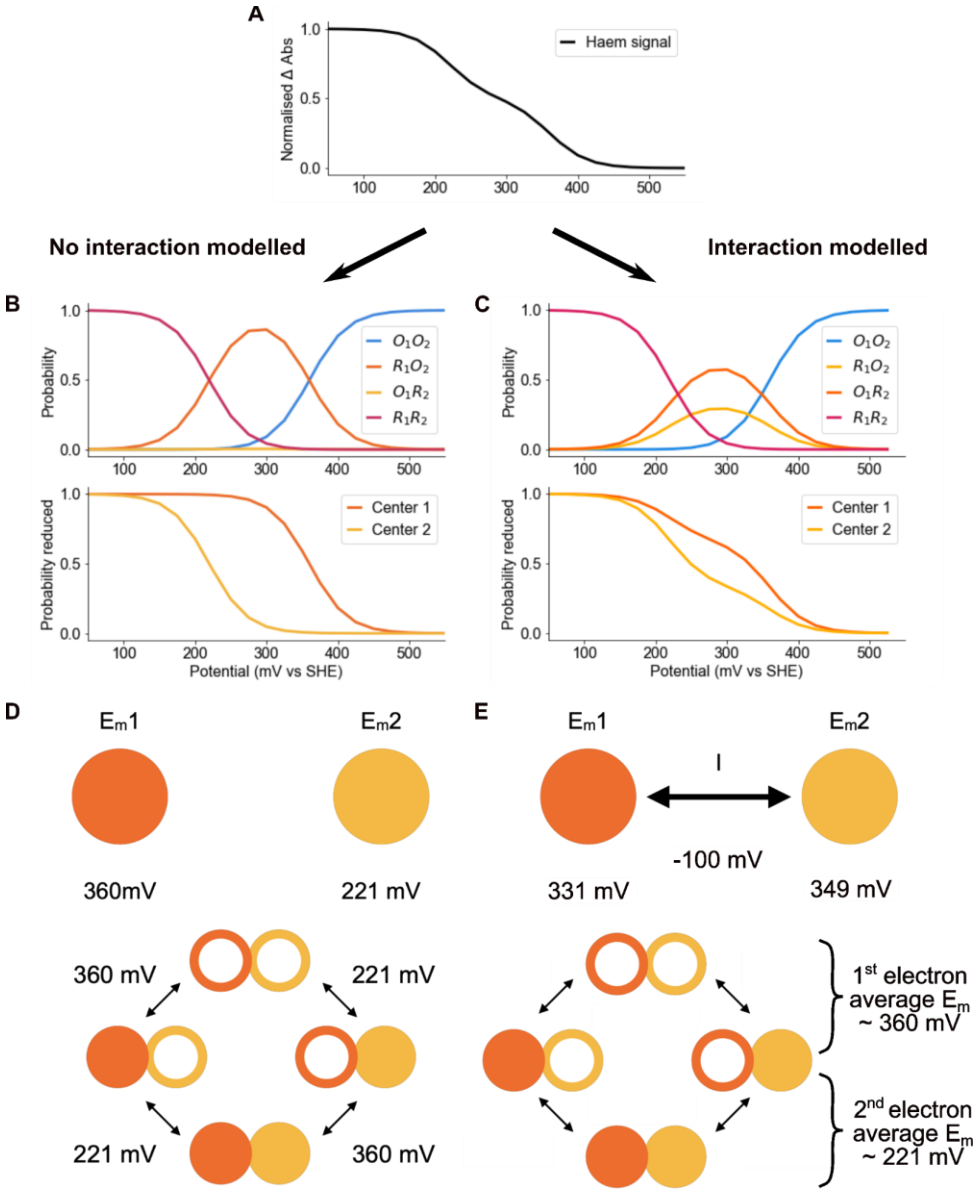

Figure 4.18 - Simulation of anti-cooperativity between haem centres using the parameters, *as determined in (Hendler and Westerhoff, 1992; Tiesjema et al., 1973). (A) Example of the change in absorbance at 600 nm during a redox titration on a cytochrome c oxidase (**B** & **C**) plot of the probability of each state and the probability of each haem being reduced as a function of the potential if no interaction is modelled. I.e. two Nernst functions (**B**) or if an interaction is modelled between the two haems (**C**). (**D** & **E**) are diagrammatic representations of each model, (**D**) no interaction modelled, (**E**) interaction modelled.*

Introducing statistical mechanics for a two-centre cooperative redox system

Characterising this type of behaviour is more tractable when the whole system is described using statistical mechanics, specifically using a statistical thermodynamics approach. Most biochemical experimental observations reflect the average behaviour of the population of macromolecules being observed. For example whilst a haem can be in either the oxidised state or reduced state, the spectral handles we use to observe them reflect the concentration of the reduced species only. This can then be normalised across a titration to show the average oxidation state of the centre during the experiment.

Within statistical thermodynamics, statistical weights describe the probability of different states occurring. Statistical weighting is where the abundance of all states is related to a reference state. Using the anti-cooperativity between the *a*-haems in haem-cooper oxidases as an example, we can describe all the possible haem states in relation to the doubly oxidised state. By rearranging the Nernst equation (Eq. 4.5), Equation 4.9 demonstrates how the concentration of the reduced haem [R] relates to the oxidised form of the haem [O] depending on its midpoint E_m and the redox potential E_h.

$$[R] = [O]e^{\frac{nF}{RT}(E_m - E_h)} \qquad \text{Equation 4.9}$$

The statistical weight of each state can then be described as a function of the potential in relation to the doubly oxidised state by Equations 4.10 to 4.13, where E_{m1} and E_{m2} are the midpoint potentials of the two centres and *I* is the interaction between the two centres, all in mV.

$$\omega_{OO} = 1 \qquad \text{Equation 4.10}$$

$$\omega_{RO} = [OO]e^{\frac{nF}{RT}(E_{m1} - E_h)} \qquad \text{Equation 4.11}$$

$$\omega_{OR} = [OO]e^{\frac{nF}{RT}(E_{m2} - E_h)} \qquad \text{Equation 4.12}$$

$$\omega_{RR} = [OO]e^{\frac{nF}{RT}(E_{m1} + E_{m2} + I - 2E_h)} \qquad \text{Equation 4.13}$$

The probability of each haem centre being reduced can then be calculated by these statistical weights (Equations 4.15 & 4.16) where ω_T is the total of all the states (Eq 4.14).

$$\omega_T = \omega_{OO} + \omega_{RO} + \omega_{OR} + \omega_{RR} \qquad \text{Equation 4.14}$$

$$P(R1) = \frac{\omega_{RO} + \omega_{RR}}{\omega_T} \qquad \text{Equation 4.15}$$

$$P(R2) = \frac{\omega_{OR} + \omega_{RR}}{\omega_T}$$ Equation 4.16

If each centre contributes equally to the haem signal the normalised change in absorbance can be described by Eq 4.17

$$\Delta Abs = P(R1) * 0.5 + P(R2) * 0.5$$ Equation 4.17

If the two centres cannot be spectrally separated, then it is 'difficult' to characterise the individual centres Em. Without more information about the other factors affecting the distribution of electrons within the enzyme, the exact 'actual' midpoints of the two centres cannot be determined. This means that the solution modelling this -100 mV interaction will give the midpoints of the two centres as equal. Even if the signals can be separated without the degree of the interaction and the actual ΔE_m it would be difficult to calculate the exact E_m.

Anti-cooperativity in the cyt bc_1 complex

The same anti-cooperativity behaviour has also been observed for mitochondrial/canonical cyt bc_1, with an interaction in the range of 60-70 mV (Shinkarev et al., 2001). If this behaviour is ignored, the E_h of the two *b*-haems would be miscalculated. However, to date, titrations that have been performed on cyt *bc* type complexes that use menaquinol have not calculated the degree of anti-cooperativity between the *b*-haems (Bergdoll et al., 2016). Given the conservation of the membrane domain amongst cyt *bc* type complexes it is likely that this anti-cooperativity behaviour is also at play in the mycobacterial cyt *bcc* complex. It could be assumed that the same degree of anti-cooperativity is present in the mycobacterial enzyme except with the E_m shifted by ~ -200 mV.

The interaction modelling described above is suitable for assessing the degree of anti-cooperativity in the mycobacterial enzyme. However, the current single-wavelength analysis lacks enough information either to confirm the mammalian degree of anti-cooperativity, or determine the actual degree of anti-cooperativity. To note, the output of the interaction model described above is in a different form to Fig 4.6 B (four E_m compared to two E_m and an interaction describing the same behaviour of two centres). Both describe the same behaviour of the two centres.

4.3.13 Using mycobacterial reference spectra to decompose titration data and measure redox potentials

During the titration a full spectrum from 350 nm - 800 nm was collected at every ambient redox potential, meaning a decomposition approach could be used as an alternative way to determine the redox state of the haem centres, as described in section 4.3.11.1. The reference spectra described in sections 4.3.6 were collected between 510 nm and 620 nm, allowing the fitting of the titration spectra across this region. Given the increase in the data point used to determine the behaviour of each centre (1 or 2 wavelengths increased to 90 wavelengths), this should hope to provide a better characterisation of the centres and so the degree of anti-cooperativity between the *b*-haems. It should also have the added benefit of assigning the isolated signals to an E_m, which may help to clarify the nature of the *b* haem signals.

Four iterations of reference spectra sets were used in Fig 4.19. These different reference spectra sets were the result of improvements to the mycobacterial reference spectra, allowing the effect of the changes to be observed. The composition of the fits is summarised in Table 4.3.

Table 4.4 - Composition of the spectral models used to deconvolute the titration data.

Name	Component	Origin	α - peak maxima (nm)	Reference
Spectral Model 1 (As in Fig 4.6 A)	c_1	*B. taurus* (c_1) shifted + 0.4 nm	553.3	(Kim et al., 2011)
	c_2	*B. taurus* (c_1) shifted - 2.6 nm	550.3	(Kim et al., 2011)
	b_H	B. taurus (b_H)	562	(Kim et al., 2011)
	b_L	B. taurus (b_L)	557.5, 566.1	(Kim et al., 2011)
	aa_3	*B. taurus* (cyt *a*) shifted - 4.9 nm	600.2	(Liao and Palmer, 1996)
Spectral model 2 (Myco *c* haem and *a* haem)	*cc*	M. smeg & B. taurus	552	This work
	b_H	B. taurus (b_H)	562	(Kim et al., 2011)
	b_L	B. taurus (b_L)	557.5, 566.1	(Kim et al., 2011)
	aa_3	M. smeg	599.2	This work
Spectral model 3 (Spectral model 2 with the position of the *b*-haems switched)	Cyt *cc*	M. smeg & B. taurus	552	This work
	b_H	B. taurus (b_H) + 3 nm	565	(Kim et al., 2011)
	b_L	*B. taurus* (b_L) - 4 nm	553.5, 562.1	(Kim et al., 2011)
	Cyt aa_3	M. smeg	599.2	This work
Final spectral model (as in Fig 4.13)	Cyt *cc*	M. smeg & B. taurus	552	This work
	b_H	*B. taurus* (b_H) + 3.3 nm	565.3	(Kim et al., 2011)
	b_L	M. smeg	562.9	This work
	Cyt aa_3	M. smeg	599.2	This work

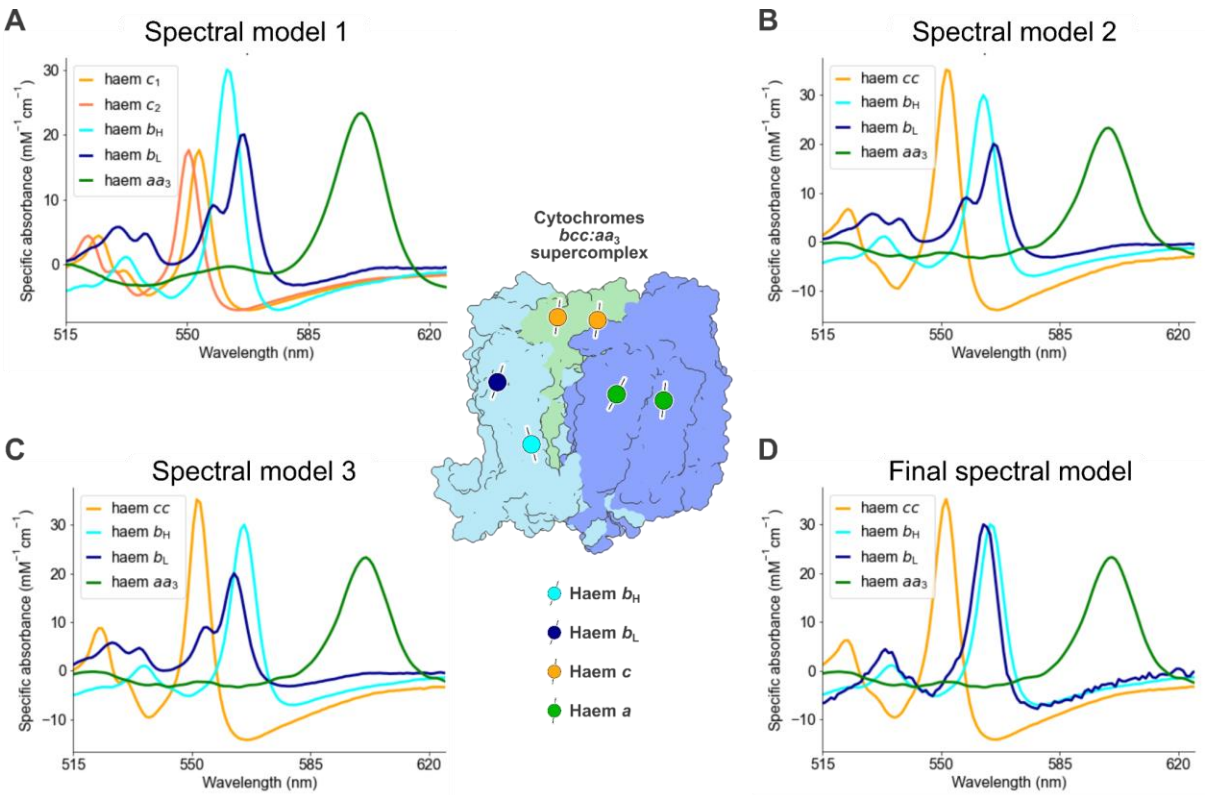

Figure 4.19 - Different spectral models used to deconvolute the titration data *(**A**) Spectral model 1, (**B**) Spectral model 2, (**C**) Spectral model 3 and (**D**) the Final spectral model. (**Centre**) is a cartoon representation of the mycobacterial cyt bcc:aa$_3$ supercomplex (monomer) and the location of the 6 haem centres. The colour of the spectrum in each fit matches the haem centre in the cartoon as assigned. (**A**) is identical to Fig 4.6 A and (**D**) is identical to Fig 4.13.*

4.3.13.1 Deconvolution using Spectral Model 1 and Spectral Model 2

Fig 4.20 shows the decomposition of the titration by spectral model 1 and spectral model 2. Spectral model 1 is the same as in Fig 4.6 A, derived from the mammalian spectral model used by Kim et al., 2012, with adjustments to account for the observed signals in cells. When this is applied to the titration data it is apparent that the two *c* haem signals are unnecessary, given that only c_2 titrates as expected. This matches the behaviour observed when the same spectral model was used to deconvolute cuvette experiments performed on purified protein (Fig 4.10). Spectral model 2 uses the mycobacterial reference spectra for *c* haem and *a* haem derived in this chapter. These mycobacteria reference spectra titrate at the expected potentials (~150 mV for *c* haem and between 150 - 310 mV for *a* haem). Comparing the fits between the reductive direction and oxidative direction, it appears that the haem signals follow the same pattern in both directions however in the oxidative direction the quantity of the haems signals appears more out of proportion. There also appears to be a greater residual around the β-peak region in the oxidative direction (515 - 545 nm).

The *b* haem signals, identical in both fits, matched previous observations in cuvette experiments with the isolated enzyme. Assigning the *b* haem signals as for the mammalian enzyme, b_H α - peak maxima at 562 nm and b_L α - peak maxima at ~ 566 nm, results in the 'wrong' E_m. The b_H signal titrates at a lower midpoint potential than the b_L signal, which is particularly confusing given their notation of L (low) and H (high). This is consistent with the prior observation in the cuvette when the isolated supercomplex is reduced by dithionite, the decomposition using spectral model 1 showed mammalian b_H taking longer to reduce than mammalian b_L (Fig 4.10).

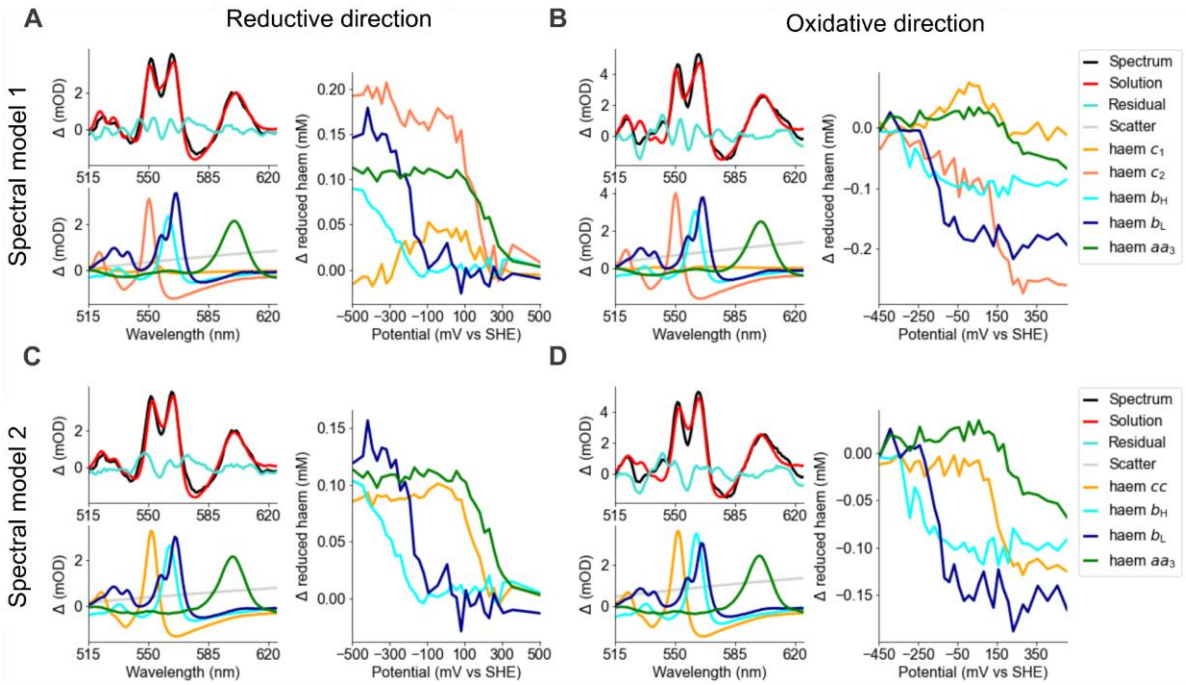

Figure 4.20 - Deconvolute the titration data by spectral model 1 (A & B) and spectral model 2 (B & D). *(**A** & **C**) The titration in the reductive direction, (**B** & **D**) The titration in the oxidative direction. For each model and titration, the fit of the spectral model on the total difference spectrum is shown (Top left panel), the composition of the spectral model with any scatter components is shown (Bottom left panel), and the titration curves of each of the haem centres (right panel)*

4.3.13.2 Assigning b_L and b_H to match the apparent E_m values

To explore this further, the wavelength positions of the two *b*-haems were switched, so that the α - peak maxima for b_L was ~ 562 nm and b_H was ~ 565 nm. The positioning of this was judged by where the positions of the two were switched but still accounted for the total observed signal in a difference spectrum of purified protein. The result of the decomposition using this spectral model (no. 3) is shown in Fig 4.21 A & B. With this spectral assignment of the *b* haem signals, the centre titrate with the expected orientation of E_m, with b_L being more

negative than b_H. The same behaviour was observed for the final fit, where the mycobacteria-derived b_L is used and the mammalian b_H has been adjusted to account for the total difference spectrum, shifting the spectrum by 3.3 nm. This shift in wavelength for the b_H signal is very similar to spectral model 3, where it was shifted by 3 nm. The change in the shape of the b_L signal does not seem to alter the overall titration behaviour, instead, it appears to improve the fit of the total difference spectrum. This is demonstrated by the reduction of the size of features in the residual. The size of the scatter components fitted is also decreased. However, using the mammalian b_H to normalise the mycobacterial b_L signal appears to underestimate the concentration of the b_L

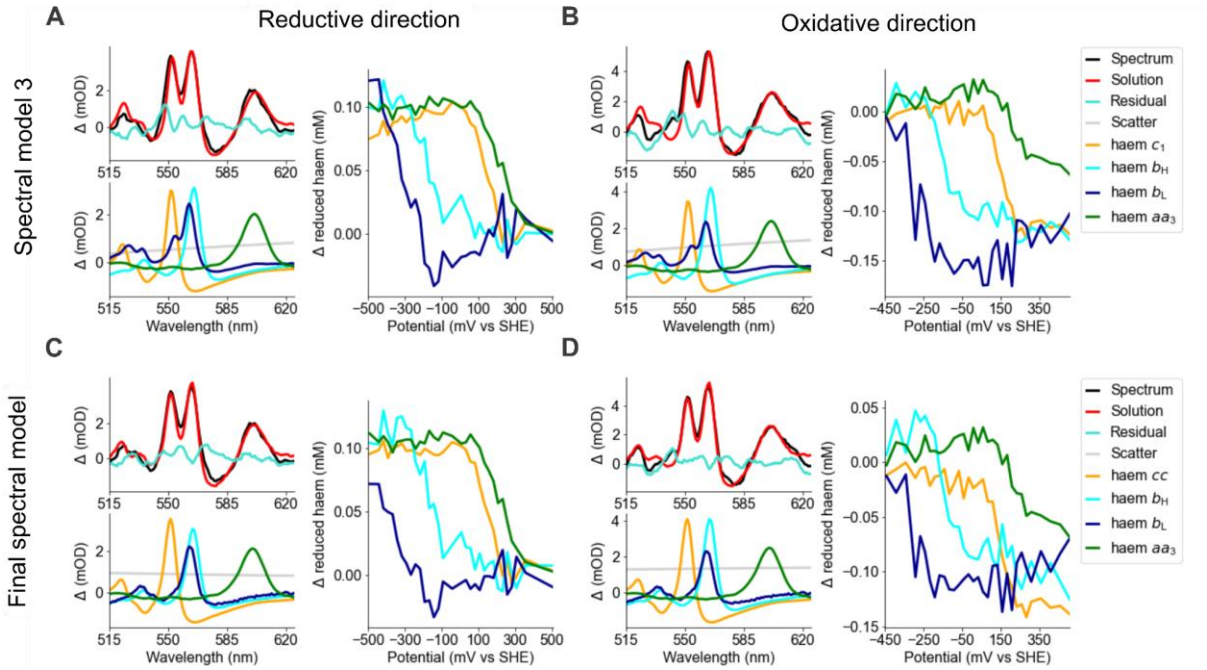

Figure 4.21 - Deconvolute the titration data by spectral model 3 (A & B) and the final spectral model (C & D). *(**A** & **C**) The titration in the reductive direction, (**B** & **D**) The titration in the oxidative direction. For each model and titration, the fit of the spectral model on the total difference spectrum is shown (Top left panel), the composition of the spectral model with any scatter components is shown (Bottom left panel), and the titration curves of each of the haem centres (right panel)*

4.3.13.3 Characterising the anti-cooperativity of the mycobacterial *b*-haems

To assess the anti-cooperativity of the two *b*-haems, a similar model as described for the cyt c oxidase (Fig 4.18) was applied to the decomposed *b* haem titration curves, from spectral model 3 and the final spectral model. This was implemented in Python using the SciPy module optimize curve_fit function on the reductive direction titration as described in section 4.3.11.2. The results are shown in Figure 4.22 and compared to just fitting a Nernst function

in Table 4.5. This includes an assessment of the 'goodness' of the fit in the residual summed squared (Σr^2). This is a measure of the difference between the data and model, where a smaller value represents a better fit. As expected, for both models the main difference is a more positive E_m of the b_L centre if an anti-cooperative interaction is modelled as compared to a Nernst function.

The ΔE_m of the two centres is larger in the final spectral model than in spectral model 3. Whilst the overall residual summed squared (Σr^2) is less for the final model, the standard error of some of the fit parameters is very high. Part of this may be the separation of the E_m of the two *b*-haems. Because their E_m values are so separated, there is a narrow range of ambient redox potentials where there is a likelihood that b_L when b_H is oxidised. This means that apparent E_m of b_L is more affected by the interaction than the apparent E_m of b_H. Without a greater overlap between their E_m or more in-depth characterisation of the enzyme, it is difficult to estimate the actual ΔE_m or the size of the interaction.

Given the points outlined above and the risk that the measured mycobacterial b_L spectrum may have some b_H contaminating it, it is difficult to be certain that this is the right thermodynamics model or the right spectral model for that matter. However, given the lack of prior characterisation of these parameters, it is a reasonable starting point for translating this to measuring $\Delta\Psi$ in mycobacterial cells.

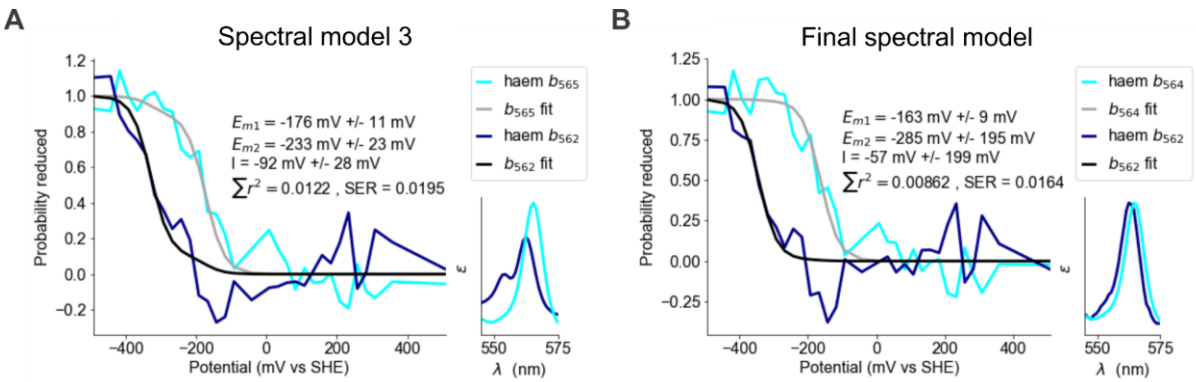

***Figure 4.22 - The result of fitting a thermodynamics model of the b haem with an interaction**, (**A**) Spectral model 3, (**B**) Final spectral model, The haems are noted with their α - peak maxima instead of b_L or b_H, but the colour schemes are set to as they were originally assigned in the fit, dark blue - b_L, light blue - b_H. Inserts for each graph show the spectral shape of the fitted b-haems for each spectral model. The parameters of the fit and their standard error are shown. The calculated $\sum r^2$ and SER are also shown for each graph.*

Table 4.5 - Determined parameters for the two thermodynamic models applied to the b-haems*. Applied to the decomposed b haem reductive direction titration curves from spectra model 3 and the final spectral model. The parameters give ± their standard error.*

Fit	Haem	No interaction modelled			Interaction modelled		
		Em (mV)	Σr^2 (each haem)	Σr^2 (both haem)	E_m (mV)	Interaction (mV)	Σr^2
Spectral model 3	b_H	-174 ± 8	0.00355	0.01264	-176 ± 11	- 92 ± 28	0.0122
	b_L	-316 ± 12	0.00909		-233 ± 23		
Final spectral model	b_H	-163 ± 9	0.00483	0.00862	-163 ± 9	-57 ± 199	0.00862
	b_L	-343 ± 13	0.00379		-285 ± 195		

4.3.13.4 Characterising the anti-cooperativity of the other mycobacterial haems

The same analysis approach can also be applied to the haem C and haem A centres. Figure 4.23 shows a comparison of fitting for a single centre, fitting two centres with no interaction or modelling two centres with an interaction. The parameters of this are summarised in Table 4.6. For both types of haems, fitting for two centres provided a better solution for the decomposed titration data. The 'gradient' of a single Nernst function is too steep for the titration of either haem type. Fitting of two E_m values accommodates this shallower gradient and is a better reflection of the physical enzyme. This justifies using these spectral signals to account for both centres. Like with the *b* haem anti-cooperativity model, there is insufficient information characterising an interaction between the centres with confidence.

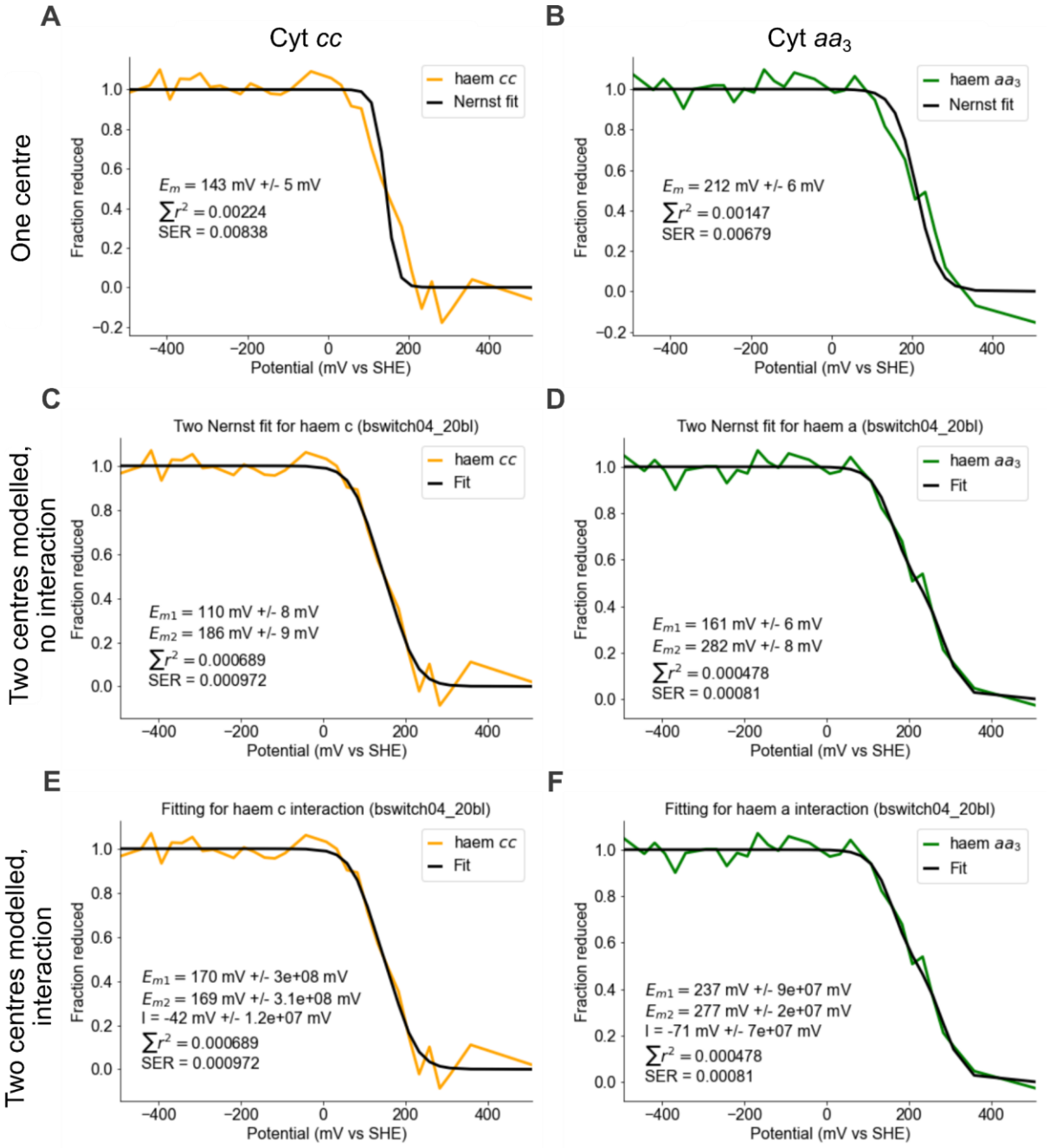

Figure 4.23 - The result of fitting thermodynamic models of the c haem (A, C, & E) and a haem (B, D, & F) from the final spectral model. *(**A** & **B**) The fitting of a signal Nernst functions. (**C** & **D**) The fitting of two Nernst functions. (**E** & **F**) The fitting of two centres with an interaction. The parameters of the fit and their standard error are shown. The calculated $\sum r^2$ and SER are also shown for each graph.*

***Table 4.6 - Determined parameters for the 3 thermodynamic models applied to the c and a haems**. Applied to the decomposed c haem and c haem a reductive direction titration curves from the final spectral model. The parameters give ± their standard error.* * indicated where the standard error is larger than the bounds of the data*

Haem	Centre	One centre modelled		Two centres, no interaction modelled		Interaction modelled		
		Em (mV)	Σr^2	Em (mV)	Σr^2	E_m (mV)	Interaction (mV)	Σr^2
c	1	143 ± 5	0.00224	110 ± 8	6.89×10^{-4}	$170 \pm 3 \times 10^{8}$ *	$-42 \pm 1.2 \times 10^{7}$ *	6.89×10^{-4}
	2			186 ± 9		$169 \pm 3.1 \times 10^{8}$ *		
a	1	212 ± 6	0.00147	161 ± 6	4.78×10^{-4}	$237 \pm 9 \times 10^{7}$ *	$-71 \pm 7 \times 10^{7}$ *	4.78×10^{-4}
	2			282 ± 8		$277 \pm 2 \times 10^{7}$ *		

4.3.14 Simultaneously deriving the spectra and thermodynamic model

Given the 'bias' of inputting spectra and deriving a thermodynamic model of the enzyme decomposing the titration based on these predetermined spectra, I considered if there was an approach that would avoid this. If instead a thermodynamic model of the enzyme could be fitted to the data, including interactions between the haem centres, this may offer an approach to simultaneously characterise the thermodynamic parameters and the spectra signals associated with the centres. This has previously been described for redox titration performed on cytochromes, such as the cyt *bd* quinol oxidase in a more recent example (Bloch et al., 2009). This approach utilised a similar approach to the matrix decomposition discussed previously, combined with least squares fitting as can be implemented in programs like SciPy's optimize curve_fit.

The main difficulty with implementing in this case is the complexity of the mycobacterial cyt *bcc:aa*$_3$ supercomplex. In the previous example, the cyt *bd* has only 3 redox centres. In comparison, the monomer of the mycobacterial supercomplex contains 6 haems centres. In addition to this, each monomer has an iron sulphur cluster, 3 Copper centres, and likely two additional divalent cations (Mg^{2+} & Ca^{2+}). If we just consider the 6-haem centre, there are 64 possible states ($2^6 = 64$), compared to 8 states for a 3-haem centre system ($2^3 = 8$).

To simplify this, to begin with, I considered a model with 4 centres. For each of the *b*-haems, one E_m was assigned (E_m^{bH}, E_m^{bL}) with an interaction between the two centres (I_b). The two *c*-haems and *a*-haems were assigned to one centre each to simplify the initial model (E_m^{cc}, E_m^{aa3}). The occupancy of a state (x_s) can then be described by Eq.4.18

$$x_s(s = 1 \ldots 16) = \frac{y_s}{\Sigma y_s} \qquad \text{Equation 4.18}$$

Where:

$$y_1 = 1 \qquad y_9 = e^{\frac{F}{RT}(E_m^{aa3} - E_h)}$$

$$y_2 = e^{\frac{F}{RT}(E_m^{cc} - E_h)} \qquad y_{10} = e^{\frac{F}{RT}(E_m^{cc} + E_m^{aa3} - 2E_h)}$$

$$y_3 = e^{\frac{F}{RT}(E_m^{bL} - E_h)} \qquad y_{11} = e^{\frac{F}{RT}(E_m^{bL} + E_m^{aa3} - 2E_h)}$$

$$y_4 = e^{\frac{F}{RT}(E_m^{cc} + E_m^{bL} - 2E_h)} \qquad y_{12} = e^{\frac{F}{RT}(E_m^{cc} + E_m^{bL} + E_m^{aa3} - 3E_h)}$$

$$y_5 = e^{\frac{F}{RT}(E_m^{bH} - E_h)} \qquad y_{13} = e^{\frac{F}{RT}(E_m^{bH} + E_m^{aa3} - 2E_h)}$$

$$y_6 = e^{\frac{F}{RT}(E_m^{cc} + E_m^{bH} - 2E_h)} \qquad y_{14} = e^{\frac{F}{RT}(E_m^{cc} + E_m^{bh} + E_m^{aa3} - 3E_h)}$$

$$y_7 = e^{\frac{F}{RT}(E_m^{bL} + E_m^{bH} + I_b - 2E_h)} \qquad y_{15} = e^{\frac{F}{RT}(E_m^{bL} + E_m^{bH} + E_m^{aa3} + I_b - 3E_h)}$$

$$y_8 = e^{\frac{F}{RT}(E_m^{cc} + E_m^{bL} + E_m^{bH} + I_b - 3E_h)} \qquad y_{16} = e^{\frac{F}{RT}(E_m^{cc} + E_m^{bL} + E_m^{bH} + E_m^{aa3} + I_b - 4E_h)}$$

Where F, R and T are Faraday's constant, the gas constant and the temperature, in Kelvin, respectively. The probability of each haem being reduced can then be described by Eq. 4.19:

$$P(h) = \frac{Occupancy\ of\ all\ states\ with\ haem\ reduced}{Occupancy\ of\ all\ possible\ states\ of\ the\ enzyme} \qquad \text{Equation 4.19}$$

Where:

$$P(cc) = \frac{y_2 + y_4 + y_6 + y_8 + y_{10} + y_{12} + y_{14} + y_{16}}{\Sigma y_l} \qquad P(b_L) = \frac{y_3 + y_4 + y_7 + y_8 + y_{11} + y_{12} + y_{15} + y_{16}}{\Sigma y_l}$$

$$P(b_H) = \frac{y_5 + y_6 + y_7 + y_8 + y_{13} + y_{14} + y_{15} + y_{16}}{\Sigma y_l} \qquad P(aa_3) = \frac{y_9 + y_{10} + y_{11} + y_{12} + y_{13} + y_{14} + y_{15} + y_{16}}{\Sigma y_l}$$

Eq. 4.20 will then describe the spectra from the titration (in the form of a *j* x *k* matrix) where S is a *j* x *i* matrix of the difference spectrum of each haem centre and P is a *i* x *k* matrix of the probabilities of each centre being reduced at the measured voltages. This creates a model that can describe the changes in the absorbance during the titration based on the probability

of each centre being reduced, described by the E_m and interactions between the haems. From this, the spectral identity of the centres can be extracted

$$\mathbf{A}^{theor} = \mathbf{S.P} \qquad \text{Equation 4.20}$$

The parameters describing the **P** matrix (E_m and I) and the parameters making up the difference spectra matrix (**S**) are all optimised during the fitting process, where the residual summed squared of $\mathbf{A}^{obs}$ compared to $\mathbf{A}^{theor}$ is minimised.

The results for fitting this first model are shown in Figure 4.24 and Table 4.7. The spectra and thermodynamic parameters for the two *b*-haems are very similar to the anti-cooperativity modelled with the final spectral model. The α-peaks of the b_L and b_H difference spectra were 562 & 564 nm which match the spectrum in the final spectral model. This supports the spectra isolated in Fig 4.12 as being b_L. The electrochemical parameters match the estimated parameters for the decomposed curves, however, the standard error for these parameters is very high. Interestingly the difference spectra found for cyt *cc* and cyt aa_3 appear to be contaminated with features from the other. This is most apparent in the 'cyt *cc*' or 144 mV E_m curve that has a peak at ~445 nm and ~600 nm that is usually associated with the *a* haem. The contamination in the cyt aa_3 is somewhat overpowered by the noise, but there are hints of a peak at ~550, usually associated with haem C.

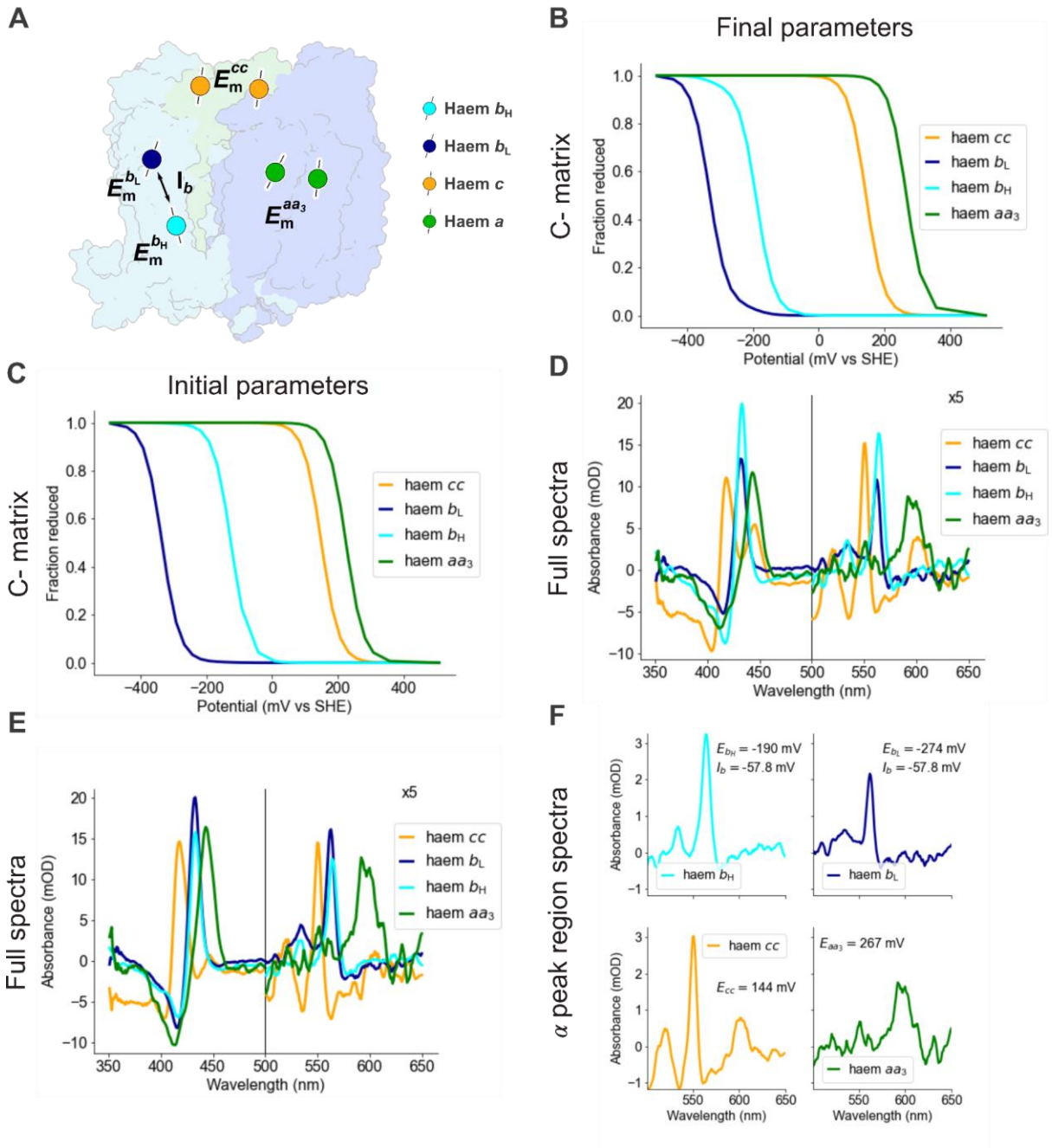

Figure 4.24 - Input and results from 4 centre model *(**A**) Midpoint potentials and interaction used within the model, assigned to their presumed corresponding haem. (**C** & **E**) Plots of the redox curves of the input model and the reference spectra based upon the decomposition of the titration data based on the input model. (**B** & **D**) Plots of the redox curves of the final parameters determined by the fitting and the reference spectra based upon the decomposition of the titration data based on the final parameters determined by the fitting. (**F**) α-peak region of the fitted reference spectra.*

***Table 4.7 - Initial guess, bounds, and Found parameters for a 4 centres 1 interaction model**, * indicated where the standard error is larger than the bounds of the data*

Parameter	Initial	Lower bound	Upper bound	Final	Standard error
E_m^{bL}	-275	-400	-150	-274	5.8×10^6 *
E_m^{bH}	-125	0	-250	-190	2.5×10^5 *
I_b	-60	-10	-100	-58	5.5×10^6 *
E_m^{cc}	150	0	200	144	1
E_m^{aa3}	225	150	300	267	1

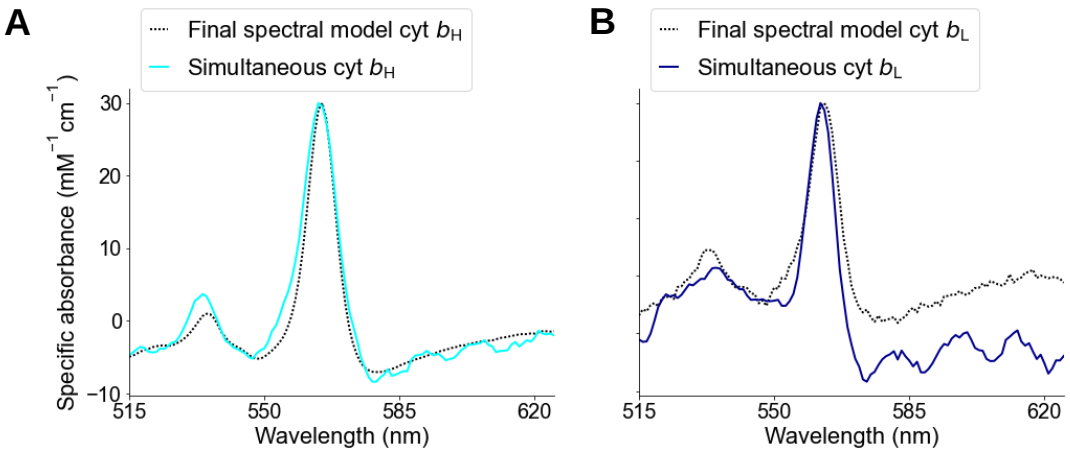

***Figure 4.25 - Comparison of the b-haems in the final spectral model and those isolated using the simultaneous decomposition of fitting of the titration data** (**A**) b_H (**B**) b_L. The dotted line shows the previous isolated signal or adjusted mammalian signal (section 4.3.6.2), and the solid line shows the fitted signal from Fig 4.24.*

To try to improve this model to better separate the *c*-haems and *a*-haems, a six-centre model was considered with three interactions between the closest haem pairs (I_b, I_c and I_a). A schematic of the E_m and interactions included are shown in Fig 4.26 A. These haem pairs are the only haem pairing where the distance is within 14 Å, therefore it is unlikely that any other interaction will contribute to the redox behaviour of the centre other than these. Other redox

centres in close proximity could influence the redox behaviour of the haems, for example, the coppers within the oxidase. As they are not visible in the current experimental approach, they were ignored for now. The results of fitting with this model are shown in Fig 4.26 C. Whilst the features in the difference spectra are more haem-like than the equivalent using the input parameters (Fig 4.26 B), the fitting fails to produce two *c* haem and two *a* haem signals. This may be due to the signals for the same chemical haem types being too similar, or the E_m not being different enough. The minimised solution had no interaction between the *c*-haems and *a*-haems centres, Table 4.8. All of this points to the current model insufficiently describing the system to properly separate all of the haem centres.

Table 4.8 - Initial guess, bounds, and found parameters for a 6 centres 3 interactions model, * *indicated where the standard error is larger than the bounds of the data.*

Parameter	Input	Lower bounds	Upper bounds	Final	Covariance
$E_m{}^{bL}$	-274	-400	-150	-281	4.2×10^6 *
$E_m{}^{bH}$	-190	-250	0	-189	1.0×10^4 *
I_b	-58	-100	0	-50	4.1×10^6 *
$E_m{}^{cc\ (1)}$	170	0	300	152	5.9×10^3 *
$E_m{}^{cc\ (2)}$	169	0	300	89	7.6×10^4 *
I_c	-42	-100	0	0	7.1×10^4 *
$E_m{}^{aa3\ (1)}$	237	100	400	222	3.8×10^5 *
$E_m{}^{aa3\ (2)}$	277	100	400	280	3.4×10^4 *
I_a	-71	-200	0	-5	3.4×10^5 *

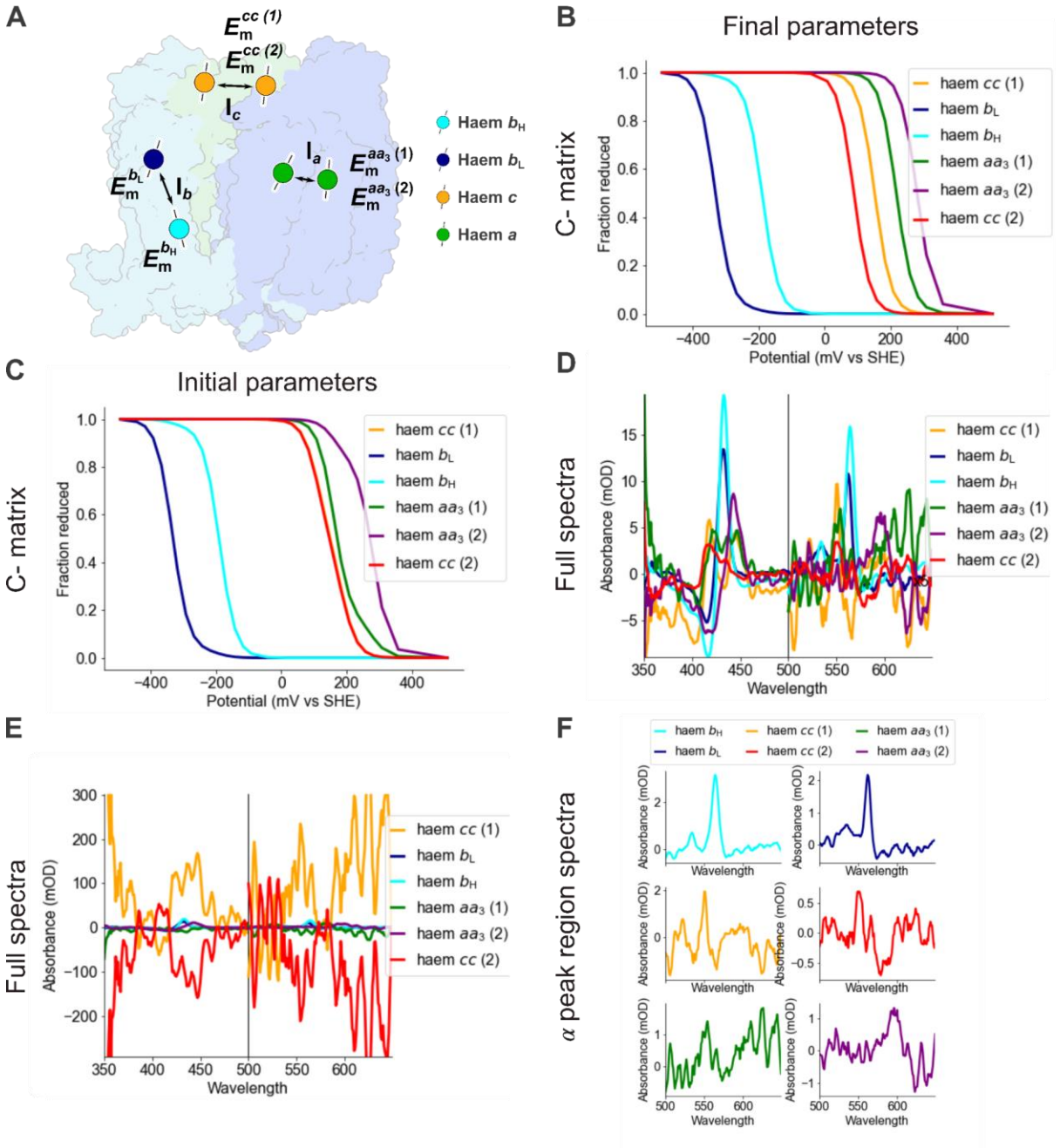

Figure 4.26 - 6 centre model, deconvolution based on input parameters and result from fitting *(**A**) Midpoint potentials and interactions used within the model, assigned to their presumed corresponding haem. (**C** & **E**) Plots of the redox curves of the input model and the reference spectra based upon the decomposition of the titration data based on the input model. (**B** & **D**) Plots of the redox curves of the final parameters determined by the fitting and the reference spectra based upon the decomposition of the titration data based on the final parameters determined by the fitting. (**F**) α-peak region of the fitted reference spectra.*

To try and improve the certainty of the parameters, this 6-centre model was carefully restrained. Firstly, in relation to the *b*-haems, other than the coulombic repulsion between the centres, the redox behaviour of the *b*-haems will be dictated by the difference in the individual centre's affinity for electrons (ΔE_m^b). This ΔE_m^b can be measured by determining the K constant of the equilibrium of electrons between the b_L and b_H. This K constant has previously been measured in the *R. sp* homologue of the cyt bc_1 complex, with a value between 10-25 (Shinkarev et al., 2001). This equates to an ΔE_m^b of ~ 70 mV. Given the fold conservation and conservation of the spatial arrangement of the *b*-haems between homologues of the cyt bc_1 complex, it is a reasonable restriction of the possible parameters for the *b*-haems.

The results of the two-centre modelling of the decomposed *c* haem and *a* haem signals (Fig 4.23) suggest that the *c* haem and *a* haem signals should titrate with behaviour more complex than a single Nernst. To force this type of redox behaviour four E_m for the *c*-haems and *a*-haems were included in the model but only two were used in the matrix used to predict $\mathbf{P}^{pred}$. The results of this restrained model are shown in Figure 4.27 and Table 4.9.

Table 4.9 - Initial guess, bounds, and found parameters for the restrained model.

Parameter	Input	Lower bounds	Upper bounds	Final	Standard error
E_m^{bL}	-283	-370	-200	-260	1
E_m^{bH}	(-213)			(-190)	
I_b	-57	-100	10	-71	1
E_m^{cc}	168	100	200	168	1
E_m^{cc*}	170	100	200	170	5
I_c	-41	-100	10	-38	2
E_m^{aa3}	263	100	400	265	1
E_m^{aa3*}	265	200	400	254	2
I_a	-84	-150	10	-75	2

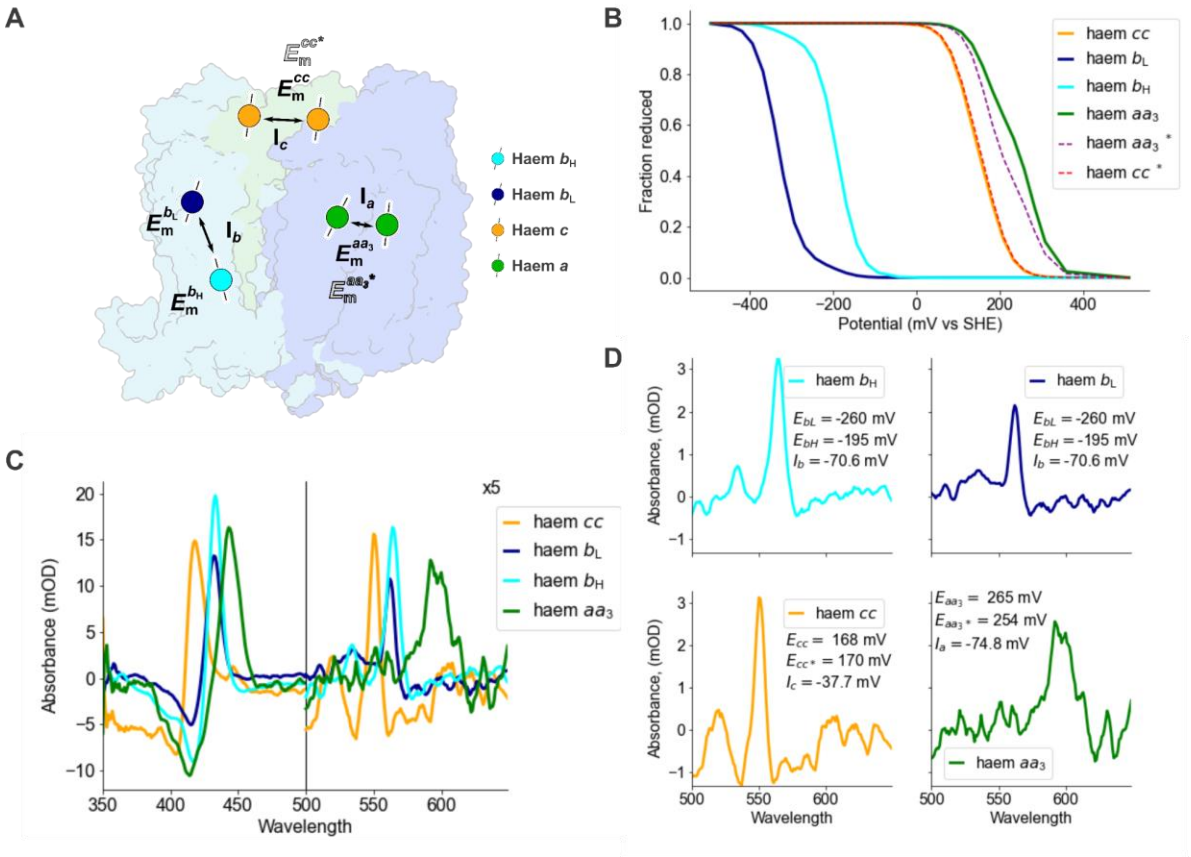

Figure 4.27 - The restrained model and the results from fitting *(**A**) Midpoint potentials and interactions used within the model, assigned to their presumed corresponding haems. (**B** & **C**) Plots of the redox curves of the final parameters determined by the fitting and the reference spectra based upon the decomposition of the titration data based on the final parameters determined by the fitting. (**D**) α-peak region of the fitted reference spectra.*

This 'restrained' model has much more certainty on parameters. Whilst there is still some *a* haem signal contamination in the cyt *cc* difference spectrum, out of the three models used, it appears to be the most *c* haem-like signal. The same is true for the cyt aa_3 signal. Using the $\Delta E_m{}^b$ derived from the K constant for *R. sp* cyt bc_1 complex altered the thermodynamic parameters for the *b*-haems, bringing the interaction closer to values estimated for the cyt bc_1 (Kim et al., 2012; Shinkarev et al., 2001).

4.3.15 Applying the spectral model of the mycobacterial cyt *bcc:aa*$_3$ supercomplex to live cells: finding an additional cytochrome

Once the cyt *bcc:aa*$_3$ supercomplex had been characterised, the spectral and thermodynamic models could then be applied to runs performed on live cells, realising the aim of measuring

the ∆Ψ in living mycobacteria. In Figure 4.28, the final spectral model was applied to the original run from Figure 4.7. The *b* haem signals from this new spectral model behaved unexpectedly, the b_H signal did not reduce as the cells were taken anoxic, at ~15 mins. As oxygen is removed the haems should become reduced. The lack of reduction in the b_H may be the result of mis-fitting, likely driven by additional cytochromes, other than the cyt *bcc:aa*$_3$ supercomplex, contributing to the overall spectrum. This mis-fitting prevents the accurate calculation of the oxidation states of b_L and b_H and so precludes the measurement of the ΔΨ. To correct for this mis-fitting any contributions from non-cyt *bcc:aa*$_3$ cytochromes will have to be accounted for within the fit. Depending on the nature of the additional cytochrome, a strain where this cytochrome has been knocked out could be used, but this may be detrimental to the fitness of the cell.

If the total difference spectrum of purified cyt *bcc:aa*$_3$ supercomplex is compared to a difference spectrum from cells (Fig 4.29), it is clear that they do not match. In the purified protein spectrum, the *c* haem and *b* haem signals are distinct from each other, with a trough in between the two peaks. In the cell difference spectrum, the two signals are not as spatially separated. Whilst some of this lack of separation may be due to being unable to fully transform the cytochromes from fully oxidised and reduced inside the cell, and so reducing the apparent concentration of the *b*-haems, it also appears that there is an additional haem signal (between 550 – 560 nm) that is present in the cells but not the purified protein. This is most apparent by a signal in the residual at ~557 nm (Fig 4.29B in light blue).

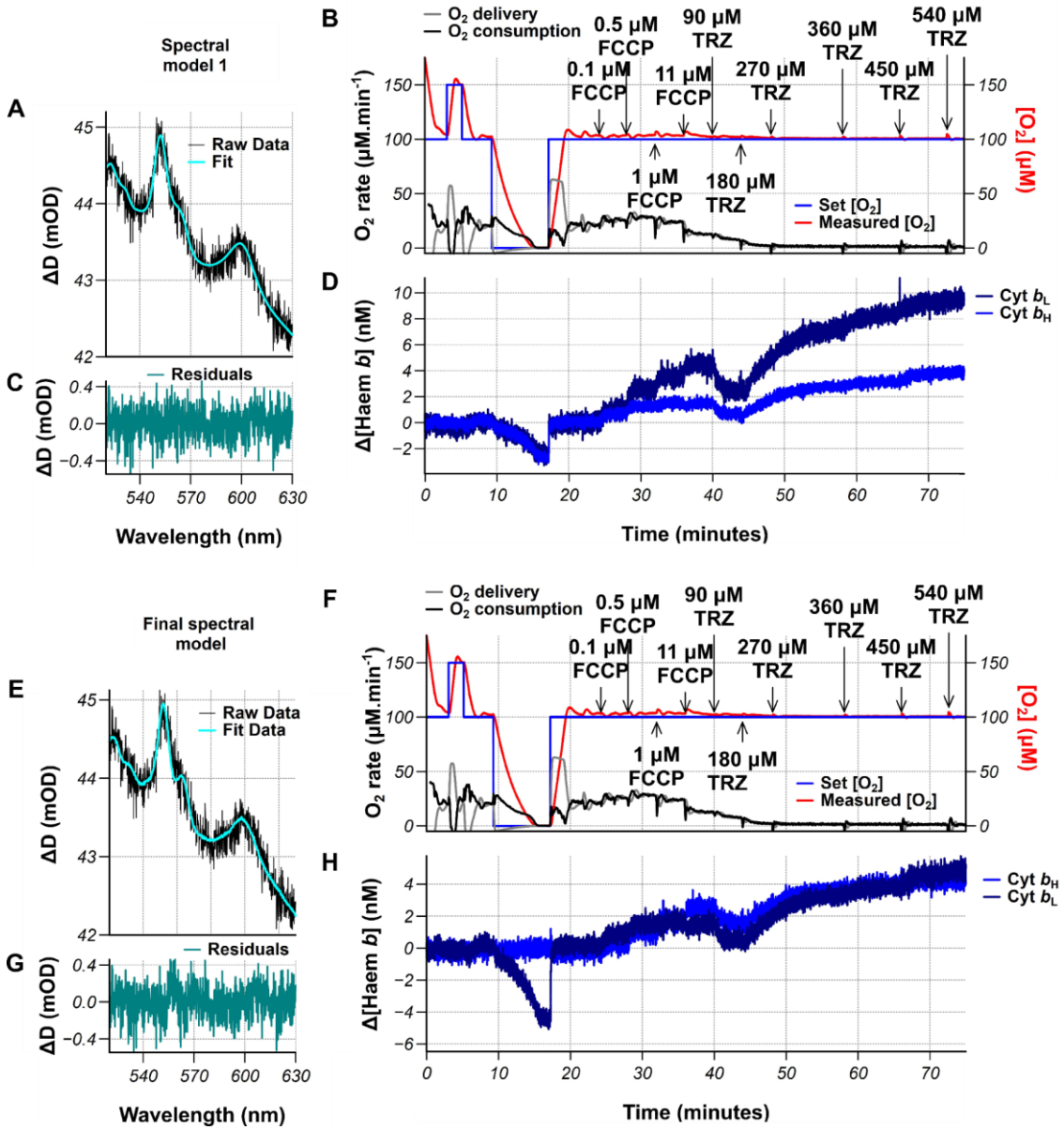

Figure 4.28 – Comparing the results of fitting spectra collected from cells with spectral model 1 as compared to fitting with the final spectral model. *(Top panels, **A**-**D**) – Results from decomposition with spectral model 1, mammalian reference spectra. (bottom panels **E**-**H**) – Results from decomposition with the final spectral model, mycobacterial reference spectra. For each model the oxygen consumption (**B** & **F**) and changes in the haem concentration based on decomposition using the spectral model (**D** & **H**). An example of the fitting during the period of anoxia is shown (**A** & **E**) along with the residual of this fit (**C** & **G**)*

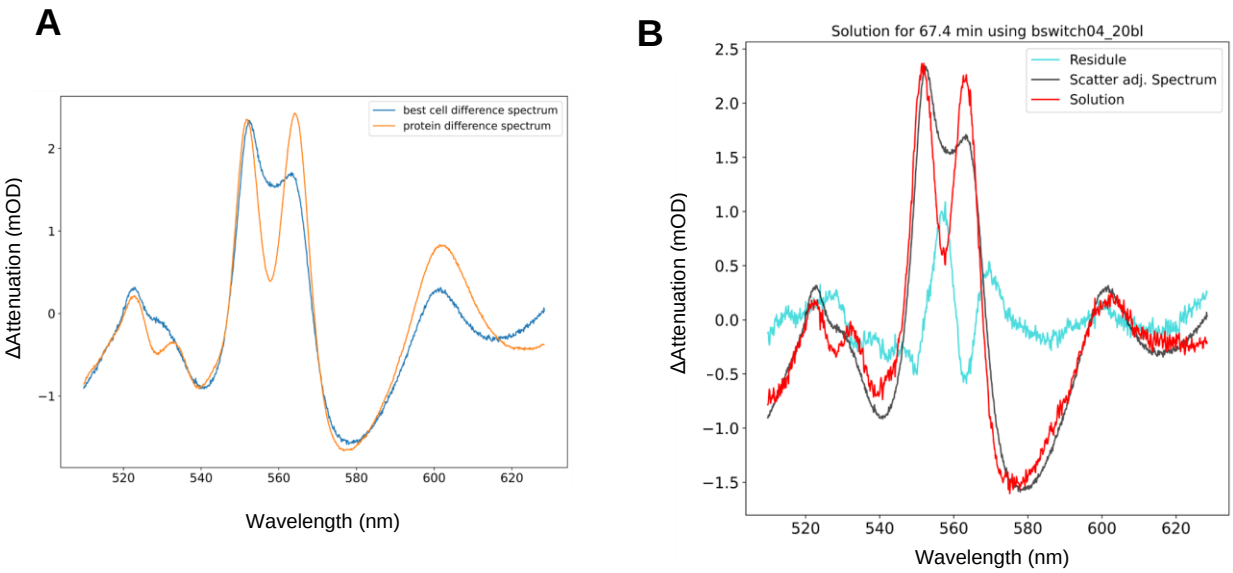

Figure 4.29 – Spectral differences between isolated cyt bcc:aa₃ and M. smeg cells *(**A**) Comparison of the total difference spectrum in cells and purified cyt bcc:aa₃ supercomplex. (**B**) The goodness of the final spectral model on the total difference spectrum from the cell. Black – Difference spectrum from cells with the fitted scatter components subtracted (Scatter adj. spectrum), Red – Solution of the fit of the difference spectrum, sum of all the fitted haem components, Light blue – residual, the difference between the solution and the difference spectrum.*

4.3.16 Characterising the contribution of non cyt *bcc:aa*$_3$ supercomplex cytochromes to the overall mycobacterial haem spectrum

In the mycobacterial chain the cyt *bcc:aa*$_3$ supercomplex is not the only cytochrome that may contribute to the overall spectrum. Mycobacteria also contain several other cytochromes that are likely present in sufficient abundance to contribute to the overall spectra, Fig 4.30 A. From wider spectra, into the 600 – 700 nm region, it is apparent that there is some *d* haem present in the cell membrane of exponentially growing mycobacteria, Fig 4.30 B. The haem D has a distinctive signal with a peak at 630 nm in the reduced spectrum and a peak at 650 nm in the as-prepared spectrum, from oxygen-bound haem d^{2+} (d^{2+}-O_2). This peak is not present in the membranes of Δ*cydAB M. smeg*, Fig 4.30 C. Unexpectedly the difference between the strains is not as apparent when a difference of anoxic minus steady steady aerobic cells is examined, Fig 4.30 D & E. This haem is specific to the cyt *bd* oxidase, which contains two *b*-haems. Because it was apparent that the cyt *bd* oxidase might be contributing to the overall spectrum and as it is not detrimental to the growth of the cell, the chosen example run was performed with the Δ*cydAB* strain of *M. smeg*.

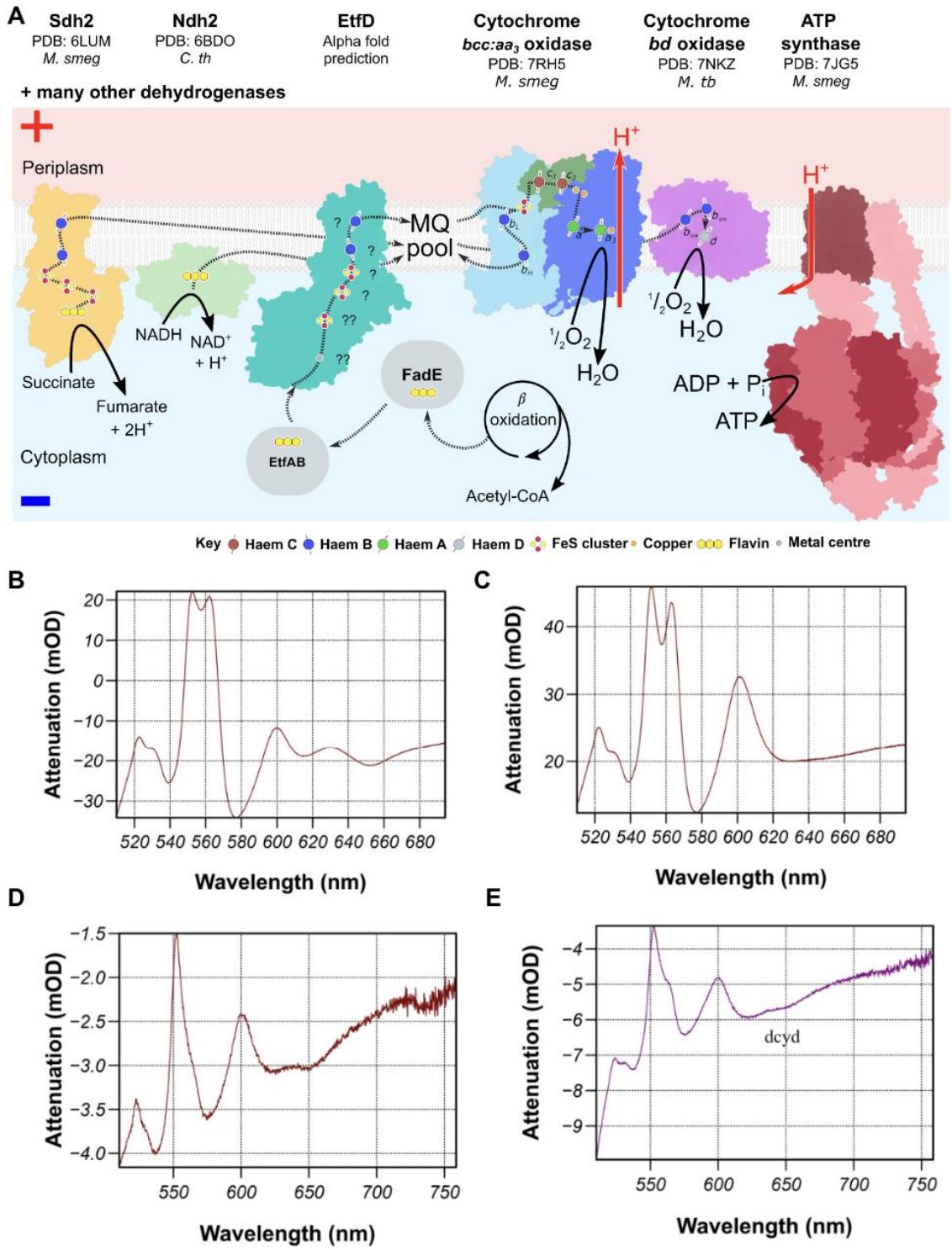

Figure 4.30 – Cytochromes present in the mycobacterial membrane and presence of bd oxidase in exponentially growing mycobacteria *(**A**) The mycobacterial OxPhos system, including the cytochromes, thought to be present and or abundant in exponentially growing M. smeg. (**B** & **C**) Difference spectrum from Wild-type and ΔcydAB membranes grown in TSB. (**D** & **E**) Anoxia-steady state spectrum from mc²155 and ΔcydAB M. smeg. Both the live cells and membranes were taken from cells in the exponential phase of growth, OD ~ 1.*

Mycobacteria also have a class A succinate dehydrogenase that is near essential for exponential growth in *M. smegmatis,* Sdh2. Sdh2 had been thought to be essential in *M. smeg* (Pecsi et al., 2014) but has since been successfully knocked out (personal communication with Chen-Yi Cheung in the Cook group). This succinate dehydrogenase contains two *b*-haems that are part of the electron transfer chain from the flavodomain of the protein to the quinone reduction site (Gong et al., 2018; Pecsi et al., 2014). Sdh2 and cyt *bd* oxidase are the best candidates for other cytochromes that could be detectable in the mycobacterial membranes but this does not exclude the possibility of other unidentified cytochromes significantly contributing to the overall spectrum. From examining the sequence and alpha fold prediction of the etfD, protein involved in *β*-oxidation of fatty acids, it appears that this complex may contain up to two haems (Beites et al., 2021 & personal communication with Dr Morwan Osman).

To help characterise the contributions to the spectrum of cells, membranes from wild-type *M.smeg* (mc^2155) and ***ΔcydAB*** *M. smeg* were examined. The advantage of membranes is that a greater haem signal can be measured whilst still maintaining control over the oxygenation of the chamber than in runs with cells whilst examining the whole mycobacterial membrane. Both sets of membranes were run in the chamber system and throughout the run were oxidised with $K_3[Fe(CN)_6]$, then reduced with sodium dithionite and finally reoxidised with oxygen and $K_3[Fe(CN)_6]$, Fig 4.31. The *b* haem traces from either strain are not roughly equal as you would expect. From looking at the residual, the same feature is present between the *c* haem and *b* haem signals.

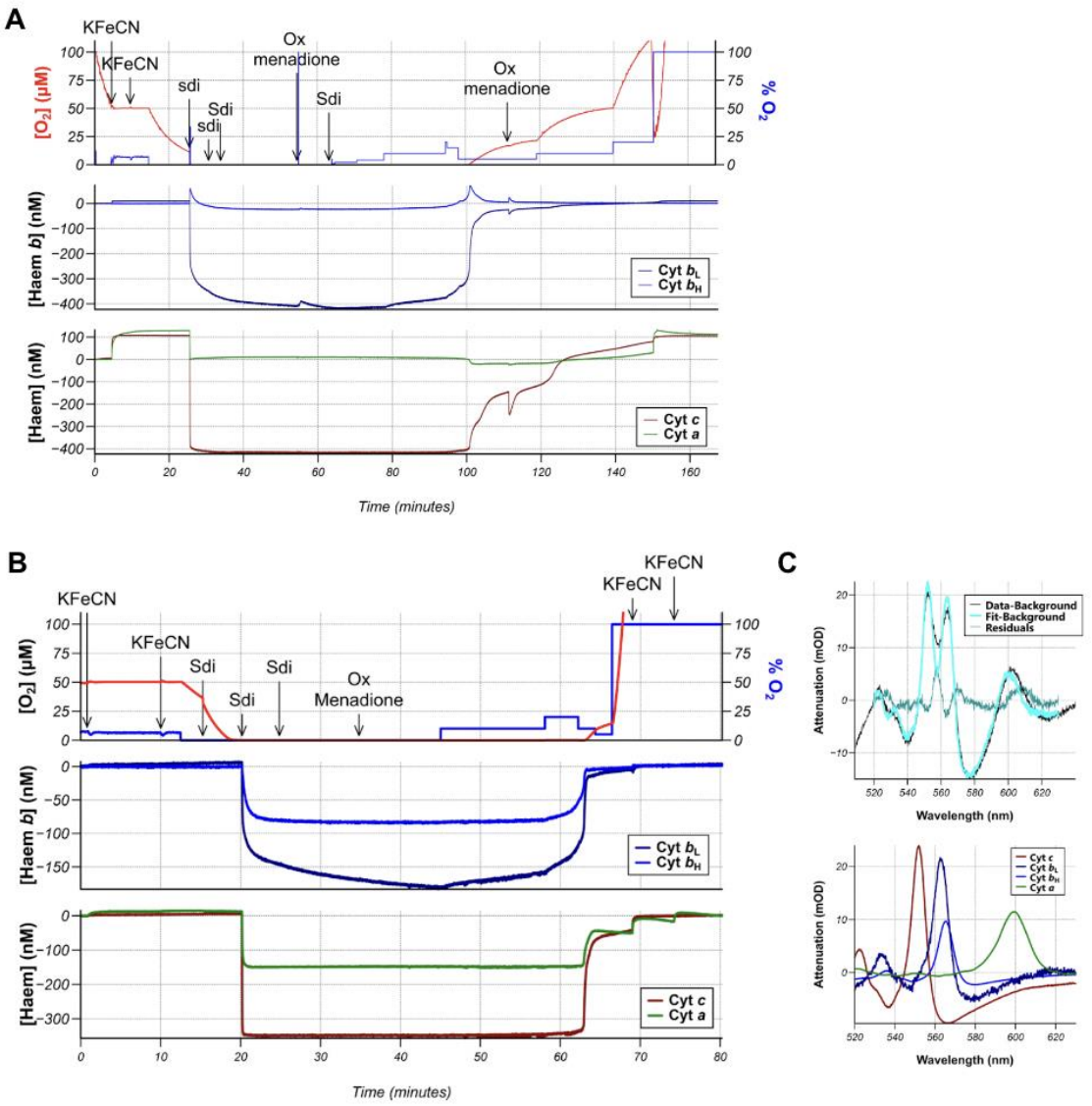

Figure 4.31 - The results of decomposing using the final spectral model experiments with wild-type membranes or Δcyd membranes*. (**A**) Experiment with wild-type membranes. (**B**) Experiment with Δcyd membranes. (**C**) Example of the fitting on Δcyd membranes.*

To address this an additional *b* haem signal was added to the fit, the mammalian b_H, transformed by shifting its spectrum by -5 nm, to have its α-peak centre at 557 nm. This additional cytochrome improved the performance of the fit in the membranes of both strains (Fig 4.32). The ratio of b_L to b_H signals was closer to a 1:1 ratio as expected. In the wild-type membranes, the contribution of the b_{557} signal was greater than in the *ΔcydAB* membranes, suggesting that some of this signal was a result of the cyt *bd* oxidase. Based on comparing the change in fraction reduced over time for each of the haem signals, this b_{557} has an E_m greater than both cyt *bcc:aa*$_3$ *b*-haems ($E_m{}^{b_{557}}$> ~-160 mV) and less than the cyt *cc* ($E_m{}^{b_{557}}$< 140 mV).

In a closely related cyt *bd* (*C. glut*), the *b*-haems have been reported to have E_m values of 102 mV & 160 mV (Nikolaev et al., 2021), with the caveat of high reported errors for these experiments (±40 mV). The reported E_m values for the cofactors of the menaquinol:succinate dehydrogenase in *B. subtilis,* which like the mycobacterial Sdh2 contains two b-type haems, were -95 mV and + 65 mV (Haegerhaell et al., 1992). Therefore, based on literature values, *b*-haems from either of these two complexes would fit these approximate spectral and redox features.

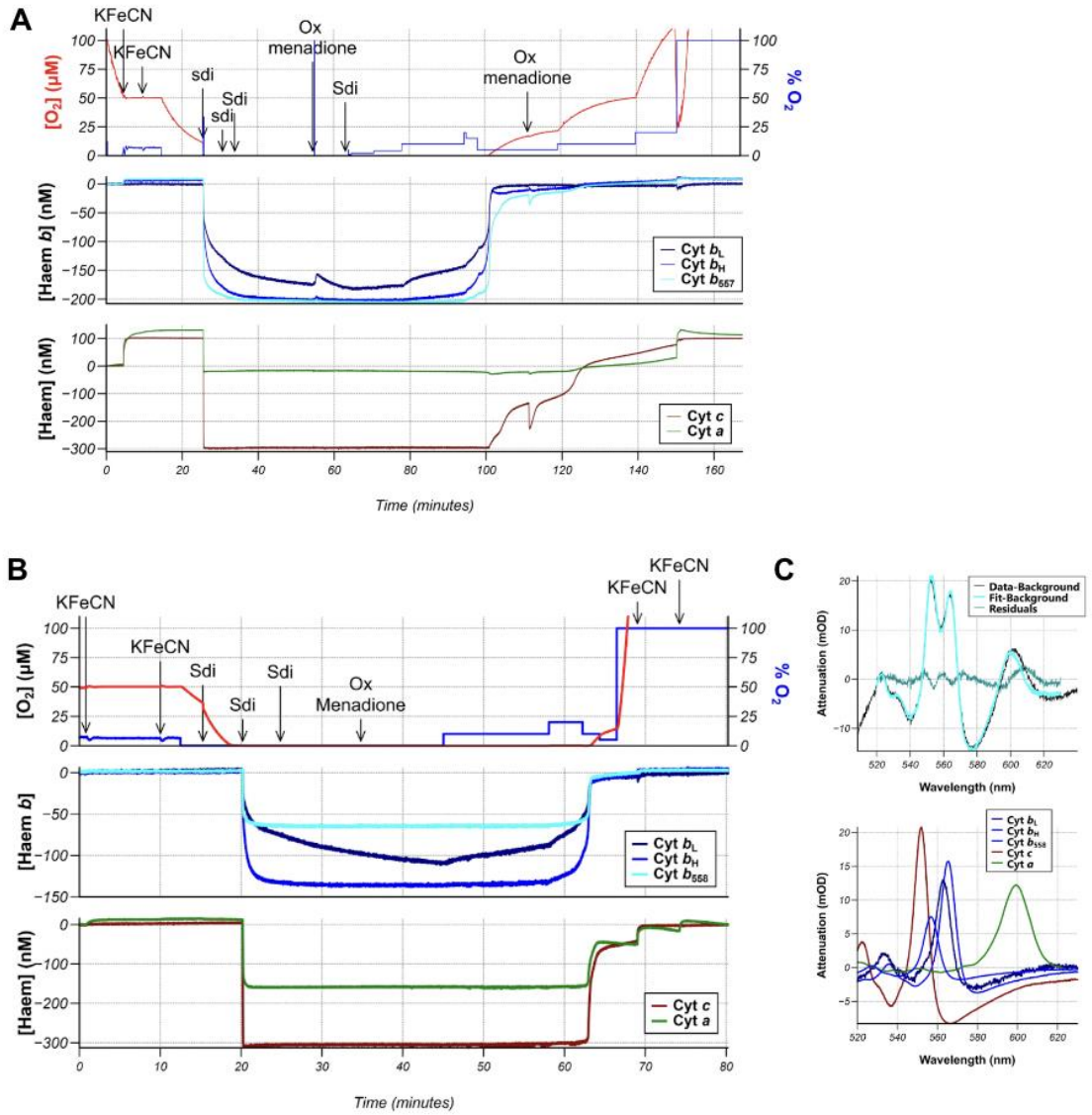

Figure 4.32 - The results of adding a b_{557} signal to the experiments with wild-type membranes or Δcyd membranes*. (**A**) Experiment with wild-type membranes. (**B**) Experiment with Δcyd membranes. (**D**) Example of the fitting on Δcyd membranes.*

No matter which cytochrome or cytochrome(s) is the source of the b_{557} signal, it is an important addition to the fit to appropriately account for the b_L and b_H signal to be fitted.

Indeed, applying this fit with the addition of the b_{557} signal improved the fitting of the spectra collected on live cells (Fig 4.33). The residual, between the raw data and the fit, no longer has a feature around 555 nm and the b_H reduces as the cells are taken anoxic.

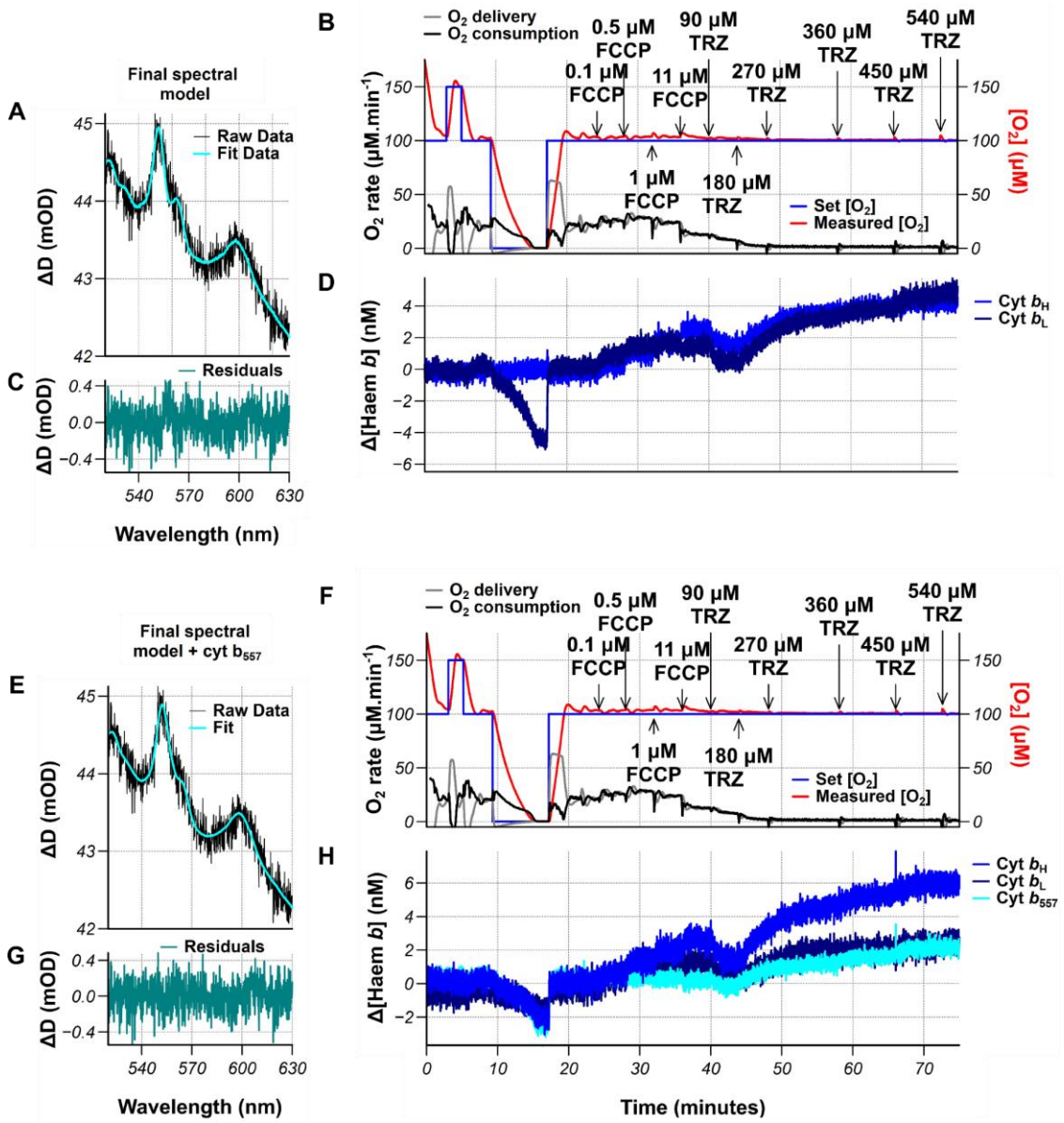

Figure 4.33 - Comparing the results of the final spectral model +/- the b_{557} signal *(Top panels, **A**-**D**) - Results from decomposition with the final spectral model. (bottom panels **E**-**H**) - Results from decomposition with the final spectral model with an additional signal with a peak maxima at 557 nm. For each model the oxygen consumption (**B** & **F**) and changes in the haem concentration based on decomposition using the spectral model (**D** & **H**). An example of the fitting during the period of anoxia is shown (**A** & **E**) along with the residual of this fit (**C** & **G**)*

4.3.17 Measuring/estimating the ΔΨ in mycobacterial cells utilising improved spectral and thermodynamic models.

With this improved spectral model, a measurement of ΔΨ in live *M. smeg* could be made. Initially, I compared the estimated ΔΨ when the culture had been decomposed by spectral model 1 or the final spectral model, plus the b_{557}, The original mammalian model was then used to estimate the ΔΨ (Fig 4.34). The difference in the spectral model used did change the fraction oxidised of the two haem centres during the run. For example, the starting point oxidation state of b_H and b_L was ~20 % and ~40 % respectively when spectral model 1 was used. In comparison the oxidation states when the 'final spectral model' was used were ~30% for both centres. These changes resulted in different patterns of changes in ΔΨ throughout the run for the different fits. The ΔΨ continued to drop after the addition of 0.5 μM FCCP (as with spectral model one) but stopped falling after the 0.5 μM FCCP addition with the final spectral model.

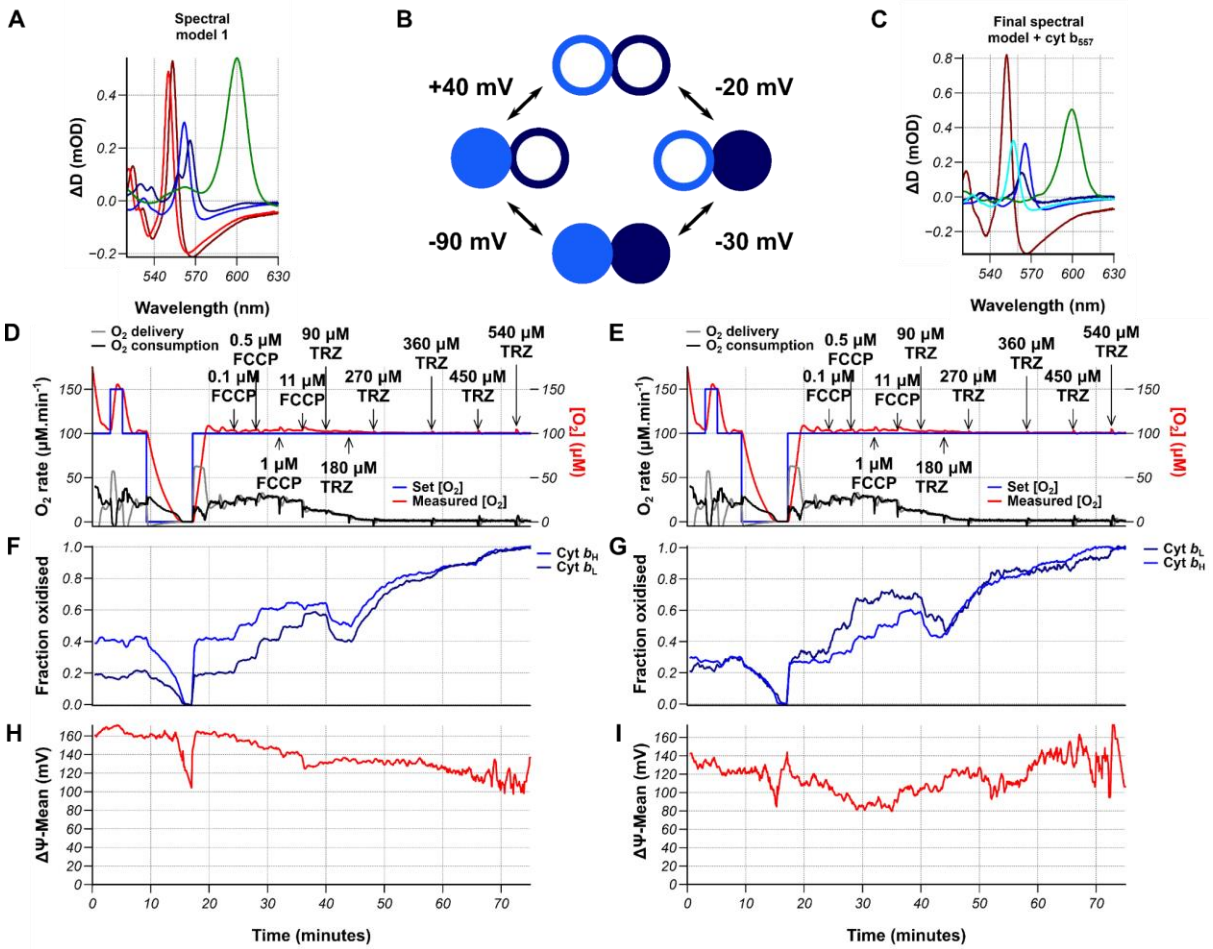

Figure 4.34 - Difference in ΔΨ measurements depending on the spectral model used to decompose the spectra from the live cell experiment *(**A**) Spectral model 1, mammalian reference spectra. (**B**) The mammalian thermodynamic model was used to measure ΔΨ with both spectral models (**D**, **F** & **H**) the ideal experiment decomposed with spectral model 1, the b haem oxidation states calculated (oxidised point after 540 µM TRZ, reduced point anoxia) and used to measure the ΔΨ.(**E**, **G** & **I**) the ideal experiment decomposed with spectral model 1, the b haem oxidation states calculated (same as for spectral model 1) and used to measure the ΔΨ.*

To determine the effect of altering the thermodynamic model, the estimated ΔΨ was compared from three different thermodynamic models, parameters described in Fig 4.35 B. The three models were the original mammalian thermodynamic model, and the two thermodynamic models as determined in Fig 4.22, unrestricted parameters (myco redox model 1), and in Fig 4.27, restricted parameters (myco redox model 2). Myco 1, from the decomposed titration, using directly measured reference spectra, unrestricted parameter fitting. When these were applied to the fraction oxidised traces from the 'final spectral model' all three thermodynamic models gave the same pattern of changes in the ΔΨ and E_h MQH_2

during the run, Fig 4.35 D & F. The gap in the E_m of the two *b*-haems, ΔE_m^b, is the greatest determiner of the size of ΔΨ estimated. An ΔE_m^b of 120 mV in myco model 1 estimates a starting ΔΨ of ~225 mV ΔΨ and an ΔE_m^b of ~65 mV estimates a starting ΔΨ of ~120 mV (the mammalian and myco model 2). As part of the calculation, the E_h of the Q pool is also estimated. Compared to the ΔΨ, the negative more E_m values of the myco models have a much greater effect on the E_h of the Q pool, estimating it between -170 mV to -250 mV. This is considerably more negative than the E_h estimated with the mammalian model, ~ 0 mV.

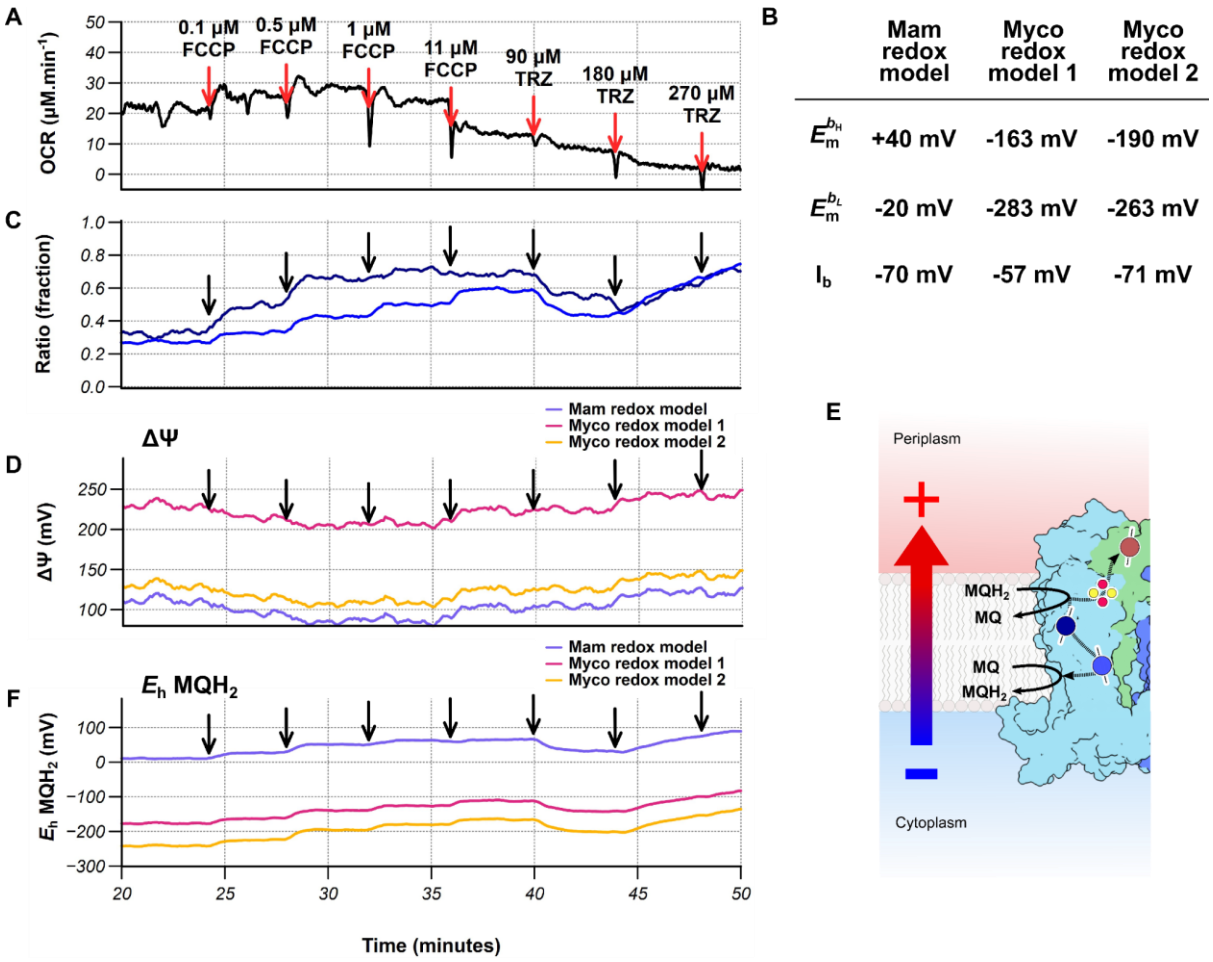

Figure 4.35 - Difference in the measured ΔΨ and E_h using the different thermodynamic models generated in this chapter. *(**A**) Oxygen consumption and FCCP or TRZ additions during the experiment (**B**) The three thermodynamic models used. (**C**) The oxidation state of the b-haems from the decomposition of the spectrum with the final spectral model + the b_{577} signal. The oxidation states of b_L and b_H are in dark and light blue respectively. (**D**) Measure ΔΨ for each of the three thermodynamic models (**E**) Measure E_h Q-pool for each of the three thermodynamic models*

4.4 Discussion and further work

4.4.1 The utility of the estimation of ΔΨ developed in this chapter

Logically to check this ΔΨ measurement it would be sensible to compare the results to measurements made using another method. The difficulty with this is finding a good method to use as a comparison given all of the issues that other ΔΨ measurements have. The alternative is to 'sanity' check the changes in ΔΨ when metabolic effectors are added. The changes upon the addition of lower concentration FCCP are as expected a decrease in ΔΨ. After 11 μM FCCP there is an increase in ΔΨ coinciding with a decrease in the oxygen consumption, suggesting that FCCP may no longer be solely acting as an uncoupler. The bioenergetic chamber has previously been used to make Fluorescent NAD(P)H measurements which may offer some insight into the NADH oxidation state and so may clarify what is happening to the NADH pool when cells are treated with FCCP.

Unsurprisingly, it appears that the goodness of the spectral fitting is the biggest determinant in the relative changes in ΔΨ during a run. Given that we cannot confidently assign the total spectrum exclusive to the cyt *bcc:aa*$_3$ it is likely that other cytochromes are also contributing to the overall spectrum in live cells. This means that the mis-fitting of the overall spectra is the largest contributor of error to this ΔΨ measurement. Several possible fits were tried including adding a difference spectrum from Sdh2 (generated from preliminary spectral characterisation presented in Chapter 5), however, this still led to the same mis-fitting of the *b*-haems. The decomposition will just provide the 'simplest' solution, often leading to peaks cancelling each other out and it cannot fit signals which have not been provided.

The use of knockouts is one way to simplify the spectral fitting, as here with Δ*cydAB*. However, knocking out respiratory complexes is likely to change the composition of the respiratory chain and not always in predictable ways. The difference spectrum appears to indicate an increase in the *b* haem signal and potentially a decrease in the amount of cyt *bcc:aa*$_3$. This could potentially be from etfD as discussed above or could be another cytochrome. As compared to the mammalian chain where there are only 3 *b*-haems of particular abundance present, there could be more than 6 *b*-haems to fit in wild-type mycobacteria. Even with an accurate reference spectrum, this could be a difficult task, knockouts and specialised experimental protocols may be the only way to accurately determine ΔΨ.

The difficulty in fully transforming the signals is another source of error within these measurements, but difficult to achieve without careful experimentation and nanomolar inhibitors of the dehydrogenases to fully oxidise the haem signals.

Between the different thermodynamic models of the enzyme does not alter the pattern of change in $\Delta\Psi$, instead altering the absolute estimate of $\Delta\Psi$. The calculated $\Delta\Psi$ reflects the ΔE_m between the two *b*-haems, and the estimation of E_h of the Q pool reflects the general E_ms of the model. For the two mycobacterial models, this means the E_h of the Q-pool is much more negative than the mammalian model. This is not an entirely unexpected E_h as the E_m of the MQ/MQH_2 couple is -74 mV (Schnort, 1966; Thauer et al., 1977; Wagner et al., 1974). However, based on the calculated E_h of -200 mV the MQ-pool would be < 1 % oxidised, one would expect the E_h to be closer to the E_m of MQ (50% oxidised). It could be that the prior E_m of MQ titration measurement does not reflect the E_m of MQ in a hydrophobic membrane environment. Titrations of MQ have been performed in a membrane on an electrode, and the E_m was marginally more negative (E_m = -88 mV, Dharmaraj et al., 2020) but this is not negative enough to explain the E_h of the Q-pool. Alternatively, it could be that in the mycobacterial chain, the Q pool redox state is further away from equilibrium (50% oxidised) than the Q pool in mitochondria, or the assumption that the *b*-haems are in equilibrium with the Q pool is not true for mycobacteria.

4.4.2 Potential haem protein environment reasons for spectral differences between the mammalian and mycobacterial *b*-haems?

The most unexpected finding in the development of the spectral model of the cyt *bcc:aa*$_3$ supercomplex was the difference in the shape of the spectra of the mycobacterial b_L and the b_H. The α-peak maxima of the mycobacterial *b*-haems are switched relative to the mammalian *b*-haems, Fig 4.36. It is not possible to confirm the spatial arrangement of the *b*-haems in the mycobacterial cyt *bcc* with the data in this chapter or published data i.e. the b_H could be closer to the P-side of the membrane and the Q_o site and the b_L could be closer to the N-side of the membrane and the Q_i site. This would be one explanation for the switch in the centre maxima. However, it would mean a considerable change in the energy landscape of the low potential chain. The hypothetical transfer from b_H to b_L would be both against the $\Delta\Psi$ and working against their respective E_m, and so would be a very endergonic step. This unfavourable step could be compensated by other exergonic steps within the complex's mechanism but I think would be unlikely for a cyt *bc* type complex. It is more likely that the energy landscape is similar to canonical cyt *bc* complexes, Fig 4.36 C.

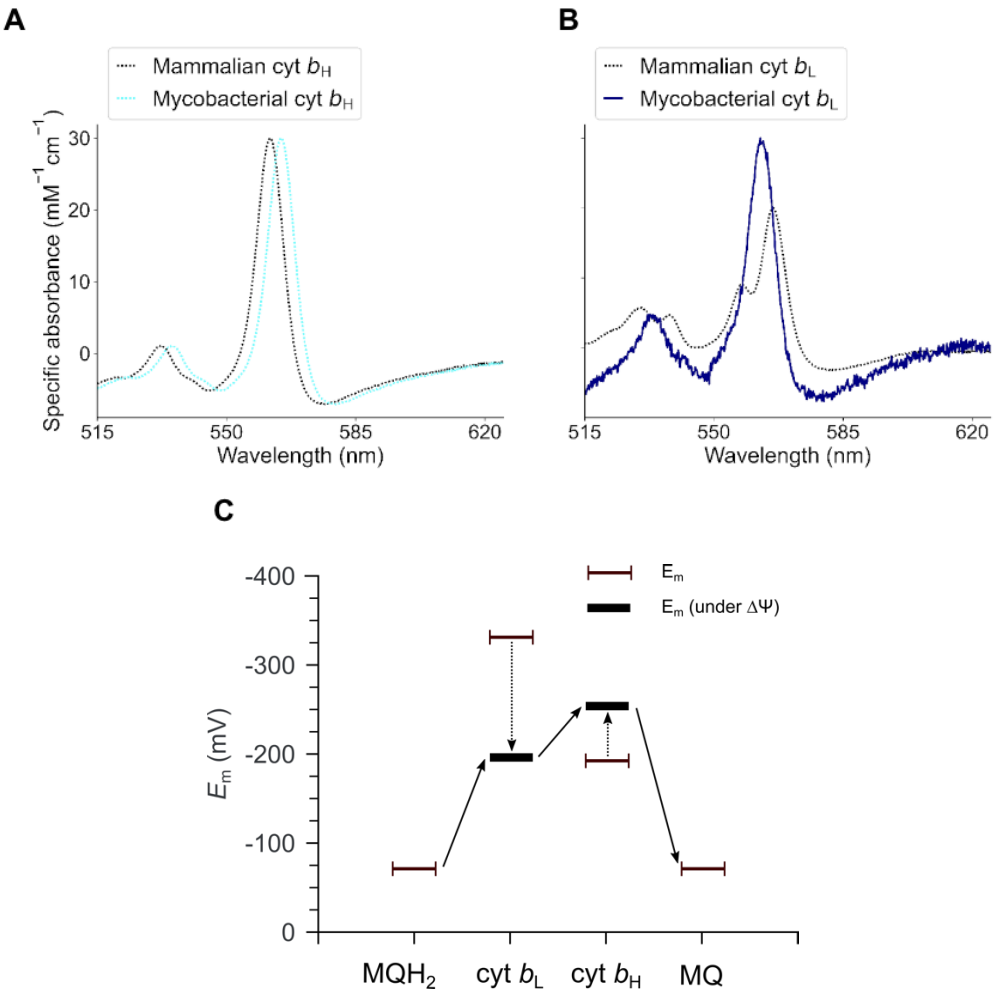

Figure 4.36 - Developed spectral and thermodynamic model of the mycobacterial cyt bcc *(**A** & **B**) Comparison of the spectrum from mammalian cyt bc_1 and mycobacterial cyt bcc, **Am** - b_H **B** - b_L (**C**) Most likely energy landscape of the mycobacterial cyt bcc.*

Mutating surrounding residues, say the axial residues of the respective haem would be one way to determine the spatial arrangement of the haems. Either the mutation would result in the loss of the proximal haem centre or a change in the spectrum of the haem centre. However, the mutation may create a non-functional and potentially unstable enzyme which is non-ideal. Inhibitors of the Q_o and Q_i sites, the two quinol sites of the cyt *bc* complex, may help to determine the spatial arrangement of the *b*-haems. As far as I have been able to determine, a traditional Q_o inhibitor Myxiothiazol does not work on the mycobacterial cyt *bcc*. Other traditional Qo inhibitors could tried but as part of drug discovery for *M. tb*, Q203 or telacebec has been developed as an inhibitor of the cyt *bcc:aa*$_3$. Structural studies and the location of resistance mutations demonstrated that it binds to the Q_o site (Pethe et al., 2013; Yanofsky et al., 2021), so this is a promising candidate for manipulating the cyt *bcc* complex.

Canonical inhibitors have been known to affect the spectral and redox properties of the nearby haem, (Berden and Slater, 1972). With careful consideration of any of the spectral effects of the inhibitors, redox titration performed in the presence of inhibitors may demonstrate effects on the E_m of the closest haem to the inhibitor binding site (Rich et al., 1990).

The mycobacterial b_L spectrum also appears to lack the double peak feature in the α-peak region, present in all other previously measured b_L from *R. sp* or bovine cyt bc_1. Using previously published structures of the cyt *bcc:aa*$_3$ supercomplex and cyt *bc* type complexes from other species (bovine, mouse, and *R. sp*) showed some relevant differences. The surrounding protein environment around b_L, the *b* hae*m* closer to the Q_o site, showed some change in the protein fold near the propionate groups (Fig 4.37). There appears to be an additional potential hydrogen bonding partner for one of the propionate groups in the mycobacterial structure (Asn 282 in the qcrB subunit). This asparagine is not present in the other cyt bc_1 complexes, and the structure-aligned sequences show that two residues are missing in this region in the mycobacterial sequence which appears to have brought this asparagine in closer proximity to the propionate than in other cyt *bc* complexes. It is not yet possible to predict the exact spectral contribution of the individual centres based on their structures; it is plausible that this difference around the propionate groups may explain the difference in the mycobacterial b_L spectrum.

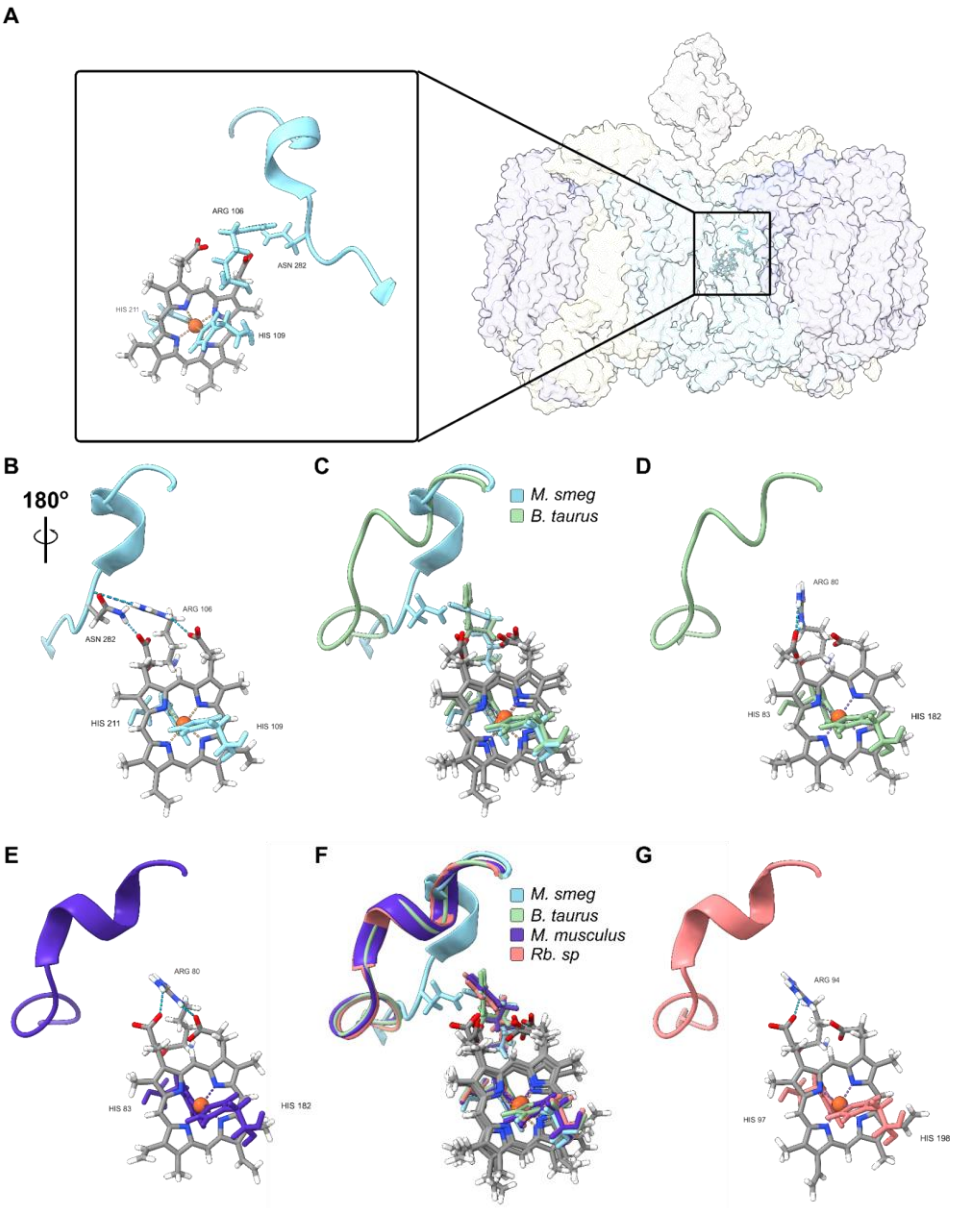

Figure 4.37 - Differences in the residues within H bonding distance to the propionate groups of the b_L *(**A**) Location of the b_L in the cyt bcc:aa$_3$ supercomplex (M. smeg) within the right monomer. (**B**) In blue the axial ligands and residues that are within H bonding distance to the propionate groups of the haem in the M. smeg enzyme, (PDB 7RH5, Yanofsky et al., 2021). This includes a short sequence that orientates the asparagine towards the propionate. (**C** & **D**) The b_L from M. smeg compared to the bovine b_L. In green the bovine b_L, (PDB 1NTZ, Gao et al., 2003), overlayed (**C**) on its own (**D**). The equivalent short sequence is shown with no residue presented to the propionate group in the bovine structure. The same is shown for the mouse b_L (**E**, in purple, PDB 7O3H, Vercellino and Sazanov, 2021) and the R. sp (**G** in coral, PDB 8ASI, Swainsbury et al., 2023). (**F**) All the b_Ls are overlayed.*

4.4.3 Redox titrations and simultaneous deriving the spectral and thermodynamic properties of cytochromes

The data described in this chapter is insufficient to fully determine the parameters for a complete thermodynamic model with reasonable certainty. The apparent ΔE_m between two interacting centres will be dictated by several factors as described by Eq. 4.21.

$$\Delta E^{app} = \Delta E^{o} + \Delta E^{Coulombic} + \Delta E^{Solvent\ Environment} \qquad \text{Equation 4.20}$$

ΔE^o is the actual difference in electron affinity between the centres, determined by the nature of the redox centre and the local protein environment of the centres. $\Delta E^{Coulombic}$ is the coulombic repulsion of nearby redox cofactors that will be insulated to some degree by the nature of the protein environment between the redox centres. This can also be across multimeric complexes rather than just within a monomer. This may be the sum of several different interactions. For example, in a dimeric complex like the cyt bc_1, there will be interactions within the monomer or between dimers as the two b_L are if the distances are close enough.

Given the larger errors of the parameters of the anti-cooperativity models calculated in this chapter, the minimization algorithms may be getting stuck in local minima. More information such as the ΔE^o or $\Delta E^{Coulombic}$ would aid them in determining the true parameters to describe the system. One could assume that the conservation of parameters such as the K constant for electron transfer between b_L and b_H measured in a homologue is a fair assumption, as for the restricted model (myco redox model 2). For the *c*-haems where there are not well-described homologues, these properties would have to be determined. The thermodynamic model within the simultaneous method has the benefit of being able to accommodate these parameters to improve the final characterisation of the centres.

There is also an interactive Python package, BioDC, that may help to estimate some of these parameters. Given an inputted structure of a complex BioDC can estimate the interaction between centres present (Guberman-Pfeffer, 2023; Hardy et al., 2024). BioDC can also delineate between the coulombic repulsion, $\Delta E^{Coulombic}$, and the influence of the protein environment (interior and exterior), $\Delta E^{Solvent\ Environment}$. In the case of membrane proteins, they have a lower dielectric environment in their interior. This means that the protein interior less efficiently screens the electrostatic field felt by each haem centre, enlarging the ΔE^{app}.

The simultaneous determination of thermodynamic and spectral properties has merit beyond cyt *bcc:aa*$_3$ supercomplex. The workflow does not require the reference spectra or the E_m of

the cofactors to be known. Information from orthogonal techniques, such as structural biology, can help to direct the number of centres and interactions to be included in the thermodynamic model. This would have utility for cytochromes where there is a lack of well-characterised inhibitors but some idea of the component cofactors. It also avoids the distortion that inhibitors can cause to the spectral and redox properties of enzymes.

More generally, exploiting the differences in the E_m of redox centres proved the most successful strategy for isolating the spectral contribution of the redox centres. Given the interest in mycobacterial bioenergetics, and bacterial bioenergetics more widely, if more specific inhibitors become more widely available there may be other strategies in the future for this type of work. It may be possible to separate the signals from haem *a* from haem a_3 by using the affinity of the a_3 site for various ligands (CO, CN, and azide). These all can distort the spectra and can bind the *a* site at higher concentrations. Therefore, the use of these inhibitors to isolate the spectra would have to be carefully controlled.

More carefully controlled redox titrations performed in membranes also offer an opportunity to understand the E_m of the haem components present in the membrane. In the experiments in Figures 4.31 & 4.32, even though the transformations of the difference haem centres were very rapid, the signals do seem to be separated. If the E_h of the experiment could be controlled via a chemical reductant or a working electrode and measured either by a reference electrode or a redox indicator, a similar analysis workflow as for the potentiometric redox titration could be used to determine the spectral and thermodynamics properties of the haem cofactors present in the membrane.

4.4.4 Improvement to the measured turnover rates of the cyt *bcc:aa*$_3$

Whilst the estimated turnover rates for intact cells vs the isolated enzyme were rough and ready calculations, the isolated enzyme turnover was 6-fold slower than the estimated turnover in cells. These turnover rates from purified complex may be improved if the E_h of the quinol substrate is kept sufficiently reduced during the measurement of the turnover rate. I hypothesise that for the isolated enzyme the quinol E_h quickly becomes unfavourable during the enzyme turnover. A coupled enzymatic system could be used to keep the quinol reduction state favourable. Recombinantly expressed and purified Ndh2 from the thermophilic bacteria *Caldalkalibacillus thermarum* is a type-II NADH dehydrogenase that will reduce quinones to quinols (Blaza et al., 2017; Heikal et al., 2014). This means the E_h of the quinone couple can be kept reduced using NADH. This is actively being pursued by a PhD student with the group, Ben Hartmann, with the aim of reconstituting both components into proteoliposomes to allow the measurements of turnover rates in a membrane with a $\Delta\Psi$ across the membrane, similar

to the system that has been described for mammalian complex I (Jones et al., 2016). This may also improve the measured turnover rate as $\Delta\Psi$ alters the energy landscape of the cyt *bc*c enzyme, favouring catalysis.

4.5 Conclusion

This chapter has described the purification of pure mycobacterial cyt *bcc:aa*$_3$ with activity equivalent to published rates of isolated cyt *bcc:aa*$_3$. These turnover rates appear to be several-fold less than the apparent turnover rate *in vivo*, which may be a result of the difficulty in retaining a negative E_h of the substrate and the difference in the energy landscape of the enzyme under $\Delta\Psi$. From exploiting the difference in the E_m of the different haem centres, I have been able to build a set of reference spectra that account for the individual haem centres. The reference spectra for the *b*-haems appear to deviate from previously characterised cyt *bc*$_1$ spectra. With the aid of these reference spectra, I have begun to characterise the thermodynamics landscape of the cyt *bcc:aa*$_3$ supercomplex. This allowed the assignment of E_m and difference spectrum to likely haem centres.

The cyt *bcc:aa*$_3$ is not the only spectral contribution to the spectrum of exponential phase *M. smeg*. The addition of an extra *b* haem signal (maxima 557 nm) improves the fitting result of the spectral model. Using this unified spectral and thermodynamics model, I have a first estimation of change in $\Delta\Psi$ when live *M. smeg* cells are perturbed by the uncoupler FCCP using the changes in the redox poise between the *b*-haems of the cyt *bcc* complex. This offers a new intrinsic approach to measuring $\Delta\Psi$ in mycobacteria. Given the interest in the bioenergetics of mycobacteria as a new target space for anti-TB agents, having additional tools to characterise the key bioenergetic parameter $\Delta\Psi$ should help clarify the mechanism of action of bioenergetic targeting agents. An improved understanding of the mechanism of action offers the potential to improve the next generation of anti-TB agents and guide the design of synergistic drug regimes.

Chapter 5 - Developing preparations of the mycobacterial cyt *bd* quinol oxidase and Sdh2

5.1 Introduction

5.1.1 The presence of non-cyt *bcc:aa*$_3$ supercomplex mycobacterial cytochromes

Previous work in this thesis has indicated that the cyt *bcc:aa*$_3$ supercomplex is not the only cytochrome contributing to the overall haem spectra of mycobacteria. From mass spectrometry data and spectra of the membranes and cells, it is clear that the cytochromes sdh2 and cyt *bd* are present in aerobically grown cells, albeit contributing less to the overall haem spectra than the supercomplex. The roles of Sdh2 and cyt *bd* in the mycobacterial respiratory chain are also interesting given the plasticity of the mycobacterial respiratory chain. It has become apparent during this work that a putative cytochrome etfD (Beites et al., 2021) may also contribute to the overall spectrum. It has not been isolated as part of the work in this chapter but would be worthy of further investigation. There may also be other haem-containing complexes, such as the haem-containing protein DosS and DosT which are redox and hypoxia sensor kinases (Kumar et al., 2007). They may be contributing to the total haem spectrum and so require further characterisation.

5.1.2 Prior studies of mycobacterial cyt *bd* quinol oxidase before beginning this work

The cyt *bd* menaquinol oxidase provides an alternative route to oxygen. The fact that it is less bioenergetically efficient than the haem-cooper oxidase (cyt *aa*$_3$) in terms of proton pumping offers a route to oxygen that is less affected by back pressure for the mycobacterial chain. This would expand the cyt *bd*'s roles beyond just being a high-affinity oxidase for use under oxygen-limited conditions as has traditionally been assigned. Before beginning this work, the structure of several cyt *bd* quinol oxidases had been determined (Safarian et al., 2019, 2016; Theßeling et al., 2019) but no mycobacterial cyt *bd* oxidase had been determined. Subsequently, structures of the *M. smeg* and *M. tb* enzymes have been solved (Safarian et al., 2021; Wang et al., 2021). Both of these structures were determined using enzymes expressed and purified using tagged plasmids constructs.

Interestingly neither structure contained any additional subunits other than the cydAB. In the prior structures from *E. coli* and *Geobacillus thermodenitrificans* additional single transmembrane helix subunits were found bound in clefs of the *bd* oxidase (Safarian et al., 2019, 2016; Theßeling et al., 2019). Accessory helices like those found in some of the cyt *bd* structures can originate from genes outside the main operon for the cyt *bd* complex. This means that plasmid expression approaches could result in the additional subunits being missed and the purification of an incomplete enzyme. It is unclear how the expression of these small proteins is coordinated with the expression of the core subunits. These small accessory helices, encoded outside the main operon, are found in many other respiratory complexes. Their exact role is not clear but one could envisage stability and regulatory roles for them.

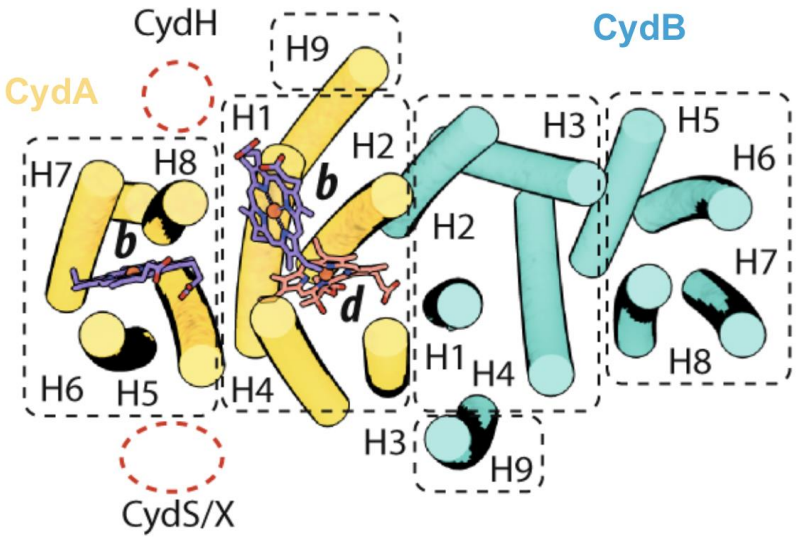

Figure 5.1 - Structure of the M. tb cyt bd oxidase and the location of known accessory helices subunits that have been found in the structure of the cyt bd. *CydH and CydX were found in the E. coli structures (Safarian et al., 2019; Theßeling et al., 2019) and CydS was found in the G. thermodenitrificans structure (Safarian et al., 2016). The absence of the subunits in the M. tb structure is shown by red dashed line circles. Figure taken from Safarian et al., 2021. A slice view of the helices through the plane of the membrane, with the periplasmic side towards the reader and the cytoplasmic side behind the image.*

The lack of this accessory helix leaves the cyt b_{595} more accessible in the mycobacterial structure. In the *M. smeg* structure, this was proposed to be an additional oxygen channel (Wang et al., 2021). They also could not resolve the Q-loop of the enzyme due to its flexibility, similar to other cyt *bd* structurally characterised from other species. In the *M. tb* structure, they were able to resolve the Q loop, finding a disulphide bond had stabilised the Q-loop

(Safarian et al., 2021). The responsible cysteine residues are present in the *M. smeg* Q-loop, so it is not clear why the loop was more stable for the *M. tb* preparation. This may be due to other differences in the Q loop or more likely due to differences in the two enzyme preparations. A more recent pre-print has observed that M. tb cyt bd activity is decreased in the presence of reducing agents (Velden et al., 2024), the same effect was not seen on the activity of *E. coli* cyt *bd*-I. These assays were performed in proteoliposomes with Ndh2, from *C. thermarum,* an ideal platform for further investigation of menaquinol using bacterial oxidases for the reasons described in the discussion of Chapter 4. No effort has previously been made to separate the spectral contributions of the three haem centres in the mycobacterial cyt *bd*. This has been done for the cyt *bd*-I in *E. coli* (Bloch et al., 2009), which could be used as a starting point for spectral analysis of the mycobacterial cyt *bd* prior to the isolation of mycobacterial reference spectra.

5.1.3 The mycobacterial succinate dehydrogenases

M. smeg has two succinate dehydrogenases at the succinate fumarate junction, sdh1 and sdh2. The menaquinone-linked succinate oxidation is unfavourable due to the redox potentials of the two couples (succinate/fumarate E_m = +30 mV, MQ/MQH_2 = -74 mV). For Sdh2 this unfavourable reaction is compensated for by consumption of the *pmf*. It is unclear how the unfavorability of menaquinone reduction by succinate is accounted for in Sdh1. One might hypothesise that it is a quinol fumarate reductase (QFR) rather than a succinate dehydrogenase (SDH) as annotated. However, no fumarate reductase activity has been measured from the membranes of *M. smeg*. Some have hypothesised that Sdh1 may use polyketide quinones with a more positive redox potential, making the reaction favourable (Hards et al., 2019; Zhou et al., 2021). Sdh1 does not contain haems and so would be ‘invisible’ to the haem spectroscopy techniques of the chamber it does raise an intriguing question as to how it functions if it is indeed an SDH, and under what circumstances it is used in mycobacterial ETCs.

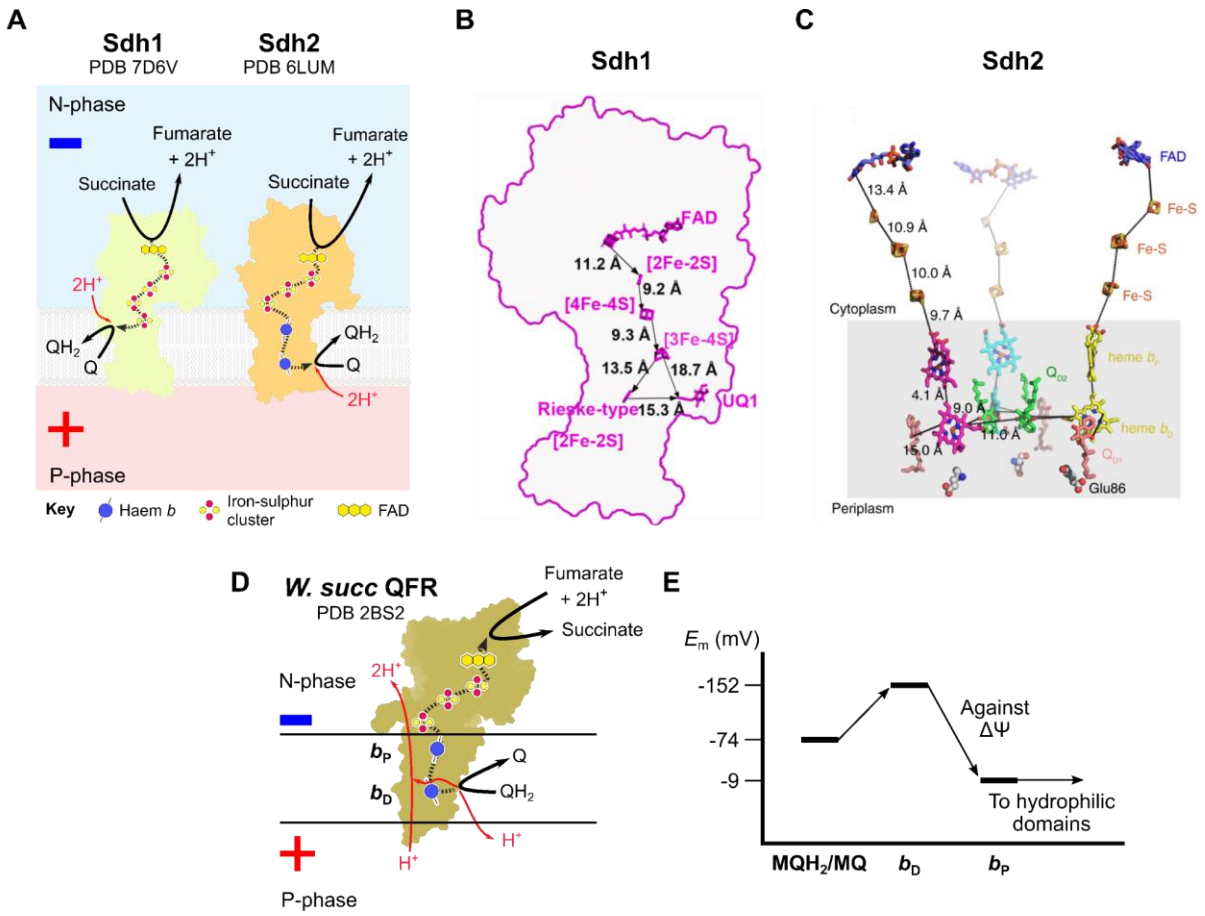

Figure 5.2 - Electron transfer pathways in the mycobacterial succinate dehydrogenase and the energy landscape of the QFR from W. succinogenes. *(**A**) A cartoon representation of the two succinate dehydrogenases present in M. smeg with the cofactors, electron transfer pathway and Q-sites indicated. These have been switched in orientation (P-Phase and N-Phase) relative to previous thesis figures to match the subsequent figures. (**B**) The distances between the cofactors in Sdh1, figure taken from (Zhou et al., 2021). (**C**) The distances between the cofactors in Sdh2 in all units of the trimer, figure taken from (Gong et al., 2020). (**D**) The QFR from W. succinogenes, PDB 2BS2 (Lancaster, 2002). The hypothesised 'E-pathway' is indicated, one proton is supplied from the quinol oxidation and the other from the P-phase. The standard notation of the b-haems is shown. This can be particularly confusing with the cyt b_6 complexes b haem notation, which are often notated b_P and b_N. (**E**) The energy landscape of the QFR from W. succ. The transfer from b_P to b_D will be against the ΔΨ. For succinate dehydrogenases, such as Sdh2, this will be in the opposite direction.*

As described in this thesis's introduction, the structure of both the *M. smeg* succinate dehydrogenase have recently been determined (Gong et al., 2020; Zhou et al., 2021). The redox potentials of several SDH and QFR have been characterised, as summarised in

(Lancaster, 2013). The most well-studied is the QFR from *Wolinella succinogenes* from class B (Figure 5.2 D). The *W. succ* QFR uses menaquinol to reduce fumarate. It is hypothesised to have an 'E-pathway' that allows for the reduction of fumarate to be electroneutral (Lancaster, 2002). This E-pathway is not present in Sdh2. The experimental midpoints of *W. succ* QFR's two *b*-haems have been determined to be -152 mV and -9 mV (Mileni et al., 2006). Prior simulations of redox titrations using continuum electrostatics calculations led to the assignment of the more positive redox potential to the proximal *b* haem (b_P) and the more negative redox potential to the distal *b* haem (b_D) (Haas and Lancaster, 2004). The examination of redox titrations of mutants of the closely related *B. subtilis* SDH supported this assignment (Matsson et al., 2000).

The reference spectra for SDH or QFR with multiple *b*-haems have not been determined. There is likely a similar split in the redox potentials of the *b*-haems of Sdh2 that may facilitate their spectral separation. It would be wise to carefully consider the assignment of the *b*-haems redox potentials, in case there are differences between the enzymes. There is also likely to be redox anti-cooperativity between the two *b*-haems due to their proximity which would have to be considered to accurately calculate their redox potential.

5.2 Aims for this chapter

Aim:

Develop purifications of the cyt *bd* menaquinol oxidase and Sdh2 to be able to spectral characterise their haem groups to add to the spectral model of mycobacterial haem spectra.

Objectives:

Develop a native purification of the cyt *bd* quinol oxidase, using conditions which induce increased expression of the oxidase

Using the same system previously developed to purify cyt *bcc:aa*$_3$, purify Sdh2 using a chromosomal FLAG-tag

Determine what cytochromes are spectrally detectable in strains where cytochrome components have been knockout

5.3 Results

5.3.1 Trial of native purification of the *bd* oxidase

The early growth conditions development, in Chapter 3, demonstrated that growing *M. smeg* in oxygen-limited conditions on glycerol increased the expression of cyt *bd*. These conditions were chosen as a starting point to purify cyt *bd* from. Initially, a native non-tagged approach was trialled. This approach offers the advantage of authentic composition of subunits, cofactors, and bound lipids without the potentially destabilising effects of a tag.

As a first step to remove contaminants an ion exchange chromatography approach was used with a strong anion exchanger (HiTrap HP Q column). Monitoring the absorbance at 420 nm and 650 nm allowed the identification of haem-containing and cyt *bd* oxidase-containing fractions respectively. Roughly the absorbance at 420 nm should be in the order 1 magnitude more intense than the absorbance at 650 nm. *d* haem containing fractions were pooled, concentrated and further purified using size exclusion chromatography (Superdex 200 10/30 GL column). The fractions were analysed via BN-PAGE gels, additionally, the fractions were analysed using haem spectroscopy.

5.3.1.1 Ion exchange gradient length

Several NaCl gradients were trialled to purify cyt *bd*. Initially, this began with a 30 cv gradient to 100 % buffer B (Figure 5.3 A). This has increased to a 120 cv gradient to 50% buffer B (Figure 5.1B) to improve the separation of peaks. The longer gradient reduced the number of contaminants (Figure 5.3C & D) however, this gradient change did not remove a more persistent contaminant. This contaminant corresponded to a ~120 kDa band on the BN-PAGE and appeared to begin eluting off the column just before the 650 nm peak. In addition, it was associated with an increase in the 420 nm absorbance and so it may be a cytochrome. The peak in the 650 nm absorbance corresponded to the band at ~75 kDa.

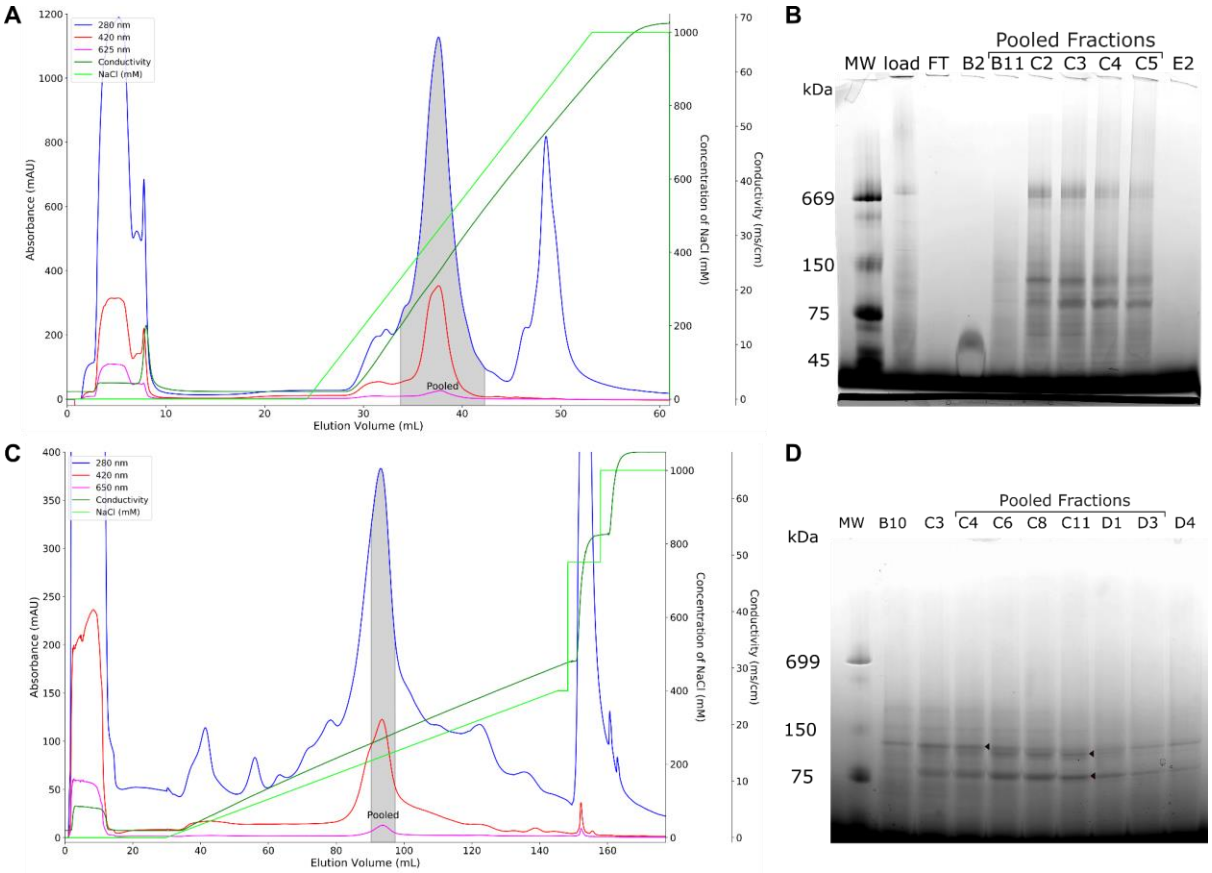

Figure 5.3 - Effect of the NaCl gradient in the IEX: *(**A** & **C**) Chromatograms (**A**) – A 30 cv gradient to 1 M NaCl (**C**) – A 120 cv gradient to 500mM NaCl. For both chromatograms: blue is the absorbance at 280nm, red is the absorbance at 420 nm (haem containing proteins), pink is the absorbance at 625 or 650 nm (d haem containing proteins), darker green is the conductivity, and the lighter green is the NaCl concentration. The grey-shaded areas marked pooled corresponds to the fractions pooled for the subsequent SEC column. (**B** & **D**) BN-PAGE gels (**B**) The gel for the steeper gradient (**A**) (**D**) – The gel for the shallower gradient (**C**) with the major bands marked with triangles. The ~120 kDa band in fraction C4 and C11 and the ~75 kDa band in C11. It is unclear if the slight difference in molecular weight/ running distance in the 120 bands corresponds to different complexes/proteins or is the result of degradation of the same protein/complex.*

5.3.1.2 Targeted ion exchange elution

Given that the contaminant appears to begin eluting off the column at a lower salt concentration than cyt *bd* the containment could potentially be eluted off by holding the salt concentration at its eluting salt concentration just below the eluting concentration for cyt *bd* oxidase. Informed by previous purifications the gradient was slowed down around the previous elution concentration of the contaminant (150-180 mM) and held once the 420 nm

absorbance began increasing (180 mM). However, the 650nm peak also began eluting off during this wash step. This ion exchange run is shown in Figure 5.4. Given the delay in UV output and the effect of changing the elution gradient, better separation might have been seen if the hold had started at a slightly lower concentration. The results suggest that under these conditions the net charge of the two complexes is very similar and would potentially be difficult to separate under these conditions.

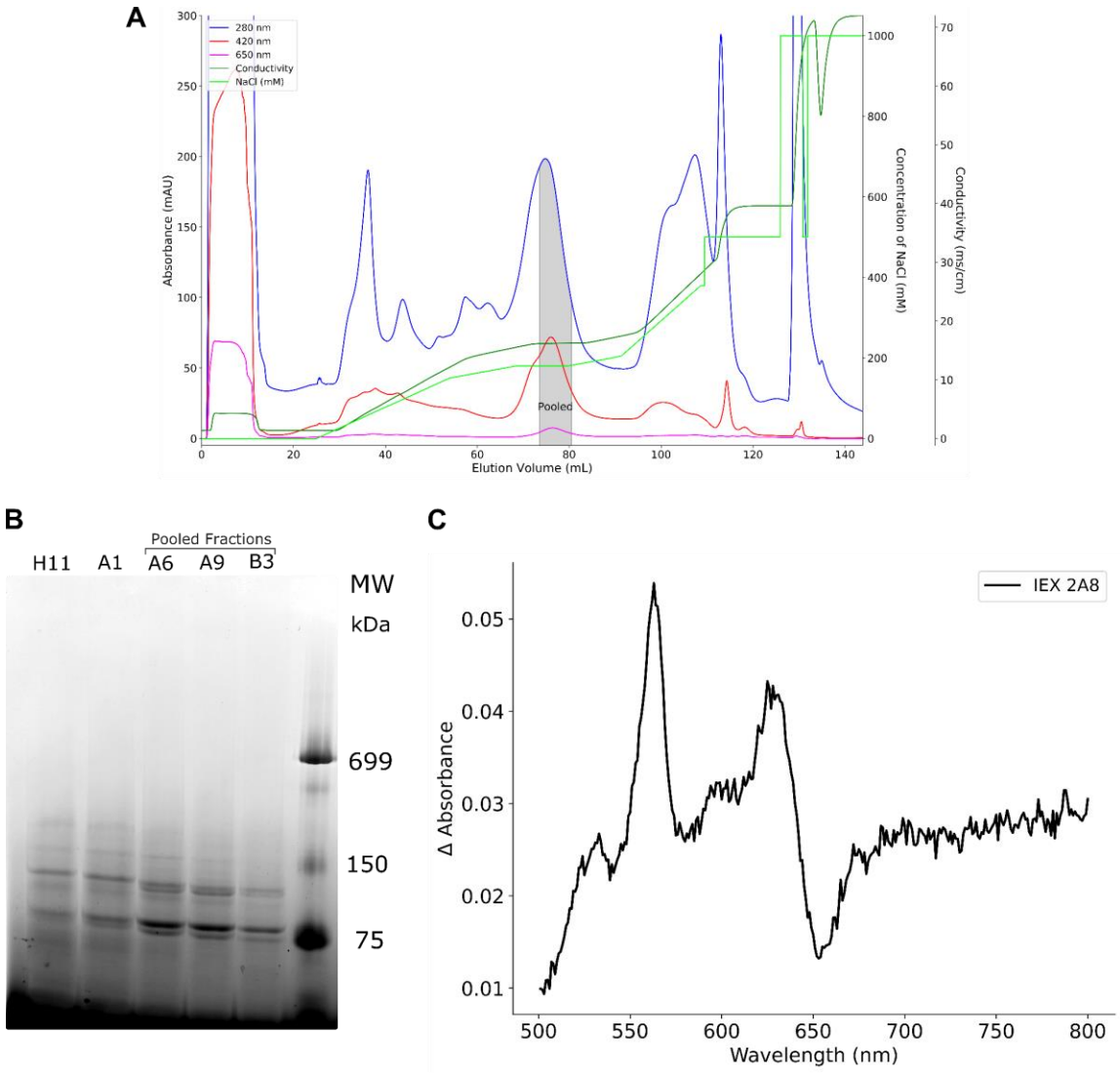

Figure 5.4 - Targeted IEX elution *(**A**) Chromatogram – The column was washed at 180 mM NaCl during a gradient to 400 mM NaCl, the shaded section corresponds to A2-B3 and a sample of which is shown on the BN gel (**B**) BN-PAGE gels – H11 and A1 are fractions in the elution just before the pooled fraction, A6, A9 & B3 are pooled fractions. All fractions appear to have the 120 and 75 kDa bands in varying intensities (**C**) Haem spectra of a pooled fraction – This spectrum was collected from fraction A8 and is very close to the spectrum reported for bd-I from E. coli*

5.3.1.3 Size exclusion step

The Superdex 200 column was chosen as its fractionation range best matched the predicted complex size (90-110 kDa region, range 10-600 kDa). Initially, more fractions from around the *d* haem elution peak were included in the pooled fractions (shaded region figure 5.4 A). This resulted in two peaks on the SEC chromatogram (Figure 5.5 A). The first peak eluted had a strong band at ~120 kDa and some weaker bands at ~700 kDa (Figure 5.5 C), which is similar to how the supercomplex has looked on BN gels in previous papers. The spectra of one of its fractions matched the spectra of the supercomplex (Figure 5.5 B).

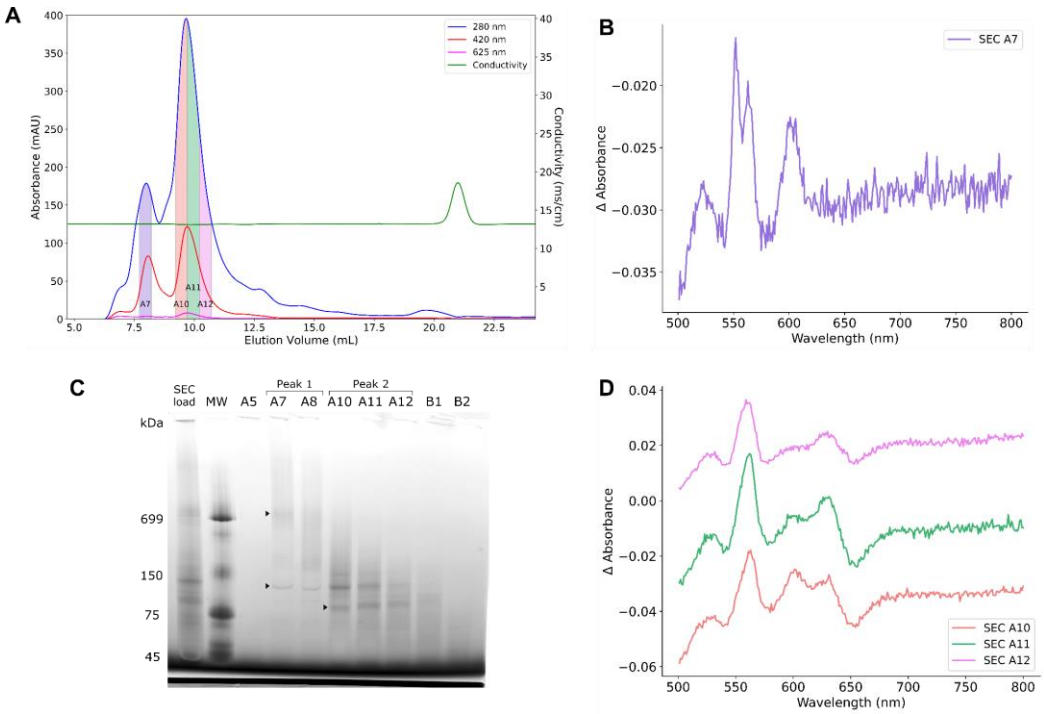

***Figure 5.5 - Initial SEC** : (**A**) Chromatogram – The shaded region from Figure 5.3 A gave two peaks when run on a Superdex 200 increase column. The first peak contained a fraction with a difference spectrum matching the cyt bcc:aa$_3$ supercomplex (**B**) and the second peak contained d haem (**D**). Differences in the elution volume of the d haem elution peak between Fig. 5.5 A and Fig. 5.6 A are likely due to the fact the sample was applied manually to the column in Fig. 5.5 A and not as part of the method, as in Fig 5.6 A. (**C**) BN-PAGE gel – The first lane shows the sample loaded onto the column, A5 is a fraction before either peak, A7 - 8 are fractions from the 1st peak and A10-12 are from the second peak., B1-2 are fractions after the 2nd peak. (**B** & **D**) Difference spectra from the SEC elution – The colour corresponds to the shaded coloured regions on the chromatogram (**A**). The spectrum for A10 was adjusted to prevent overlapping with the spectrum for A11.*

The second larger peak coincided with an increase in the 625nm (*d* haem) absorbance and a band at ~75 kDa on the BN gels. The spectra of its fractions had the *d* haem's distinctive

peak at 630 nm and trough at 650 nm but did seem to have some *a* haem contamination, particularly at the beginning of the peak. This suggests that the second peak eluting at 10 mL indeed contained the cyt *bd*.

In subsequent purification, less of the fraction surrounding the peak has been pooled for the SEC column (shaded region Figure 5.3 A) in an attempt to limit to amount of the 120 kDa contaminant carried forward. The SEC chromatograms from these pooled fractions only have one major peak (Fig. 5.6). This is likely a result of both the decrease in the pooled fraction range and the increase in the length of the IEX gradient increasing the number of contaminants removed.

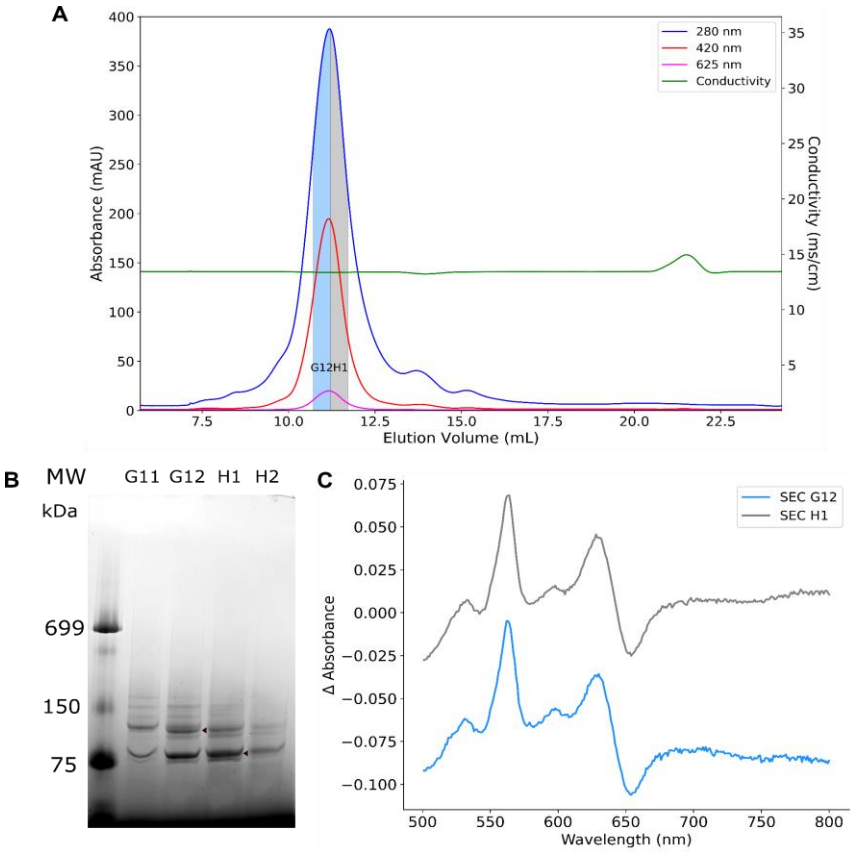

Figure 5.6 - SEC of improved IEX pooled fractions: *(**A**) Chromatogram – The shaded region from Figure 5.4A gave one peak when run on a Superdex 200 increase column. (**B**) BN-PAGE gel – G11-H2 are the 4 fractions across the peak, with G12 (blue) and H1 (grey) indicated on the chromatogram and correspond to the two difference spectra. (**C**) Difference spectra – The difference spectra corresponding to the fractions indicated on the chromatogram. Both G12 & H1 match the spectra for the bd-I from E. coli*

5.3.1.4 Identity of the 120 kDa and 75 kDa bands

To identify complexes of the two major BN bands a second SDS PAGE gel was used to further separate the excised bands into their constituent subunits (Figure 5.7, predicted sizes of subunits are in Table 1). These bands were then sent for identification by mass spectrometry. These identified that the band at 75 kDa contained the CydA of the bd oxidase. CydB was not identified, however, due to how closely the difference spectrum of the fractions match spectra for the bd oxidase in other species I believe we likely have a complete complex. Strains lacking either cydB or cydX lose their b_{595} and *d* haem centres(Green et al., 1984; Hoeser et al., 2014). As the difference spectrum of the fractions has spectral features of both b_{595} and *d*, it suggests that they contain the complete core of the enzyme, cydA and cydB.

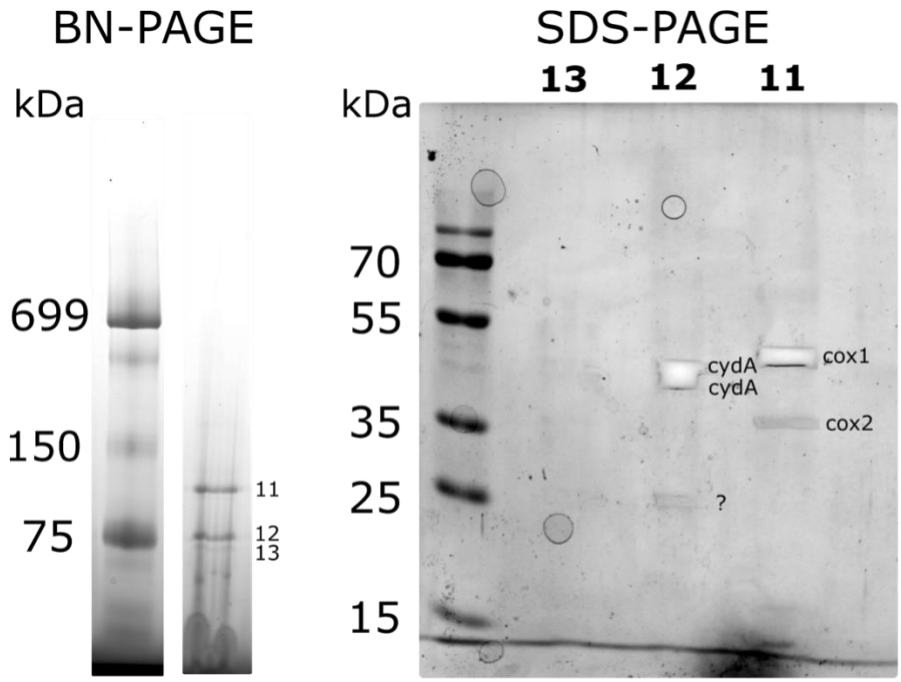

Figure 5.7 - Separation of complexes from BN gels into their subunits and their identity: *The BN gels that the bands (I – 120 kDa, II – 75 kDa, & III – a fainter band just below 75 kDa) were excised from are shown on the left. The gel on the right is the SDS PAGE gel (after excision for mass spectrometry ID) of these bands. The mass spectrometry identity is shown next to the excision. Band II subunit at 25 kDa was unable to be identified.*

The 120 kDa BN band contained 2 subunits from the aa_3 oxidase (COX 1 & 2). This is unfortunate as the b_{595} signal from the cyt *bd* oxidase will overlap with the *a* haem signal from the cyt aa_3 oxidase making it difficult to determine the presence or absence of this cyt aa_3 from the spectrum alone

Table 1 - Predicted Molecular weight of the subunits of the bd oxidase and the aa_3 oxidase.

bd oxidase		aa_3 oxidase	
Subunit	Size (kDa)	Subunit	Size (kDa)
CydA	54.0	CtaD/Cox1	64.8
CydB	38.0	CtaC/Cox2	38.0
CydX	19.6	CtaE/Cox3	22.2
		CtaF/Cox4	15.2

5.3.2 The effect of KCN on different strains of intact *M. smegmatis*

Given that other groups had determined the structure of the mycobacterial cyt *bd* complex during this work on purifying the cyt *bd* (Safarian et al., 2021; Wang et al., 2021) it was decided to leave the work on this purification for the time being. With the arrival of the chamber, the focus of my work became the in-cell haem spectroscopy measurements and the further characterization of the cyt *bcc:*aa_3 supercomplex. Initially, the interference of the optode phosphorescence peak limited the ability to study the cyt *bd* in intact cells. However, once this issue had been resolved, it offered an opportunity to further probe the utilisation of different oxidases in mycobacteria.

5.3.2.1 The effect of cyanide on wild-type *M. smeg*

To investigate the use of the mycobacterial oxidases I considered the effect of KCN on mycobacteria. KCN is a strong inhibitor of haem copper oxidases such as the cyt aa_3 as it binds in place of oxygen in the binuclear site. KCN is a less effective inhibitor of cyt *bd* so its effect on cells should indicate which oxidases are present and being used by the culture. To investigate this wild-type *M. smeg* grown as before for chamber experiments (Chapter 3) was observed in the chamber system upon the addition of KCN (Fig 5.8). At 100 µM of KCN, a transient reduction in all the haems was observed coinciding with a transient drop in oxygen consumption. Cyt aa_3 was the most affected by this. Several minutes later the haems and oxygen began to recover. Upon a second addition of KCN, bringing the chamber concentration to 200 µM, a similar response to 100 µM was seen. At 1 mM the haem signals did not recover, remaining reduced. The OCR recovery was also hampered. This was replicated in an experiment where 1 mM of KCN was added from the beginning (Fig 5.9)

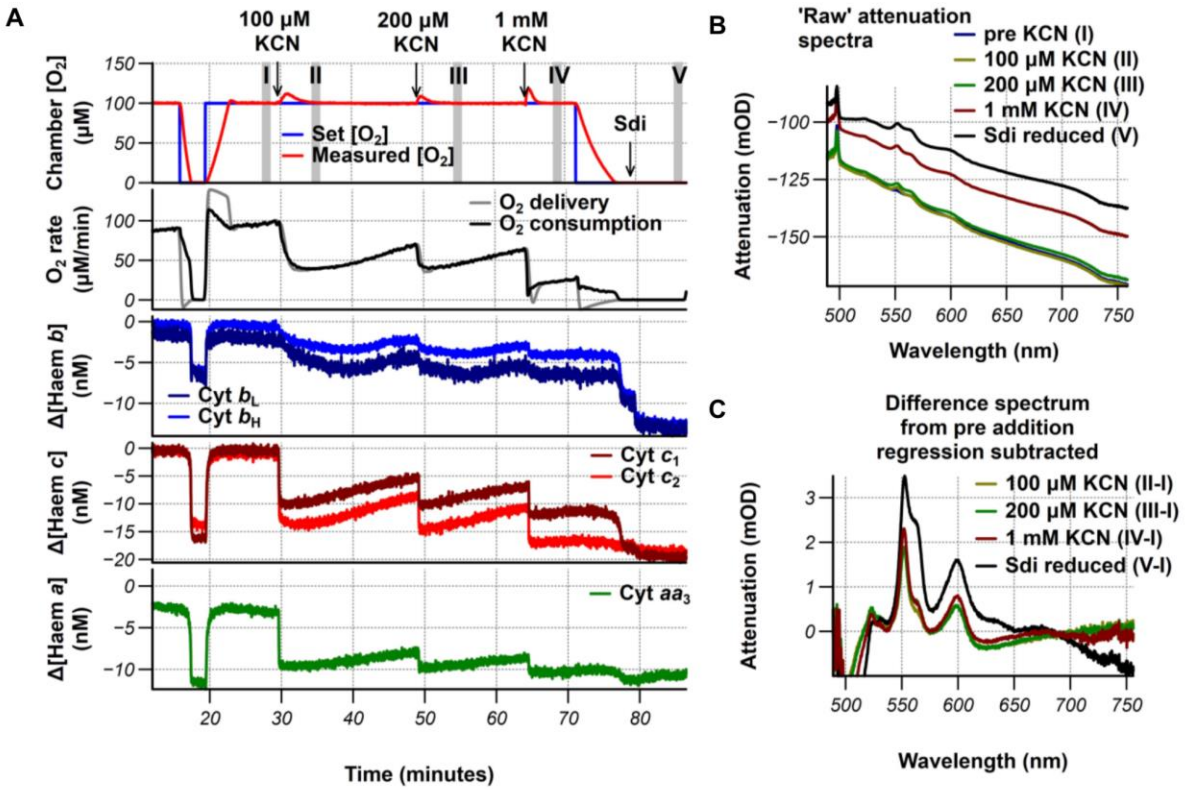

Figure 5.8 - The effect of 100 µM to 1 mM of KCN on wild-type M. smeg (OD_{600} 1) *(**A**) Chamber output, oxygenation and effector additions (top panel). Shaded areas correspond to spectra in (**B** & **C**). Oxygen delivery and consumption are shown in the second panel of (**A**). The fitting using spectral model 1 (adapted mammalian reference spectra) is shown in the bottom three panels). (**B**) The raw attenuation spectrum corresponding to the shaded area in the top panel of (**A**) before and after addition points (**C**) Difference spectra from the spectra in (**B**) as compared to before any KCN had been added (I)*

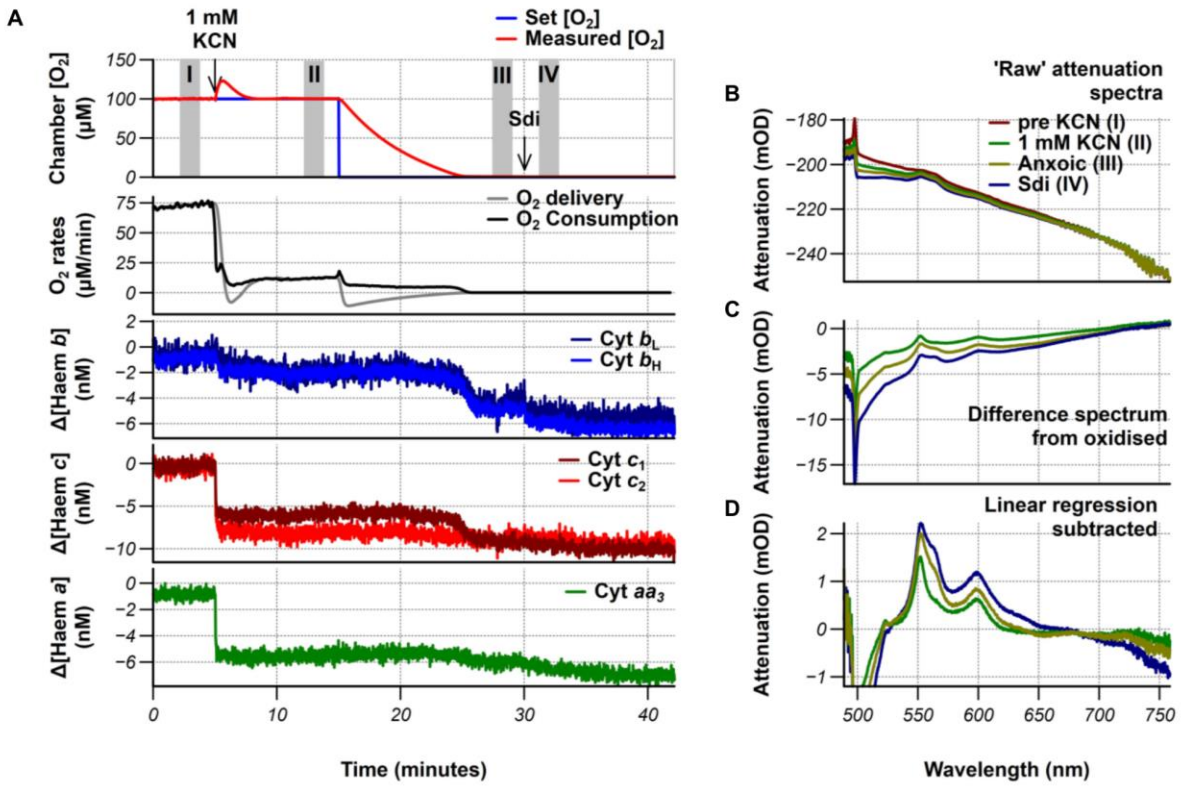

Figure 5.9 - The effect of 1 mM of KCN on wild-type M. smeg, (OD_{600} 0.88) *Same format as for figure 5.8. (**A**) Output from the chamber indicating additions, haem fitting using spectral model 1 (**B**) Raw attenuation spectra from indicated time points. (**C**) Difference spectra from pre-KCN addition (I) (**D**) Difference spectra in (**C**) with a linear regression fitted and subtracted to allow for easier interpretation.*

5.3.2.2 Cyt *bd* is responsible for a portion of the recovery in the oxygen consumption and haem oxidation state upon the addition of cyanide

It was assumed that the recovery of the oxygen consumption and the haem reduction state was because of the cyt *bd* quinol oxidase. At the lower concentration of KCN, inhibition of the cyt aa_3 route to oxygen would result in the rerouting of electrons to the cyt *bd*. The *ΔcydAB* strain of *M. smeg* was used to investigate this. In this strain, at lower concentrations of KCN, there was some recovery in the oxygen and haem reduction state but this appeared to be less than in the wild-type strain (Fig 5.10). The same response to the wild-type strain was seen for 1 mM. The difference spectrum of the dithionite-reduced cells showed some indication of *d* haem as had been seen in the *ΔcydAB* membranes.

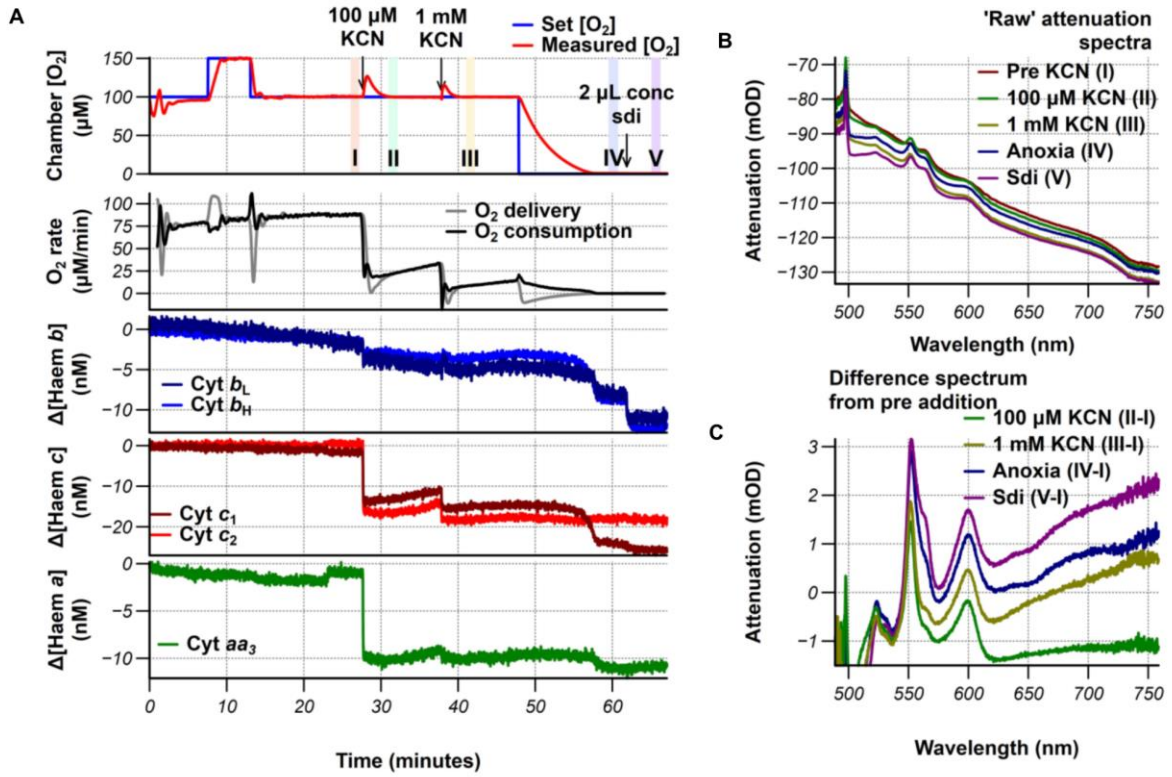

Figure 5.10 - The effect of 100 µM to 1 mM of KCN on ΔcydAB M. smeg (OD_{600} 1) *Same format as for Figure 5.8. (**A**) Output from the chamber indicating additions, haem fitting using spectral model 1 (**B**) Raw attenuation spectra from indicated time points. (**C**) Difference spectra from pre-KCN addition (I)*

5.3.2.3 Expression of cyt *aa*$_3$ in the absence of cyt *bcc*

The response of the *ΔqcrCAB M. smeg* strain to KCN was also expolored. This knockout of the cyt *bcc* component of the cyt *bcc:aa*$_3$ supercomplex presented an unusual response. Early exponential phase cells (OD_{600} 0.8) showed the same OCR drop in response to 100 µM KCN which then recovered. A *b* haem and a dominant *a* haem signal were reduced upon the addition of KCN. The haem fitting was poor for this strain, but it appeared that the reduction of the *a*-haems did not recover in the same fashion as in the wild type. The issue with the knock-out strain is that does not remove the cyt *aa*$_3$ oxidase component. The genes encoding the oxidase portion are located at a different locus on the genome to the *qcrCAB* operon. It appears that at this growth phase, the cyt *aa*$_3$ complex is being expressed and is present in the cell but it is without its cyt *bcc* partner and so therefore not connected to the ETC as normal. This may explain why the oxygen consumption recovered even if the haem oxidation state did not. The difference spectrum of the dithionite reduce cells matched the haem spectrum seen upon the addition of KCN and did not appear to contain an increasd amount of haem signals from the cyt *bd*. I had expected that the cyt *bd* would be upregulated

to compensate for the disruption of the cyt *bcc:aa*$_3$ supercomplex but it is apparent that at this growth stage, it has not increased the amount of cyt *bd* spectrally detectable as opposed to wild-type *M. smeg*.

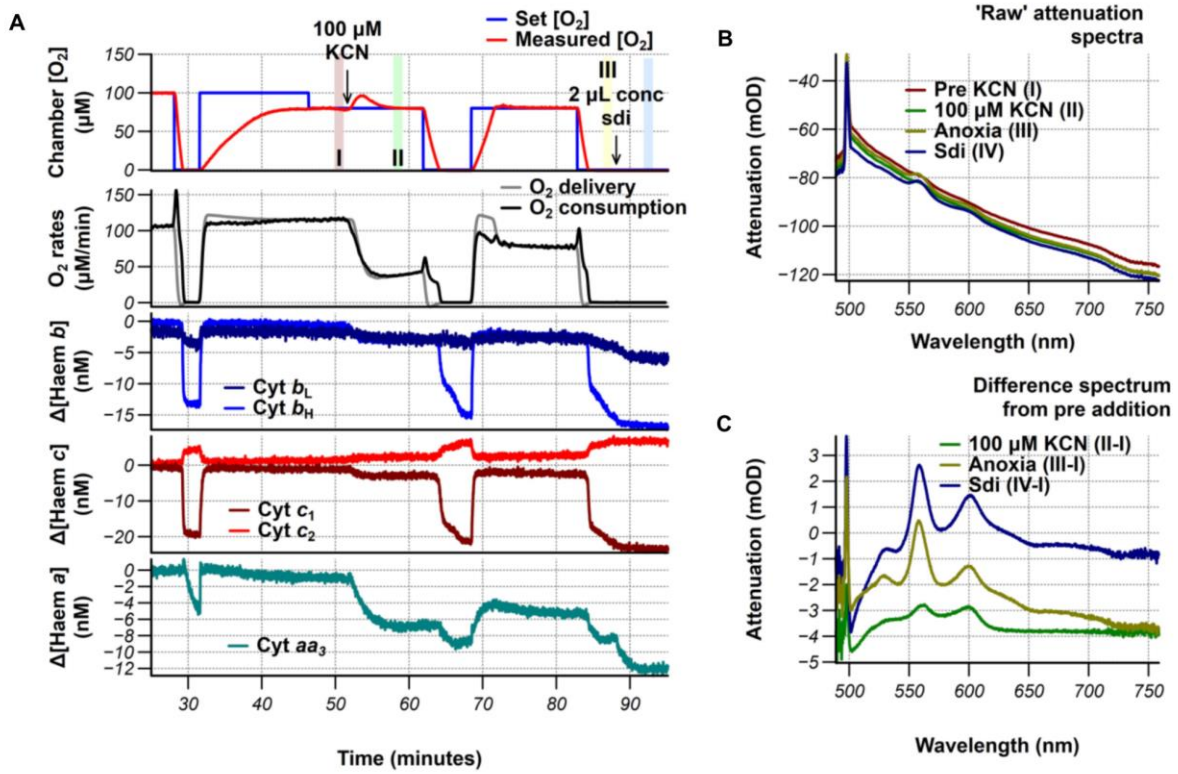

Figure 5.10 - The effect of 100 µM to 1 mM of KCN on early exponential ΔqcrCAB M. smeg, (OD$_{600}$ 0.8). *Same format as for Figure 5.8. (**A**) Output from the chamber indicating additions, haem fitting using spectral model 1 (**B**) Raw attenuation spectra from indicated time points. (**C**) Difference spectra from pre-KCN addition (I)*

If the same experiment was performed with older cells (OD$_{600}$ 2.5), the appearance and response of this extra *a* haem signal was reduced. The difference spectrum was a closer match to the cyt *bd* oxidase than that for the younger culture. The spectrum also had a larger cyt *bd* signal. The OCR was unaffected at 100 µM decreasing at 1 mM, implying that the cyt bd was affected by KCN at 1 mM but not 100 µM. Again the current haem fit did not appear to be suitable for this strain, with signs of serious misfitting. Further work would be required to understand exactly what cytochromes are present in the Δ*qcrCAB* strain and how this changes during the culture's growth. These initial experiments suggest that initially a detectable amount of cyt *aa*$_3$ is expressed. Later in the growth phase, either the expression or the stability of the complex decreases. What role, if any, the cyt *aa*$_3$ component is playing on its own early in the growth phase in this strain is not clear.

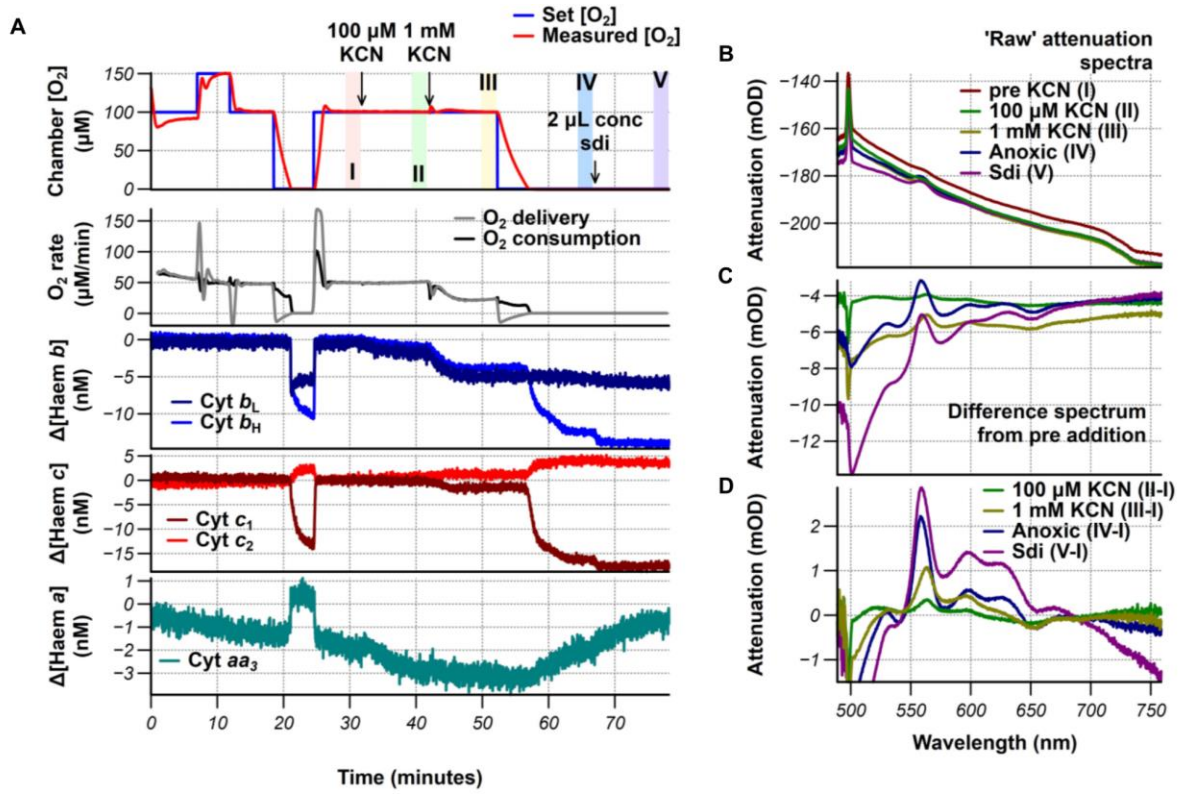

Figure 5.11 - The effect of 100 µM to 1 mM of KCN on ΔqcrCAB M. smeg later in its growth phase, (OD_{600} 2.5). *Same format as for Figure 5.8. (**A**) Output from the chamber indicating additions, haem fitting using spectral model 1 (**B**) Raw attenuation spectra from indicated time points. (**C**) Difference spectra from pre-KCN addition (I)*

5.3.3 Characterising mycobacterial Sdh2

5.3.3.1 Purifying and spectrally characterising FLAG-tagged Sdh2

Other than the cyt *bd* oxidase Sdh2 was the obvious other source of potential *b*-haems in the mycobacterial ETC. Mycobacterial Sdh2 has previously been purified and structurally characterised by Gong et al. who had cloned sdh2D (MSMEG_1671) into the expression plasmid pVV16 with a 10X His Tag at the C-terminus. This C-terminus faces into the periplasm and so should not interfere with the complex formation. Therefore my colleague Dr Morwan Osman utilised the same phage-based ORBIT recombination system ORBIT (Murphy et al., 2018) to generate a 3xFLAG sdh2D strain of *M. smeg*. The complex was purified using the same method as for the cyt *bcc:aa*$_3$ supercomplex. Figure 5.12 shows a cuvette experiment where a purified sample of Sdh2 was oxidised with potassium ferricyanide and reduced with ascorbate and dithionite. The sample showed some *b* haem oxidation upon the addition of the oxidant (5.12 C). The ascorbate reduce samples showed some *c* haem, *b*

haem, and *a* haem signals. This was only for a small fraction of the total spectra, but suggests some cyt *bcc:aa*$_3$ contamination but a BN-PAGE gel would be a better way to determine the degree of this contamination. The dithionite-reduced sample showed a *b* haem-like spectrum, the difference spectrum of this sample (V) and the oxidised spectrum (II) had a maxima at 559 nm and minima at 543 nm.

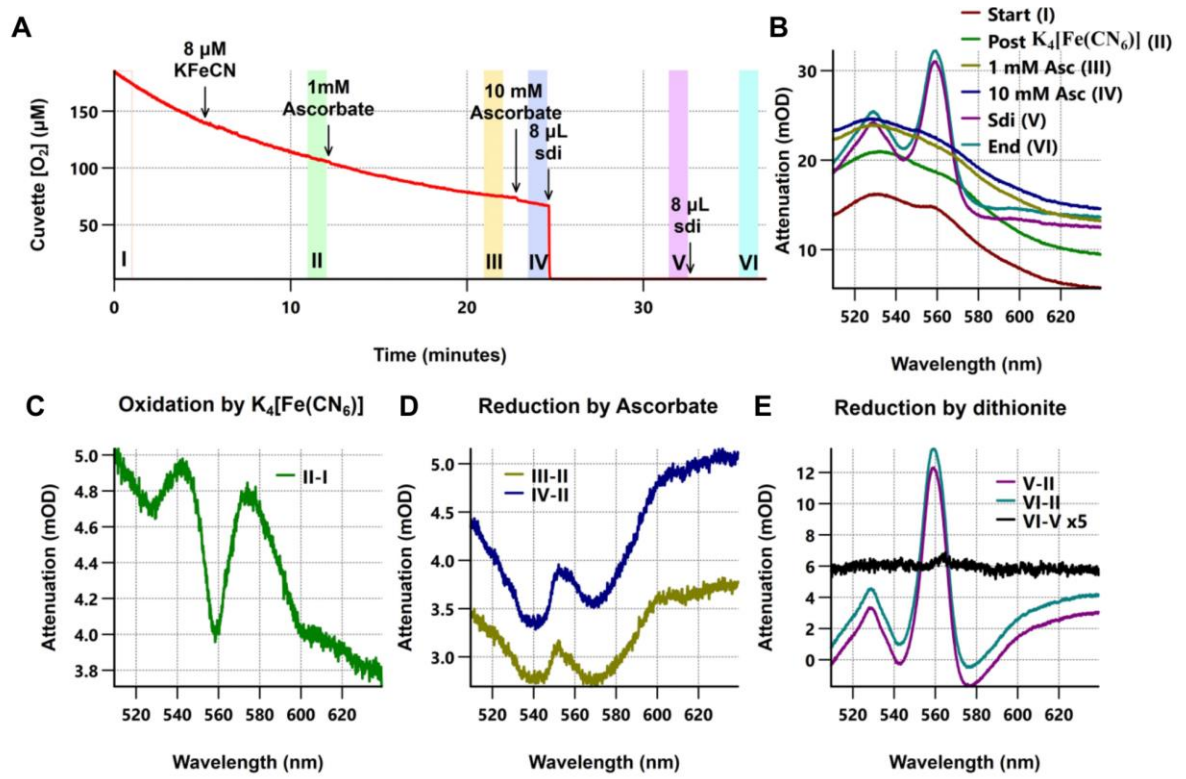

Figure 5.12 - Spectral characterisation of FLAG-Sdh2. *200 µL of purified Sdh2-FLAG oxidised and reduced by potassium ferricyanide, ascorbate and dithionite (Sdi). (**A**) Cuvette oxygen concentration during experiment and point of additions. Shaded areas indicate where the spectra in B were averaged from. (**B**) Raw attenuation spectrum from indicated points before and after additions. (**C**) Difference spectra showing the oxidation caused by potassium ferricyanide. (**D**) Difference spectrum showing the reduction caused by ascorbate (aerobic) (**E**) Difference spectrum upon the reduction with dithionite minus oxidised spectrum (with potassium ferricyanide). The black line shows the difference between the two dithionite additions. This sample and experiment were prepared and performed with Ben Hartmann, another PhD student in the group.*

5.3.3.2 Preliminary activity assay with Sdh2

To determine if the purified sample was active, the spectral effect of adding succinate was observed by using the cuvette system (Fig 5.13). To fit the collected spectra, a normalised difference spectrum of Sdh2 (purple line in Figure 5.12 E as shown normalised in the lower

panel of Fig 5.13 B) was used as the reference spectrum. The result of this fitting is shown in the lower panel of Figure 5.13 A. Upon the addition of succinate the signal reduced, this reduction was slightly increased upon a second addition of succinate. The addition of menadione briefly partially oxidised the sample (Figure 5.13 E) which then returned to the prior level of reduction.

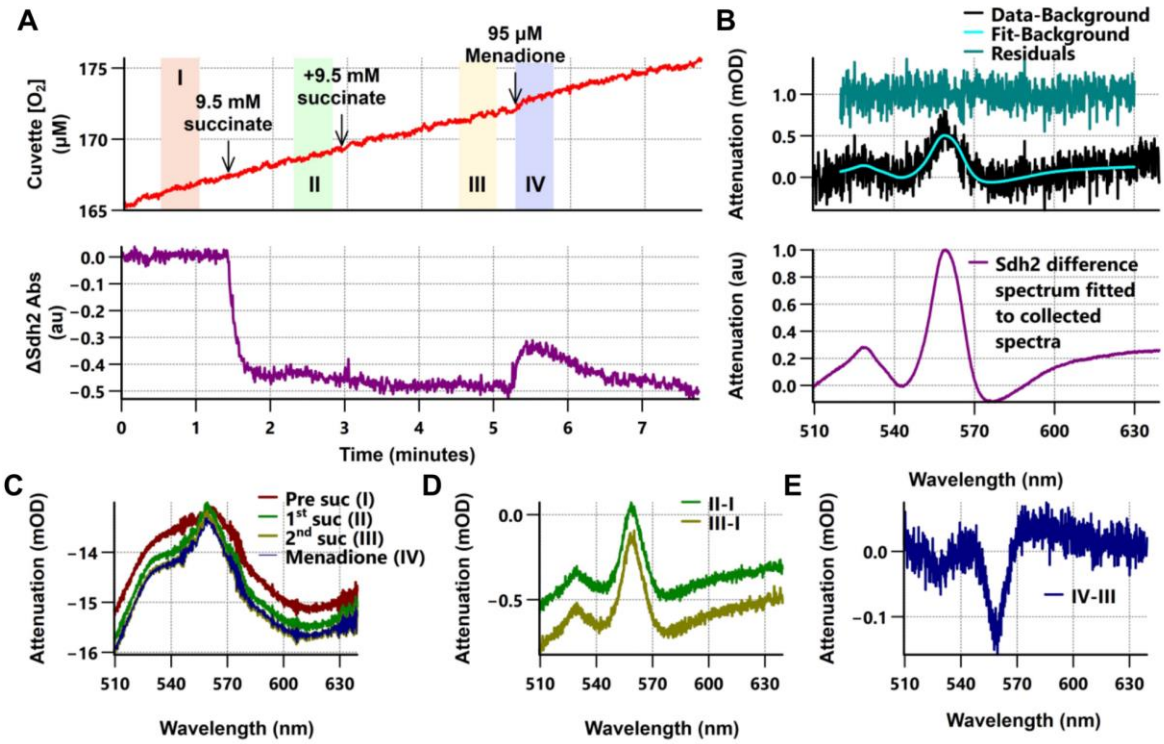

Figure 5.13 - Preliminary activity assay with FLAG-Sdh2. *For this experiment, 5 μL of the prepared sample was added to the cuvette (**A**) The top panel shows the oxygen concentration in the cuvette and the points at which either succinate or menadione was added to the cuvette. The lower panel shows the result of the fitting with the normalised Sdh2 difference spectra. (**B**) The top panel shows an example of the fit on the collected spectra. The lower panel shows the difference spectrum of sdh2, as collected in Fig 5. 12 E (purple line) normalised such that 543 nm is equal to 0 and the maxima at 559 nm is equal to 1. (**C**) The average attenuation spectra from indicated shaded areas. (**D**) The reduction of the b haem centres caused by the addition of succinate to the sample. (**E**) The transient oxidation of the b-haems caused by the addition of menadiol to the sample. This experiment was performed with Dr Morwan Osman who had prepared the FLAG-Sdh2 for this experiment.*

5.3.4 What remodelling occurs when respiratory components are genetically knocked out?

As a way of determining what the individual complexes contribute to the overall spectrum and what remodelling occurs when they are knocked out the spectrum of membranes isolated from wild type, *ΔcydAB*, and *Δsdh2 M. smeg* were examined. The cells were grown up to the early exponential phase, OD_{600} ~1, and their membranes were harvested. The oxidised (potassium ferricyanide) and reduced (dithionite) spectra were then collected in the chamber and used to generate the difference spectrum. The spectra for the wild type and *ΔcydAB M. smeg* had very similar difference spectra, dominated by signals from the cyt *bcc:aa*$_3$ supercomplex. The only difference between the two was that the *d* haem signal was reduced in the *ΔcydAB*. This could either be due to contamination of the knock strain with the wild-type or the presence of the other *bd*-type oxidase present in mycobacteria encoded by the *appBC* operon.

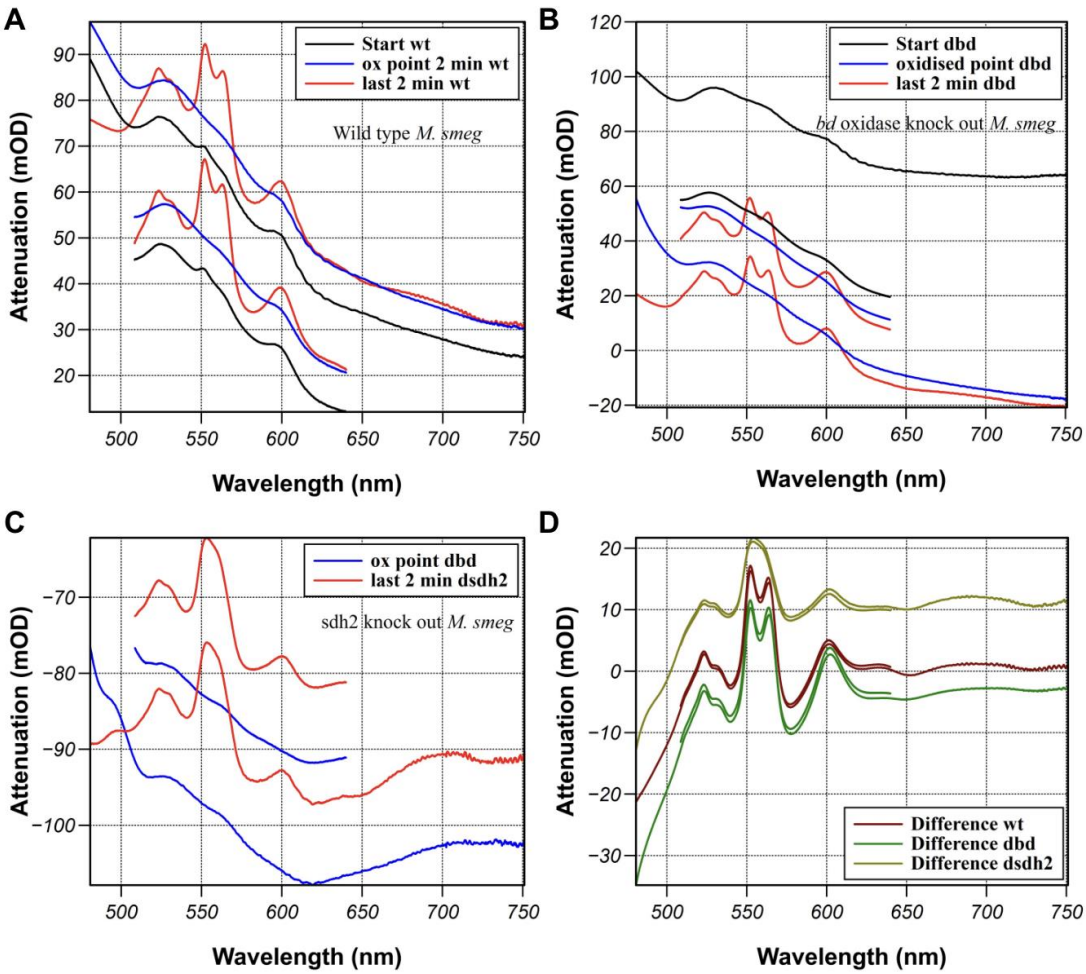

***Figure 5.14 - The difference spectrum of wild-type, ΔcydAB and Δsdh2 membranes grown on 7H9 media to early exponential growth phase (OD_{600} ~1)**, Two CCDs were set to collect a narrow and wide spectrum in the chamber system. (**A**) Wild-type membranes, in black is the spectrum of the membranes 'as-prepared', in blue is the spectrum of the membranes oxidised with potassium ferricyanide, and in red is the spectrum of the membranes reduced with dithionite. (**B**) ΔcydAB membranes, as for the wild-type membranes, 'as-prepared', potassium ferricyanide oxidised and dithionite reduced. (**C**) Δsdh2 membranes, in blue is the spectrum of the membranes oxidised with potassium ferricyanide, and in red is the spectrum of the membranes reduced with dithionite. (**D**) Difference spectrum of each of the three membrane types, dithionite reduce minus potassium ferricyanide oxidised.*

The *Δsdh2* strain unexpectedly had an increased amount of *b* haem signal and a reduced spectral contribution from the cyt *bcc:aa*$_3$ supercomplex. This is somewhat difficult to distinguish, given the lack of distinct *c* haem and *b* haem signals in this strain but the *a* haem signal does not appear to match the size of the *b*/*c* haem signal. To further investigate this the same hr-CNE gels and in-gel activity assays were performed with the *Δsdh2*. The band pattern of the gel looks different to the wild type or *ΔcydAB* membranes. The distinctive band of the cyt *bcc:aa*$_3$ supercomplex was not present. Instead when the gel was stained with DAB, a smear below 720 kDa was seen for the *Δsdh2* membranes. This is difficult to see in Figure 5.15 A IV, but was more obvious in a preliminary gel run without a molecular weight ladder, Figure 5.15 B I. Potentially, knocking out Sdh2 has interfered with the stability or formation of the supercomplex. The staining for NADH dehydrogenases and succinate dehydrogenases also showed a different pattern as compared to wild-type and *ΔcydAB* membranes. For the NADH dehydrogenase, bands further down the gel were seen and the smear down the lane was not seen. For the succinate dehydrogenase activity, instead of a thick band between 720 and 480 kDa, several more distinct bands were observed.

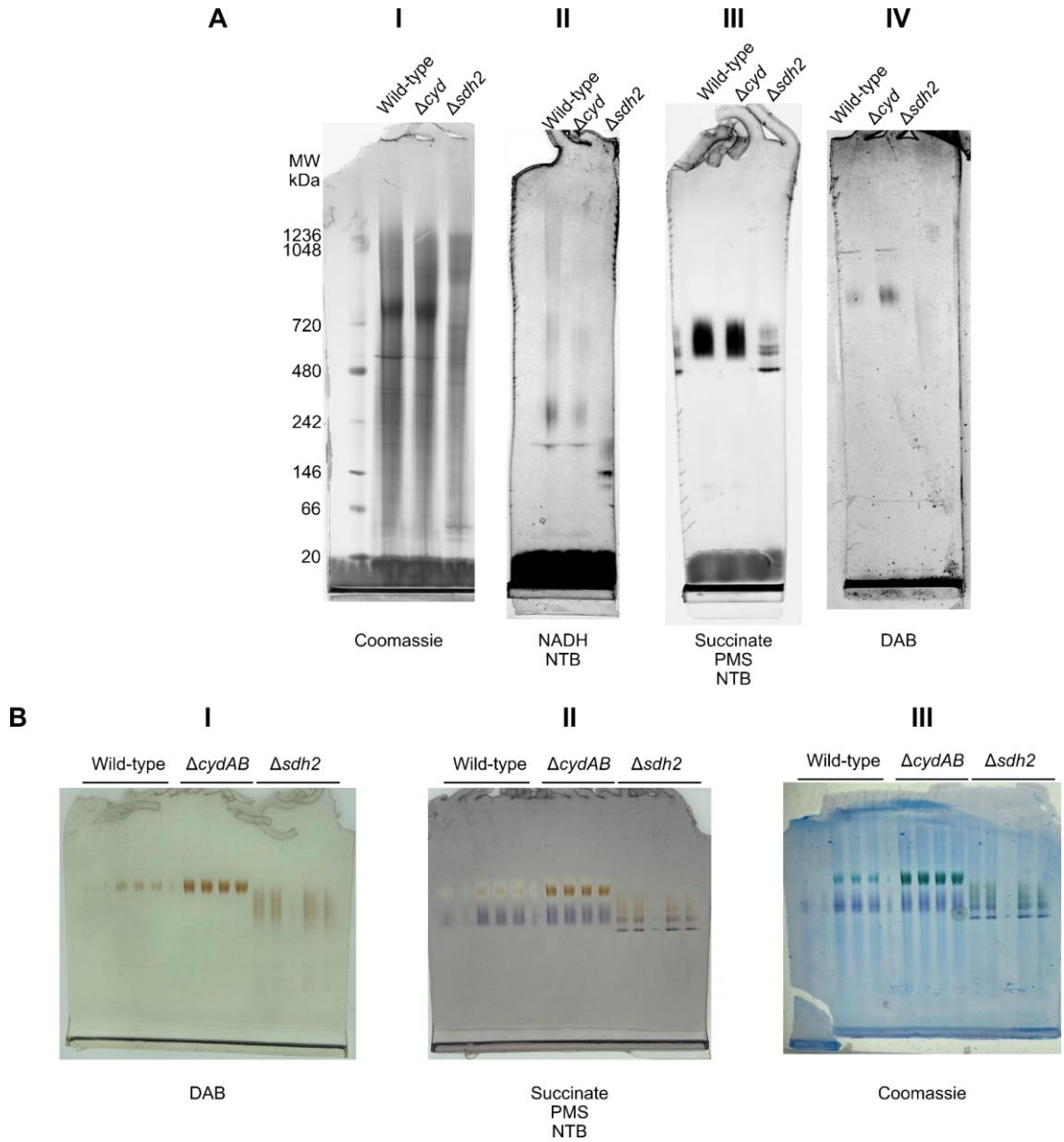

Figure 5.15 - hr-CNE and in-gel activity assays of Δsdh2 membranes compared to wild-type and ΔcydAB membranes *(**A**) Hr-CNE gels with a variety of staining procedures for wild-type, ΔcydAB and Δsdh2 membranes. These are the same gels that were shown in Chapter 3 figure 3.41. I - coomassie stain for total protein distribution. II - stained for NADH dehydrogenase activity. III - stained for succinate dehydrogenase activity, likely some non-specific staining of redox-active proteins due to the PMS in the staining mixture. IV - staining with DAB for cyt bcc:aa$_3$ or quinol oxidases. Note that the gels are not completely aligned as the staining procedure results in differential shrinking of the gel strips. (**B**) A preliminary gel staining of a hr-CNE gel with wild-type, ΔcydAB and Δsdh2 membranes. The gel was initially stained with DAB (I), it was then stained for succinate dehydrogenase activity (II). The same gel was then stained with Coomassie dye for total protein content. A similar pattern was observed with the same stains of the individual strips of gel in (**A**).*

Over concerns that the strain may have become contaminated, a fresh inoculate of the strain was obtained and used to produce membranes. For this membrane preparation, the cells were grown in tryptic soy broth (TSB). This is the media that had been used to recover the Δsdh2 strain during its generation (personal communication with Chen-Yi Cheung). This may be related to the pH of the media as it was observed that the growth of Δsdh2 on succinate is permitted if the media's pH is dropped below pH 7 (personal communication with Chen-Yi Cheung). TSB is not buffered like the traditional 7H9 media used to culture mycobacteria. Membranes of cells grown on TSB for wild-type, Δsdh2, and ΔqcrCAB were compared as before. The wild-type and Δsdh2 difference spectra looked similar to before. The TSB-grown Δsdh2 difference spectrum looked to have less cyt *bcc:aa*$_3$ haems or more non-supercomplex *b* haem, as indicated by the peak at ~556 nm. Interestingly, the ΔqcrCAB membranes looked very similar to the Δsdh2 difference spectrum. On solid media, Δsdh2 and ΔqcrCAB cannot grow on succinate but can grow on glucose or glycerol (personal communication with Chen-Yi Cheung). This may explain why their spectra look similar. If knocking out of these operons (sdh2 and qcrCAB) results in similar remodelling of the chain, then that would explain why the total spectrum looks so similar and why both strains have the same carbon source preferences.

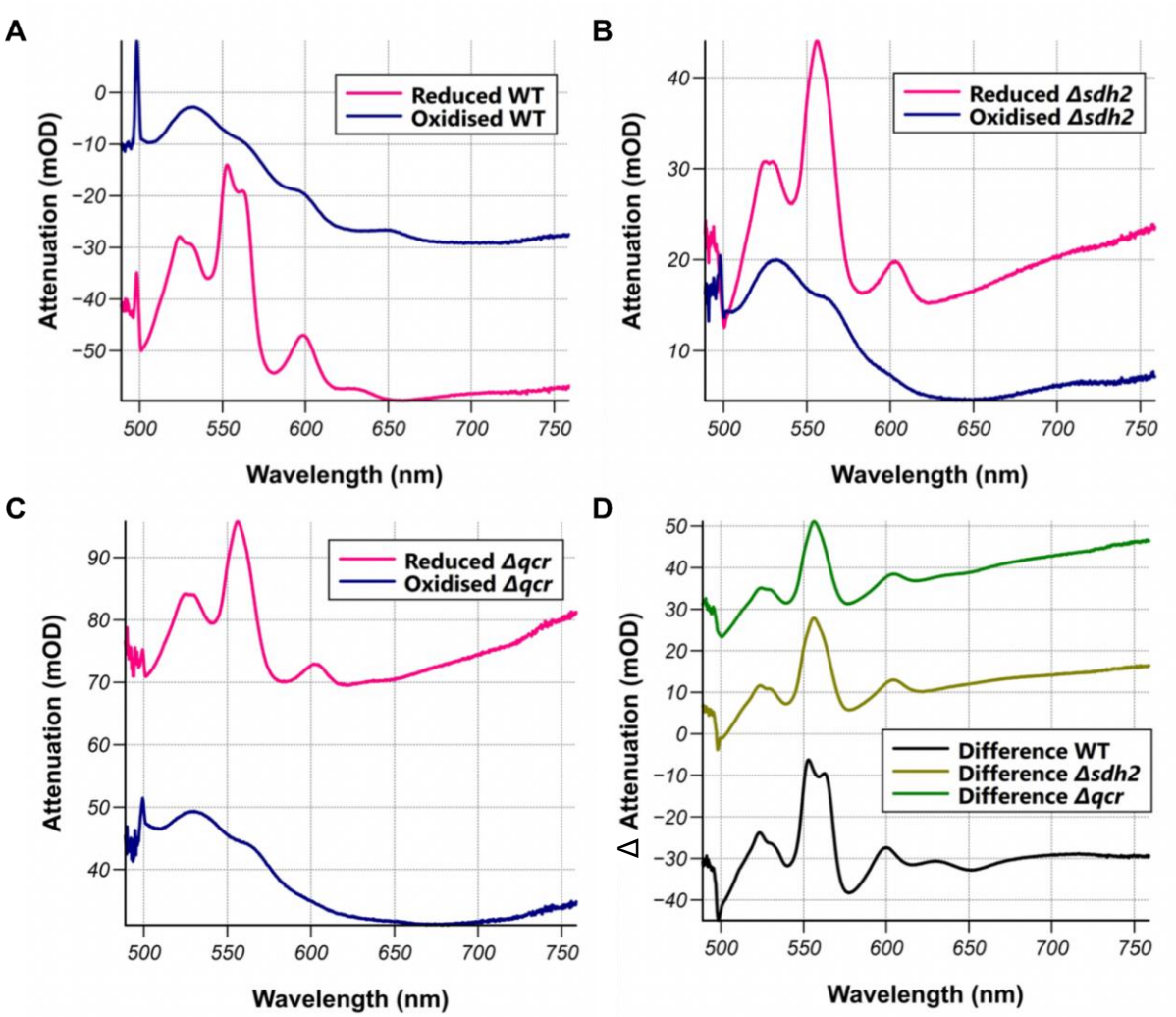

***Figure 5.16 - The difference spectrum of wild-type, ΔcydAB and ΔqcrCAB membranes grown on TSB media to early exponential growth phase (OD_{600} ~1)**, One CCD was set to collect a wide spectrum in the chamber system. (**A**) Wild-type membranes - in dark blue is the spectrum of the membranes oxidised with potassium ferricyanide, and in pink is the spectrum of the membranes reduced with dithionite. (**B**) Δsdh2 membranes - as for the wild-type membranes, potassium ferricyanide oxidised and dithionite reduced. (**C**) ΔqcrCAB membranes - as for the wild-type membranes, potassium ferricyanide oxidised and dithionite reduced. (**D**) Difference spectrum of each of the three membrane types, dithionite reduce minus potassium ferricyanide oxidised.*

5.4 Discussion

5.4.1 Drawbacks of native purification approach for cyt *bd*

Further work by a project student (Lauren Layland) to try and improve the purification of cyt *bd* still struggled to fully remove the cyt aa_3 contaminant. This informed subsequent purification of the cyt *bcc:*aa_3 supercomplex, directing the purification strategy toward a chromosomal tag to allow for a one-step purification process. I believe it is likely that the cyt aa_3 component of the supercomplex falls apart during ion exchange. Unconnected or not to this, the high *a* haem context on the *ΔqcrCAB* strain suggests that the regulation of the expression of the *a* haem-containing subunit (CtaD) is not immediately responsive to the abundance of the cyt *bcc* subunits (qcrCAB). This is not unexpected given that the two (CtaD and qcrCAB) are in very spatially separated operons as a result of their separate evolutionary histories. Cyt aa_3's presence in early exponential *ΔqcrCAB* cells does indicate that it can exist on its own in some circumstances.

Native untagged purification strategies can offer additional insight into the enzyme such as additional accessory subunits, limiting the interference of tags with the formation of complexes and retaining native factor synthesis pathways. However, in some cases native untagged purification of delicate membrane proteins may be more troublesome than it is worth. Chromosomal tags offer similar benefits of native approaches, in terms of the full complement of subunits, including those not included in the core operons. This approach also offers the benefit of an affinity tag, allowing for quick purification processes, and limiting the time for delicate complexes to fall apart. The location of the tag does have to be thought about carefully so that it does not interfere with the complex formation. This can be difficult with the genetic techniques available in some bacteria, such as mycobacteria. The ORBIT system only allows for C-terminal tags and leaves a large scar in the genome from the payload plasmid used to introduce the tag (Murphy et al., 2018). My colleague Dr Morwan Osman has been working to try and adapt the system to excise this scar that would resolve some of these issues. Recent advances in structure prediction tools allow for reasonable 'guess' of whether a tag at a particular site might interfere with the complex formation, i.e. is the site buried in the protein complex or is it accessible and so not going to interfere with the complex formation? A such, these tools are informative to any tag design process.

Both the native and chromosomal tagged approaches are more likely to result in the full complement of subunits of the enzyme. Whilst the 2D-gels did not indicate the presence of additional subunits, it would be worth further investigation to see if there are any associated

with the mycobacterial cyt *bd.* Small single transmembrane helices sometimes do not appear on SDS-PAGE, particularly 2D-gels due to their small size.

5.4.2 Further spectral characterisation of the mycobacterial cyt *bd* and Sdh2

To be able to better understand the role of both the cyt *bd* and Sdh2 in intact mycobacteria, the individual spectral contributions of each of the haem centres will have to be spectrally characterised. The preparation for the Sdh2 as described above would be a suitable starting material to apply similar approaches described in Chapter 4, particularly the simultaneous thermodynamic and spectral characterisation given that the enzyme has fewer haem centres than the cyt *bcc:aa*$_3$, making the thermodynamic model simpler. Because of the contamination of the cyt *aa*$_3$ subunits, it would be better to use a tagged preparation of the cyt *bd* to spectrally characterise its haem centres. Again the simultaneous approaches as described for the cyt *bcc:aa*$_3$ supercomplex would be suitable for separating the spectral components of the cyt *bd*. In fact, the original paper that I used to develop my Python scripts was characterising the haem spectra of *E. coli*'s cyt *bd*-I (Bloch et al., 2009).

The main stumbling block for spectrally characterising both of these proteins is the quantity required for the thin-layer electrochemical cell. The spectrograph system that is used to collect the spectra from the cuvette and the chamber is much faster and has a better signal-to-noise ratio than the traditional Cary spectrophotometer used in combination with the electrochemical thin cell. This thin-layer electrochemical cell has been optimised for use with IR spectroscopy, hence why the system has such a small path length (Moss et al., 1990). This is not necessary for visible-wavelength spectroscopy and so the signal is increased in the cuvette system by the greater path length. If an electrode could be inserted into the side of the cuvette it would allow the ambient redox potential of a sample to be measured. This would also allow for the use of the cuvette spectroscopy which is more advanced than the Cary 300 spectrometer currently used to collect the redox titration spectra. Chemical oxidants and reductants could then be used to change the ambient redox potential of the system, a more traditional potentiometric redox titration. We would then be able to use this system for performing redox titrations on membranes which would be powerful and would help to clarify the nature of the cytochrome present in the membrane.

5.4.3 What is the cytochrome origin of the b_{557} signal?

In the last Chapter, I introduced an additional *b* haem to allow reasonable fitting of a spectral model including reference spectra from cyt *bcc:aa*$_3$. This signal maxima was at 557 nm and so assumed to originate from a *b* haem. The titration experiments on the wild-type and Δ*cydAB* membranes indicated that some of this signal originates from the cyt *bd* but given that the b_{557} signal was present in Δ*cydAB* membranes it suggests that this was not all from the cyt *bd*. Based on the maxima of the Sdh2 difference spectrum, at 559 nm, I do not believe it is originating from Sdh2. Attempts to add the Sdh2 difference spectrum to the spectral model resulted in the mis-fitting of the cyt b_L from the cyt *bcc:aa*$_3$ supercomplex (data not shown) and was worse than the addition of the b_{557} signal.

The exact maxima of the signal may not be 557 nm given that it was selected purely based on giving a fitting result that appeared sensible, (haems reducing when the cells were taken anoxic). It also cannot be excluded that the 'b_{557}' signal may originate from one of the Sdh2 *b*-haems but given the presence of a peak at ~556 nm in the Δ*sdh2* membranes I think this is unlikely. This has led me to the conclusion that another cytochrome is contributing to the total haem spectrum and interfering with the fitting. I believe EtfD is the most likely candidate as it was present in the membrane of wild-type *M. smeg.* From examining the alpha-fold predicted structure of EtfD, the pair histidine residues required to ligate a haem group are present for at least one haem. Further examination of the Δ*sdh2* and Δ*qcrCAB* membranes may also have it in high abundance, offering a starting point to purify from.

This additional signal could be from other haem-containing proteins (P450s, peroxidases, and other redox sensors like DosT and DosS), that may not be part of the ETC. This is where a more in-depth survey of the mycobacterial proteome for haem binding sites would be valuable. This could either be purely based on the total genome or by using mass-spectrometry to determine what proteins are abundant in the membrane of wild-type mycobacteria and contain haem binding sites.

5.4.4 The influence of Sdh2 on the cyt *bcc:aa*$_3$ supercomplex

Interestingly both the spectra and native gels of the Δ*sdh2* membranes suggest that Sdh2 may be influencing the stability of the cyt *bcc:aa*$_3$ supercomplex. Without more information it is difficult to determine how the Sdh2 is influencing the behaviour of the cyt *bcc:aa*$_3$ supercomplex. The crowded nature of biological membranes is increasingly appreciated and the influence this has on the organisation of the complicated bioenergetic complexes. The observations in this work and the unpublished work of others (Chen Yi Cheung) suggest

some kind of interaction. A recent paper monitoring the acidification of mycobacterial IMVs via ACMA, could not differentiate between supercomplex inhibitors and Sdh2 inhibitors when the IMVs were energised with succinate again suggesting that these two complexes may be interacting somehow (Harden et al., 2024).

5.5 Conclusion

This work in this chapter has begun to establish protocols for purifying and characterising two mycobacterial cytochromes, cyt *bd* and Sdh2. The native approach shown here for cyt *bd* may not be suitable for the delicate membrane complexes in bacteria. The tagged approach applied to Sdh2 and previously to the cyt *bcc:aa*$_3$ supercomplex appears to generate cleaner preparations of the proteins. The chromosomal tag approaches could be applied to many other respiratory complexes in mycobacteria and other bacterial species if genetic techniques are available. Further work is required to spectrally characterise the individual haem centres in both of the isolated complexes. The simultaneous thermodynamic and spectral characterisation described in Chapter 4 would be very applicable to both of these proteins as they are simpler in terms of the number of haem centres.

The mycobacterial cyt *bd* oxidase allows for the recovery of oxygen consumption and haem oxidation state when the cyt *bcc:aa*$_3$ is inhibited by lower concentrations of cyanide. At higher concentrations of cyanide, the mycobacterial cyt *bd* is also inhibited. In the early stages of growth of the Δ*qcrCAB* (cyt *bcc* knockout), the cyt *aa*$_3$ is present and can be reduced when cyanide is added to the cultures. The presence of the cyt aa3 reduces as the cultures get further through the growth cycle. The complement of cytochromes present in the ETC of the Δ*qcrCAB* and Δ*sdh2* strains appears to be similar. Both of these strains' total spectrum is dominated by an unknown *b* haem signal with fewer spectral features from the cyt *bcc:aa*$_3$ supercomplex features. Native PAGE analysis of the *Δsdh2* membranes suggests that the cyt *bcc:aa*$_3$ supercomplex may be less stable without Sdh2 in the membrane.

Chapter 6 - Conclusion

The work within this thesis has mainly concerned the adaptation of tools and concepts to study mycobacterial bioenergetics. The recurring theme has been that the models used for the mammalian electron transport chain, and general mammalian bioenergetics, typically offer useful concepts and qualitative parameters but do not translate perfectly. This observation is not surprising, as the two systems are separated by billions of years of evolution and have different selection pressures: the mammalian bioenergetic system is mostly kept in constant conditions and operates close maximum efficiency, while the mycobacterial bioenergetics faces changing conditions and can compromise efficiency to cope with that. However, the expansion of the tools now available within the York Bioenergetics Laboratory offers a unique opportunity to expand the understanding of mycobacterial bioenergetics for both practical applications in drug design and to understand the divergent biochemistry of this group of bacteria.

It has been apparent that having multiple 'windows' into the operation of the bioenergetic system in intact living cells enables a better understanding of the system as a whole. This work has focused on oxygen consumption rates and haem electron occupancy. Other measurements of different components of the bioenergetic system would likely offer additional insight into the operation of the system and help to clarify phenomena that are not easy to explain currently. As touched upon in Chapter 3, the chamber is capable of NAD(P)H fluorescence measurements. Until these types of measurements have been applied to bacterial systems, it is difficult to know how useful the measurement would be. The other non-invasive approach would be to use ^{31}P NMR spectroscopy. Suzy Harrison, another PhD student in the group, has made some hard-won progress in designing an oxygenation system that would allow these measurements on mycobacteria but this is a very technically challenging design problem.

In Chapter 3 we were able to see the impact of metabolic effectors on the mycobacterial ETC, including enzyme inhibitors and uncouplers. This understanding is now at a point where a standardised protocol of systematic additions of effectors and changing conditions could be developed to examine the ETC of bacteria grown under different conditions. Critically, the protocol would need to provided an oxidised point and reduced point so that all changes to the haem redox states can be quantified. This approach would allow for the assessment of parameters like respiratory capacity, OCR per OD of culture (or even per cell), and the complement of cytochromes present in the chain. This would be akin to the protocols used in commercial systems with mitochondria or mammalian cells such as with the Seahorse or Oroboros (Mayberry et al., 2024; Pesta and Gnaiger, 2012). A standardised approach would

allow careful comparison between growth conditions and in response to the additions of drugs such as bedaquiline or telacebec.

Within both Chapter 4 and Chapter 5 the use of chromosomal tags provided a way to easily isolate the bioenergetic complexes with rapid purification processes. This has been thanks to the genetic expertise of Dr Morwan Osman. With the expanding toolkit of genetic techniques for chromosomal tagging this offers a strategy for purifying native bioenergetic complexes particularly given their often-complicated genetic organisation and frequency of small subunits not encoded in the core operon and complex assembly pathways. The tools developed in this thesis and by others in the group offers the opportunity to study the function both *in vitro* and *in vivo* of any bacterial cytochrome of interest, allowing both descriptions of action *in vivo* (turnover number, redox state) and fine-brush investigations of purified material *in vitro* (EPR, electrochemistry, and structural analysis with cryo-EM)

Chapter 4 covered spectral and thermodynamic characterisation of the haem cofactors of the chromosomally tagged and purified mycobacterial cyt *bcc:aa*$_3$ supercomplex. This was done by extracting the spectra from the complex by differentially oxidising and reducing its haem centres it with chemical agents and confirming these observed spectra with a simultaneous spectral and thermodynamic analysis. This was then applied to the thermodynamic analysis of intact cells to allow the measurement of $\Delta\Psi$ via the intrinsic sensor of the cyt *bcc* complex *b*-haems. The spectral and thermodynamic analysis tools developed in this chapter are readily applicable to other cytochromes including those purified in Chapter 5. Not only might this approach provide new insights into how energy-transducing enzymes function, but it may also offer new methods to measure bioenergetics in living cells.

References

Adolph, C., Cheung, C.-Y., McNeil, M.B., Jowsey, W.J., Williams, Z.C., Hards, K., Harold, L.K., Aboelela, A., Bujaroski, R.S., Buckley, B.J., Tyndall, J.D.A., Li, Z., Langer, J.D., Preiss, L., Meier, T., Steyn, A.J.C., Rhee, K.Y., Berney, M., Kelso, M.J., Cook, G.M., 2024. A dual-targeting succinate dehydrogenase and F1Fo-ATP synthase inhibitor rapidly sterilizes replicating and non-replicating *Mycobacterium tuberculosis*. Cell Chem. Biol. 31, 683-698.e7. https://doi.org/10.1016/j.chembiol.2023.12.002

Adolph, C., McNeil, M.B., Cook, G.M., 2022. Impaired Succinate Oxidation Prevents Growth and Influences Drug Susceptibility in Mycobacterium tuberculosis. mBio 13, e01672-22. https://doi.org/10.1128/mbio.01672-22

Andries, K., Verhasselt, P., Guillemont, J., Göhlmann, H.W.H., Neefs, J.-M., Winkler, H., Van Gestel, J., Timmerman, P., Zhu, M., Lee, E., Williams, P., de Chaffoy, D., Huitric, E., Hoffner, S., Cambau, E., Truffot-Pernot, C., Lounis, N., Jarlier, V., 2005. A Diarylquinoline Drug Active on the ATP Synthase of Mycobacterium tuberculosis. Science 307, 223–227. https://doi.org/10.1126/science.1106753

Arora, K., Ochoa-Montaño, B., Tsang, P.S., Blundell, T.L., Dawes, S.S., Mizrahi, V., Bayliss, T., Mackenzie, C.J., Cleghorn, L.A.T., Ray, P.C., Wyatt, P.G., Uh, E., Lee, J., Barry, C.E., Boshoff, H.I., 2014. Respiratory Flexibility in Response to Inhibition of Cytochrome c Oxidase in Mycobacterium tuberculosis. Antimicrob. Agents Chemother. 58, 6962–6965. https://doi.org/10.1128/aac.03486-14

Asano, A., Brodie, A.F., 1964. Oxidative Phosphorylation in Fractionated Bacterial Systems: XIV. RESPIRATORY CHAINS OF MYCOBACTERIUM PHLEI. J. Biol. Chem. 239, 4280–4291. https://doi.org/10.1016/S0021-9258(18)91170-1

Barcroft, J., Haldane, J.S., 1902. A method of estimating the oxygen and carbonic acid in small quantities of blood. J. Physiol. 28, 232–240.

Basan, M., Hui, S., Okano, H., Zhang, Z., Shen, Y., Williamson, J.R., Hwa, T., 2015. Overflow metabolism in Escherichia coli results from efficient proteome allocation. Nature 528, 99–104. https://doi.org/10.1038/nature15765

Baymann, F., Schoepp-Cothenet, B., Lebrun, E., van Lis, R., Nitschke, W., 2012. Phylogeny of Rieske/cytb Complexes with a Special Focus on the Haloarchaeal Enzymes. Genome Biol. Evol. 4, 832–841. https://doi.org/10.1093/gbe/evs056

Beites, T., Jansen, R.S., Wang, R., Jinich, A., Rhee, K.Y., Schnappinger, D., Ehrt, S., 2021. Multiple acyl-CoA dehydrogenase deficiency kills Mycobacterium tuberculosis in vitro and during infection. Nat. Commun. 12, 6593. https://doi.org/10.1038/s41467-021-26941-1

Beites, T., O'Brien, K., Tiwari, D., Engelhart, C.A., Walters, S., Andrews, J., Yang, H.-J., Sutphen, M.L., Weiner, D.M., Dayao, E.K., Zimmerman, M., Prideaux, B., Desai, P.V., Masquelin, T., Via, L.E., Dartois, V., Boshoff, H.I., Barry, C.E., Ehrt, S., Schnappinger, D., 2019. Plasticity of the Mycobacterium tuberculosis respiratory chain and its impact on tuberculosis drug development. Nat. Commun. 10, 4970. https://doi.org/10.1038/s41467-019-12956-2

Bender, N., Goetschy, A., Hsu, C.W., Yilmaz, H., Palacios, P.J., Yamilov, A., Cao, H., 2022. Coherent enhancement of optical remission in diffusive media. Proc. Natl. Acad. Sci. U. S. A. 119, e2207089119. https://doi.org/10.1073/pnas.2207089119

Berden, J.A., Slater, E.C., 1972. The allosteric binding of antimycin to cytochrome *b* in the mitochondrial membrane. Biochim. Biophys. Acta BBA - Bioenerg. 256, 199–215. https://doi.org/10.1016/0005-2728(72)90053-9

Bergdoll, L., ten Brink, F., Nitschke, W., Picot, D., Baymann, F., 2016. From low- to high-potential bioenergetic chains: Thermodynamic constraints of Q-cycle function. Biochim. Biophys. Acta BBA - Bioenerg. 1857, 1569–1579. https://doi.org/10.1016/j.bbabio.2016.06.006

Berney, M., Cook, G.M., 2010. Unique Flexibility in Energy Metabolism Allows Mycobacteria to Combat Starvation and Hypoxia. PLoS ONE 5, e8614. https://doi.org/10.1371/journal.pone.0008614

Blaza, J.N., Bridges, H.R., Aragão, D., Dunn, E.A., Heikal, A., Cook, G.M., Nakatani, Y., Hirst, J., 2017. The mechanism of catalysis by type-II NADH:quinone oxidoreductases. Sci. Rep. 7, 40165. https://doi.org/10.1038/srep40165

Bloch, D.A., Borisov, V.B., Mogi, T., Verkhovsky, M.I., 2009. Heme/heme redox interaction and resolution of individual optical absorption spectra of the hemes in cytochrome *bd* from *Escherichia coli*. Biochim. Biophys. Acta BBA - Bioenerg. 1787, 1246–1253. https://doi.org/10.1016/j.bbabio.2009.05.003

Blum, T.B., Hahn, A., Meier, T., Davies, K.M., Kühlbrandt, W., 2019. Dimers of mitochondrial ATP synthase induce membrane curvature and self-assemble into rows. Proc. Natl. Acad. Sci. 116, 4250–4255. https://doi.org/10.1073/pnas.1816556116

Blumwald, E., Mario Wolosin, J., Packer, L., 1984. Na^+/H^+ exchange in the cyanobacterium Synechococcus 6311. Biochem. Biophys. Res. Commun. 122, 452–459. https://doi.org/10.1016/0006-291X(84)90497-2

Borisov, S.M., 2018. Fundamentals of Quenched Phosphorescence O2 Sensing and Rational Design of Sensor Materials. https://doi.org/10.1039/9781788013451-00001

Borisov, V.B., Gennis, R.B., Hemp, J., Verkhovsky, M.I., 2011. The cytochrome *bd* respiratory oxygen reductases. Biochim. Biophys. Acta BBA - Bioenerg. 1807, 1398–1413. https://doi.org/10.1016/j.bbabio.2011.06.016

Broco, M., Rousset, M., Oliveira, S., Rodrigues-Pousada, C., 2005. Deletion of flavoredoxin gene in Desulfovibrio gigas reveals its participation in thiosulfate reduction. FEBS Lett. 579, 4803–4807. https://doi.org/10.1016/j.febslet.2005.07.044

Brodie, A.F., Davis, B.R., Fieser, L.F., 1958. A NEW BIOLOGICALLY ACTIVE NAPHTHOQUINONE [1]. J. Am. Chem. Soc. 80, 6454–6454. https://doi.org/10.1021/ja01556a071

Brodie, T.G., 1910. Some new forms of apparatus for the analysis of the gases of the blood by the chemical method. J. Physiol. 39, 391–396.

Brøndsted, L., Atlung, T., 1996. Effect of growth conditions on expression of the acid phosphatase (cyx-appA) operon and the appY gene, which encodes a transcriptional activator of Escherichia coli. J. Bacteriol. 178, 1556–1564. https://doi.org/10.1128/jb.178.6.1556-1564.1996

Buttress, J.A., Halte, M., te Winkel, J.D., Erhardt, M., Popp, P.F., Strahl, H., 2022. A guide for membrane potential measurements in Gram-negative bacteria using voltage-sensitive dyes. Microbiology 168, 001227. https://doi.org/10.1099/mic.0.001227

Cabezón, E., Arechaga, I., Jonathan, P., Butler, G., Walker, J.E., 2000. Dimerization of Bovine F1-ATPase by Binding the Inhibitor Protein, IF1*. J. Biol. Chem. 275, 28353–28355. https://doi.org/10.1074/jbc.C000427200

Chance, B., 1954. Spectrophotometry of Intracellular Respiratory Pigments. Science 120, 767–775. https://doi.org/10.1126/science.120.3124.767

Chance, B., Williams, G.R., 1955. RESPIRATORY ENZYMES IN OXIDATIVE PHOSPHORYLATION: I. KINETICS OF OXYGEN UTILIZATION. J. Biol. Chem. 217, 383–393. https://doi.org/10.1016/S0021-9258(19)57189-7

Chauhan, P., van der Meulen, S.A., Simões Caetano, J.M., Goojani, H.G., Botman, D., van Spanning, R., Lill, H., Bald, D., 2022. Response of Mycobacterium smegmatis to the Cytochrome bcc Inhibitor Q203. Int. J. Mol. Sci. 23, 10331. https://doi.org/10.3390/ijms231810331

Chess, D.J., Billings, E., Covian, R., Glancy, B., French, S., Taylor, J., de Bari, H., Murphy, E., Balaban, R.S., 2013. Optical spectroscopy in turbid media using an integrating sphere: Mitochondrial chromophore analysis during metabolic transitions. Anal. Biochem. 439, 161–172. https://doi.org/10.1016/j.ab.2013.04.017

Chong, S.M.S., Manimekalai, M.S.S., Sarathy, J.P., Williams, Z.C., Harold, L.K., Cook, G.M., Dick, T., Pethe, K., Bates, R.W., Grüber, G., 2020. Antituberculosis Activity of the

Antimalaria Cytochrome bcc Oxidase Inhibitor SCR0911. ACS Infect. Dis. 6, 725–737. https://doi.org/10.1021/acsinfecdis.9b00408
Clark, L.C., Wolf, R., Granger, D., Taylor, Z., 1953. Continuous Recording of Blood Oxygen Tensions by Polarography. J. Appl. Physiol. 6, 189–193. https://doi.org/10.1152/jappl.1953.6.3.189
Cohen, N.S., Bogin, E., Higashi, T., Brodie, A.F., 1973. Multiple cytochromes b in Mycobacterium phlei. Biochem. Biophys. Res. Commun. 54, 800–807. https://doi.org/10.1016/0006-291X(73)91495-2
Cole, S.T., Brosch, R., Parkhill, J., Garnier, T., Churcher, C., Harris, D., Gordon, S.V., Eiglmeier, K., Gas, S., Barry, C.E., Tekaia, F., Badcock, K., Basham, D., Brown, D., Chillingworth, T., Connor, R., Davies, R., Devlin, K., Feltwell, T., Gentles, S., Hamlin, N., Holroyd, S., Hornsby, T., Jagels, K., Krogh, A., McLean, J., Moule, S., Murphy, L., Oliver, K., Osborne, J., Quail, M.A., Rajandream, M.-A., Rogers, J., Rutter, S., Seeger, K., Skelton, J., Squares, R., Squares, S., Sulston, J.E., Taylor, K., Whitehead, S., Barrell, B.G., 1998. Deciphering the biology of Mycobacterium tuberculosis from the complete genome sequence. Nature 393, 537–544. https://doi.org/10.1038/31159
Conradie, F., Diacon, A.H., Ngubane, N., Howell, P., Everitt, D., Crook, A.M., Mendel, C.M., Egizi, E., Moreira, J., Timm, J., McHugh, T.D., Wills, G.H., Bateson, A., Hunt, R., Niekerk, C.V., Li, M., Olugbosi, M., Spigelman, M., 2020. Treatment of Highly Drug-Resistant Pulmonary Tuberculosis. N. Engl. J. Med. 382, 893–902. https://doi.org/10.1056/NEJMoa1901814
Cook, G.M., Hards, K., Vilchèze, C., Hartman, T., Berney, M., 2014. Energetics of Respiration and Oxidative Phosphorylation in Mycobacteria. Microbiol. Spectr. 10.1128/microbiolspec.mgm2-0015–2013. https://doi.org/10.1128/microbiolspec.mgm2-0015-2013
Covian, R., Edwards, L.O., Balaban, R.S., 2024. Effect of the mitochondrial membrane potential on the absorbance of the reduced form of cytochrome *c* oxidase. Biochim. Biophys. Acta BBA - Bioenerg. 1865, 149048. https://doi.org/10.1016/j.bbabio.2024.149048
Cox, E., Laessig, K., 2014. FDA Approval of Bedaquiline — The Benefit–Risk Balance for Drug-Resistant Tuberculosis. N. Engl. J. Med. 371, 689–691. https://doi.org/10.1056/NEJMp1314385
Cremer, J., Honda, T., Tang, Y., Wong-Ng, J., Vergassola, M., Hwa, T., 2019. Chemotaxis as a navigation strategy to boost range expansion. Nature 575, 658–663. https://doi.org/10.1038/s41586-019-1733-y
Crofts, A.R., Meinhardt, S.W., Jones, K.R., Snozzi, M., 1983. The role of the quinone pool in the cyclic electron-transfer chain of *Rhodopseudomonas sphaeroides* A modified Q-cycle mechanism. Biochim. Biophys. Acta BBA - Bioenerg. 723, 202–218. https://doi.org/10.1016/0005-2728(83)90120-2
Dassa, J., Fsihi, H., Marck, C., Dion, M., Kieffer-Bontemps, M., Boquet, P.L., 1991. A new oxygen-regulated operon in Escherichia coli comprises the genes for a putative third cytochrome oxidase and for pH 2.5 acid phosphatase (appA). Mol. Gen. Genet. MGG 229, 341–352. https://doi.org/10.1007/BF00267454
Davies, P.W., Brink, F., Jr., 1942. Microelectrodes for Measuring Local Oxygen Tension in Animal Tissues. Rev. Sci. Instrum. 13, 524–533. https://doi.org/10.1063/1.1769961
Delbrück, M., 1970. A Physicist's Renewed Look at Biology: Twenty Years Later. Science 168, 1312–1315. https://doi.org/10.1126/science.168.3937.1312
Delpy, D.T., Cope, M., Zee, P. van der, Arridge, S., Wray, S., Wyatt, J., 1988. Estimation of optical pathlength through tissue from direct time of flight measurement. Phys. Med. Biol. 33, 1433. https://doi.org/10.1088/0031-9155/33/12/008
Dharmaraj, K., Román Silva, J.I., Kahlert, H., Lendeckel, U., Scholz, F., 2020. The acid–base and redox properties of menaquinone MK-4, MK-7, and MK-9 (vitamin K2) in DMPC monolayers on mercury. Eur. Biophys. J. 49, 279–288. https://doi.org/10.1007/s00249-020-01433-0

Dixon, M., Hill, R., Keilin, D., 1931. The Absorption Spectrum of the Component c of Cytochrome. Proc. R. Soc. Lond. Ser. B Contain. Pap. Biol. Character 109, 29–34. https://doi.org/10.1098/rspb.1931.0066

Dongarra, J.J., Moler, C.B., Bunch, J.R., Stewart, G.W., 1979. LINPACK users' guide. Society for Industrial and Applied Mathematics.

Dunn, E.A., Roxburgh, M., Larsen, L., Smith, R.A.J., McLellan, A.D., Heikal, A., Murphy, M.P., Cook, G.M., 2014. Incorporation of triphenylphosphonium functionality improves the inhibitory properties of phenothiazine derivatives in *Mycobacterium tuberculosis*. Bioorg. Med. Chem. 22, 5320–5328. https://doi.org/10.1016/j.bmc.2014.07.050

El-Khoury, R., Rak, M., Bénit, P., Jacobs, H.T., Rustin, P., 2022. Cyanide resistant respiration and the alternative oxidase pathway: A journey from plants to mammals. Biochim. Biophys. Acta Bioenerg. 1863, 148567. https://doi.org/10.1016/j.bbabio.2022.148567

Felle, H., Porter, J.S., Slayman, C.L., Kaback, H.R., 1980. Quantitative measurements of membrane potential in Escherichia coli. Biochemistry 19, 3585–3590. https://doi.org/10.1021/bi00556a026

Gale, P.H., Arison, B.H., Trenner, N.R., Page, A.C.Jr., Folkers, K., Brodie, A.F., 1963. Characterization of Vitamin K9(H) from Mycobacterium phlei. Biochemistry 2, 200–203. https://doi.org/10.1021/bi00901a038

Gao, X., Wen, X., Esser, L., Quinn, B., Yu, L., Yu, C.-A., Xia, D., 2003. Structural Basis for the Quinone Reduction in the bc1 Complex: A Comparative Analysis of Crystal Structures of Mitochondrial Cytochrome bc1 with Bound Substrate and Inhibitors at the Qi Site,. Biochemistry 42, 9067–9080. https://doi.org/10.1021/bi0341814

Georgiou, C.D., Fang, H., Gennis, R.B., 1987. Identification of the cydC locus required for expression of the functional form of the cytochrome d terminal oxidase complex in Escherichia coli. J. Bacteriol. 169, 2107–2112. https://doi.org/10.1128/jb.169.5.2107-2112.1987

Ghazi, A., Schechter, E., Letellier, L., Labedan, B., 1981. Probes of membrane potential in *Escherichia coli* cells. FEBS Lett. 125, 197–200. https://doi.org/10.1016/0014-5793(81)80717-X

Gnaiger, E., Méndez, G., Hand, S.C., 2000. High phosphorylation efficiency and depression of uncoupled respiration in mitochondria under hypoxia. Proc. Natl. Acad. Sci. 97, 11080–11085. https://doi.org/10.1073/pnas.97.20.11080

Gong, H., Gao, Y., Zhou, X., Xiao, Y., Wang, W., Tang, Y., Zhou, S., Zhang, Y., Ji, W., Yu, L., Tian, C., Lam, S.M., Shui, G., Guddat, L.W., Wong, L.-L., Wang, Q., Rao, Z., 2020. Cryo-EM structure of trimeric Mycobacterium smegmatis succinate dehydrogenase with a membrane-anchor SdhF. Nat. Commun. 11, 4245. https://doi.org/10.1038/s41467-020-18011-9

Gong, H., Li, Jun, Xu, A., Tang, Y., Ji, W., Gao, R., Wang, S., Yu, L., Tian, C., Li, Jingwen, Yen, H.-Y., Man Lam, S., Shui, G., Yang, X., Sun, Y., Li, X., Jia, M., Yang, C., Jiang, B., Lou, Z., Robinson, C.V., Wong, L.-L., Guddat, L.W., Sun, F., Wang, Q., Rao, Z., 2018. An electron transfer path connects subunits of a mycobacterial respiratory supercomplex. Science 362, eaat8923. https://doi.org/10.1126/science.aat8923

Gostimskaya, I.S., Grivennikova, V.G., Zharova, T.V., Bakeeva, L.E., Vinogradov, A.D., 2003. In situ assay of the intramitochondrial enzymes: use of alamethicin for permeabilization of mitochondria. Anal. Biochem. 313, 46–52. https://doi.org/10.1016/S0003-2697(02)00534-1

Guberman-Pfeffer, M.J., 2023. From Hot Water to Dry Dirt: Microbes Use Cytochrome 'Nanowires' of Similar Conductivity but Different Structure. https://doi.org/10.1101/2023.06.12.544705

Guo, H., Courbon, G.M., Bueler, S.A., Mai, J., Liu, J., Rubinstein, J.L., 2021. Structure of mycobacterial ATP synthase bound to the tuberculosis drug bedaquiline. Nature 589, 143–147. https://doi.org/10.1038/s41586-020-3004-3

Haas, A.H., Lancaster, C.R.D., 2004. Calculated Coupling of Transmembrane Electron and Proton Transfer in Dihemic Quinol:Fumarate Reductase. Biophys. J. 87, 4298–4315. https://doi.org/10.1529/biophysj.104.042945

Haegerhaell, C., Aasa, R., Von Wachenfeldt, C., Hederstedt, L., 1992. Two hemes in Bacillus subtilis succinate:menaquinone oxidoreductase (complex II). Biochemistry 31, 7411–7421. https://doi.org/10.1021/bi00147a028

Haller, T., Ortner, M., Gnaiger, E., 1994. A Respirometer for Investigating Oxidative Cell Metabolism: Toward Optimization of Respiratory Studies. Anal. Biochem. 218, 338–342. https://doi.org/10.1006/abio.1994.1188

Hamann, N., Bill, E., Shokes, J.E., Scott, R.A., Bennati, M., Hedderich, R., 2009. The CCG-domain-containing subunit SdhE of succinate:quinone oxidoreductase from Sulfolobus solfataricus P2 binds a [4Fe–4S] cluster. J. Biol. Inorg. Chem. 14, 457–470. https://doi.org/10.1007/s00775-008-0462-8

Harden, S.A., Courbon, G.M., Liang, Y., Kim, A.S., Rubinstein, J.L., 2024. A simple assay for inhibitors of mycobacterial oxidative phosphorylation. J. Biol. Chem. 300. https://doi.org/10.1016/j.jbc.2023.105483

Hards, K., Cook, G.M., 2018. Targeting bacterial energetics to produce new antimicrobials. Drug Resist. Updat. 36, 1–12. https://doi.org/10.1016/j.drup.2017.11.001

Hards, K., McMillan, D.G.G., Schurig-Briccio, L.A., Gennis, R.B., Lill, H., Bald, D., Cook, G.M., 2018. Ionophoric effects of the antitubercular drug bedaquiline. Proc. Natl. Acad. Sci. U. S. A. 115, 7326–7331. https://doi.org/10.1073/pnas.1803723115

Hards, K., Rodriguez, S.M., Cairns, C., Cook, G.M., 2019. Alternate quinone coupling in a new class of succinate dehydrogenase may potentiate mycobacterial respiratory control. FEBS Lett. 593, 475–486. https://doi.org/10.1002/1873-3468.13330

Hardy, B.J., Dubiel, P., Bungay, E.L., Rudin, M., Williams, C., Arthur, C.J., Guberman-Pfeffer, M.J., Sofia Oliveira, A., Curnow, P., Anderson, J.L.R., 2024. Delineating redox cooperativity in water-soluble and membrane multiheme cytochromes through protein design. Protein Sci. 33, e5113. https://doi.org/10.1002/pro.5113

Harold, L.K., Jinich, A., Hards, K., Cordeiro, A., Keighley, L.M., Cross, A., McNeil, M.B., Rhee, K., Cook, G.M., 2022. Deciphering functional redundancy and energetics of malate oxidation in mycobacteria. J. Biol. Chem. 298, 101859. https://doi.org/10.1016/j.jbc.2022.101859

Harris, C.R., Millman, K.J., van der Walt, S.J., Gommers, R., Virtanen, P., Cournapeau, D., Wieser, E., Taylor, J., Berg, S., Smith, N.J., Kern, R., Picus, M., Hoyer, S., van Kerkwijk, M.H., Brett, M., Haldane, A., del Río, J.F., Wiebe, M., Peterson, P., Gérard-Marchant, P., Sheppard, K., Reddy, T., Weckesser, W., Abbasi, H., Gohlke, C., Oliphant, T.E., 2020. Array programming with NumPy. Nature 585, 357–362. https://doi.org/10.1038/s41586-020-2649-2

Hartman, T., Weinrick, B., Vilchèze, C., Berney, M., Tufariello, J., Cook, G.M., Jr, W.R.J., 2014. Succinate Dehydrogenase is the Regulator of Respiration in Mycobacterium tuberculosis. PLOS Pathog. 10, e1004510. https://doi.org/10.1371/journal.ppat.1004510

Heikal, A., Nakatani, Y., Dunn, E., Weimar, M.R., Day, C.L., Baker, E.N., Lott, J.S., Sazanov, L.A., Cook, G.M., 2014. Structure of the bacterial type II NADH dehydrogenase: a monotopic membrane protein with an essential role in energy generation. Mol. Microbiol. 91, 950–964. https://doi.org/10.1111/mmi.12507

Hellwig, P., Grzybek, S., Behr, J., Ludwig, B., Michel, H., Mäntele, W., 1999. Electrochemical and Ultraviolet/Visible/Infrared Spectroscopic Analysis of Heme a and a3 Redox Reactions in the Cytochrome c Oxidase from Paracoccus denitrificans: Separation of Heme a and a3 Contributions and Assignment of Vibrational Modes. Biochemistry 38, 1685–1694. https://doi.org/10.1021/bi982282+

Hendler, R.W., Westerhoff, H.V., 1992. Redox interactions in cytochrome c oxidase: from the “neoclassical” toward “modern” models. Biophys. J. 63, 1586–1604.

Hodgkin, A.L., Huxley, A.F., 1939. Action Potentials Recorded from Inside a Nerve Fibre. Nature 144, 710–711. https://doi.org/10.1038/144710a0

Hollis, V.S., Palacios-Callender, M., Springett, R.J., Delpy, D.T., Moncada, S., 2003. Monitoring cytochrome redox changes in the mitochondria of intact cells using multi-

wavelength visible light spectroscopy. Biochim. Biophys. Acta BBA - Bioenerg. 1607, 191–202. https://doi.org/10.1016/j.bbabio.2003.09.012
Hudson, A.T., Dickins, M., Ginger, C.D., Gutteridge, W.E., Holdich, T., Hutchinson, D.B., Pudney, M., Randall, A.W., Latter, V.S., 1991. 566C80: a potent broad spectrum anti-infective agent with activity against malaria and opportunistic infections in AIDS patients. Drugs Exp. Clin. Res. 17, 427–435.
Huq, S., Palmer, J.M., 1978. Isolation of a cyanide-resistant duroquinol oxidase from Arum maculatum mitochondria. FEBS Lett. 95, 217–220. https://doi.org/10.1016/0014-5793(78)80997-1
Iverson, T.M., Luna-Chavez, C., Croal, L.R., Cecchini, G., Rees, D.C., 2002. Crystallographic Studies of the *Escherichia coli* Quinol-Fumarate Reductase with Inhibitors Bound to the Quinol-binding Site*. J. Biol. Chem. 277, 16124–16130. https://doi.org/10.1074/jbc.M200815200
Iverson, T.M., Singh, P.K., Cecchini, G., 2023. An evolving view of complex II—noncanonical complexes, megacomplexes, respiration, signaling, and beyond. J. Biol. Chem. 299. https://doi.org/10.1016/j.jbc.2023.104761
Iwata, S., Lee, J.W., Okada, K., Lee, J.K., Iwata, M., Rasmussen, B., Link, T.A., Ramaswamy, S., Jap, B.K., 1998. Complete Structure of the 11-Subunit Bovine Mitochondrial Cytochrome bc1 Complex. Science 281, 64–71. https://doi.org/10.1126/science.281.5373.64
Jackson, J. b., Crofts, A. r., 1969. The high energy state in chromatophores from Rhodopseudomonas spheroides. FEBS Lett. 4, 185–189. https://doi.org/10.1016/0014-5793(69)80230-9
Jager, V.R. de, Dawson, R., Niekerk, C. van, Hutchings, J., Kim, J., Vanker, N., Merwe, L. van der, Choi, J., Nam, K., Diacon, A.H., 2020. Telacebec (Q203), a New Antituberculosis Agent. N. Engl. J. Med. 382, 1280–1281. https://doi.org/10.1056/NEJMc1913327
Jin, X., Zhang, X., Ding, X., Tian, T., Tseng, C.-K., Luo, X., Chen, X., Lo, C.-J., Leake, M.C., Bai, F., 2023. Sensitive bacterial Vm sensors revealed the excitability of bacterial Vm and its role in antibiotic tolerance. Proc. Natl. Acad. Sci. 120, e2208348120. https://doi.org/10.1073/pnas.2208348120
Jindal, S., Yang, L., Day, P.J., Kell, D.B., 2019. Involvement of multiple influx and efflux transporters in the accumulation of cationic fluorescent dyes by Escherichia coli. BMC Microbiol. 19, 195. https://doi.org/10.1186/s12866-019-1561-0
Jones, A.J.Y., Blaza, J.N., Bridges, H.R., May, B., Moore, A.L., Hirst, J., 2016. A Self-Assembled Respiratory Chain that Catalyzes NADH Oxidation by Ubiquinone-10 Cycling between Complex I and the Alternative Oxidase. Angew. Chem. Int. Ed. 55, 728–731. https://doi.org/10.1002/anie.201507332
Jormakka, M., Törnroth, S., Byrne, B., Iwata, S., 2002. Molecular Basis of Proton Motive Force Generation: Structure of Formate Dehydrogenase-N. Science 295, 1863–1868. https://doi.org/10.1126/science.1068186
Jumper, J., Evans, R., Pritzel, A., Green, T., Figurnov, M., Ronneberger, O., Tunyasuvunakool, K., Bates, R., Žídek, A., Potapenko, A., Bridgland, A., Meyer, C., Kohl, S.A.A., Ballard, A.J., Cowie, A., Romera-Paredes, B., Nikolov, S., Jain, R., Adler, J., Back, T., Petersen, S., Reiman, D., Clancy, E., Zielinski, M., Steinegger, M., Pacholska, M., Berghammer, T., Bodenstein, S., Silver, D., Vinyals, O., Senior, A.W., Kavukcuoglu, K., Kohli, P., Hassabis, D., 2021. Highly accurate protein structure prediction with AlphaFold. Nature 596, 583–589. https://doi.org/10.1038/s41586-021-03819-2
Kadigamuwa, C.C., Mapa, S.T., Wimalasena, K., 2016. Lipophilic Cationic Cyanines are Potent Complex I Inhibitors and Specific in vitro Dopaminergic Toxins with Mechanistic Similarities to both Rotenone and MPP+. Chem. Res. Toxicol. 29, 1468–1479. https://doi.org/10.1021/acs.chemrestox.6b00138
Kalia, N.P., Hasenoehrl, E.J., Ab Rahman, N.B., Koh, V.H., Ang, M.L.T., Sajorda, D.R., Hards, K., Grüber, G., Alonso, S., Cook, G.M., Berney, M., Pethe, K., 2017. Exploiting the synthetic lethality between terminal respiratory oxidases to kill Mycobacterium

tuberculosis and clear host infection. Proc. Natl. Acad. Sci. 114, 7426–7431. https://doi.org/10.1073/pnas.1706139114
Kalia, N.P., Shi Lee, B., Ab Rahman, N.B., Moraski, G.C., Miller, M.J., Pethe, K., 2019. Carbon metabolism modulates the efficacy of drugs targeting the cytochrome bc1:aa3 in Mycobacterium tuberculosis. Sci. Rep. 9, 8608. https://doi.org/10.1038/s41598-019-44887-9
Kalia, N.P., Singh, S., Hards, K., Cheung, C.-Y., Sviriaeva, E., Banaei-Esfahani, A., Aebersold, R., Berney, M., Cook, G.M., Pethe, K., 2023. M. tuberculosis relies on trace oxygen to maintain energy homeostasis and survive in hypoxic environments. Cell Rep. 42, 112444. https://doi.org/10.1016/j.celrep.2023.112444
Kana, B.D., Weinstein, E.A., Avarbock, D., Dawes, S.S., Rubin, H., Mizrahi, V., 2001. Characterization of the cydAB-Encoded Cytochrome bd Oxidase from Mycobacterium smegmatis. J. Bacteriol. 183, 7076–7086. https://doi.org/10.1128/JB.183.24.7076-7086.2001
Kao, W.-C., Kleinschroth, T., Nitschke, W., Baymann, F., Neehaul, Y., Hellwig, P., Richers, S., Vonck, J., Bott, M., Hunte, C., 2016. The obligate respiratory supercomplex from Actinobacteria. Biochim. Biophys. Acta 1857, 1705–1714. https://doi.org/10.1016/j.bbabio.2016.07.009
Kao, W.-C., Ortmann De Percin Northumberland, C., Cheng, T.C., Ortiz, J., Durand, A., Von Loeffelholz, O., Schilling, O., Biniossek, M.L., Klaholz, B.P., Hunte, C., 2022. Structural basis for safe and efficient energy conversion in a respiratory supercomplex. Nat. Commun. 13, 545. https://doi.org/10.1038/s41467-022-28179-x
Karavaeva, V., Sousa, F.L., 2023. Modular structure of complex II: An evolutionary perspective. Biochim. Biophys. Acta BBA - Bioenerg. 1864, 148916. https://doi.org/10.1016/j.bbabio.2022.148916
Keilin, D., 1966. The History of Cell Respiration and Cytochrome. CUP Archive.
Keilin, D., 1925. On cytochrome, a respiratory pigment, common to animals, yeast, and higher plants. Proc. R. Soc. Lond. Ser. B Contain. Pap. Biol. Character 98, 312–339. https://doi.org/10.1098/rspb.1925.0039
Keilin, D., Hartree, E.F., 1949. Effect of Low Temperature on the Absorption Spectra of Hæmoproteins; with Observations on the Absorption Spectrum of Oxygen. Nature 164, 254–259. https://doi.org/10.1038/164254a0
Keilin, D., Hartree, E.F., 1939. Cytochrome and cytochrome oxidase. Proc. R. Soc. Lond. Ser. B - Biol. Sci. 127, 167–191. https://doi.org/10.1098/rspb.1939.0016
Kessl, J.J., Lange, B.B., Merbitz-Zahradnik, T., Zwicker, K., Hill, P., Meunier, B., Pálsdóttir, H., Hunte, C., Meshnick, S., Trumpower, B.L., 2003. Molecular Basis for Atovaquone Binding to the Cytochrome *bc* 1 Complex*. J. Biol. Chem. 278, 31312–31318. https://doi.org/10.1074/jbc.M304042200
Kim, N., Ripple, M.O., Springett, R., 2012. Measurement of the Mitochondrial Membrane Potential and pH Gradient from the Redox Poise of the Hemes of the bc1 Complex. Biophys. J. 102, 1194–1203. https://doi.org/10.1016/j.bpj.2012.02.003
Kim, N., Ripple, M.O., Springett, R., 2011. Spectral components of the α-band of Cytochrome Oxidase. Biochim. Biophys. Acta 1807, 779–787. https://doi.org/10.1016/j.bbabio.2011.03.008
Kleinschroth, T., Castellani, M., Trinh, C.H., Morgner, N., Brutschy, B., Ludwig, B., Hunte, C., 2011. X-ray structure of the dimeric cytochrome bc1 complex from the soil bacterium *Paracoccus denitrificans* at 2.7-Å resolution. Biochim. Biophys. Acta BBA - Bioenerg., Special Section: Peter Mitchell - 50th anniversary of the chemiosmotic theory 1807, 1606–1615. https://doi.org/10.1016/j.bbabio.2011.09.017
Koland, J.G., Miller, M.J., Gennis, R.B., 1984. Potentiometric analysis of the purified cytochrome d terminal oxidase complex from Escherichia coli. Biochemistry 23, 1051–1056. https://doi.org/10.1021/bi00301a003
Koren, K., Borisov, S.M., Saf, R., Klimant, I., 2011. Strongly Phosphorescent Iridium(III)–Porphyrins – New Oxygen Indicators with Tuneable Photophysical Properties and

Functionalities. Eur. J. Inorg. Chem. 2011, 1531–1534. https://doi.org/10.1002/ejic.201100089
Korshunov, S.S., Skulachev, V.P., Starkov, A.A., 1997. High protonic potential actuates a mechanism of production of reactive oxygen species in mitochondria. FEBS Lett. 416, 15–18. https://doi.org/10.1016/S0014-5793(97)01159-9
Koul, A., Dendouga, N., Vergauwen, K., Molenberghs, B., Vranckx, L., Willebrords, R., Ristic, Z., Lill, H., Dorange, I., Guillemont, J., Bald, D., Andries, K., 2007. Diarylquinolines target subunit c of mycobacterial ATP synthase. Nat. Chem. Biol. 3, 323–324. https://doi.org/10.1038/nchembio884
Kralj, J.M., Hochbaum, D.R., Douglass, A.D., Cohen, A.E., 2011. Electrical spiking in Escherichia coli probed with a fluorescent voltage-indicating protein. Science 333, 345–348. https://doi.org/10.1126/science.1204763
Krasnopeeva, E., Barboza-Perez, U.E., Rosko, J., Pilizota, T., Lo, C.-J., 2021. Bacterial flagellar motor as a multimodal biosensor. Methods, Correlative approaches in single-molecule biophysics: a review of the progress in methods and applications 193, 5–15. https://doi.org/10.1016/j.ymeth.2020.06.012
Krishtalik, L.I., 1985. The negative cooperativity in cytochrome c oxidase redox reactions: The electrostatic effect. Arch. Biochem. Biophys. 243, 701–702. https://doi.org/10.1016/0003-9861(85)90549-1
Król, S., Fedotovskaya, O., Högbom, M., Ädelroth, P., Brzezinski, P., 2022. Electron and proton transfer in the *M. smegmatis* III2IV2 supercomplex. Biochim. Biophys. Acta BBA - Bioenerg. 1863, 148585. https://doi.org/10.1016/j.bbabio.2022.148585
Kumar, A., Toledo, J.C., Patel, R.P., Lancaster, J.R., Steyn, A.J.C., 2007. Mycobacterium tuberculosis DosS is a redox sensor and DosT is a hypoxia sensor. Proc. Natl. Acad. Sci. 104, 11568–11573. https://doi.org/10.1073/pnas.0705054104
Lai, S.-W., Hou, Y.-J., Che, C.-M., Pang, H.-L., Wong, K.-Y., Chang, C.K., Zhu, N., 2004. Electronic Spectroscopy, Photophysical Properties, and Emission Quenching Studies of an Oxidatively Robust Perfluorinated Platinum Porphyrin. Inorg. Chem. 43, 3724–3732. https://doi.org/10.1021/ic049902h
Lamprecht, D.A., Finin, P.M., Rahman, M.A., Cumming, B.M., Russell, S.L., Jonnala, S.R., Adamson, J.H., Steyn, A.J.C., 2016. Turning the respiratory flexibility of Mycobacterium tuberculosis against itself. Nat. Commun. 7, 12393. https://doi.org/10.1038/ncomms12393
Lancaster, C.R.D., 2013. The di-heme family of respiratory complex II enzymes. Biochim. Biophys. Acta BBA - Bioenerg., Respiratory complex II: Role in cellular physiology and disease 1827, 679–687. https://doi.org/10.1016/j.bbabio.2013.02.012
Lancaster, C.R.D., 2002. *Wolinella succinogenes* quinol:fumarate reductase—2.2-Å resolution crystal structure and the E-pathway hypothesis of coupled transmembrane proton and electron transfer. Biochim. Biophys. Acta BBA - Biomembr., Membrane Protein Structure 1565, 215–231. https://doi.org/10.1016/S0005-2736(02)00571-0
Lauraeus, M., Haltia, T., Saraste, M., Wikström, M., 1991. Bacillus subtilis expresses two kinds of haem-A-containing terminal oxidases. Eur. J. Biochem. 197, 699–705. https://doi.org/10.1111/j.1432-1033.1991.tb15961.x
Lechartier, B., Cole, S.T., 2015. Mode of Action of Clofazimine and Combination Therapy with Benzothiazinones against Mycobacterium tuberculosis. Antimicrob. Agents Chemother. 59, 4457–4463. https://doi.org/10.1128/aac.00395-15
Lee, B.S., Hards, K., Engelhart, C.A., Hasenoehrl, E.J., Kalia, N.P., Mackenzie, J.S., Sviriaeva, E., Chong, S.M.S., Manimekalai, M.S.S., Koh, V.H., Chan, J., Xu, J., Alonso, S., Miller, M.J., Steyn, A.J.C., Grüber, G., Schnappinger, D., Berney, M., Cook, G.M., Moraski, G.C., Pethe, K., 2021. Dual inhibition of the terminal oxidases eradicates antibiotic-tolerant Mycobacterium tuberculosis. EMBO Mol. Med. 13, e13207. https://doi.org/10.15252/emmm.202013207
Lee, S.-K., Okura, I., 1997a. Photoluminescent Oxygen Sensing on a Specific Surface area Using Phosphorescence Quenching of Pt-Porphyrin. Anal. Sci. 13, 535–540. https://doi.org/10.2116/analsci.13.535

Lee, S.-K., Okura, I., 1997b. Photostable Optical Oxygen Sensing Material: PlatinumTetrakis(pentafluorophenyl)porphyrin Immobilized in Polystyrene. Anal. Commun. 34, 185–188. https://doi.org/10.1039/A701130J

Levitsky, Y., Pegouske, D.J., Hammer, S.S., Frantz, N.L., Fisher, K.P., Muchnik, A.B., Saripalli, A.R., Kirschner, P., Bazil, J.N., Busik, J.V., Proshlyakov, D.A., 2019. Micro-respirometry of whole cells and isolated mitochondria. RSC Adv. 9, 33257–33267. https://doi.org/10.1039/C9RA05289E

Liang, Y., Plourde, A., Bueler, S.A., Liu, J., Brzezinski, P., Vahidi, S., Rubinstein, J.L., 2023. Structure of mycobacterial respiratory complex I. Proc. Natl. Acad. Sci. 120, e2214949120. https://doi.org/10.1073/pnas.2214949120

Liao, G.-L., Palmer, G., 1996. The reduced *minus* oxidized difference spectra of cytochromes *a* and *a*3. Biochim. Biophys. Acta BBA - Bioenerg. 1274, 109–111. https://doi.org/10.1016/0005-2728(96)00014-X

Liberman, E.A., Topaly, V.P., Tsofina, L.M., Jasaitis, A.A., Skulachev, V.P., 1969. Mechanism of Coupling of Oxidative Phosphorylation and the Membrane Potential of Mitochondria. Nature 222, 1076–1078. https://doi.org/10.1038/2221076a0

Lighton, J.R.B., 2018. Measuring Metabolic Rates: A Manual for Scientists. Oxford University Press.

Lim, B.S., Holm, R.H., 1998. Molecular Heme−Cyanide−Copper Bridged Assemblies: Linkage Isomerism, Trends in vCN Values, and Relation to the Heme-a3/CuB Site in Cyanide-Inhibited Heme−Copper Oxidases. Inorg. Chem. 37, 4898–4908. https://doi.org/10.1021/ic9801793

Liu, Z., Pouli, D., Alonzo, C.A., Varone, A., Karaliota, S., Quinn, K.P., Münger, K., Karalis, K.P., Georgakoudi, I., 2018. Mapping metabolic changes by noninvasive, multiparametric, high-resolution imaging using endogenous contrast. Sci. Adv. 4, eaap9302. https://doi.org/10.1126/sciadv.aap9302

Lo, C.-J., Leake, M.C., Pilizota, T., Berry, R.M., 2007. Nonequivalence of Membrane Voltage and Ion-Gradient as Driving Forces for the Bacterial Flagellar Motor at Low Load. Biophys. J. 93, 294–302. https://doi.org/10.1529/biophysj.106.095265

Lo, W.-C., Krasnopeeva, E., Pilizota, T., 2024. Bacterial Electrophysiology. Annu. Rev. Biophys. 53, 487–510. https://doi.org/10.1146/annurev-biophys-030822-032215

Lu, X., Williams, Z., Hards, K., Tang, J., Cheung, C.-Y., Aung, H.L., Wang, B., Liu, Z., Hu, X., Lenaerts, A., Woolhiser, L., Hastings, C., Zhang, X., Wang, Z., Rhee, K., Ding, K., Zhang, T., Cook, G.M., 2019. Pyrazolo[1,5-a]pyridine Inhibitor of the Respiratory Cytochrome bcc Complex for the Treatment of Drug-Resistant Tuberculosis. ACS Infect. Dis. 5, 239–249. https://doi.org/10.1021/acsinfecdis.8b00225

Lümmen, P., 1998. Complex I inhibitors as insecticides and acaricides1. Biochim. Biophys. Acta BBA - Bioenerg. 1364, 287–296. https://doi.org/10.1016/S0005-2728(98)00034-6

MacMunn, C.A., 1886. On the Presence of Haematoporphyrin in the Integument of certain Invertebrates. J. Physiol. 7, 240–252. https://doi.org/10.1113/jphysiol.1886.sp000219

Madej, M.G., Nasiri, H.R., Hilgendorff, N.S., Schwalbe, H., Lancaster, C.R.D., 2006. Evidence for transmembrane proton transfer in a dihaem-containing membrane protein complex. EMBO J. 25, 4963–4970. https://doi.org/10.1038/sj.emboj.7601361

Marcus, R.A., Sutin, N., 1985. Electron transfers in chemistry and biology. Biochim. Biophys. Acta BBA - Rev. Bioenerg. 811, 265–322. https://doi.org/10.1016/0304-4173(85)90014-X

Mase, S., Chorba, T., Lobue, P., Castro, K., 2013. Provisional CDC Guidelines for the Use and Safety Monitoring of Bedaquiline Fumarate (Sirturo) for the Treatment of Multidrug-Resistant Tuberculosis [WWW Document]. URL https://www.cdc.gov/mmwr/preview/mmwrhtml/rr6209a1.htm (accessed 11.20.24).

Matcher, S.J., Cope, M., Delpy, D.T., 1994. Use of the water absorption spectrum to quantify tissue chromophore concentration changes in near-infrared spectroscopy. Phys. Med. Biol. 39, 177. https://doi.org/10.1088/0031-9155/39/1/011

Mathiyazakan, V., Wong, C.-F., Harikishore, A., Pethe, K., Grüber, G., 2023. Cryo-Electron Microscopy Structure of the Mycobacterium tuberculosis Cytochrome bcc:aa3 Supercomplex and a Novel Inhibitor Targeting Subunit Cytochrome cI. Antimicrob. Agents Chemother. 67, e01531-22. https://doi.org/10.1128/aac.01531-22

Matsoso, L.G., Kana, B.D., Crellin, P.K., Lea-Smith, D.J., Pelosi, A., Powell, D., Dawes, S.S., Rubin, H., Coppel, R.L., Mizrahi, V., 2005. Function of the Cytochrome bc1-aa3 Branch of the Respiratory Network in Mycobacteria and Network Adaptation Occurring in Response to Its Disruption. J. Bacteriol. 187, 6300–6308. https://doi.org/10.1128/JB.187.18.6300-6308.2005

Matsson, M., Tolstoy, D., Aasa, R., Hederstedt, L., 2000. The Distal Heme Center in Bacillus subtilis Succinate:Quinone Reductase Is Crucial for Electron Transfer to Menaquinone. Biochemistry 39, 8617–8624. https://doi.org/10.1021/bi000271m

Mayberry, C.L., Wilson, J.J., Sison, B., Chang, C.-H., 2024. Protocol to assess bioenergetics and mitochondrial fuel usage in murine autoreactive immunocytes using the Seahorse Extracellular Flux Analyzer. STAR Protoc. 5, 102971. https://doi.org/10.1016/j.xpro.2024.102971

McKinney, W., 2010. Data Structures for Statistical Computing in Python. Presented at the Python in Science Conference, Austin, Texas, pp. 56–61. https://doi.org/10.25080/Majora-92bf1922-00a

McNeil, M.B., Cheung, C.-Y., Waller, N.J.E., Adolph, C., Chapman, C.L., Seeto, N.E.J., Jowsey, W., Li, Z., Hameed, H.M.A., Zhang, T., Cook, G.M., 2022a. Uncovering interactions between mycobacterial respiratory complexes to target drug-resistant Mycobacterium tuberculosis. Front. Cell. Infect. Microbiol. 12. https://doi.org/10.3389/fcimb.2022.980844

McNeil, M.B., Ryburn, H.W., Tirados, J., Cheung, C.-Y., Cook, G.M., 2022b. Multiplexed transcriptional repression identifies a network of bactericidal interactions between mycobacterial respiratory complexes. iScience 25, 103573. https://doi.org/10.1016/j.isci.2021.103573

Megehee, J.A., Hosler, J.P., Lundrigan, M.D., 2006. Evidence for a cytochrome bcc–aa3 interaction in the respiratory chain of Mycobacterium smegmatis. Microbiology 152, 823–829. https://doi.org/10.1099/mic.0.28723-0

Merlino, A., 2018. X-ray structure of bovine heart cytochrome c at high ionic strength. BioMetals 31, 277–284. https://doi.org/10.1007/s10534-018-0090-x

Mileni, M., MacMillan, F., Tziatzios, C., Zwicker, K., Haas, A.H., Mäntele, W., Simon, J., Lancaster, C.R.D., 2006. Heterologous production in Wolinella succinogenes and characterization of the quinol:fumarate reductase enzymes from Helicobacter pylori and Campylobacter jejuni. Biochem. J. 395, 191–201. https://doi.org/10.1042/BJ20051675

Mitchell, P., 1975. The protonmotive Q cycle: A general formulation. FEBS Lett. 59, 137–139. https://doi.org/10.1016/0014-5793(75)80359-0

Mitchell, P., 1966. Chemiosmotic coupling in oxidative and photosynthetic phosphorylation. Biol. Rev. 41, 445–501. https://doi.org/10.1111/j.1469-185X.1966.tb01501.x

Mitchell, P., 1961. Coupling of Phosphorylation to Electron and Hydrogen Transfer by a Chemi-Osmotic type of Mechanism. Nature 191, 144–148. https://doi.org/10.1038/191144a0

Mitchell, P., Moyle, J., 1969. Estimation of Membrane Potential and pH Difference across the Cristae Membrane of Rat Liver Mitochondria. Eur. J. Biochem. 7, 471–484. https://doi.org/10.1111/j.1432-1033.1969.tb19633.x

Montgomery, M.G., Petri, J., Spikes, T.E., Walker, J.E., 2021. Structure of the ATP synthase from Mycobacterium smegmatis provides targets for treating tuberculosis. Proc. Natl. Acad. Sci. U. S. A. 118, e2111899118. https://doi.org/10.1073/pnas.2111899118

More, J.J., Garbow, B.S., Hillstrom, K.E., 1980. User guide for MINPACK-1. [In FORTRAN] (No. ANL-80-74). Argonne National Lab. (ANL), Argonne, IL (United States). https://doi.org/10.2172/6997568

Moser, C.C., Keske, J.M., Warncke, K., Farid, R.S., Dutton, P.L., 1992. Nature of biological electron transfer. Nature 355, 796–802. https://doi.org/10.1038/355796a0

Moss, D., Nabedryk, E., Breton, J., Mantele, W., 1990. Redox-linked conformational changes in proteins detected by a combination of infrared spectroscopy and protein electrochemistry. Evaluation of the technique with cytochrome c. Eur. J. Biochem. 187, 565–572. https://doi.org/10.1111/j.1432-1033.1990.tb15338.x

Mueller, J.P., Taber, H.W., 1989. Isolation and sequence of ctaA, a gene required for cytochrome aa3 biosynthesis and sporulation in Bacillus subtilis. J. Bacteriol. 171, 4967–4978.

Mühleip, A., Kock Flygaard, R., Ovciarikova, J., Lacombe, A., Fernandes, P., Sheiner, L., Amunts, A., 2021. ATP synthase hexamer assemblies shape cristae of Toxoplasma mitochondria. Nat. Commun. 12, 120. https://doi.org/10.1038/s41467-020-20381-z

Murali, R., Gennis, R.B., Hemp, J., 2021. Evolution of the cytochrome bd oxygen reductase superfamily and the function of CydAA' in Archaea. ISME J. 15, 3534–3548. https://doi.org/10.1038/s41396-021-01019-4

Murali, R., Hemp, J., Gennis, R.B., 2022. Evolution of quinol oxidation within the heme-copper oxidoreductase superfamily. Biochim. Biophys. Acta BBA - Bioenerg. 1863, 148907. https://doi.org/10.1016/j.bbabio.2022.148907

Muramoto, K., Shinzawa-Itoh, K., 2023. Calcium-bound structure of bovine cytochrome *c* oxidase. Biochim. Biophys. Acta BBA - Bioenerg. 1864, 148956. https://doi.org/10.1016/j.bbabio.2023.148956

Murphy, K.C., Nelson, S.J., Nambi, S., Papavinasasundaram, K., Baer, C.E., Sassetti, C.M., 2018. ORBIT: a New Paradigm for Genetic Engineering of Mycobacterial Chromosomes. mBio 9, e01467-18. https://doi.org/10.1128/mBio.01467-18

Murugesan, D., Ray, P.C., Bayliss, T., Prosser, G.A., Harrison, J.R., Green, K., Soares de Melo, C., Feng, T.-S., Street, L.J., Chibale, K., Warner, D.F., Mizrahi, V., Epemolu, O., Scullion, P., Ellis, L., Riley, J., Shishikura, Y., Ferguson, L., Osuna-Cabello, M., Read, K.D., Green, S.R., Lamprecht, D.A., Finin, P.M., Steyn, A.J.C., Ioerger, T.R., Sacchettini, J., Rhee, K.Y., Arora, K., Barry, C.E.I., Wyatt, P.G., Boshoff, H.I.M., 2018. 2-Mercapto-Quinazolinones as Inhibitors of Type II NADH Dehydrogenase and Mycobacterium tuberculosis: Structure–Activity Relationships, Mechanism of Action and Absorption, Distribution, Metabolism, and Excretion Characterization. ACS Infect. Dis. 4, 954–969. https://doi.org/10.1021/acsinfecdis.7b00275

Nakatani, Y., Shimaki, Y., Dutta, D., Muench, S.P., Ireton, K., Cook, G.M., Jeuken, L.J.C., 2020. Unprecedented Properties of Phenothiazines Unraveled by a NDH-2 Bioelectrochemical Assay Platform. J. Am. Chem. Soc. 142, 1311–1320. https://doi.org/10.1021/jacs.9b10254

Nasiri, M.J., Haeili, M., Ghazi, M., Goudarzi, H., Pormohammad, A., Imani Fooladi, A.A., Feizabadi, M.M., 2017. New Insights in to the Intrinsic and Acquired Drug Resistance Mechanisms in Mycobacteria. Front. Microbiol. 8. https://doi.org/10.3389/fmicb.2017.00681

Nicholls, D.G., 1974. The Influence of Respiration and ATP Hydrolysis on the Proton-Electrochemical Gradient across the Inner Membrane of Rat-Liver Mitochondria as Determined by Ion Distribution. Eur. J. Biochem. 50, 305–315. https://doi.org/10.1111/j.1432-1033.1974.tb03899.x

Nicholls, D.G., Ferguson, S.J., 2013. Bioenergetics, 4th ed. Academic Press.

Nicholls, P., Petersen, L.Chr., 1974. Haem—haem interactions in cytochrome *aa*3 during the anaerobic-aerobic transition. Biochim. Biophys. Acta BBA - Bioenerg. 357, 462–467. https://doi.org/10.1016/0005-2728(74)90038-3

Nicolay, K., Scheffers, W.A., Bruinenberg, P.M., Kaptein, R., 1982. Phosphorus-31 nuclear magnetic resonance studies of intracellular pH, phosphate compartmentation and phosphate transport in yeasts. Arch. Microbiol. 133, 83–89. https://doi.org/10.1007/BF00413516

Niebisch, A., Bott, M., 2001. Molecular analysis of the cytochrome bc1-aa3 branch of the Corynebacterium glutamicum respiratory chain containing an unusual diheme

cytochrome c1. Arch. Microbiol. 175, 282–294. https://doi.org/10.1007/s002030100262
Nikitushkin, V.D., Shleeva, M.O., Zinin, A.I., Trutneva, K.A., Ostrovsky, D.N., Kaprelyants, A.S., 2016. The main pigment of the dormant Mycobacterium smegmatis is porphyrin. FEMS Microbiol. Lett. 363, fnw206. https://doi.org/10.1093/femsle/fnw206
Nikolaev, A., Safarian, S., Thesseling, A., Wohlwend, D., Friedrich, T., Michel, H., Kusumoto, T., Sakamoto, J., Melin, F., Hellwig, P., 2021. Electrocatalytic evidence of the diversity of the oxygen reaction in the bacterial *bd* oxidase from different organisms. Biochim. Biophys. Acta BBA - Bioenerg. 1862, 148436. https://doi.org/10.1016/j.bbabio.2021.148436
Noens, E.E., Williams, C., Anandhakrishnan, M., Poulsen, C., Ehebauer, M.T., Wilmanns, M., 2011. Improved mycobacterial protein production using a Mycobacterium smegmatis groEL1ΔCexpression strain. BMC Biotechnol. 11, 27. https://doi.org/10.1186/1472-6750-11-27
Nowicka, B., Kruk, J., 2010. Occurrence, biosynthesis and function of isoprenoid quinones. Biochim. Biophys. Acta BBA - Bioenerg. 1797, 1587–1605. https://doi.org/10.1016/j.bbabio.2010.06.007
Nunn, A.J., Rusen, I., Van Deun, A., Torrea, G., Phillips, P.P., Chiang, C.-Y., Squire, S.B., Madan, J., Meredith, S.K., 2014. Evaluation of a standardized treatment regimen of anti-tuberculosis drugs for patients with multi-drug-resistant tuberculosis (STREAM): study protocol for a randomized controlled trial. Trials 15, 353. https://doi.org/10.1186/1745-6215-15-353
O'Haver, T., 2021. Intro. to Signal Processing:Curve fitting B. Multicomponent Spectroscopy [WWW Document]. URL https://terpconnect.umd.edu/~toh/spectrum/CurveFittingB.html#cls (accessed 8.20.24).
Otten, M.F., van der Oost, J., Reijnders, W.N.M., Westerhoff, H.V., Ludwig, B., Van Spanning, R.J.M., 2001. Cytochromes c550,c552, and c1 in the Electron Transport Network of Paracoccus denitrificans: Redundant or Subtly Different in Function? J. Bacteriol. 183, 7017–7026. https://doi.org/10.1128/jb.183.24.7017-7026.2001
Page, C.C., Moser, C.C., Chen, X., Dutton, P.L., 1999. Natural engineering principles of electron tunnelling in biological oxidation–reduction. Nature 402, 47–52. https://doi.org/10.1038/46972
Pecsi, I., Hards, K., Ekanayaka, N., Berney, M., Hartman, T., Jacobs, W.R., Cook, G.M., 2014. Essentiality of Succinate Dehydrogenase in Mycobacterium smegmatis and Its Role in the Generation of the Membrane Potential Under Hypoxia. mBio 5, e01093-14. https://doi.org/10.1128/mBio.01093-14
Pereira, M.M., Santana, M., Teixeira, M., 2001. A novel scenario for the evolution of haem–copper oxygen reductases. Biochim. Biophys. Acta BBA - Bioenerg. 1505, 185–208. https://doi.org/10.1016/S0005-2728(01)00169-4
Perlin, D.S., Latchney, L.R., Senior, A.E., 1985. Inhibition of *Escherichia coli* H+-ATPase by venturicidin, oligomycin and ossamycin. Biochim. Biophys. Acta BBA - Bioenerg. 807, 238–244. https://doi.org/10.1016/0005-2728(85)90254-3
Pesta, D., Gnaiger, E., 2012. High-Resolution Respirometry: OXPHOS Protocols for Human Cells and Permeabilized Fibers from Small Biopsies of Human Muscle, in: Palmeira, C.M., Moreno, A.J. (Eds.), Mitochondrial Bioenergetics: Methods and Protocols. Humana Press, Totowa, NJ, pp. 25–58. https://doi.org/10.1007/978-1-61779-382-0_3
Petering, H.G., Daniels, F., 1938. The Determination of Dissolved Oxygen by Means of the Dropping Mercury Electrode, with Applications in Biology. J. Am. Chem. Soc. 60, 2796–2802. https://doi.org/10.1021/ja01278a073
Pethe, K., Bifani, P., Jang, J., Kang, S., Park, S., Ahn, S., Jiricek, J., Jung, J., Jeon, H.K., Cechetto, J., Christophe, T., Lee, H., Kempf, M., Jackson, M., Lenaerts, A.J., Pham, H., Jones, V., Seo, M.J., Kim, Y.M., Seo, M., Seo, J.J., Park, D., Ko, Y., Choi, I., Kim, R., Kim, S.Y., Lim, S., Yim, S.-A., Nam, J., Kang, H., Kwon, H., Oh, C.-T., Cho, Y., Jang, Y., Kim, Junghwan, Chua, A., Tan, B.H., Nanjundappa, M.B., Rao, S.P.S.,

Barnes, W.S., Wintjens, R., Walker, J.R., Alonso, S., Lee, S., Kim, Jungjun, Oh, S., Oh, T., Nehrbass, U., Han, S.-J., No, Z., Lee, J., Brodin, P., Cho, S.-N., Nam, K., Kim, Jaeseung, 2013. Discovery of Q203, a potent clinical candidate for the treatment of tuberculosis. Nat. Med. 19, 1157–1160. https://doi.org/10.1038/nm.3262

Preiss, L., Klyszejko, A.L., Hicks, D.B., Liu, J., Fackelmayer, O.J., Yildiz, Ö., Krulwich, T.A., Meier, T., 2013. The c-ring stoichiometry of ATP synthase is adapted to cell physiological requirements of alkaliphilic Bacillus pseudofirmus OF4. Proc. Natl. Acad. Sci. U. S. A. 110, 7874–7879. https://doi.org/10.1073/pnas.1303333110

Pryde, K.R., Hirst, J., 2011. Superoxide Is Produced by the Reduced Flavin in Mitochondrial Complex I: A SINGLE, UNIFIED MECHANISM THAT APPLIES DURING BOTH FORWARD AND REVERSE ELECTRON TRANSFER *. J. Biol. Chem. 286, 18056–18065. https://doi.org/10.1074/jbc.M110.186841

Rao, M., Streur, T.L., Aldwell, F.E., Cook, G.M., 2001. Intracellular pH regulation by Mycobacterium smegmatis and Mycobacterium bovis BCG. Microbiology 147, 1017–1024. https://doi.org/10.1099/00221287-147-4-1017

Rao, S.P.S., Alonso, S., Rand, L., Dick, T., Pethe, K., 2008. The protonmotive force is required for maintaining ATP homeostasis and viability of hypoxic, nonreplicating Mycobacterium tuberculosis. Proc. Natl. Acad. Sci. 105, 11945–11950. https://doi.org/10.1073/pnas.0711697105

Rich, P.R., Jeal, A.E., Madgwick, S.A., Moody, A.J., 1990. Inhibitor effects on redox-linked protonations of the *b* haems of the mitochondrial *bc*1 complex. Biochim. Biophys. Acta BBA - Bioenerg. 1018, 29–40. https://doi.org/10.1016/0005-2728(90)90106-E

Riepl, D., Gamiz-Hernandez, A.P., Kovalova, T., Król, S.M., Mader, S.L., Sjöstrand, D., Högbom, M., Brzezinski, P., Kaila, V.R.I., 2024. Long-range charge transfer mechanism of the III2IV2 mycobacterial supercomplex. Nat. Commun. 15, 5276. https://doi.org/10.1038/s41467-024-49628-9

Ripple, M.O., Abajian, M., Springett, R., 2010. Cytochrome c is rapidly reduced in the cytosol after mitochondrial outer membrane permeabilization. Apoptosis 15, 563–573. https://doi.org/10.1007/s10495-010-0455-2

Ripple, M.O., Kim, N., Springett, R., 2013a. Mammalian Complex I Pumps 4 Protons per 2 Electrons at High and Physiological Proton Motive Force in Living Cells*. J. Biol. Chem. 288, 5374–5380. https://doi.org/10.1074/jbc.M112.438945

Ripple, M.O., Kim, N., Springett, R., 2013b. Mammalian Complex I Pumps 4 Protons per 2 Electrons at High and Physiological Proton Motive Force in Living Cells*. J. Biol. Chem. 288, 5374–5380. https://doi.org/10.1074/jbc.M112.438945

Ripple, M.O., Kim, N., Springett, R., 2013c. Acute Mitochondrial Inhibition by Mitogen-activated Protein Kinase/Extracellular Signal-regulated Kinase Kinase (MEK) 1/2 Inhibitors Regulates Proliferation*. J. Biol. Chem. 288, 2933–2940. https://doi.org/10.1074/jbc.M112.430082

Ritchie, R.J., 1984. A critical assessment of the use of lipophilic cations as membrane potential probes. Prog. Biophys. Mol. Biol. 43, 1–32. https://doi.org/10.1016/0079-6107(84)90002-6

Rocha, M.C., Springett, R., 2018. Spectral components of detergent-solubilized bovine cytochrome oxidase. Biochim. Biophys. Acta BBA - Bioenerg. 1859, 555–566. https://doi.org/10.1016/j.bbabio.2018.04.009

Rodriguez, G.M., Sharma, Nishant, Biswas, A., Sharma, Nevadita, 2022. The Iron Response of Mycobacterium tuberculosis and Its Implications for Tuberculosis Pathogenesis and Novel Therapeutics. Front. Cell. Infect. Microbiol. 12. https://doi.org/10.3389/fcimb.2022.876667

Ruas, J.S., Siqueira-Santos, E.S., Amigo, I., Rodrigues-Silva, E., Kowaltowski, A.J., Castilho, R.F., 2016. Underestimation of the Maximal Capacity of the Mitochondrial Electron Transport System in Oligomycin-Treated Cells. PLOS ONE 11, e0150967. https://doi.org/10.1371/journal.pone.0150967

Rumsey, W.L., Vanderkooi, J.M., Wilson, D.F., 1988. Imaging of Phosphorescence: A Novel Method for Measuring Oxygen Distribution in Perfused Tissue. Science 241, 1649–1651. https://doi.org/10.1126/science.3420417

Safarian, S., Hahn, A., Mills, D.J., Radloff, M., Eisinger, M.L., Nikolaev, A., Meier-Credo, J., Melin, F., Miyoshi, H., Gennis, R.B., Sakamoto, J., Langer, J.D., Hellwig, P., Kühlbrandt, W., Michel, H., 2019. Active site rearrangement and structural divergence in prokaryotic respiratory oxidases. Science 366, 100–104. https://doi.org/10.1126/science.aay0967

Safarian, S., Opel-Reading, H.K., Wu, D., Mehdipour, A.R., Hards, K., Harold, L.K., Radloff, M., Stewart, I., Welsch, S., Hummer, G., Cook, G.M., Krause, K.L., Michel, H., 2021. The cryo-EM structure of the bd oxidase from M. tuberculosis reveals a unique structural framework and enables rational drug design to combat TB. Nat. Commun. 12, 5236. https://doi.org/10.1038/s41467-021-25537-z

Safarian, S., Rajendran, C., Müller, H., Preu, J., Langer, J.D., Ovchinnikov, S., Hirose, T., Kusumoto, T., Sakamoto, J., Michel, H., 2016. Structure of a bd oxidase indicates similar mechanisms for membrane-integrated oxygen reductases. Science 352, 583–586. https://doi.org/10.1126/science.aaf2477

Sarewicz, M., Pintscher, S., Pietras, R., Borek, A., Bujnowicz, Ł., Hanke, G., Cramer, W.A., Finazzi, G., Osyczka, A., 2021. Catalytic Reactions and Energy Conservation in the Cytochrome bc1 and b6f Complexes of Energy-Transducing Membranes. Chem. Rev. 121, 2020–2108. https://doi.org/10.1021/acs.chemrev.0c00712

Schnort, U., 1966. Der Einfluß von Substituenten auf Redoxpotential und Wuchseigenschaften von Chinonen. ETH Zürich.

Schrodinger, E., 1944. What is life? : the physical aspect of the living cell.

Serrill, J.D., Tan, M., Fotso, S., Sikorska, J., Kasanah, N., Hau, A.M., McPhail, K.L., Santosa, D.A., Zabriskie, T.M., Mahmud, T., Viollet, B., Proteau, P.J., Ishmael, J.E., 2015. Apoptolidins A and C activate AMPK in metabolically sensitive cell types and are mechanistically distinct from oligomycin A. Biochem. Pharmacol. 93, 251–265. https://doi.org/10.1016/j.bcp.2014.11.015

Shiba, T., Kido, Y., Sakamoto, K., Inaoka, D.K., Tsuge, C., Tatsumi, R., Takahashi, G., Balogun, E.O., Nara, T., Aoki, T., Honma, T., Tanaka, A., Inoue, M., Matsuoka, S., Saimoto, H., Moore, A.L., Harada, S., Kita, K., 2013. Structure of the trypanosome cyanide-insensitive alternative oxidase. Proc. Natl. Acad. Sci. U. S. A. 110, 4580–4585. https://doi.org/10.1073/pnas.1218386110

Shinkarev, V.P., Crofts, A.R., Wraight, C.A., 2006a. Spectral analysis of the *bc*1 complex components in situ: Beyond the traditional difference approach. Biochim. Biophys. Acta BBA - Bioenerg. 1757, 67–77. https://doi.org/10.1016/j.bbabio.2005.11.006

Shinkarev, V.P., Crofts, A.R., Wraight, C.A., 2006b. Spectral and kinetic resolution of the *bc*1 complex components in situ: A simple and robust alternative to the traditional difference wavelength approach. Biochim. Biophys. Acta BBA - Bioenerg. 1757, 273–283. https://doi.org/10.1016/j.bbabio.2006.04.003

Shinkarev, V.P., Crofts, A.R., Wraight, C.A., 2006c. In Situ Kinetics of Cytochromes c1 and c2. Biochemistry 45, 7897–7903. https://doi.org/10.1021/bi060172u

Shinkarev, V.P., Crofts, A.R., Wraight, C.A., 2001. The Electric Field Generated by Photosynthetic Reaction Center Induces Rapid Reversed Electron Transfer in the bc1 Complex. Biochemistry 40, 12584–12590. https://doi.org/10.1021/bi011334j

Shinkarev, V.P., Wraight, C.A., 2007. Intermonomer electron transfer in the *bc*1 complex dimer is controlled by the energized state and by impaired electron transfer between low and high potential hemes. FEBS Lett. 581, 1535–1541. https://doi.org/10.1016/j.febslet.2007.03.037

Snapper, S.B., Melton, R.E., Mustafa, S., Kieser, T., Jr, W.R.J., 1990. Isolation and characterization of efficient plasmid transformation mutants of Mycobacterium smegmatis. Mol. Microbiol. 4, 1911–1919. https://doi.org/10.1111/j.1365-2958.1990.tb02040.x

Sone, N., Tsuchiya, N., Inoue, M., Noguchi, S., 1996. *Bacillus stearothermophilus qcr* Operon Encoding Rieske FeS Protein, Cytochrome *b*6, and a Novel-type Cytochrome *c*1 of Quinol-cytochrome *c* Reductase (∗). J. Biol. Chem. 271, 12457–12462. https://doi.org/10.1074/jbc.271.21.12457

Spikes, T.E., Montgomery, M.G., Walker, J.E., 2021. Interface mobility between monomers in dimeric bovine ATP synthase participates in the ultrastructure of inner mitochondrial membranes. Proc. Natl. Acad. Sci. 118, e2021012118. https://doi.org/10.1073/pnas.2021012118

Springett, R., 2015a. Novel Methods for Measuring the Mitochondrial Membrane Potential, in: Weissig, V., Edeas, M. (Eds.), Mitochondrial Medicine: Volume I, Probing Mitochondrial Function. Springer, New York, NY, pp. 195–202. https://doi.org/10.1007/978-1-4939-2257-4_18

Springett, R., 2015b. Novel Methods for Measuring the Mitochondrial Membrane Potential, in: Weissig, V., Edeas, M. (Eds.), Mitochondrial Medicine, Methods in Molecular Biology. Springer New York, New York, NY, pp. 195–202. https://doi.org/10.1007/978-1-4939-2257-4_18

Sun, F., Huo, X., Zhai, Y., Wang, A., Xu, J., Su, D., Bartlam, M., Rao, Z., 2005. Crystal Structure of Mitochondrial Respiratory Membrane Protein Complex II. Cell 121, 1043–1057. https://doi.org/10.1016/j.cell.2005.05.025

Swainsbury, D.J.K., Hawkings, F.R., Martin, E.C., Musiał, S., Salisbury, J.H., Jackson, P.J., Farmer, D.A., Johnson, M.P., Siebert, C.A., Hitchcock, A., Hunter, C.N., 2023. Cryo-EM structure of the four-subunit Rhodobacter sphaeroides cytochrome bc1 complex in styrene maleic acid nanodiscs. Proc. Natl. Acad. Sci. 120, e2217922120. https://doi.org/10.1073/pnas.2217922120

Świerczek, M., Cieluch, E., Sarewicz, M., Borek, A., Moser, C.C., Dutton, P.L., Osyczka, A., 2010. An Electronic Bus Bar Lies in the Core of Cytochrome bc1. Science 329, 451–454. https://doi.org/10.1126/science.1190899

Teuber, M., Rögner, M., Berry, S., 2001. Fluorescent probes for non-invasive bioenergetic studies of whole cyanobacterial cells. Biochim. Biophys. Acta BBA - Bioenerg. 1506, 31–46. https://doi.org/10.1016/S0005-2728(01)00178-5

Thauer, R.K., Jungermann, K., Decker, K., 1977. Energy conservation in chemotrophic anaerobic bacteria. Bacteriol. Rev. 41, 100–180.

Theßeling, A., Rasmussen, T., Burschel, S., Wohlwend, D., Kägi, J., Müller, R., Böttcher, B., Friedrich, T., 2019. Homologous bd oxidases share the same architecture but differ in mechanism. Nat. Commun. 10, 5138. https://doi.org/10.1038/s41467-019-13122-4

Tiesjema, R.H., Muijsers, A.O., Van Gelder, B.F., 1973. Biochemical and biophysical studies on cytochrome *c* oxidase. X. Spectral and potentiometric properties of the hemes and coppers. Biochim. Biophys. Acta BBA - Bioenerg. 305, 19–28. https://doi.org/10.1016/0005-2728(73)90227-2

To, W.-P., Liu, Y., Lau, T.-C., Che, C.-M., 2013. A Robust Palladium(II)–Porphyrin Complex as Catalyst for Visible Light Induced Oxidative C□H Functionalization. Chem. – Eur. J. 19, 5654–5664. https://doi.org/10.1002/chem.201203774

Tran, Q.M., Rothery, R.A., Maklashina, E., Cecchini, G., Weiner, J.H., 2007. Escherichia coli succinate dehydrogenase variant lacking the heme b. Proc. Natl. Acad. Sci. 104, 18007–18012. https://doi.org/10.1073/pnas.0707732104

Tran, S.L., Cook, G.M., 2005. The F1Fo-ATP Synthase of Mycobacterium smegmatis Is Essential for Growth. J. Bacteriol. 187, 5023–5028. https://doi.org/10.1128/jb.187.14.5023-5028.2005

Turrens, J.F., Alexandre, A., Lehninger, A.L., 1985. Ubisemiquinone is the electron donor for superoxide formation by complex III of heart mitochondria. Arch. Biochem. Biophys. 237, 408–414. https://doi.org/10.1016/0003-9861(85)90293-0

Van Rossum, G., Drake, F.L., 2009. Python 3 reference manual. CreateSpace100 Enterprise Way, Suite A200Scotts ValleyCA.

Varadi, M., Anyango, S., Deshpande, M., Nair, S., Natassia, C., Yordanova, G., Yuan, D., Stroe, O., Wood, G., Laydon, A., Žídek, A., Green, T., Tunyasuvunakool, K., Petersen,

S., Jumper, J., Clancy, E., Green, R., Vora, A., Lutfi, M., Figurnov, M., Cowie, A., Hobbs, N., Kohli, P., Kleywegt, G., Birney, E., Hassabis, D., Velankar, S., 2022. AlphaFold Protein Structure Database: massively expanding the structural coverage of protein-sequence space with high-accuracy models. Nucleic Acids Res. 50, D439–D444. https://doi.org/10.1093/nar/gkab1061

Velden, T.T. van der, Waterham, C.Y.J., Jeuken, L.J.C., 2024. Menaquinone-specific oxidation by M. tuberculosis cytochrome bd is redox regulated by the Q-loop disulfide bond. https://doi.org/10.1101/2024.01.09.574813

Vercellino, I., Sazanov, L.A., 2021. Structure and assembly of the mammalian mitochondrial supercomplex CIII2CIV. Nature 598, 364–367. https://doi.org/10.1038/s41586-021-03927-z

Verstraeten, N., Knapen, W.J., Kint, C.I., Liebens, V., Van den Bergh, B., Dewachter, L., Michiels, J.E., Fu, Q., David, C.C., Fierro, A.C., Marchal, K., Beirlant, J., Versées, W., Hofkens, J., Jansen, M., Fauvart, M., Michiels, J., 2015. Obg and Membrane Depolarization Are Part of a Microbial Bet-Hedging Strategy that Leads to Antibiotic Tolerance. Mol. Cell 59, 9–21. https://doi.org/10.1016/j.molcel.2015.05.011

Virtanen, P., Gommers, R., Oliphant, T.E., Haberland, M., Reddy, T., Cournapeau, D., Burovski, E., Peterson, P., Weckesser, W., Bright, J., van der Walt, S.J., Brett, M., Wilson, J., Millman, K.J., Mayorov, N., Nelson, A.R.J., Jones, E., Kern, R., Larson, E., Carey, C.J., Polat, İ., Feng, Y., Moore, E.W., VanderPlas, J., Laxalde, D., Perktold, J., Cimrman, R., Henriksen, I., Quintero, E.A., Harris, C.R., Archibald, A.M., Ribeiro, A.H., Pedregosa, F., van Mulbregt, P., 2020. SciPy 1.0: fundamental algorithms for scientific computing in Python. Nat. Methods 17, 261–272. https://doi.org/10.1038/s41592-019-0686-2

Vugrin, K.W., Swiler, L.P., Roberts, R.M., Stucky-Mack, N.J., Sullivan, S.P., 2007. Confidence region estimation techniques for nonlinear regression in groundwater flow: Three case studies. Water Resour. Res. 43. https://doi.org/10.1029/2005WR004804

Wagner, G.C., Kassner, R.J., Kamen, M.D., 1974. Redox Potentials of Certain Vitamins K: Implications for a Role in Sulfite Reduction by Obligately Anaerobic Bacteria. Proc. Natl. Acad. Sci. 71, 253–256. https://doi.org/10.1073/pnas.71.2.253

Wallace, B.J., Young, I.G., 1977. Role of quinones in electron transport to oxygen and nitrate in *Escherichia coli*. Studies with a *ubiA*− *menA*− double quinone mutant. Biochim. Biophys. Acta BBA - Bioenerg. 461, 84–100. https://doi.org/10.1016/0005-2728(77)90071-8

Wang, W., Gao, Y., Tang, Y., Zhou, X., Lai, Y., Zhou, S., Zhang, Y., Yang, X., Liu, F., Guddat, L.W., Wang, Q., Rao, Z., Gong, H., 2021. Cryo-EM structure of mycobacterial cytochrome bd reveals two oxygen access channels. Nat. Commun. 12, 4621. https://doi.org/10.1038/s41467-021-24924-w

Warburg, O., 1925. Iron, the Oxygen-Carrier of Respiration-Ferment. Science 61, 575–582. https://doi.org/10.1126/science.61.1588.575

Warburg, O.W., 1931. The oxygen-transferring ferment of respiration [WWW Document]. URL https://www.nobelprize.org/prizes/medicine/1931/warburg/lecture/ (accessed 9.7.24).

Watanabe, S., Zimmermann, M., Goodwin, M.B., Sauer, U., Barry 3rd, C.E., Boshoff, H.I., 2011. Fumarate Reductase Activity Maintains an Energized Membrane in Anaerobic Mycobacterium tuberculosis. PLOS Pathog. 7, e1002287. https://doi.org/10.1371/journal.ppat.1002287

Watt, I.N., Montgomery, M.G., Runswick, M.J., Leslie, A.G.W., Walker, J.E., 2010. Bioenergetic cost of making an adenosine triphosphate molecule in animal mitochondria. Proc. Natl. Acad. Sci. 107, 16823–16827. https://doi.org/10.1073/pnas.1011099107

Weinstein, E.A., Yano, T., Li, L.-S., Avarbock, D., Avarbock, A., Helm, D., McColm, A.A., Duncan, K., Lonsdale, J.T., Rubin, H., 2005. Inhibitors of type II NADH:menaquinone oxidoreductase represent a class of antitubercular drugs. Proc. Natl. Acad. Sci. 102, 4548–4553. https://doi.org/10.1073/pnas.0500469102

WHO, 2023. Global Tuberculosis Report 2023 [WWW Document]. URL https://www.who.int/teams/global-tuberculosis-programme/tb-reports/global-tuberculosis-report-2023 (accessed 9.27.24).

WHO, 2022. WHO consolidated guidelines on tuberculosis. Module 4: treatment - drug-resistant tuberculosis treatment, 2022 update [WWW Document]. URL https://www.who.int/publications/i/item/9789240063129 (accessed 9.12.24).

Wikström, M.K.F., Berden, J.A., 1972. Oxidoreduction of cytochrome *b* in the presence of antimycin. Biochim. Biophys. Acta BBA - Bioenerg. 283, 403–420. https://doi.org/10.1016/0005-2728(72)90258-7

Wiseman, B., Nitharwal, R.G., Fedotovskaya, O., Schäfer, J., Guo, H., Kuang, Q., Benlekbir, S., Sjöstrand, D., Ädelroth, P., Rubinstein, J.L., Brzezinski, P., Högbom, M., 2018. Structure of a functional obligate complex III2IV2 respiratory supercomplex from Mycobacterium smegmatis. Nat. Struct. Mol. Biol. 25, 1128–1136. https://doi.org/10.1038/s41594-018-0160-3

Wittig, I., Karas, M., Schägger, H., 2007. High Resolution Clear Native Electrophoresis for In-gel Functional Assays and Fluorescence Studies of Membrane Protein Complexes*. Mol. Cell. Proteomics 6, 1215–1225. https://doi.org/10.1074/mcp.M700076-MCP200

Wu, D., Mehdipour, A.R., Finke, F., Goojani, H.G., Groh, R.R., Grund, T.N., Reichhart, T.M.B., Zimmermann, R., Welsch, S., Bald, D., Shepherd, M., Hummer, G., Safarian, S., 2023. Dissecting the conformational complexity and mechanism of a bacterial heme transporter. Nat. Chem. Biol. 19, 992–1003. https://doi.org/10.1038/s41589-023-01314-5

Wu, M., Neilson, A., Swift, A.L., Moran, R., Tamagnine, J., Parslow, D., Armistead, S., Lemire, K., Orrell, J., Teich, J., Chomicz, S., Ferrick, D.A., 2007. Multiparameter metabolic analysis reveals a close link between attenuated mitochondrial bioenergetic function and enhanced glycolysis dependency in human tumor cells. Am. J. Physiol.-Cell Physiol. 292, C125–C136. https://doi.org/10.1152/ajpcell.00247.2006

Yano, T., Kassovska-Bratinova, S., Teh, J.S., Winkler, J., Sullivan, K., Isaacs, A., Schechter, N.M., Rubin, H., 2011. Reduction of Clofazimine by Mycobacterial Type 2 NADH:Quinone Oxidoreductase: A PATHWAY FOR THE GENERATION OF BACTERICIDAL LEVELS OF REACTIVE OXYGEN SPECIES *. J. Biol. Chem. 286, 10276–10287. https://doi.org/10.1074/jbc.M110.200501

Yano, T., Li, L.-S., Weinstein, E., Teh, J.-S., Rubin, H., 2006. Steady-state Kinetics and Inhibitory Action of Antitubercular Phenothiazines on Mycobacterium tuberculosis Type-II NADH-Menaquinone Oxidoreductase (NDH-2) *. J. Biol. Chem. 281, 11456–11463. https://doi.org/10.1074/jbc.M508844200

Yanofsky, D.J., Di Trani, J.M., Król, S., Abdelaziz, R., Bueler, S.A., Imming, P., Brzezinski, P., Rubinstein, J.L., 2021. Structure of mycobacterial CIII2CIV2 respiratory supercomplex bound to the tuberculosis drug candidate telacebec (Q203). eLife 10, e71959. https://doi.org/10.7554/eLife.71959

Yodh, A., Chance, B., 1995. Spectroscopy and Imaging with Diffusing Light. Phys. Today 48, 34–40. https://doi.org/10.1063/1.881445

Yu, J., Hederstedt, L., Piggot, P.J., 1995. The cytochrome bc complex (menaquinone:cytochrome c reductase) in Bacillus subtilis has a nontraditional subunit organization. J. Bacteriol. 177, 6751–6760. https://doi.org/10.1128/jb.177.23.6751-6760.1995

Zerbetto, E., Vergani, L., Dabbeni-Sala, F., 1997. Quantification of muscle mitochondrial oxidative phosphorylation enzymes via histochemical staining of blue native polyacrylamide gels. ELECTROPHORESIS 18, 2059–2064. https://doi.org/10.1002/elps.1150181131

Zhang, Yuying, Lai, Y., Zhou, S., Ran, T., Zhang, Yue, Zhao, Z., Feng, Z., Yu, L., Xu, J., Shi, K., Wang, J., Pang, Y., Li, L., Chen, H., Guddat, L.W., Gao, Y., Liu, F., Rao, Z., Gong, H., 2024. Inhibition of M. tuberculosis and human ATP synthase by BDQ and TBAJ-587. Nature 631, 409–414. https://doi.org/10.1038/s41586-024-07605-8

Zhang, Z., Huang, L., Shulmeister, V.M., Chi, Y.-I., Kim, K.K., Hung, L.-W., Crofts, A.R., Berry, E.A., Kim, S.-H., 1998. Electron transfer by domain movement in cytochrome bc1. Nature 392, 677–684. https://doi.org/10.1038/33612

Zhou, X., Gao, Y., Wang, W., Yang, Xiaolin, Yang, Xiuna, Liu, F., Tang, Y., Lam, S.M., Shui, G., Yu, L., Tian, C., Guddat, L.W., Wang, Q., Rao, Z., Gong, H., 2021. Architecture of the mycobacterial succinate dehydrogenase with a membrane-embedded Rieske FeS cluster. Proc. Natl. Acad. Sci. 118, e2022308118. https://doi.org/10.1073/pnas.2022308118

Appendix 1

Hemeheme_4_1int_thesis.py

```
#!/usr/bin/env python3
# -*- coding: utf-8 -*-
"""
Created on Thu Jun 20 13:28:13 2024
@author: rowan
"""
import numpy as np
import matplotlib.pyplot as plt
from scipy.optimize import curve_fit

#Setting up default parameters for plots
from matplotlib import rcParams
rcParams['axes.spines.top'] = False
rcParams['axes.spines.right'] = False
rcParams['font.family'] = 'Arial'#Setting up default parameters for plots
rcParams['axes.labelsize'] = 16
rcParams['legend.fontsize'] = 16
rcParams['lines.linewidth'] = 2.8
rcParams['legend.handlelength'] = 0.8
rcParams['xtick.labelsize'] = 16
```

```
rcParams['ytick.labelsize'] = 16


# Working directory, Fit applied and red or ox

wd='/Users/rowan/Documents/Y3
PhD/delta_psi/Titrationprocessing/Tidied_spectra_process'

ox_red ='red'#'ox'##


#file locaitons

titration_location = wd +'/stras_data/'+ox_red+'_titration.csv'

voltage_location = wd +'/stras_data/'+ox_red+'_voltages.csv'


# Importing titration data

data = np.genfromtxt(titration_location, delimiter = ',')## Data location

start =1

end =451


# Import and assign the data to var

titr = np.flip(data[start:end:,5::2],0)

wavelength = np.flip(data[start:end:,0],0)

volt = np.genfromtxt(voltage_location, delimiter = ',') # voltage location

voltages=volt[1::,1]+208

voltages=voltages

oxind = np.argmin(voltages)
```

```
# Constants

# Scaled for mV inputs

F = 96485/1000 # in Joules, Faraday's constant#

R = 8.3145 # J.mol-1.K-1, Gas constant

n = 1# 2 electrons

T = 310.15 # K, kelvin, temperature

constant = ((R*T)/(n*F))



# Parameters for graphs, legends and colours

C_para = ['_haem_CC_','orange','haem $\mathit{cc}$' ]

Bh_para = ['_haem_BH_','cyan','haem $\mathit{b}_\mathregular{H}$']

Bl_para = ['_haem_BL_','darkblue','haem $\mathit{b}_\mathregular{L}$']

A_para = ['_haem_AA3_','green','haem $\mathit{aa}_\mathregular{3}$']


haems = (C_para[2], Bl_para[2], Bh_para[2] ,A_para[2])


bdelta = 70

nC = len(haems)

nI = 1

nCI = nC +1

nP = len(haems) +nI
```

```
def pf_c(voltages,em):
        return np.exp((em-voltages)/constant)
nC = len(haems)
# No. components, number of haems + no. interactions
nCI = nC+1
def bin_four(v,Em_1,Em_2,Em_3,Em_4, I1):#
    I1 = np.exp(I1/constant)
    y1 = 1
    h1, h2, h3, h4= pf_c(v,Em_1),pf_c(v,Em_2),pf_c(v,Em_3),pf_c(v,Em_4)
    y2 = y1*h1
    y3 = y1*h2
    y4 = y1*h1*h2
    y5 = y1*h3
    y6 = y1*h1*h3
    y7 = y1*h2*h3*I1
    y8 = y1*h1*h2*h3*I1
    y9 = y1*h4
    y10 = y1*h1*h4
    y11 = y1*h2*h4
    y12 = y1*h1*h2*h4
    y13 = y1*h3*h4
    y14 = y1*h1*h3*h4
    y15 = y1*h2*h3*h4*I1
    y16 = y1*h1*h2*h3*h4*I1
```

```
    sumY = [y1,y2,y3,y4,y5,y6,y7,y8,y9,y10,y11,y12,y13,y14,y15,y16]
    yT = sum(sumY)
    p1 = sum(( y2, y4, y6, y8,y10,y12,y14,y16)/yT)
    p2 = sum(( y3, y4, y7, y8,y11,y12,y15,y16)/yT)
    p3 = sum(( y5, y6, y7, y8,y13,y14,y15,y16)/yT)
    p4 = sum(( y9,y10,y11,y12,y13,y14,y15,y16)/yT)
    return p1,p2,p3,p4


def ther_abs_func(voltages,par):
    fp = bin_four(voltages, par[-5],par[-4], par[-3],par[-2], par[-1])
    p1, p2,p3,p4 = fp
    p= np.stack((p1,p2,p3,p4),axis = 1)
    e = par[:-nCI]
    e = e.reshape(len(wavelength),nC)
    A = np.matmul(e,np.transpose(p))
    return A.reshape(-1)


def fun(P,V, T):
    return ther_abs_func(V, P) - T.reshape(-1)

m= [150,-275, -125, 225, -60]# half way between bounds
def specdeco_func(voltages,Em_1,Em_2,Em_3,Em_4, I):#
```

```
fp = bin_four(voltages,Em_1, Em_2, Em_3, Em_4 , I)#)

p1, p2,p3,p4 = fp#, p5

p= np.stack((p1,p2,p3,p4),axis = 1)#

fig1, (ax1) = plt.subplots(figsize=[6.67,5])

ax1.plot(voltages,p1, color = 'orange', label = haems[0])

ax1.plot(voltages,p2, color = 'darkblue', label = haems[1])

ax1.plot(voltages,p3, color = 'cyan', label = haems[2])

ax1.plot(voltages,p4, color = 'green', label = haems[3])

ax1.set(xlabel = 'Potential (mV vs SHE)', ylabel = 'Fraction reduced')

ax1.legend(bbox_to_anchor=(0.75, 0.8), loc='upper left')

plt.show()

d = np.matmul(np.matmul(titr, p), np.linalg.inv(np.matmul(np.transpose(p),p)))

D = d*1000

dmax = np.max(D)+1

dmin = np.min(D)-1

fig, (ax3) = plt.subplots(figsize=[6.67,5])

ax3.plot(wavelength[:150],D[:150,0], color = 'orange', label = haems[0])

ax3.plot(wavelength[:150],D[:150,1], color = 'darkblue', label = haems[1])

ax3.plot(wavelength[:150],D[:150,2], color = 'cyan', label = haems[2])

ax3.plot(wavelength[:150],D[:150,3], color = 'green', label = haems[3])

ax3.axvline(x = 500, color = 'black', linewidth = 1 )

ax3.plot(wavelength[150:300],D[150:300,0]*5, color = 'orange', label = haems[0])

ax3.plot(wavelength[150:300],D[150:300,1]*5, color = 'darkblue', label = haems[1])

ax3.plot(wavelength[150:300],D[150:300,2]*5, color = 'cyan', label = haems[2])
```

```
    ax3.plot(wavelength[150:300],D[150:300,3]*5, color = 'green', label = haems[3])
    ax3.set_ylim(dmin,dmax)
    pos = ax3.get_position()
    ax3.set_position([pos.x0, pos.y0, pos.width * 0.95, pos.height])
    ax3.set(xlabel = 'Wavelength (nm)', ylabel = 'Absorbance (mOD)')
    ax3.legend(haems, bbox_to_anchor=(0.85, 0.9), loc='upper left')
    ax3.text((wavelength[280]),20,('x5'), fontsize = 16)
    plt.show()
    fig5, (ax5) = plt.subplots(2,2, figsize = [6.67,8])
    ax5[1,0].plot(wavelength[150:300],D[150:300,0], color = 'orange', label = haems[0])
    ax5[1,0].text(575,1.5,("$E_{cc} =$"+f'{Em_1:.3g} mV'),fontsize = 16)
    ax5[0,1].plot(wavelength[150:300],D[150:300,1], color = 'darkblue', label = haems[1])
    ax5[0,1].text(575,2.2,("$E_{b_{L}} =$"+f'{Em_2:.3g} mV\n'+"$I_{b} =$"+ f'{I:.3g}
mV'),fontsize = 16)
    ax5[0,0].plot(wavelength[150:300],D[150:300,2], color = 'cyan', label = haems[2])
    ax5[0,0].text(575,2.2,("$E_{b_{H}} =$"+f'{Em_3:.3g} mV\n'+"$I_{b} =$"+ f'{I:.3g}
mV'),fontsize = 16)
    ax5[1,1].plot(wavelength[150:300],D[150:300,3], color = 'green', label = haems[3])
    ax5[1,1].text(507,2.7,("$E_{aa_{3}} =$"+f'{Em_4:.3g} mV'),fontsize = 16)
    pos = ax5[0,0].get_position()
    ax5[0,0].set_position([pos.x0, pos.y0, pos.width , pos.height])
    pos = ax5[0,1].get_position()
    ax5[0,1].set_position([pos.x0, pos.y0, pos.width, pos.height])
    pos = ax5[1,0].get_position()
    ax5[1,0].set_position([pos.x0, pos.y0, pos.width , pos.height])
```

```
    pos = ax5[1,1].get_position()
    ax5[1,1].set_position([pos.x0, pos.y0, pos.width , pos.height])
    for ax in ax5.flat:
        ax.set(xlabel = 'Wavelength (nm)', ylabel = 'Absorbance (mOD)')
        ax.set_xlim(wavelength[150], wavelength[299])
        ax.set_ylim(np.min(D[150:300]), np.max(D[150:300]))
    for ax in ax5.flat:
        ax.label_outer()
        ax.legend(bbox_to_anchor=(0.02, 0.0),loc = 'lower left')
    ax5[1,0].legend(bbox_to_anchor=(1.05,1),loc = 'upper right')
    plt.show()
    return d, fp

D, fp = specdeco_func(voltages,m[0],m[1],m[2],m[3], m[4])

blanks = np.zeros(len(wavelength)*nC).reshape(len(wavelength),nC)#pred_DS.reshape(-1)

params = np.append(blanks.reshape(-1), m)

upboun =  np.zeros(len(wavelength)*nC) +0.025
lowboun =  np.zeros(len(wavelength)*nC) -0.015

upboun = np.append(upboun, [200,-150,0, 300, -10])
lowboun = np.append(lowboun, [0,-400,-250, 150, -100])
```

```
fig4, (ax4,ax41) = plt.subplots(1,2,figsize=[8,6])
ax4.plot(wavelength[:150],blanks[:150,0]*1000, color = 'orange', label = haems[0])
ax4.plot(wavelength[:150],blanks[:150,1]*1000, color = 'darkblue', label = haems[1])
ax4.plot(wavelength[:150],blanks[:150,2]*1000, color = 'cyan', label = haems[2])
ax4.plot(wavelength[:150],blanks[:150,3]*1000, color = 'green', label = haems[3])
ax41.plot(wavelength[150:300],blanks[150:300,0]*1000, color = 'orange', label = haems[0])
ax41.plot(wavelength[150:300],blanks[150:300,1]*1000, color = 'darkblue', label = haems[1])
ax41.plot(wavelength[150:300],blanks[150:300,2]*1000, color = 'cyan', label = haems[2])
ax41.plot(wavelength[150:300],blanks[150:300,3]*1000, color = 'green', label = haems[3])



def _fun(M, *args):
    voltages = M
    par = args[-nP:]
    fp = bin_four(voltages,*par)
    p1, p2,p3,p4= fp
    p= np.stack((p1,p2,p3,p4),axis = 1)
    e = np.array(args[:-nP])
    e = e.reshape(len(wavelength),nC)
    A = np.matmul(e,np.transpose(p))
    return A.reshape(-1)
```

```
par, cov = curve_fit(_fun,voltages, titr.reshape(-1) , params.reshape(-1), bounds = (lowboun,upboun))


new_DS = (par[:-nP]).reshape(len(wavelength),nC)

new_Em = par[-nP:]


answer = specdeco_func(voltages, *new_Em)


cov1 = np.sqrt(np.diag(cov))

cov2  = (cov1[:-nP]).reshape(len(wavelength),nC)*1000


spec_cov = (cov1[-nP:])



fig5, (ax5) = plt.subplots(2,2, figsize = [8,10])

D = answer[0]

Em_1, Em_2,Em_3, Em_4 , I = new_Em

ax5[1,0].plot(wavelength[150:300],D[150:300,0], color = "orange", label = haems[0])

ax5[1,0].text(570,1,("$E_{c1} =$"+f" {Em_1:.3g} mV"),fontsize = 16)

ax5[0,1].plot(wavelength[150:300],D[150:300,1], color = "darkblue", label = haems[1])

ax5[0,1].text(575,1,("$E_{bL} =$"+f"{Em_2:.3g} mV\n "

                    "$E_{bH} =$"+f"{Em_3:.3g} mV\n "

                    "$I_{b} =$"+f"{I:.3g} mV"),fontsize = 16)

ax5[0,0].plot(wavelength[150:300],D[150:300,2], color = "cyan", label = haems[2])
```

```
ax5[0,0].text(575,1,("$E_{bL} =$"+f"{Em_2:.3g} mV\n "
                    "$E_{bH} =$"+f"{Em_3:.3g} mV\n "
                    "$I_{b} =$"+f"{I:.3g} mV"),fontsize = 16)
ax5[1,1].plot(wavelength[150:300],D[150:300,3], color = "green", label = haems[3])
ax5[1,1].text(507,1.5,("$E_{a1} =$"+f" {Em_4:.3g} mV"),fontsize = 16)


for ax in ax5.flat:
    ax.set(xlabel = "Wavelength"
           , ylabel = "Absorbance (mOD)")
for ax in ax5.flat:


    ax.legend(bbox_to_anchor=(1, 1),loc = "upper right")
ax5[1,1].legend(bbox_to_anchor=(0.02, 0.0),loc = "lower left")
```